# Molecular Regulation of Satellite Cell Fate

Peter Feige

A thesis submitted to the University of Ottawa
in partial fulfillment of the requirements for the
Doctorate of Philosophy in Cellular & Molecular Medicine

Department of Cellular & Molecular Medicine
Faculty of Medicine
University of Ottawa

**Table of Contents**

## List of Figures

### General Introduction



### Manuscript I



### Manuscript II



### Manuscript III



### Manuscript IV



### Manuscript V



### General Discussion

**List of Appendix Figures**

## Appendix A – Supplemental data for Manuscript I



## Appendix B – Supplemental data for Manuscript II



## Appendix C – Supplemental data for Manuscript III



## Appendix D – Supplemental data for Manuscript IV



## Appendix E – Supplemental data for Manuscript V

## List of abbreviations

| | |
|---|---|
| **ADP** | Adenosine diphosphate |
| **ANP** | Atrial Natriuretic Peptide |
| **ATP** | Adenosine triphosphate |
| **Aurka** | Aurora kinase A |
| **BAT** | Brown Adipose Tissue |
| **bFGF** | Basic fibroblast growth factor |
| **C/EBP** | CCAAT-enhancer-binding proteins |
| **Cidea** | Cell Death Inducing DFFA Like Effector A |
| **cKO** | Conditional Knockout |
| **CTX** | Cardiotoxin |
| **DAPI** | 4',6-diamidino-2-phenylindole |
| **DGC** | Dystrophin-associated glycoprotein |
| **Dio2** | Type II iodothyronine deiodinase |
| **DMD** | Duchenne muscular dystrophy |
| **DNA** | Deoxyribonucleic acid |
| **ECM** | Extracellular matrix |
| **EDL** | *Extensor Digitorum Longus* muscle |
| **EdU** | 5-ethynyl-2'-deoxyuridine |
| **EGF** | Epidermal growth factor receptor |
| **EGFR** | Epidermal growth factor receptor |
| **eYFP** | Enhanced Yellow fluorescent protein |
| **FACS** | Fluorescence-activated cell sorting |
| **FDA** | U.S. Food and Drug Administration |
| **FGF2** | Fibroblast growth factor 2 |
| **HSP90** | 90 kDa heat shock protein |
| **JAK** | Janus kinase |
| **LNA** | Locked Nucleic Acid |
| **MAPK** | Mitogen-activated protein kinase |
| **MARK2** | Microtubule Affinity Regulating Kinase |
| **M-cad** | Muscle-specific cadherin |
| **miRNA** | Micro RNA |
| **MRF** | Myogenic regulatory factor |
| **mRNA** | Messenger RNA |
| **Myf5** | Myogenic factor 5 |
| **Myod1** | Myogenic differentiation 1 |
| **NCAM-1** | Neural cell adhesion molecule |
| **nGFP** | Nuclear green fluorescent protein |
| **nTdT** | Nuclear TdTomato |
| **P38** | P38 mitogen-activated protein kinase |
| **PAR** | Partition-defective |
| **Pard3** | Par-3 Family Cogell Polarity Regulator |
| **PARP1/2** | Poly [ADP-ribose] polymerase 1/2 |
| **Pax3** | Paired-box protein 3 |
| **Pax7** | Paired-box protein 7 |
| **PFTα** | Pifithrin-α |
| **Pgc1α** | PPARG Coactivator 1 Alpha |
| **PPARα** | Peroxisome proliferator-activated receptor |
| **PPARγ** | Peroxisome proliferator-activated receptor |
| **Prdm16** | PR domain containing 16 |
| **Pre-miRNA** | Precursor Micro RNA |
| **Pri-miRNA** | Primary Micro RNA |
| **RFP** | Red fluorescent protein |
| **RNA** | Ribonucleic acid |
| **SERCA** | Sarco/endoplasmic reticulum Ca2+ -ATPase |
| **siRNA** | Small interfering RNA |
| **siRNA** | Silencing RNA |
| **Spry1** | Sprouty RTK Signalling Antagonist 1 |
| **STAT** | Signal transducer and activator of |
| **TA** | *Tibialis Anterior* muscle |
| **TTP** | Tristetraprolin |
| **UCP1** | Uncoupling Protein 1 |
| **VEGFR** | Vascular endothelial growth factor receptor |

“Everyman ought to be inquisitive through every hour of his great adventure down to the day when he shall no longer cast a shadow in the sun. For if he dies without a question in his heart, what excuse is there for his continuance?”

Frank Moore Colby

## Acknowledgements

I am fortunate to have had an extraordinary mentor in Dr. Michael Rudnicki who has provided an exceptional training environment for my graduate studies. Michael has nurtured a raw sense of curiosity in me and provided the freedom to explore my research questions. Michael's supportive nature has been instrumental in overcoming the challenges of graduate research and in planning for the future. The skills learned in the lab have built the foundation upon which I will grow my career.

I am grateful for the financial support from the Canadian Institutes of Health Research (CIHR) CGS-D award, financial support from the University of Ottawa and tremendous financial and training support from the Stem Cell Network which have all helped enrich my graduate training.

The environment at the Ottawa Hospital Research Institute has been critical in my research success, providing an abundance of opportunities to further my research knowledge, skills and collaborate with exemplary mentors. I am grateful for the friendship and support I received from lab mates past and present. I am thankful for the guidance of Dr. Marjorie Brand, Dr. Mary-Ellen Harper and Dr. Lynn Megeney who facilitated my thesis advisory committee. I am especially grateful for the continued support from Dr. Nadine Wiper-Bergeron who has been an exceptional mentor throughout my graduate studies and has provided countless hours supporting my endeavours.

I would like to thank my wife, Bridget, daughter, Ava, and family who have been supportive and patient with the lows and highs of my graduate studies. For all the family dinners cut short, missed dates and long hours, at least now my thesis has form.

## Abstract

Muscle homeostasis and regeneration are complex cellular processes orchestrated by muscle stem cells and their interaction with their stem cell microenvironment. The fate of a muscle stem cell is influenced by different conditions such as muscle injury, cold stress, or disease. During extensive muscle repair and in the context of muscular dystrophy, we identified the critical function of the Epidermal Growth Factor Receptor (EGFR) in establishing cell polarity and in turn the efficient formation of myogenic progeny able to repair muscle. Using a novel drug screen, we identified the p53 protein to regulate muscle stem cell fate decision to repress the formation of brown adipose tissue as a means to regulate whole-body metabolism. To increase the impact of our research we also optimized protocols evaluating mouse satellite cell transplantation to delineate stem cell hierarchy and developed a new paradigm to model human muscle stem cell fate to better translate our findings into the clinical arena. These findings reveal the tunable nature of stem cell fate decisions and highlight the development of research tools to accelerate the translation of research findings to improve human health.

## Copyright Authorizations

**Manuscript II was published in the journal *Cell Stem Cell* in 2019:**

Reprinted from Cell Stem Cell, Volume 24 issue 3, Wang YX, Feige P, Brun CE, Hekmatnejad B, Dumont NA, Renaud JM, Faulkes S, Guindon DE, Rudnicki MA, pages 419-432, copyright 2019.

> As an author, non-exclusive rights including the right "To reproduce, or allow a third party to reproduce the Article in whole or in part in any printed volume (book or thesis) authored by you", is retained as per Elsevier's publishing policy.

**Manuscript III was published in the journal *Nature Protocols* in 2020:**

Reprinted from Nature Protocols, Volume 15, Feige, P and Rudnicki, M.A. Pages 1082-1097, copyright 2020.

> As an author, non-exclusive rights including the right "To reproduce, or allow a third party to reproduce the Article in whole or in part in any printed volume (book or thesis) authored by you", is retained as per Springer's publishing policy.

Figure 1, Figure 2 and Figure 35 are reused from cited reviews within publishing rights as the author.

Figure 3, Figure 4, Figure 34 are original.

## General introduction

## Skeletal muscle stem cells

Skeletal muscle is a complex tissue, responsible for mobility, thermoregulation and breathing. Skeletal muscle maintenance, growth, and repair is facilitated by muscle stem cells (satellite cells) which reside within skeletal muscle. Satellite cells sit within a specialized cleft beneath the muscle fibre basal lamina and in contact with the myofibre. Satellite cells are maintained in a mitotically quiescent state but are poised to become active and enter the cell cycle in response to external cues such as weight-bearing, trauma or injury[1]. Satellite cell activation from quiescence creates transient amplifying cells termed myogenic progenitors, that divide for multiple rounds before terminally differentiating to form new or repair existing muscle fibres. The stem cell pool is maintained through satellite cell self-renewal, sustaining satellite cells over time[2]. With age, however, the progressive loss of satellite cell number is observed with a functional decline in skeletal muscle[3,4].

The balance of cellular commitment and self-renewal is critical to maintaining efficient muscle regeneration over a lifetime. A mechanism of balancing self-renewal and commitment is through asymmetric cell division, where asymmetric segregation of intrinsic fate determinants prior to division facilitates divergent daughter cell fate. The resultant satellite cell division gives rise to a new satellite cell and a committed daughter cell able to amplify and facilitate muscle repair. Resulting stem cells and committed progeny can propagate through planar symmetric divisions to expand their numbers and maintain homeostatic levels. Tight regulation of this balance is critical to producing enough committed progeny for efficient muscle repair while maintaining an appropriate stem cell pool for future needs[5].

In conditions of muscle wasting, such as Duchenne's Muscular Dystrophy (DMD), progressive degeneration in skeletal muscle is observed due to mutations in the

dystrophin gene resulting in truncation or loss of the dystrophin protein. This phenotype is due to the role of dystrophin in connecting the extracellular matrix of the muscle to the myofibre and the function of dystrophin in promoting satellite stem cell polarity during asymmetric division. In the absence of dystrophin, muscle fibre integrity is compromised[6] and satellite cell homeostasis is perturbed resulting in muscle stem cell hyperplasia[7](Figure 1). Patients with DMD suffer progressive muscle fibrosis, loss of ambulation, cardiac dysfunction and severely limited lifespan[8]. In contrast, ageing skeletal muscle in rodents exhibits reduced self-renewal, increased asymmetric division leading to increased stem cell commitment[9–12] resulting in age-related muscle weakness and sarcopenia. These insights highlight the utility in understanding the cause of satellite cell fate decisions to design therapeutics able to correct deficits in regeneration and promote muscle repair in conditions such as muscular dystrophy or age.

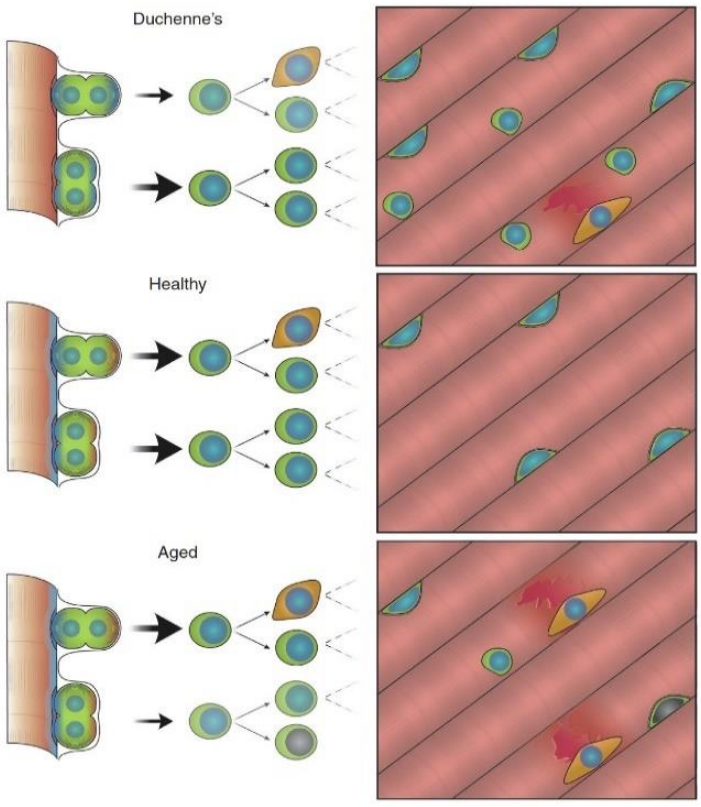


Figure 1**: Satellite cell self-renewal and commitment are critical for muscle regeneration.** Regeneration is impaired during age and disease due to altered cell signalling and changes to the satellite cell niche. In Duchenne muscular dystrophy (DMD), loss of dystrophin protein results in myofiber fragility and constant damage in DMD muscle. This results in increased numbers of satellite cells that inefficiently differentiate, resulting eventually in satellite cell exhaustion. With age, accumulation of DNA damage, altered niche signalling and an increasingly stiff myofiber result in precocious myogenic commitment as well as cellular senescence. The resulting muscle has an inability to repair due to exhaustion of the satellite cell pool. Adapted from Feige & Rudnicki 2018.

## The Satellite cell niche establishes cell polarity and asymmetric division

Quiescent satellite cells reside within the satellite cell niche and express adhesion proteins in a polarized manner on the basal versus apical cell surface which acts to influence cell polarity and stem cell quiescence[5](Figure 2). The basal surface of quiescent satellite cells is enriched for Integrin-A7, Integrin-B1 and dystroglycan while the sarcolemmal surface is enriched for M-cadherin and NCAM[13–15]. Satellite cells are able to sequester soluble growth factors and interact with components in the extracellular matrix through the heparan sulphate proteoglycans Syndecan-3 and -4 that are functional co-receptors to Notch, Frizzled-7 and integrins[16–18].

Satellite cell interactions with the niche functionally maintain quiescence. Loss of satellite cell interactions through Notch results in impaired satellite cell adhesion within the niche[19], loss of collagen V expression from satellite cells and in turn precocious exit from quiescence[20] while the loss of Notch1 and Notch2 result in loss of the satellite cell pool[21]. Accumulation of the notch inhibitor Numb in satellite cells represses Notch activity resulting in myogenic commitment[22,23].

The polarized satellite cell and niche establish internal cell polarity by spatially restricting fate determinants prior to cell division. Following apical-basal oriented asymmetric division, one daughter cell loses contact with the basal lamina, whereas the cell maintaining niche interactions is thought to maintain stemness and return to quiescence. Establishing an apical-basal oriented mitotic spindle through the PAR polarity complex and proper sequestering of cell fate determinants prior to division facilitates divergent cell fate in the resultant asymmetric division[5]. Loss of internal cell polarity through PAR mislocalization in dystrophin-deficient satellite cells reduces the rate of asymmetric division and in turn limits the production of myogenic progenitors required for efficient muscle repair[7].

Asymmetric division facilitates divergent cell fates in daughter cells through asymmetric inheritance of niche interactions, epigenetic regulators, transcription factors dictating myogenic fate and proteins integrating discrete ques from soluble growth factors. Following an asymmetric division, the committed daughter cell is epigenetically primed for myogenic commitment by the arginine methyltransferase Carm1 which methylates Pax7 to facilitate the recruitment of histone methyltransferases to the Myf5 promoter, resulting in a permissive chromatin landscape allowing transcription of Myf5[24]. Additionally, the PAR polarity complex is restricted to the apical cell where it activates p38A-B MAP kinase resulting in MyoD expression[25] and facilitating transient amplification of committed myogenic cells. P38α-β activity is regulated by Integrin-β1 and Spry1 which limit FGF2 signalling within satellite cells and restrict p38α-β MAPK activity within quiescent satellite cells[26,27], suggesting Integrin-β1 and Spry1 sense the niche to maintain satellite cell quiescence and homeostasis. The asymmetric nature of the niche and internal polarity within satellite cells allows for divergent daughter cell fate and support the idea that the spatial localization of satellite cells and their interaction with the niche dictate inheritance of cell fate determinants.

Apico-basal oriented satellite cell divisions have additionally been observed during homeostatic maintenance *in vivo*[22,28] and following acute injury[22,29] where a subset of satellite cells preferentially divide in a polarized manner. These observations are consistent with the theory that a subset of satellite cells undergo apical-basal oriented asymmetric division to maintain satellite stem cells and produce committed myogenic progeny that expand symmetrically to create sufficient numbers of cells for efficient muscle repair.

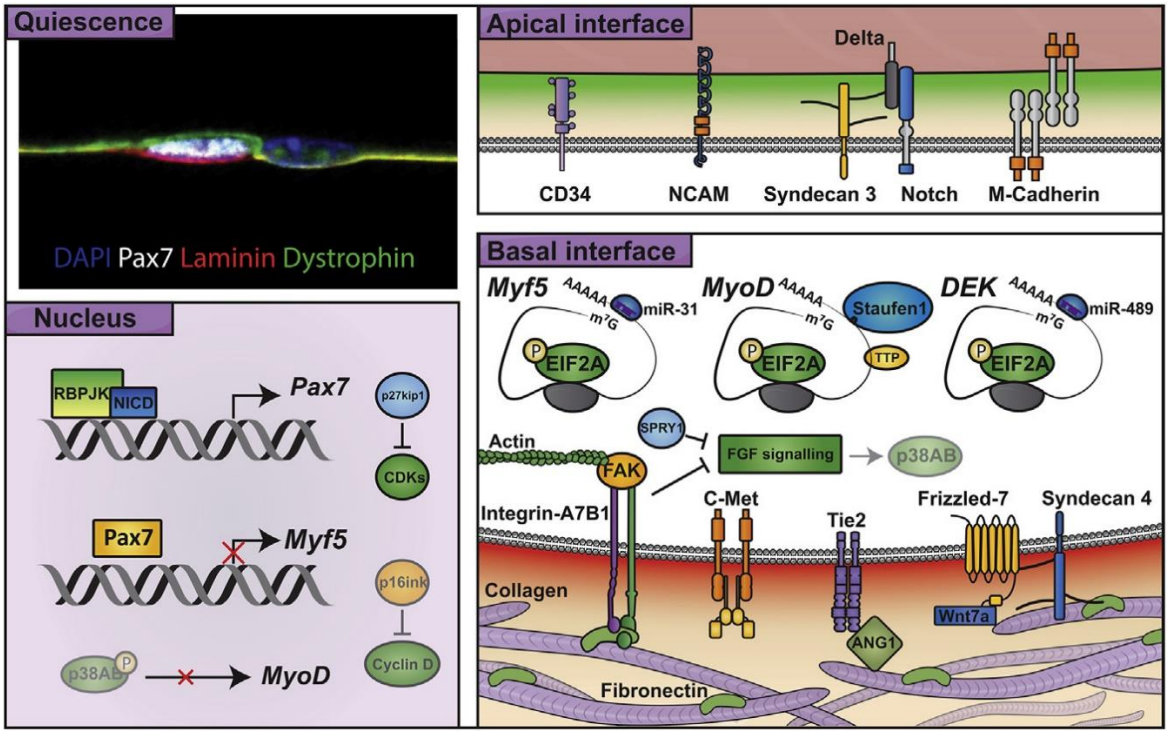


Figure 2: **The Satellite Cell Niche Establishes Polarity.** Quiescent satellite cells (white) sit below the basal lamina enriched in high-molecular-weight proteins, such as laminin (red) and fibronectin, and atop the muscle fiber sarcolemma expressing dystrophin (green), as depicted on the immunofluorescence micrograph. This anatomical location within the niche establishes satellite cell polarity. The apical interface between the satellite cell and the myofiber is enriched for CD34, Notch, Sdc-3, NCAM, and M-cadherin, and the basal interface is enriched for Tie2, c-MET, integrin-α7β1, and Sdc-4 and Fzd7 receptors. Satellite cells are characterized by Pax7 expression. Satellite cell quiescence is maintained by Notch signalling through NCID-RBPJK activity that promotes Pax7 expression, and non-methylated Pax7 limits Myf5 transcription. FGF signalling is mitigated by Spry1 and integrin-β1, which repress both p38α-β activation and, in turn, MyoD expression. Accumulation of p27kip1 inhibits cyclin-dependent kinases, maintaining satellite cells in a quiescent state. During ageing, accumulation of p16INK4a inhibits cyclin D, causing cells to be non-refractory to cell cycle entry, leading to cell senescence. Cytoplasmic Myf5 mRNA bound by miR-31 is sequestered to repress its translation. MyoD mRNA is degraded by TTP and Staufen1, and Dek is repressed by miR-489 to inhibit cell cycle entry. Phosphorylated eIF2α selectively blocks translation to further repress cell cycle entry and myogenic commitment. Adapted from Feige et al., 2018.

## Satellite cell heterogeneity affects cell fate

Satellite cells were originally considered a homogeneous population of committed muscle resident progenitors[30], however, growing evidence suggests satellite cells are distinct from amplifying progenitor cells and a subpopulation of satellite cells represents a long term

self-renewing population of multi-potent muscle stem cells that functions to balance self-renewal and commitment[22,31].

Heterogeneity within the satellite cell compartment is apparent in studies on satellite cell gene expression, satellite cell response to injury and satellite cell transplantation potential. Satellite cells uniformly express the transcription factor Pax7 with some cells co-expressing Pax7 and Pax3. Pax7 and Pax3 lie genetically upstream the myogenic regulatory factors Myf5 and MyoD[32]. Following satellite cell activation, the myogenic regulatory factors are required to promote transient amplification of myogenic progenitors and a facilitate subset of satellite cells to return to quiescence. Single-cell analysis of satellite cell populations suggests there exists extensive heterogeneity within the satellite cell pool and there is a subset of satellite cells expressing high Pax7 levels and low levels of Myf5[33,34]. Differences in satellite cell activation were observed in TetO-H2B-GFP studies where pulsed-chase administration of doxycycline resulted in heterogeneous populations of slow-cycling GFP label-retaining satellite cells and highly proliferative non-label retaining satellite cells[35]. Through transplantation studies, it was shown label-retaining satellite cells self-renewed while non-label retaining cells formed new muscle fibres. Notably, label-retaining satellite cells can be distinguished by expressing low levels of Myf5 transcript. Genetic labelling of Myf5 expression using mice harbouring *Myf5-Cre* and *R26R-YFP* Cre reporter alleles identified that a subpopulation of satellite cells (~10%) have never expressed Myf5 ($Myf5^{neg}$) and that these cells efficiently engraft following transplantation, giving rise to Myf5 expressing cells ($Myf5^{pos}$) and maintaining a pool of $Myf5^{neg}$ satellite cells[22]. In contrast, $Myf5^{pos}$ satellite cells have 8-fold less engraftment as satellite cells and instead fuse together to form new myofibres.

Together these studies support a relationship between heterogeneous gene expression with satellite cell function. Importantly, the $Myf5^{neg}$ satellite cells represent a satellite stem cell, capable of undergoing symmetric expansion to replenish the stem cell

pool or asymmetric division to produce Myf5$^{pos}$ myogenic progenitors[22]. The Myf5$^{neg}$ satellite stem cell provides a unique tool to investigate stem cell fate decisions and determine the genetic hierarchy that maintains its permissive state to regenerate the stem cell pool or undergo alternative division strategies in response to injury. Additionally, the Myf5$^{neg}$ satellite stem cell population is also heterogeneous in adult skeletal muscle, where ~10% of Myf5$^{neg}$ satellite stem cells maintain multipotent potential and are able to differentiate towards the brown adipogenic lineage *in vitro*, and *in vivo* in response to cold[31]. Brown adipose is able to increase whole-body energy expenditure and protect against obesity through mitochondrial uncoupled respiration[36]. Understanding the signalling pathways promoting multipotency in the Myf5$^{neg}$ satellite cell pool is of therapeutic interest to identify pathways promoting satellite cell longevity and means to promote energy expenditure by stimulating brown adipose formation.

## Thermogenesis is a key function of muscle and brown adipose

Thermoregulation is a critical requirement for body function and is a dynamic process mediated by the central nervous system in response to external temperature. When ambient temperature drops, humans adapt by peripheral vasoconstriction, piloerection increased shivering and non-shivering thermogenesis[37]. Both shivering and non-shivering thermogenesis generate heat through the hydrolysis of ATP. In a biochemical process, when the energy released by ATP hydrolysis to ADP exceeds that required to drive a reaction, the excess is dissipated as heat. During shivering thermogenesis or muscle contraction for locomotion, the energy released by ATP hydrolysis through myosin-ATPase exceeds that required to modify myosin protein conformation facilitating the myosin-actin binding power stroke and muscle contraction. Similarly, inefficiency in the reuptake of calcium by sarcoplasmic reticulum $Ca^{2+}$ ATPase (SERCA) required for muscle

relaxation, generates heat[38-39]. These inefficiencies are the biochemical basis for temperature increase during shivering or exercise[40].

Non-shivering thermogenesis also maintains basal thermoregulation during acute cold stress and in response to cold adaption. In muscle, calcium handling by SERCA can be uncoupled, where the protein Sarcolipin facilitates ATP hydrolysis without $Ca^{2+}$ movement into the sarcoplasmic reticulum, releasing heat as a by-product. This mechanism can occur without contraction[41] however it may disrupt calcium handling during locomotion. In other energy dispensing tissue such as brown adipose tissue (BAT), mitochondrial respiration can become uncoupled through the enrichment of Uncoupling Protein 1 (UCP1) in the inner mitochondrial membrane. UCP1 functions as a proton transporter, allowing accumulated protons to move out of the inner mitochondrial membrane and partially bypass ATP synthase, thus uncoupling the mitochondrial respiration chain from ATP production. Presence of UCP1 limits the negative feedback loop exerted by high levels of ATP on mitochondrial respiration[42] resulting in accelerated rates of fatty acid oxidation. The futile cycling of the respiratory chain causes the energy of substrate oxidation and inefficiency in each enzymatic step of respiration to be converted into heat[36]. UCP1-independent mechanisms such as futile substrate cycling through creatine metabolism also play a physiologic role in non-shivering thermogenesis[43]. The abundance of mitochondria in BAT allows for a substantial flux of free fatty acid or glucose[44] to expend large amounts of energy and balance dietary energy intake in opposition to storage in white adipose. This paradigm is utilized in placental mammals and human newborns to combat heat loss due to a larger surface area to volume and lack of insulation following birth.

Humans contain white, brown and beige adipose[45,46] where brown adipose depots express higher basal levels of thermogenic genes and are highly innervated and vascularized while beige depots are derived from a subset of white adipose and transiently

express thermogenic genes only upon cold or sympathetic stimulation. Innate human BAT has distinct embryonic origins from beige adipose[45,47,48] and is progressively lost with age[49] where ~10-40% of adults[50] possess cold or sympathetically inducible beige adipose stores. BAT and beige adipose activity are also decreased in the aged, obese or diabetic context[51,52].

Interestingly, brown adipose and muscle share many similarities including a Pax7/Myf5 expressing embryonic origin[47,53], microRNA expression including miR-1, *miR-133* and *miR-206*[54] as well as a myogenic gene signature[55–57]. The pathways involved in embryonic and adult development of brown adipose tissue are of clinical relevance as active BAT has the potential to increase basal metabolic rates in patients with obesity[58]. It is estimated ~1g of beige adipose can expend ~10kcal of energy per day[59,60]. Increasing BAT in animals promotes a lean phenotype[61] while the loss of BAT function is associated with metabolic disease and obesity[62]. As a proportion of adults lack BAT and its presence and activity is thought to be inversely proportional to body mass index[63,64], understanding the molecular mechanisms governing brown adipogenic fate decisions in stem cells is of interest to develop therapeutics to stimulate weight loss. Obesity negatively impacts human health and is associated with diabetes, hyperlipidemia, cancer and hypertension[65,66].

## Satellite cells are bi-potent

Transcriptionally, brown adipose formation is governed by peroxisome proliferator-activated receptor gamma (PPARγ), a nuclear receptor that through cooperation with the basic leucine-zipper factor C/EBP family, promotes general adipocyte gene expression[44]. The broad set of thermogenic genes that promote uncoupled respiration include; UCP1 facilitating uncoupled respiration, Cidea a transcriptional coactivator promoting lipid droplet remodelling, PPARα promoting fatty acid metabolism, Dio2 an enzyme catalyzing

the local conversion of the prohormone thyroxin to bioactive thyroid hormone to promote basal metabolic rate and Pgc1α a transcriptional coactivator promoting mitochondrial biogenesis. Thermogenic gene expression in BAT is facilitated by the transcription factor PR domain zinc finger 16 (PRDM16) which cooperated with the mediator complex to bind BAT gene enhancers and facilitate enhancer-promoter contacts and gene expression[67]. PRDM16 also cooperates with transcriptional corepressor complexes to repress white fat and muscle-specific gene expression[68]. Ectopic expression of PRDM16 is sufficient to drive thermogenic gene expression in muscle, white preadipocyte and fibroblast[47]. PRDM16 is required in beige adipocytes to facilitate chromatin modification promoting thermogenesis in response to cold[69,70]. PRDM16 and its transcriptional targets cooperate with histone and chromatin-modifying enzymes to establish a permissive chromatin state amenable to brown fat gene expression and stem cell commitment[71]. PRDM16 protein is under positive regulation by post-translational modification including sumoylation promoting stability[72] and negative regulation by miRNA mediated repression.

Satellite cells express a specific repertoire of muscle enriched miRNA, termed “MyomiRs” which act to reinforce the myogenic lineage in a temporal manner during satellite cell activation and myogenic differentiation. The traditional MyomiRs include miR-1, miR-133 and miR-206 which are expressed at three genomic loci in mouse and man[73], consisting of miR-133a1-miR-1-2, miR-133a2-miR-1-1 and miR-133b-miR-206 sharing primary transcripts. The promoters for these MyomiR possess multiple E-boxes[74] and are temporally regulated by the MRFs as long primary transcripts containing both miRNA species or independently, where miR-206 expression is excluded in cardiac tissues[75]. The primary transcript from the miR-133b-miR-206 loci (Linc-MD1) can also act as a competing endogenous RNA and sequester mature *miR-133* in skeletal muscle[73]. Genetic ablation studies suggest the deletion of individual MyomiR loci is well tolerated in muscle, where double knockout of both miR-1-133 loci results in embryonic lethality due to cardiovascular

malformation[76]. Mechanistically, *miR-1* and *miR-206* share similar seed sequences and promote myogenic differentiation by targeting *Pax7*, *Pax3* and *HDAC4* among others[77,78], while *miR-133* promotes myogenic progenitor proliferation by targeting *Serum Response Factor*[79].

Lineage tracing studies have shown brown adipose and muscle to share a Pax7+ and Myf5+ expressing progenitor[47,53] and that in adult muscle, Myf5$^{neg}$ satellite stem cells are able to give rise to BAT *in vivo* in response to cold[31](Figure 3). Our lab previously determined *miR-133*[31] controls *PRDM16* translation and half-life to repress non-muscle specific gene expression and promote satellite cell myogenic commitment. Inhibition of *miR-133* with antisense oligonucleotide was sufficient to drive satellite cell brown adipogenic fate switching in vitro and *in vivo*. Importantly, a subpopulation of cells in the Myf5$^{neg}$ satellite stem cell pool represents a bona fide brown adipose precursor able to establish brown adipocyte colonies, sustain uncoupled respiration and derive brown adipocytes *in vivo*[31]. Identification of this bi-potent satellite cell suggests an unappreciated heterogeneity within the Myf5$^{neg}$ satellite stem cell pool and a potential source of satellite cells permissive to brown adipose signalling in adults.

It is feasible that satellite stem cells are in a permissive chromatin state for brown adipogenic differentiation prior to or during cold exposure. In response to cold, satellite cells integrate external cues to stimulate PRDM16 expression likely through repression in *miR-133*. Understanding the genetic pathways governing satellite cell fate switching could inform on therapeutics to augment basal metabolic rates and pose a potential clinical avenue targeting obesity. These pathways can also influence satellite cell multipotency and therefore provide insight into satellite cell self-renewal and may help define satellite cell hierarchy in adult tissue.

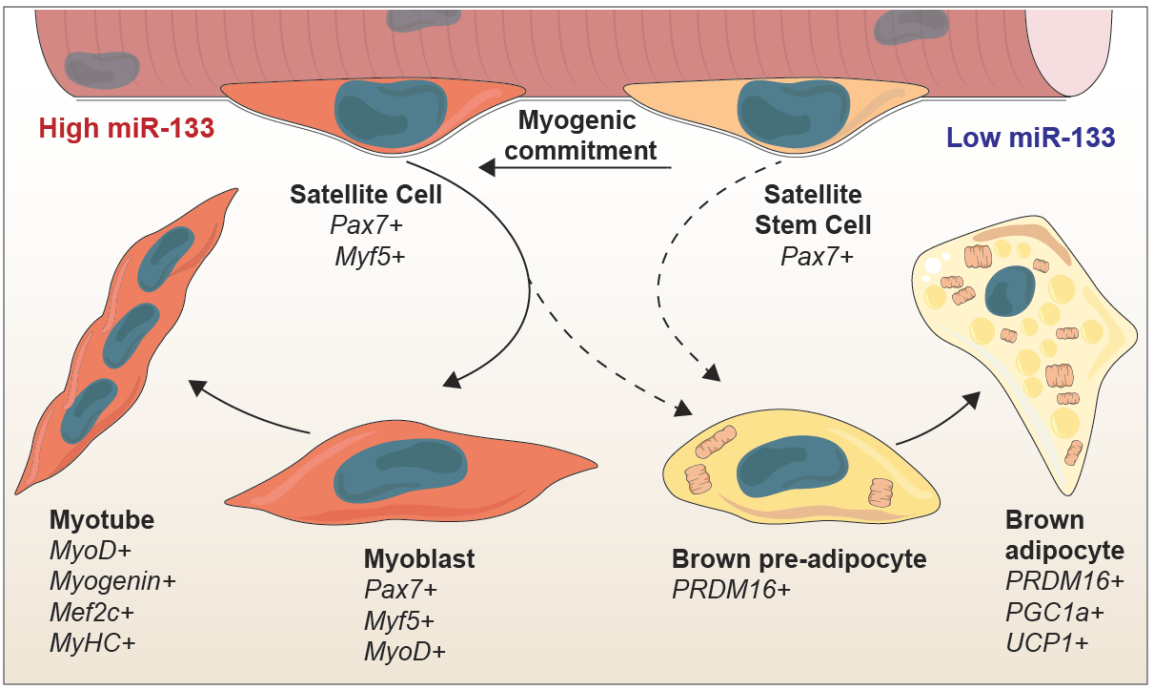


Figure 3: **Satellite cell heterogeneity and brown adipose determination**

In response to injury or homeostatic turnover, satellite stem cells activate and enter the cell cycle, progressing down the myogenic lineage in the presence of high *miR-133* to form a transiently amplifying pool of myoblasts. Myoblasts elongate and fuse to form de-novo myofibres or fuse into existing myofibres to repair injury. Satellite stem cells and a subset of *Myf5* expressing committed satellite cells can transition down the brown adipogenic lineage in response to cold, low *miR-133* levels or *miR-133* inhibition

Identifying pathways regulating satellite cell fate can uncover novel pharmaceutical targets to promote satellite cell maintenance or commitment to promote muscle repair and brown adipogenic switching to improve weight loss. Moving promising therapeutic targets into the clinical area and development of cell, gene or pharmacological therapeutics is a risk-prone and expensive endeavour. Improving pre-clinical testing and models to evaluate pathway or drug efficacy in a human-relevant context would significantly improve preclinical evaluation of therapeutics, reduce risks associated with clinical trials and accelerate therapeutic translation.

## Modelling human muscle disease

Despite years of research effort, increased quality of life and lifespan in patients with DMD has primarily been driven by refinements in respiratory support, cardiac support, steroid

use and rehabilitation[80,81]. There remains no cure for DMD, where rehabilitation and anti-inflammatory glucocorticoids slow disease progression.

Translating laboratory findings of improved repair from cell-products into clinical therapeutics promoting muscle repair has been historically unsuccessful. Early myoblast transplantation studies in boys with DMD failed due to immune rejection[82] and cell death[83,84]. By contrast, freshly isolated satellite cells can be intramuscularly transplanted to ameliorate dystrophy in *mdx* mouse muscle[85]. As the feasibility of intramuscular injections of a cell product throughout the body of a DMD patient is poor, it is unlikely cell products directly promoting repair in muscular dystrophy will be clinically viable. The therapeutic potential of satellite cell products or iPSC derived myogenic cells would be of benefit for indications such as volumetric muscle loss and wound repair[86]. Improving self-renewal of satellite cell products with p38α-β inhibition [11,87], Setd7 inhibition[88], eIF2α de-phosphorylation[89], Jak2-Stat3 inhibition[10] or treatment with Wnt7a[90] can provide a competitive advantage over endogenous patient satellite cells to promote long term engraftment. Methods improving self-renewal can also be employed to maintain desired cell states[89] and enhance yields in cell manufacturing[88] improving the clinical appeal of a therapeutic.

There are 281 clinical trials targeting Duchenne Muscular Dystrophy listed on the National Institutes of Health[91], however, the two current clinical therapeutics directly targeting the underlying cause of DMD are Ataluren, which permits ribosomal readthrough of nonsense mutations[92,93] and Eteplirsen, an antisense oligonucleotide facilitating RNA polymerase skipping exon 51 maintaining the DMD open reading frame[94,95]. Theoretically, 80% of all DMD patients could benefit from exon skipping [96] where Eteplirsen targets roughly 14% of the population [97]. Gene therapy strategies include AAV mediated delivery of micro-dystrophin[98] or CRISPR-Cas9 constructs[99,100] into a muscle to re-introduce functional dystrophin protein are also attractive methods to reduce disease progression

however these methods are inefficient in targeting satellite cells[99]. A lack of genetic repair in satellite cells would lead to a dilution of treatment over time and with muscle turnover.

Targeting endogenous repair can augment muscle repair by altering the balance of stem[10,87–90] and progenitor cells[101] in a given context. Our lab has recently shown that intrinsic polarity defects in *mdx* satellite cells lead to decreased formation of myogenic progenitors[7] where this mechanism can be directly targeted to improve muscle repair[101]. Strategies targeting endogenous repair mechanisms in conjunction with gene-mediated therapeutics are an attractive combinatorial approach, able to target whole body muscle regeneration and theoretically promote long term repair.

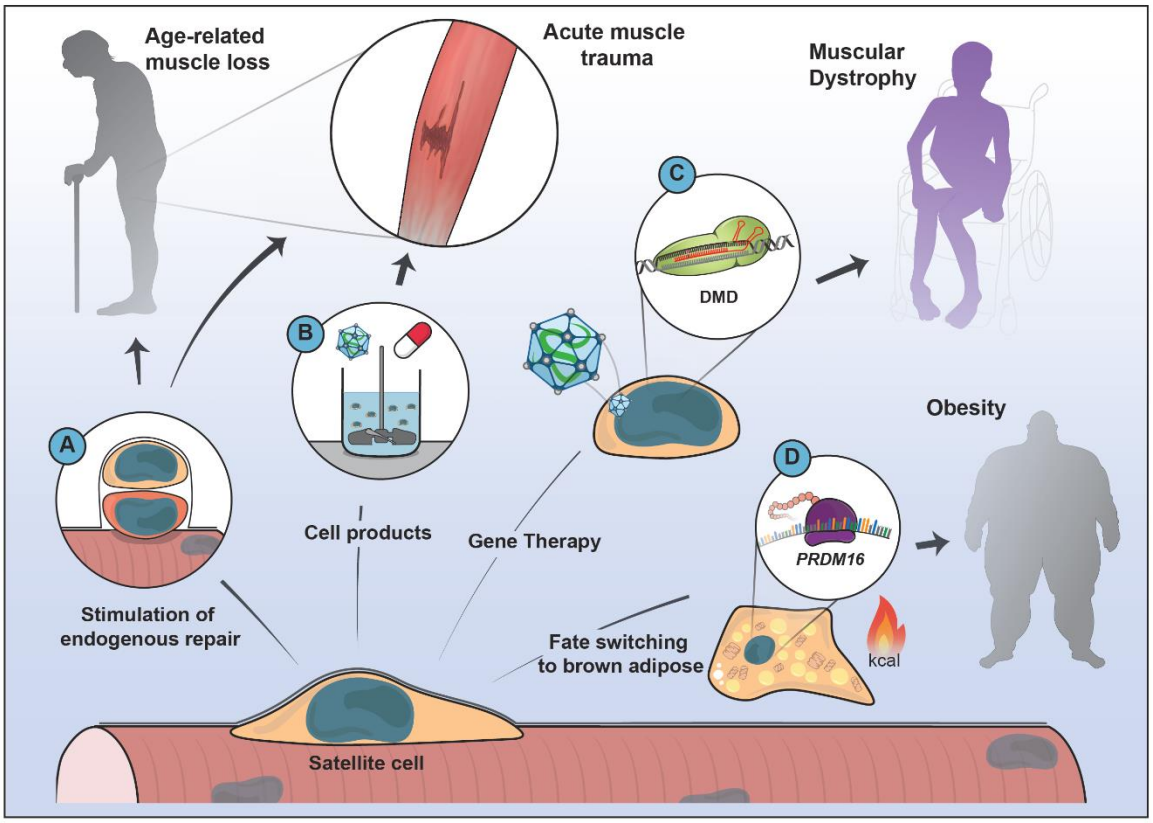


Figure 4: **Potential therapeutic interventions harnessing satellite cells.** Strategies augmenting A) endogenous repair hold potential to improve muscle repair throughout life and postpose onset of age-related muscle loss. B) The use of cell products derived from satellite cells holds the potential for acute injury and volumetric muscle loss. C) In combination with endogenous repair, gene corrective therapy to restore dystrophin expression in patients with DMD holds the potential to improve muscle repair. D) Induction

of endogenous or transplantable satellite cell-derived brown adipose holds the potential to augment basal metabolic rates in conditions such as obesity.

In all cases, therapeutic intervention in DMD is hindered due to; the large size of the dystrophin gene limiting universal gene therapies, dystrophin loss affecting all muscles in the body and therefore requiring whole-body treatments, the progressive nature of the disease requiring early treatment and critically the ability of treatments to effectively target satellite cells.

Robust modelling of the DMD phenotype is critical to understand the basic biology of the disease and translate research findings into the clinical arena. Multiple DMD animals have been developed from non-mammalian systems, small animal and large animal models which reflect varying disease phenotypes [102] however, the *mdx* mouse remains widely used and has provided critical insight into the progression and treatment of DMD [7,99,103–105]. Nonetheless, pre-clinical testing of therapeutics on animal models has limitations[106] and the development of more accurate pre-clinical models of human disease are required to predict clinically significant treatment outcomes[107]. Developing new methods to test satellite cell biology in contexts relevant to human health, will promote clinical translation of therapeutics targeting muscle repair and uncover novel signalling paradigms in human muscle.

Maintaining stem cells in physiologically relevant states is necessary to understand cell and context-specific signalling paradigms and understand complex interfaces between cells *in situ*. Understanding human stem cell function is largely based on tissue biopsies, cell culture and transplantation into model organisms. Engineering or maintaining human satellite cell extracellular niche composition, tissue microvasculature and complex cell-cell contacts is an important next step in delineating difference in human and model organism biology to appropriately generalize laboratory findings. Developing methods to culture

human satellite cells in a physiologically relevant context will be critical to interrogate genetic pathways and causatively determine the influence of self-renewal, stem cell commitment and satellite cell hierarchy on human muscle repair. Pre-clinical testing of human satellite cells in the lab can reduce clinical trial attrition by addressing therapeutic efficacy on endogenous repair, genetic recombination or personalized efficacy of a therapeutic. Applying these methods to human disease will help define the satellite cell-independent and intrinsic changes that occur with myopathy and age to understand and address the etiology muscle disease.

## Rationale and hypothesis

Satellite cells are required to facilitate muscle repair in response to homeostatic turnover or trauma. Understanding the mechanisms governing satellite cell fate decision to produce myogenic progeny, self-renew or form brown adipocytes is important to understand the process of muscle repair. Evaluating physiological signalling pathways and developing novel modelling paradigms to better reflect human satellite cell biology will better translate laboratory findings into the clinical arena. We hypothesize that satellite cell-intrinsic pathways play key roles in determining self-renewal and fate switching and that improved modelling will improve therapeutic translation.

The main objectives of manuscript I were to identify pathways governing satellite cell fate switching to the brown adipogenic lineage to better understand satellite cell multipotency. We accomplished this aim through a novel *in vitro* drug screen and further *in vitro* and *in vivo* target validation. The main objectives of manuscript II were to identify mechanisms promoting satellite cell self-renewal. We accomplished this aim through high throughput drug screening of mouse muscle fibres to detect satellite cell self-renewal and further *in vivo* functional validation. The main objective of manuscript III was to develop an accessible method for satellite cell transplantation to evaluate satellite cell fate decisions

*in vivo*. We accomplished this aim through iterative improvements of current methods, and incorporation of novel tissue processing steps and guidelines. The main objective of manuscript IV was to transparently present the consequence of dystrophin loss in satellite cells on *mdx* disease progression to resolve the controversy in the field. We accomplished this aim through a comprehensive assessment of *mdx* and C57BL/6 satellite cell response to acute and chronic injury. The main objective of manuscript V was to explore the potential of human primary tissue to model satellite cell fate decisions. We accomplished this aim by developing a method to culture human muscle fibres *ex vivo*.

## Preface to manuscripts

The results and discussion provided below were prepared during my graduate studies in the Cellular and Molecular Medicine program at the University of Ottawa Faculty of Medicine. Each manuscript was formatted according to the guidelines of the journal it was submitted or intended.

As per the University of Ottawa guidelines, all references have been condensed to a final reference section at the end of the thesis. All in-text references have been reformatted as numerical citations.

**Manuscript I** is in preparation for publication in the journal Cell Reports and is presented in the journal's format.

**Manuscript II** was published in the journal Cell Stem Cell and is presented in its published form.

**Manuscript III** was published in the journal Nature Protocols and is presented in its published form.

**Manuscript IV** s in preparation for publication in the journal Nature Communications and is presented in the journal's format.

**Manuscript V** s in preparation for publication in the journal Skeletal Muscle and is presented in the journal's format.

## Manuscripts

## Manuscript I: Satellite Cell Specification into Brown Adipose is Regulated by p53

AUTHORS: **Peter Feige[1,2,3],** Hang Yin[1,4], Hong Ming[1], Mohammad Abdul-Ghani[1,2,3], Lynn Megeney[1,2,3], and Michael. A. Rudnicki[1,2,3].

**AUTHOR AFFILIATION:** 1. Sprott Center for Stem Cell Research. Ottawa Hospital Research Institute. Regenerative Medicine Program. Ottawa, ON, Canada. 2. Department of Cellular and Molecular Medicine. Faculty of Medicine. University of Ottawa. Ottawa, ON, Canada. 3. Department of Medicine. Faculty of Medicine. University of Ottawa. Ottawa, ON, Canada. 4. Department of Biochemistry and Molecular Biology, Franklin College. University of Georgia. Athens, GA 30602, USA.

**This manuscript is in preparation for Cell Reports.**

### AUTHOR CONTRIBUTION

P.F., H.Y. and M.A.R. conceptualized the study. H.Y. developed the biosensor screen and H.M. conducted biosensor screening, optimization and analysis. M.A. conducted cardiac-ANP luciferase studies. H.Y. and P.F. performed lead compound screening in mouse and human primary myoblasts. H.Y. performed screening on rat cardiomyocytes and cold exposure in mice. P.F. assessed in vitro p53 inhibition studies and *miR-133* maturation analysis. P.F. performed all p53 cKO studies and PFTa *in vivo* studies. P.F. performed single-cell culture experiments and lineage tracing experiments. P.F. performed all in vitro fibre culture experiments in myogenic and adipogenic media. M.A.R. oversaw the experimental design, analysis of results, manuscript editing, and financial support.

**SUMMARY**

Stimulating the generation of brown adipose has been suggested as a treatment for obesity. Muscle stem cells in adult skeletal muscle are multipotent and give rise to myogenic and brown adipose progenitors. Fate switching from myogenic to brown adipogenic is regulated by microRNA-133 (*miR-133*), where *miR-133* downregulation results in the upregulation of Prdm16, a putative brown adipose determination factor. Using a biosensor for *miR-133* activity, we conducted a screen for regulators of *miR-133* expression. We found the p53 transactivation inhibitor Pifithrin-α to be a potent inhibitor of *miR-133* expression in primary myoblasts and muscle stem cells. Moreover, p53 inhibition stimulates precocious brown adipose formation within regenerating skeletal muscle. Mice exposed to cold temperatures exhibit reduced p53 expression in muscle. Notably, we found *pri-miR-133* processing was inhibited when p53 is down-regulated. Therefore, our experiments provide new insight into muscle stem cell fate determination and suggest potential therapeutic avenues to treat obesity.

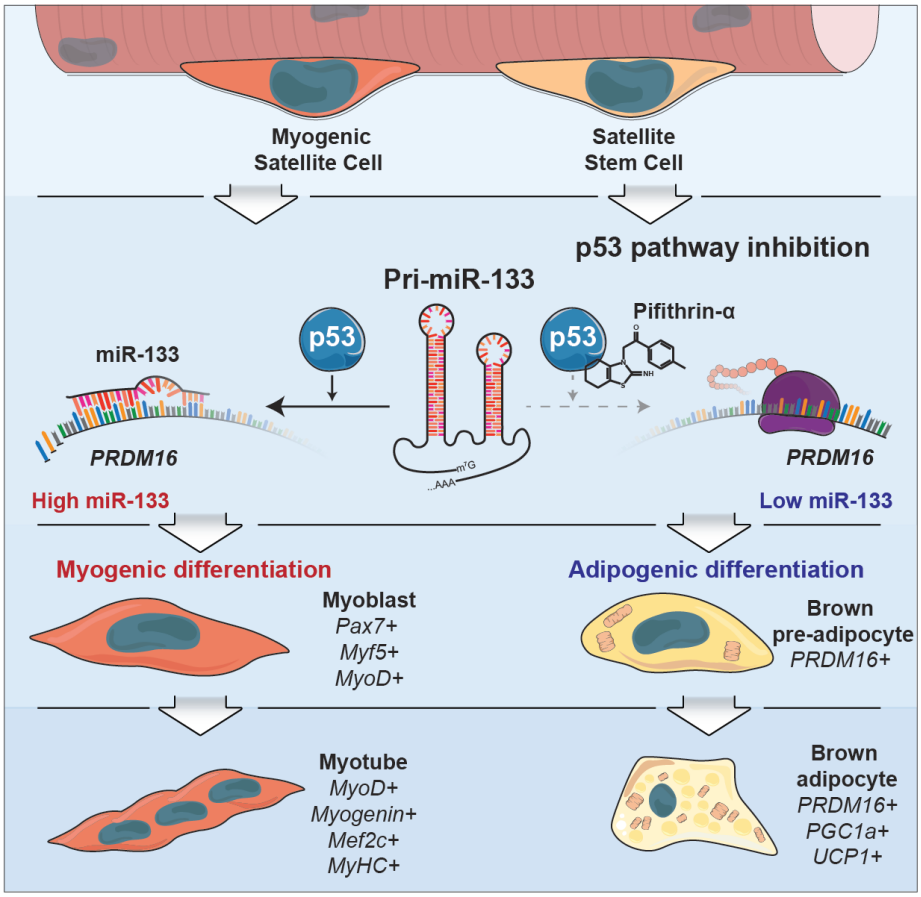


*Figure 5:* **Graphical abstract for Manuscript I**

**Highlights**

- Antagonism of *miR-133* activity regulates myogenic differentiation
- MicroRNA-133 processing is regulated by p53
- Satellite cell lineage switching is restricted by p53
- Transient p53 inhibition stimulates brown adipose formation from muscle stem cells

**eTOC Blurb**

Feige et al. found that p53 signalling in adult muscle stem cells promotes myogenic lineage specification by stimulating microRNA-133 processing. Transient p53 inhibition limits microRNA-133 activity and facilitates satellite cell adipogenic lineage switching resulting in brown adipose formation. Pifithrin-α and other transient p53 inhibitors may hold potential as anti-obesity compounds.

## INTRODUCTION

Satellite stem cells are a subset of muscle stem cells that represent multipotent stem cells capable of generating myogenic progenitors or alternatively brown adipose tissue (BAT) [31]. The myogenic identity of satellite cells is determined by the paired box transcription factors Pax7 and Pax3 that genetically regulate MRF expression. Following asymmetric division, Pax7 mediated recruitment of the MLL1-2 histone methyltransferase complex to the Myf5 and MyoD enhancers results in their expression and myogenic progression [108,109]. In addition, de-repression of mRNA decay mechanisms [110,111] and miRNA mediated silencing [112] is required for the timely production of Myf5 and MyoD protein and myogenic commitment.

MicroRNA mediated decay is an important step in the regulation of myogenic progression. Quiescent and early activated satellite cells are enriched for miR-489 whereupon asymmetric division results in repression of miR-489 in one daughter cell, stimulating proliferation and allowing translation of the oncogene Dek [113]. Similarly, Myf5 mRNA is sequestered into mRNP granules through miR-31 binding its 3'UTR [112], limiting its access to translational machinery. Upon satellite cell activation, mRNP granules are dissolved leading to the release of Myf5 mRNA and rapid accumulation of Myf5 protein. Myogenic differentiation is also regulated by ubiquitously expressed miRNA [114] and the muscle enriched miRNA, miR-1, miR-206 and miR-133 that are transcriptionally regulated by MRFs and act to regulate the timing of muscle-specific gene expression during quiescence [113], activation and myogenic differentiation [77,79,115].

Muscle and brown adipogenic precursors share similar transcriptional profiles [31,54,55] where brown adipose tissue and muscle share a Myf5+Pax7+ lineage [47]. Both muscle and BAT regulate thermogenesis, where in response to cold muscle generates heat through the action of myosin-ATPase during shivering and futile calcium cycling through sarcolipin during non-shivering thermogenesis [41]. Sympathetic activation of brown adipose tissue in cold [116] also facilitates non-shivering thermogenesis [117] through the activity of Uncoupling Protein 1 (UCP1) in BAT mitochondria which dissipate the proton gradient across the mitochondrial membrane, bypassing ATP synthase. Decreased ATP production reduces its negative feedback on the Krebs cycle [42], resulting in rapid flux of free fatty acid and glucose through BAT mitochondria. In thermogenesis,

the difference in energy required to drive reactions forward and energy released from ATP hydrolysis as well as inefficiencies in substrate-level oxidation result in heat accumulation in tissues.

Strategies targeting non-exercise induced energy expenditure remain largely unexploited to augment weight loss, where thermogenesis represents a modifiable mechanism to increase basal metabolic rates. As brown adipose is rare in humans, transplantation of BAT [118,119] or stimulating the production of endogenous BAT from satellite stem cells in muscle [31] are novel means to stimulate BAT volume. Importantly, transplantation of BAT intramuscularly improves outcomes [118], likely due to an abundance of sympathetic innervation [120] and the highly vascular nature of skeletal muscle supporting oxygen demands of non-shivering thermogenesis and by dissipating heat through the blood. This suggests muscle is an ideal tissue to stimulate brown adipose formation.

Thermogenic gene expression in BAT and satellite stem cells is facilitated by the transcription factor PR domain zinc finger 16 (PRDM16) which supports stem cell maintenance in multiple tissues [121] and binds brown fat gene enhancers in cooperation with the mediator complex to promote enhancer-promoter contacts and gene expression [67]. PRDM16 also acts to repress white fat and muscle-specific gene expression through cooperating in transcriptional corepressor complexes [68]. Ectopic expression of PRDM16 is sufficient to drive thermogenic gene expression in muscle, white preadipocyte and fibroblast [47] where PRDM16 and its transcriptional targets work together with histone and chromatin-modifying enzymes to establish a permissive chromatin state amenable to brown fat gene expression and stem cell commitment [71]. Importantly, in satellite stem cells miR-133 suppresses translation of PRDM16, where antagonism of miR-133 in muscle results in BAT formation and a lean phenotype [31].

Here we report the p53 signalling pathway as a potent regulator of miR-133 maturation in satellite cells to promote the myogenic gene program. P53 is thermoregulated in muscle and therapeutic inhibition of p53 in satellite cells limits myogenic commitment to facilitate a fate change towards the brown adipogenic lineage. Identifying pathways regulating satellite cell identity and fate

decisions provides insight into factors regulating stem cell multipotency and therapeutic interventions promoting healthy metabolism to benefit human health.

## RESULTS

### Molecular screening identified regulators of microRNA-133 expression

We hypothesized that skeletal muscle-specific regulators of *miR-133* may also functionally regulate satellite cell fate switching towards the brown adipogenic lineage. To test this hypothesis, we developed a *miR-133* biosensor screen, where a dual-luciferase reporter construct harbouring tandem *miR-133* targeting sites was infected into C2C12 myoblasts and subjected to pharmacological screening (Figure 6A).

The *miR-133* biosensor cell line carries five tandem optimized *miR-133* targeting sites downstream of a firefly luciferase ORF driven by a CMV promoter (Figure 6A). The *miR-133* targeting sites serve as an artificial 3'UTR for the firefly luciferase transcript where the renilla luciferase construct lacking the *miR-133* targeting sites acts as an internal control for the dual-luciferase assay. Transient transfection of 5nm *miR-133* mimetics into biosensor cultures resulted in a ~80% reduction in chemiluminescence per ug of protein (Figure S1A) while transfection of 10nM *miR-133* inhibitors increased luciferase activity by ~50% (Figure S1B) where Z-scores above 0.5 were achieved.

We cultured the *miR-133* biosensor line in a 96 well format and screened current FDA approved and naturally occurring compounds with reported effects in curbing obesity or increasing energy expenditure for potential drug repurposing studies. We found that Quercetin [122], Genistein [123], Metformin [124], and Rofecoxib [125], moderately increased biosensor activities (exception of Genistein at 40 nM) (Figure 6), suggesting these compounds inhibit miR-133 function and may hold potential for miR-133 antagonism studies. To identify potent inhibitors of miR-133 we further evaluated 400 compounds from the OICR Kinase Inhibitor Library and 160 compounds from OICR Tool Compound Library at 40nM and 1uM concentrations (Figure 6B, Figure S1D) to identify compounds that consistently regulate *miR-133* activity and are active across a wide therapeutic dose. We

identified 48 compounds that regulate *miR-133* and have high activity at one or both concentrations

We characterized the 560 compounds by their known targets to identify pathways important for *miR-133* activity. We found inhibitors of the p53 (p=0.016), HSP90 (p=0.012) and PARP 1/2 (P<0.001) pathways increased *miR-133* biosensor activity while the VEGFR pathway inhibitors (p=0.025) decreased *miR-133* biosensor activity by Wilcoxon-Mann-Whitney rank-sum tests (Figure S1F). This suggests the p53, HSP90 and PARP 1/2 pathways may augment *miR-133* function in muscle while the VEGFR pathway potentially inhibits *miR-133* function.

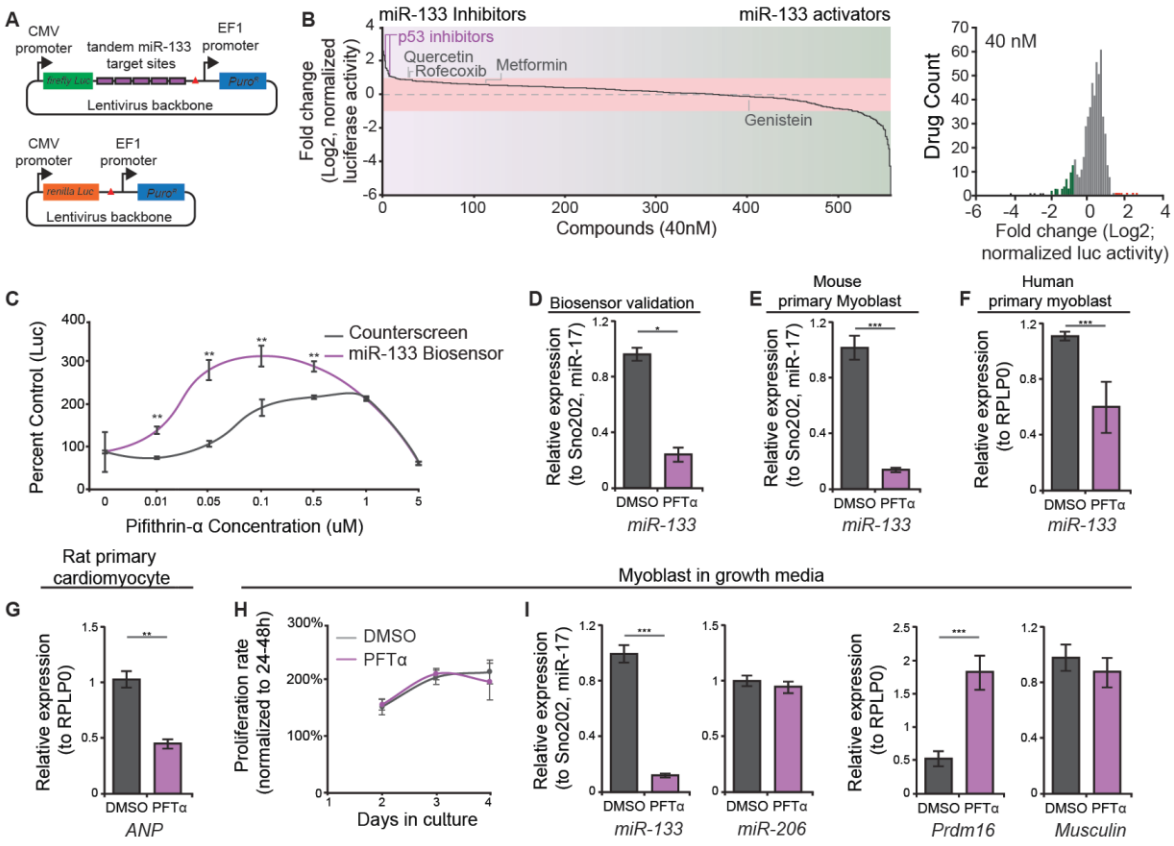


Figure 6*:* **Identification of small molecules that regulate *miR-133* in muscle cells.** A) Graphic representation of biosensor design and *renilla luc* containing control. B) Relative change in luciferase activity of biosensor with small molecule screening. Compounds with a reported effect increasing energy expenditure are highlighted. C) Relative change in Biosensor luciferase activity following PFTα dose-response. Quantitative Real-time PCR for *miR-133* miRNA levels following 50nM PFTα treatment or DMSO control in the D) Biosensor screening line, E) cultured primary mouse myoblasts, F) cultured human

primary myoblasts. G) Quantitative Real-time PCR for cardiac *ANP* levels in cultured primary cardiomyocytes following 50nM PFTα treatment or DMSO control. H) Percentage change in cell number in primary mouse myoblasts following culture in 50nM PFTα containing media or DMSO control. I) Quantitative Real-time PCR for *miR-133, miR-206, PRDM16 and Musculin* in the parental C2C12 myoblasts cell line cultured in 50nM PFTα containing media or DMSO control. (C-D, I) Error bars represent means ±SD; (E-I) Error bars represent mean ±SEM; p-values: *=<0.05, **=<0.01; ***=<0.005. (C-D) n=3 technical replicate; (I) n=6 technical replicate (E-H) n=3 biological replicates.

Antagonism of *miR-133* has implications in cardiac muscle physiology [126], cardiac remodelling following injury [127,128] and cardiac hypertrophy [129]. From our 48 compounds inhibiting *miR-133* activity, we further evaluated our top hits for their effect on the cardiac hypertrophy response through induction of the cardiac hypertrophy marker atrial natriuretic peptide (ANP). We transfected an ANP luciferase construct into rat primary cardiomyocytes and treated cells with our top compounds. Six of our hits significantly increased luciferase ANP activity (4.2-23.8-fold, Table S1), suggesting some *miR-133* inhibiting compounds do elicit hypertrophic responses in cardiomyocytes. Notably, inhibition of p53 did not elicit ANP expression.

From our top skeletal muscle-specific targets, two transactivation inhibitors of p53, Pifithrin-α (PFTα) showed the strongest inhibition of *miR-133* activities at 40nM and 1uM without a significant effect on cardiac ANP levels (Table S1). We validated the observed 3.8-fold (40nM) and 2.15-fold (1μM) increase in luciferase activity following PFTα treatment by a dose-response in our biosensor. We observed a therapeutic dose from 0.01-0.5uM PFTα in our biosensor resulting in a ~40%-270% increase in luciferase activity (Figure 6C) compared to testing in a counter screen lacking *miR-133* target sites. Validating *miR-133* levels by RT-qPCR showed a relative~70% decrease in *miR-133* miRNA levels following 50nM PFTα treatment in our biosensor (Figure 6D). To assess the specificity of PFTα on primary muscle cells, both mouse and human primary myoblasts

were cultured in the presence of 50nM PFTα resulting in a ~80% (Figure 6E) and ~50% (Figure 6F) decrease in *miR-133* RNA levels by RT-qPCR, respectively.

We further evaluated the effect of PFTα on the hypertrophy response in rat cardiomyocytes and found 50nM PFTα treatment did not induce cardiac *ANP* mRNA (Figure 6G) or the hypertrophic biomarker *miR-208* [130] (Figure S1G) by RT-qPCR. We found PFTα treatment resulted in a small increase in *miR-133* levels in treated primary cardiomyocytes (Figure S1G), suggesting the role of p53 in regulating *miR-133* activity may be tissue-specific to skeletal muscle or *miR-133* may be differentially regulated in these tissues.

To investigate if transient PFTα treatment reflected the effect of *miR-133* antagonism on cell proliferation [131] and regulation of *PRDM16* [31] we monitored proliferation and expression levels in primary myoblasts treated with 50nM PFTα. Inhibition of p53 resulted in no observable change in proliferation kinetics in myoblasts (Figure 6H, Figure S1H) but a reduction in *miR-133* RNA with a concomitant increase in the *miR-133* target and brown adipose regulator *PRDM16* (Figure 6I). As inhibitors of general microRNA biogenesis would result in increase biosensor activity, we also evaluated additional microRNA. Importantly, PFTα treatment did not alter *miR-206* or its target *Musculin* (Figure 6I) suggesting general microRNA production is not impacted. This data suggests the p53 pathway may be acting in a tissue-specific and targeted manner to regulate *miR-133* activity and restrict the adipogenic cell fate.

**PFTα impairs myogenic differentiation in muscle stem and progenitor cells**

To further confirm the specific effects of PFTα treatment on p53 signalling and explore whether inhibition of p53 prevents myogenic differentiation, siRNA against p53 (*si-p53*) was transfected into primary myoblasts in culture. Additionally, to address if the p53 pathway promotes general miRNA activity, siRNA against the core miRNA processing ribonuclease Dicer (*si-Dicer*) was transfected in tandem to correlate the expression of

myogenic markers (*Pax7, MyoG, p21, p53*) with miRNA expression (*miR-1, miR-133, miR-206*) (Figure 7A). Like PFTα treatment, *si-p53* reduced the expression of *miR-133* by 81% during differentiation. By contrast, transfection with *si-p53* did not reduce *miR-1* miRNA induction during differentiation, similar to scrambled siRNA control (siSCR). Interestingly, p53 pathway inhibition increased *Pax7* mRNA expression by 5.1-fold, reduced *MyoG* mRNA induction by 82% and cells failed to induce *p21* mRNA expression. In opposition, *si-Dicer* resulted in strong induction of *MyoG*, *p21* and *p53* with a concomitant loss of *miR-133,* and *miR-1* expression, suggesting pan inhibition of miRNA processing promotes myogenic differentiation in culture. This data suggests p53 pathway inhibition impairs myogenic differentiation in myoblasts potentially through regulating the expression of a subset of miRNAs.

To further evaluate the effect of p53 pathway inhibition in *si-p53* treated differentiating myoblasts, we examined protein levels of Pax7, MyoG and p53 by western blotting. Inhibition of p53 by siRNA maintained Pax7 protein during myogenic differentiation and reduced levels of MyoG (Figure 7B). We did not observe changes to MyoD, the miRNA endonuclease Dicer or miRISC component Ago2 (Figure S2A). This data supports the finding that p53 pathway inhibition restricts myogenic differentiation in the satellite cell lineage.

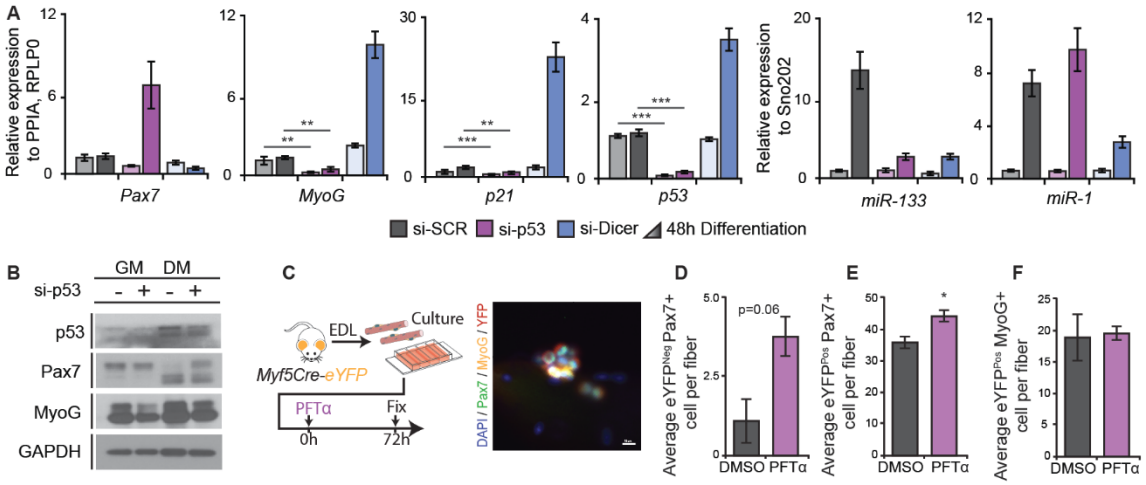

Figure 7***:*** **PFTα restricts myogenic differentiation in muscle stem and progenitor cells.** A) Quantitative Real-time PCR for *Pax7, MyoG, p21, P53, miR-133* and *miR-1* in primary mouse myoblasts harvested 48 hours after transfection or 48h after transfection in differentiation medium with scrambled control siRNA (siSCR) or siRNA against *p53* (sip53) or *Dicer* (siDicer). B) Immunoblotting analysis of Pax7, MyoG and p53 in primary mouse myoblasts harvested 48 hours after transfection or 48h after transfection in differentiation medium with scrambled control siRNA (siSCR) or siRNA against *p53* (sip53). GAPDH was used as the loading control. C) Schematic overview of EDL fibre culture from *Myf5Cre-eYFP* mice in the presence of PFTα and representative image of myofibres cultured for 72h and stained for DAPI (Blue), Pax7 (Green), MyoG (Yellow) and eYFP (Red). Quantification of Pax7-expressing D) $eYFP^{neg}$ satellite cells, E) $eYFP^{Pos}$ satellite cells and F) MyoG-expressing $eYFP^{Pos}$ satellite cells from 50nM PFTα treated *Myf5Cre-eYFP* EDL fibre culture. (A, D-F, H-M, O-Q, S) Error bars represent means ±SEM; p-values: *=<0.05, **=<0.01; ***=<0.005. (A, D-F, H-I) n = 3 biological replicates, (J-M, N-S) n = 3 DMSO, n=4 PFTα.

To assess if the effect of p53 pathway inhibition is specific to myoblasts, we evaluated PFTα treatment on satellite cells in their niche. The *Myf5-Cre/R26R-eYFP* mouse model allows visualization of yellow fluorescent protein following Cre-mediated recombination at the *R26R-eYFP* allele and discrimination between satellite stem cells ($eYFP^{Neg}$) and satellite myogenic cells ($eYFP^{Pos}$) following activation of *Myf5* [22]. Culturing single myofibres harbouring satellite cells from the *Extensor Digitorum Longus* muscle (EDL) of *Myf5-Cre/R26R-eYFP* mice and treatment with 50nM PFTα allowed us to evaluate the effect of PFTα on satellite stem cell and satellite myogenic cell activation by immunofluorescence enumeration (Figure 7C). Treatment with 50nM PFTα resulted in a 3.3-fold increase in $eYFP^{Neg}$ satellite stem cells (Figure 7D) and a 23% increase in $eYFP^{Pos}$ committed myogenic cells (Figure 7E) without affecting the total number of MyoG expressing differentiating myogenic progenitors (Figure 7F, Figure S2E). This data suggests pharmacological inhibition of p53 promotes stem cell expansion and mildly limits MyoG protein induction in satellite cells.

**The p53 pathway regulates microRNA-133 maturation**

Our identification of p53 as a regulator of *miR-133* activity and expression without affecting other miRNAs such as *miR-1* suggests p53 may be regulating a subset of miRNA during

myogenic differentiation. We hypothesized that this regulation may be attributed to miRNA transcription or miRNA processing.

To evaluate the mechanistic role of p53 on *miR-133* activity in satellite cells, RT-qPCR primers were designed to specifically amplify *miR-133* isoform for pri-miRNA and mature miRNA. Pre-miRNA transcripts cannot be detected in this manner however, as RT-qPCR primers would also amplify the shared sequences in pri-miRNA transcripts. To assess the effect PFTα on *miR-133* processing in satellite cells *in vivo,* we used the *Pax7-nGFP* mouse model [132] where expression of a nuclear green fluorescent protein accurately labels satellite cells and allows Fluorescence-activated cell sorting (FACS) isolation of pure populations following muscle injury. Prospective isolation of activated satellite cells from CTX injured and 50nM PFTα treated *Pax7-nGFP* mice revealed a significant 75% decrease in mature *miR-133a* expression without a change in *pri-miR-133a1, pri-miR-133a2* or mature *miR-133b* (Figure 8B). We additionally did not observe changes to *Pax7* or *MyoG* mRNA expression in PFTα treated activated satellite cells (

Figure S3A). This suggests that p53 pathway inhibition in satellite cells does not regulate *miR-133* transcription but likely miRNA processing.

To further explore the effect of p53 pathway inhibition on *miR-133* processing in myogenic progenitors, we treated differentiating primary myoblasts with *si-p53* prior to stimulating differentiation by serum withdrawal (Figure 8C). Inhibition of p53 by siRNA resulted in a significant 75% reduction in mature *miR-133*a and a significant 85% reduction in mature *miR-133b* following myogenic differentiation (Figure 8D). Interestingly, *si-p53* resulted in a 40% increase in *pri-miR-133a1* and 55% increase in *pri-miR-133a2* but not *pri-miR-133b* following differentiation (Figure 8D). We further validated our mature *miR-133* primers using highly specific Locked-Nucleic Acid (LNA) RT-qPCR primers, confirming *si-p53* treatment reduces both *miR-133a* and *miR-133b* (

Figure S3B). This data suggests in primary myoblasts, p53 pathway inhibition limits *miR-133* processing where induction of *pri-miR-133* transcription may reflect a compensatory response due to a deficit in mature *miR-133* or increase unprocessed transcripts.

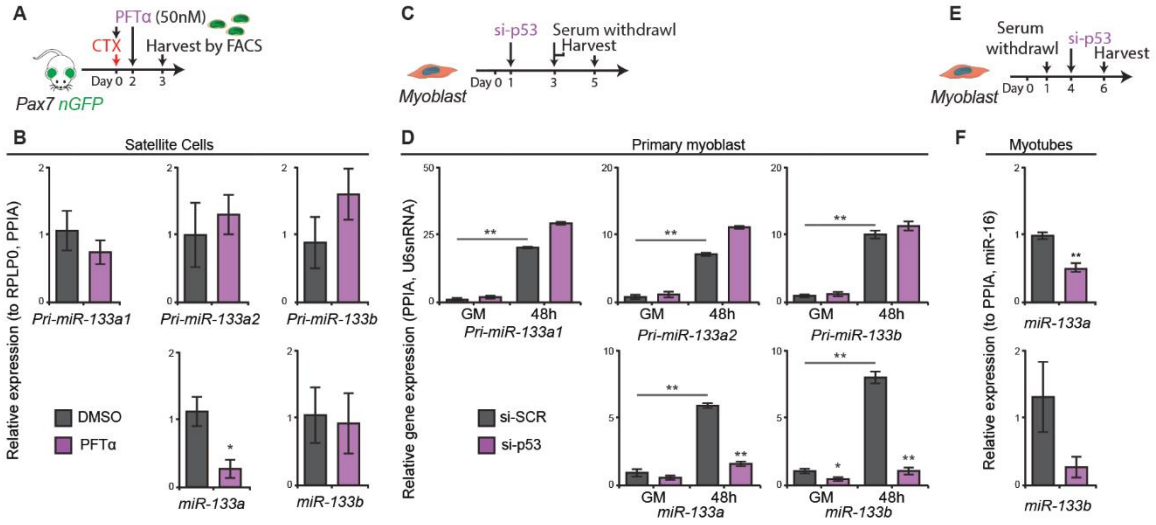


Figure 8**: MicroRNA-133 maturation is regulated by p53.** A) Graphic overview of PFTα treatment of satellite cells from *Pax7nGFP* mice prior to isolation by FACS sorting. B) Graphic overview of transfection of siRNA targeting p53 into proliferating mouse myoblasts prior to harvesting and inducing myogenic differentiation. C) Graphic overview of transfection of siRNA targeting p53 into terminally differentiated mouse myotubes. Quantitative Real-time PCR for *pri-miR-133a1, pri-miR-133a2, pri-miR-133b, miR-133a, miR-133b* in D) 50nM PFTα treated satellite cells relative to si-scr in GM , E) myoblasts transfected with siRNA targeting p53 (si-p53) or scramble siRNA control (si-SCR) harvested in growth or differentiation conditions. F) Quantitative Real-time PCR for *miR-133*a and *miR-133*b from terminally differentiated myotubes transfected with siRNA targeting p53 (si-p53) or scramble siRNA control (si-SCR). (D-F) Error bars represent means ±SEM; p-values: *=<0.05, **=<0.01; ***=<0.005. (D) n=3 DMSO biological replicates, n=6 PFTa biological replicates, (E-F) n=3 biological replicates.

To explore if the effect of p53 signalling on *miR-133* processing is a by-product of an inhibition in myogenic differentiation or cell cycle exit, we treated terminally differentiated myotubes with *si-p53* (Figure 8F). Interestingly, terminally differentiated myotubes show a significant 50% reduction in mature *miR-133a* and a 70% reduction in mature *miR-133b* (Figure 8F). Together this data suggests that the p53 pathway regulates

*miR-133* activity through promoting *miR-133* processing in a sustained manner during satellite cell activation and myogenic differentiation but independent of cell cycle exit.

**PFTα restricts muscle regeneration *in vivo***

To better understand the effect of transient p53 inhibition on satellite cell activity *in vivo*, we injured the *Tibialis Anterior* (TA) muscle by intramuscular injection of cardiotoxin (CTX) and treatment with 50nM PFTα or equivalent DMSO containing saline at the time of injury and 2 days after (Figure 9A). By performing acute injury and assessment of muscle recovery at early (7 days) and late (21 days) time points, we can measure the effect of PFTα on satellite cell and myogenic progenitor expansion as well as the impact on muscle repair (Figure 9A). Notably, 7 days post-injury PFTα injected muscle contain a significant 14% increase in satellite cell number (Figure 9B) without effecting total MyoG expressing cells (Figure 9C). The observed increase in satellite cells with PFTα treatment persisted 21 days post-injury with a significant 22% increase in resting satellite cell numbers in the treated muscle (Figure 9D). This data supports EDL myofibre studies, where PFTα treatment results in hyperplasia of the satellite cell pool with a mild inhibition in myogenic differentiation (Figure 7D-F).

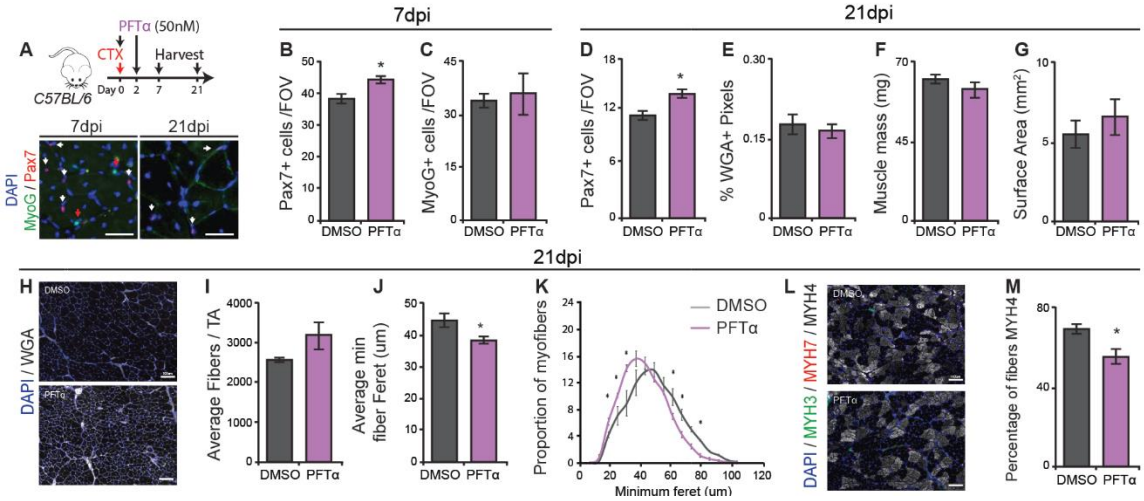


Figure 9***:*** **PFTα restricts muscle regeneration in vivo.** A) Schematic overview of muscle injury and PFTα treatment in *C57BL/6* mouse *Tibialis Anterior* muscle and representative image of cross-sections from 7 days post-injury (dpi) and 21dpi stained for DAPI (Blue),

Pax7 (Red), MyoG (Green). White arrows denote satellite cells, red arrows denote MyoG-expressing progenitors. Quantification of B) Pax7-expressing cells and C) MyoG expressing cells per field of view (20x) 7 days post-injury. Quantification of D) Pax7-expressing cells per field of view (20x) 21 days post-injury. E) Quantification of average Wheat Germ Agglutinin stained area per total TA cross-section, F) TA muscle mass and G) TA surface area 21 days post-injury. H) Representative image of TA muscle 21 days post-injury stained with DAPI (Blue) and Wheat Germ Agglutinin (White) used to quantify I) the average number of fibres per TA muscle, J) average minimum fibre Feret and K) minimum myofibre Feret proportion of total TA myofibres using the SMASH software. L) Representative image of TA muscle stained with DAPI (Blue), MYH3 (Green), MYH7 (Red) and MYH4 (White) with (M) quantification of MYH4 stained myofibres per TA section. (B-G, I-K, M) Error bars represent means ±SEM; p-values: *=<0.05. (A-C) n = 3 biological replicates, (D-M) n = 3 DMSO, n = 4 PFTα.

To determine the effect of transient PFTα on muscle repair, treated muscles were evaluated histologically. Muscles treated with PFTα did not display increased fibrosis as measured by wheat germ agglutinin staining (Figure 9E), altered muscle mass (Figure 9F) or surface area (Figure 9G) 21 days post-injury. PFTα treated muscles exhibit a general increase in myofibres per TA (2576 ± 61vs 3225 ± 323) (Figure 9I) with a significant 14% decrease in minimum fibre Feret (Figure 9J) and a significant leftward shift in minimum fibre Feret proportion (Figure 9K). Interestingly, 50nM PFTα treated muscle also exhibited a significant 20% reduction in MYH4 expressing type 2B fast-twitch muscle fibres (Figure 9L-M) without a change in MYH7 expressing type 1 slow-twitch fibres (Figure S4C) suggesting a fibre type transition to type 2A fibres.

Taken together, this data suggests transient inhibition of p53 with PFTα results in the expansion of the satellite cell pool with a mild inhibition in myogenic commitment, resulting in muscles with decreased myofibre size and an altered metabolic profile.

**p53 is differentially regulated in diverse tissue types in response to cold**

Satellite cells represent a highly heterogeneous stem cell in adult tissue [5] where subpopulations can be distinguished based on gene expression [33,34,133], behaviour [35,134], transplantation potential [22,101,135] and bi-potential lineage towards the muscle and brown adipogenic fate [31]. Importantly, both muscle and brown adipose are derived from a Pax7

and Myf5-expressing progenitor [47,53] and in adult tissue Pax7-expressing cells can derive brown adipose tissue *in vivo* in response to cold [31]. Recent work has elaborated on the role of p53 in mitochondrial clearance (mitophagy) during cold adaptation and beiging of white adipose where the age-related accumulation of p53 results in increased mitophagy in aged white adipocytes and cold exposure in mice reduced p53 protein to induce the beige adipogenic gene program [136]. We hypothesized that p53 may be thermoregulated in skeletal muscle as well, where cold-induced changes to p53 may restrict *miR-133* expression in satellite cells to promote the adipogenic fate [31].

To explore if p53 is thermoregulated in skeletal muscle and other tissues, we exposed C57BL/6 mice to a cold habitat for one week and harvested interscapular brown adipose, subcutaneous white adipose, visceral white adipose, Intercostal muscle, Supraspinatus muscle, Paraspinal muscle and *Tibialis Anterior* muscle (

Figure 10A). As reported previously [31], cold exposure results in repression of *miR-133* and induction of Prdm16 and UCP1 mRNA across interscapular brown adipose, subcutaneous white adipose, visceral white adipose, Intercostal muscle, Supraspinatus muscle and Paraspinal muscle while *Tibialis Anterior* muscle was resistant to cold-induced induction of Prdm16 and UCP1. Following cold exposure, RT-qPCR revealed that in all tissue types except muscle from the diaphragm (Figure S5A) that *p53* was significantly decreased between ~75% to ~20% of the level of thermoneutral controls (

Figure 10B) in a similar manner as *miR-133* [31]. Interestingly, diaphragm muscle also showed a decrease to 60% *miR-133* expression compared to thermoneutral controls without induction in brown adipogenic gene expression (Figure S5A) suggesting additional factors may be required to promote the metabolic reprogramming required for brown adipogenesis. Together this data suggests that p53 is thermoregulated in response to cold across many tissues including skeletal muscle and brown adipose.

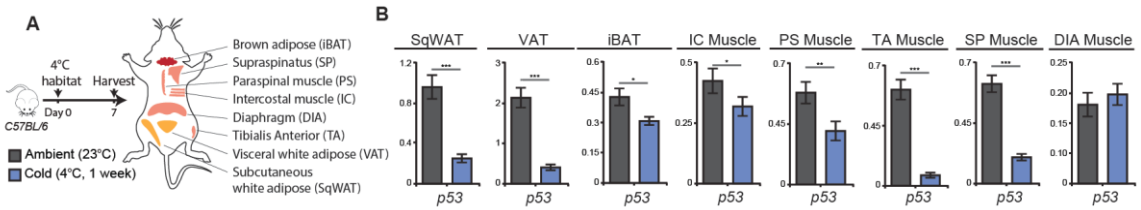


Figure 10: **Expression of p53 is differentially regulated in divergent tissue types in response to cold.** A) Graphic overview of tissue harvesting from ambient (23°C) or cold exposed (4°C 1 week) *C57BL/6* mice. B) Quantitative Real-time PCR for *p53* in the tissues listed. Error bars represent means ±SEM; p-values: *=<0.05, **=<0.01; ***=<0.005. n=3 biological replicates.

**Inhibition of the p53 pathway promotes satellite cell fate switching**

As we observed that p53 inhibition resulted in impaired *miR-133* processing and a deficit in myogenic differentiation, we hypothesized that p53 inhibition may induce satellite cells to undergo brown adipose differentiation. To investigate the capability of satellite cells to undergo adipogenic differentiation we utilized a Cre/LoxP based lineage tracing strategy where *Pax7Cre-eYFP* mice express a permanent yellow fluorescent protein in satellite cells and their progeny. We harvested EDL myofibres from *Pax7Cre-eYFP* mice which harbour mixed populations of non-eYFP expressing non-myogenic cells and eYFP expressing satellite cells. Culturing these fibres in proadipogenic conditions [47] results in PRDM16 protein expression by 42 hours in eYFP expressing satellite cells and their asymmetric progeny (Figure S6A). Treatment of EDL myofibre cultures with 50nM PFTα prior to adipogenic differentiation (Figure 11A) revealed a significant 3.96-fold increase in eYFP derived cells expressing the adipocyte marker Perilipin and the brown adipogenic marker UCP1 (Figure 11B, C). This data suggests that PFTα treatment promotes adipogenic differentiation in satellite cells *in vitro*.

The satellite cell pool represents a heterogeneous population of bi-potent satellite stem cells able to differentiate to brown adipose and myogenic satellite cells which are

resistant to adipogenic differentiation [31]. To evaluate if p53 inhibition alters the intrinsic potential of satellite cells to differentiate towards brown adipose we FACS isolated pure populations of satellite cells from *Pax7-nGFP* mice and cultured them as single-cell clones in a 96-well format under proadipogenic conditions (Figure 11D). Sorting fidelity was monitored by visual inspection. Single clones were treated with 50nM PFTα or equal DMSO two days prior to and during adipogenic induction and allowed to differentiate towards the adipogenic lineage in the absence of p53 inhibition. We observed clones composed of pure myotubes, mixed clones containing myotubes and oil red O positive adipocytes as well as clones of pure adipocytes as shown previously [31]. Treatment with PFTα did not alter the average number of myotubes (Figure 11E) or adipocytes (Figure 11F) in pure or mixed clones and did not alter the average number of cells propagated per clone (Figure 11G). Interestingly, treatment with PFTα resulted in 31% fewer clones containing purely myotubes, a 4.3-fold increase in mixed clones and a significant 3.1-fold increase in pure adipocyte clones (Figure 11H). This data suggests transient p53 inhibition facilitates intrinsic changes in satellite cells in combination with adipogenic media to promote the adipogenic conversion of satellite cells and their progeny.

To further explore if PFTα could induce brown adipogenic gene expression in myogenic cells, myoblasts were treated with 50nM PFTα or equal DMSO and cultured under proadipogenic conditions. Treatment with PFTα prior to adipogenic differentiation resulted in significant induction of *Prdm16, Pgc1a, UCP1, Cidea, Sirt1, Pparγ* and *leptin* (Figure 11I) concomitant with repression in *miR-133* (Figure S6C). Under proadipogenic conditions, PFTα treatment did not alter the myogenic markers *Pax7, MyoD* or Myosin Heavy Chain (*MyHC*) and increased *miR-206* and *Let-7a* levels (Figure S6D). This data suggests treatment with PFTα promotes brown adipogenic gene expression in committed myogenic progenitors under pro-adipogenic conditions.

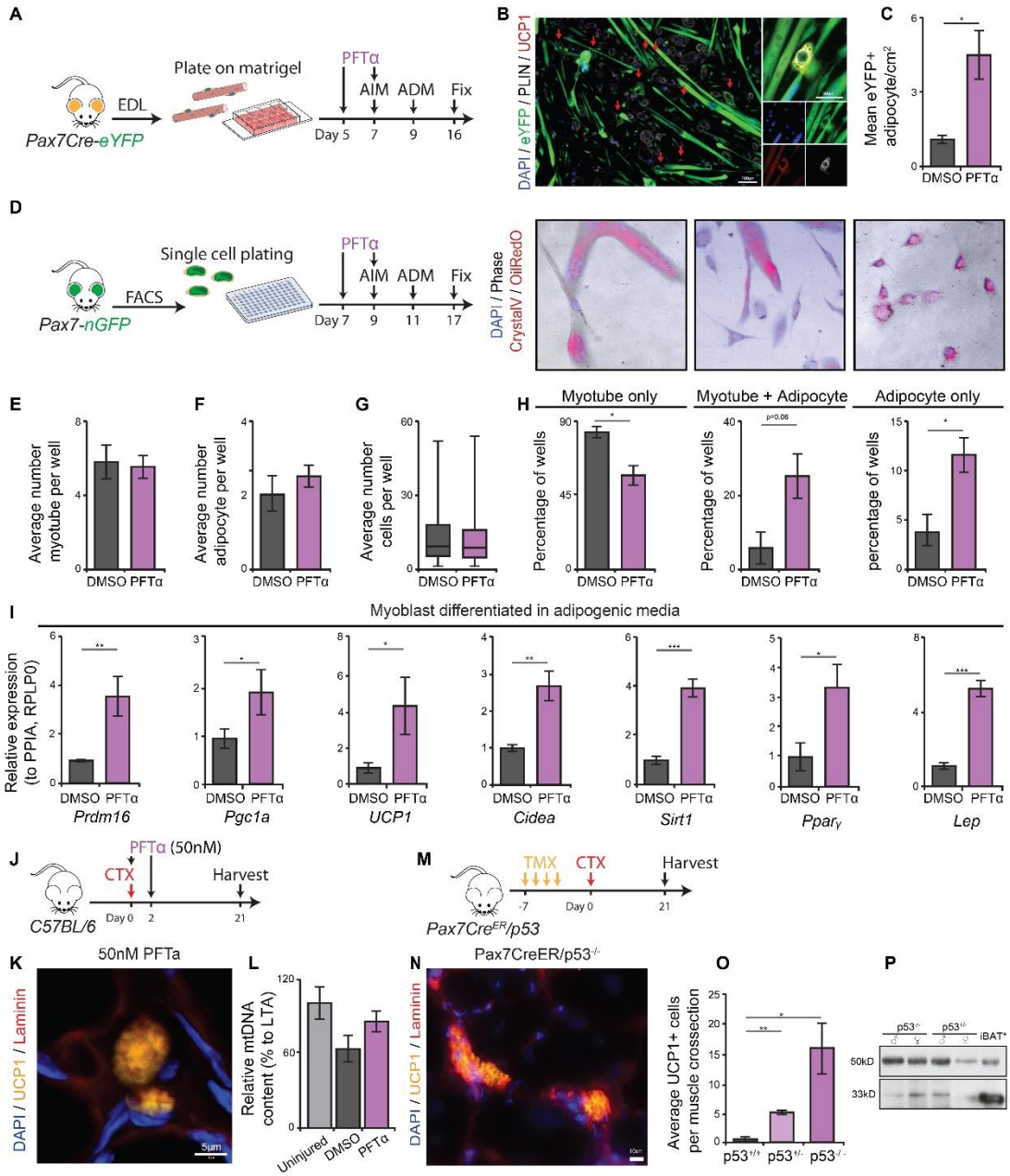


Figure 11: **Inhibition of p53 mediated *miR-133* processing promotes satellite cell fate switching.** A) Graphic overview of PFTα treatment of adipogenic EDL myofibre cultures from *Pax7Cre-eYFP* mice. B) Representative images of DAPI (Blue) eYFP (Green), UCP1 (Red) and Perilipin (PLIN - White) expressing adipose from *Pax7Cre-eYFP* myofibre cultures in adipogenic media. Red arrows denote eYFP expressing adipose tissue. C) Quantification of eYFP derived adipocytes per cell culture area following treatment with PFTα or DMSO control. D) Graphic overview of PFTα treatment of FACS isolated single satellite cell clones from *Pax7nGFP* mice cultured in adipogenic media and stained for DAPI (Blue), Crystal Violet (Fuiscia) and OilRedO (Dark Red). Quantification of E) the average number of myotubes per well containing myotubes, F) the average number of adipocytes per well containing adipocytes, G) average number of cells per well, H) proportion of well containing purely myotubes, mixed myotubes and adipocytes or purely

adipocytes in adipogenic single Pax7nGFP satellite cell clones treated with 50nM PFTα as per panel (D). I) Quantitative Real-time PCR for *Prdm16, Pgc1a, UCP1, Cidea, Sirt1, Pparγ, Lep* in C2C12 myoblasts treated with 50nM PFTα prior to culture under adipogenic conditions. J) Graphic overview of PFTα treatment in injured TA muscle of *C57BL/6* mice. K) Representative image of interstitial brown adipose in injured TA muscle from PFTα treated mice stained with DAPI (Blue), UCP1 (Yellow) and Laminin (Red). L) Quantification of relative mitochondrial content in PFTα or DMSO treated TA muscle by Quantitative Real-time PCR and relative level of COX1 to 18S normalized to percent of contralateral TA. M) Graphic overview of Tamoxifen intraperitoneal administration and muscle injury of *Pax7Cre$^{ER}$/p53* mice. N) Representative image of interstitial brown adipose in injured TA muscle from *Pax7Cre$^{ER}$/p53$^{-/-}$* mice stained with DAPI (Blue), UCP1 (Yellow) and Laminin (Red). O) Quantification of UCP1+ cells per muscle section from *Pax7Cre$^{ER}$/p53$^{+/+}$, Pax7Cre$^{ER}$/p53$^{+/-}$* heterozygotes*,* and *Pax7Cre$^{ER}$/p53$^{-/-}$* mice*.* P) Immunoblotting analysis of UCP1 from *Pax7Cre$^{ER}$/p53$^{+/-}$* heterozygotes*,* and *Pax7Cre$^{ER}$/p53$^{-/-}$* injured TA muscle and interscapular Brown adipose tissue as the positive control. Tubulin was used as a loading control and iBAT was loaded 1:2 dilution. (I) Error bars represent mean ±SD; (C, E-H, K-L, O-P) Error bars represent mean ±SEM; p-values: *=<0.05, **=<0.01; ***=<0.005. (I) n=6 technical replicates. (B-C, E-H, K-L, O-P) n=3 biological replicates.

To determine if PFTα treatment results in satellite cell adipogenic differentiation *in vivo*, we injured C57BL/6 mice TA muscle and treated with 50nM PFTα or equivalent DMSO containing saline at the time of injury and 2 days after, allowing muscles to regenerate for 21 days (Figure 11J). Following muscle regeneration, UCP1 expressing cells were observed in PFTα treated muscles along with a 35% increase in mitochondrial DNA content compared to DMSO treated controls (Figure 11K). This data suggests that PFTα treatment can facilitate adipogenic differentiation *in vivo* in response to injury.

To explore further if the observed effect of p53 inhibition was satellite cell-specific, we crossed the tamoxifen-inducible *Pax7Cre$^{ER}$* mouse with the *p53* mouse model to make a *Pax7CreER/p53* model, whereupon intraperitoneal tamoxifen treatment results in genetic excision of p53 from satellite cells. Following 5 consecutive days of tamoxifen injections to induce satellite cell-specific p53 excision, mouse TA muscles were injured with CTX and allowed to regenerate. Following muscle repair, Pax7Cre$^{ER}$/p53$^{-/-}$ homozygote muscle showed no change in average myofibres per TA (Figure S6I), no change in average minimum fibre Feret (Figure S6J) and a mild leftward shift in minimum

fibre Feret proportion (Figure S6K), suggesting p53 excision from satellite cells does not significantly impair muscle repair. Importantly, interstitial UCP1 expressing cells were significantly induced in tamoxifen-treated Pax7Cre$^{ER}$/p53$^{+/-}$ heterozygotes and Pax7Cre$^{ER}$/p53$^{-/-}$ homozygote muscle compared to Pax7Cre$^{ER}$/p53$^{+/+}$ controls (Figure 11N, O). Western blotting of TA muscle from Pax7Cre$^{ER}$/p53$^{-/-}$ mice revealed significant induction in UCP1 protein in Pax7Cre$^{ER}$/p53$^{-/-}$ muscle compared to heterozygotes and interscapular brown adipose tissue (Figure 11P). Taken together, these data support a relationship between p53 mediated *miR-133* activity and restriction of non-myogenic lineages in satellite cells.

## DISCUSSION

Using a novel screening approach, we identified multiple compounds that regulate *miR-133* in skeletal muscle without a detrimental effect in primary cardiomyocytes. We validated the p53 pathway to be a potent regulator of *miR-133* activity in mouse satellite cells and human myoblasts presumably through the regulation of *miR-133* processing from *Pri-miR-133* to mature *miR-133*. Using pharmacological and genetic models we identified the role of p53 in promoting myogenic commitment and limiting alternative cell fates in mouse satellite cells. Our data suggest that p53 functions promote myogenic differentiation in muscle stem cells and to repress the adipogenic fate. A better understanding of cell-type-specific regulatory paradigms of *miR-133* and regulators of satellite stem cell fate will help elucidate genetic pathways controlling multi-potency and fate decisions in adult stem cells.

Estimates of brown adipose activity in humans range widely from 10-25 kcal per day following mild cold exposure [137,138] where technical limitations in $^{18}$FDG-PET scanning may underestimate true contributions of BAT to thermogenesis. Conservative estimates incorporating BAT volume, oxidative potential, density and respiratory rate suggest BAT may contribute between 27-123 kcal per day at thermoneutrality and 46-211 kcal per day with mild cold exposure [139]. The limited amount of BAT present in humans makes its contribution to basal metabolism small, while in rodents, experimental increases in BAT volume increases energy expenditure [48] and improves glucose and lipid homeostasis [140]. Additionally, age, diabetes and obesity reduce BAT activity in humans [51,52], and obese individuals require lower skin temperatures to stimulate non-shivering thermogenesis due to larger body mass increasing heat generation [141].

As a therapeutic modality, active brown adipose tissue can provide a natural defence against obesity by augmenting resting metabolic rates but is relatively scarce in adult humans and negatively correlated with body mass index [142]. Experimental induction

of BAT in animal models is associated with a lean and healthy phenotype [31,58] suggesting expanding resident BAT stores could represent a novel therapeutic avenue to treat obesity and its related disorders [143]. *MiR-133* antagonism-based therapy for obesity takes advantage of the lineage plasticity of naturally existing stem cells in the human body to build functional brown adipose tissue *de novo* and holds advantages over current anti-obesity pharmaceutics. First, the irreversible nature of brown adipose differentiation suggests satellite cell fate decisions can lead to sustained metabolic benefit [31] where current anti-obesity therapeutics rely on transient pharmacokinetics to achieve long term metabolic changes. Additionally, the lineage determination of satellite cells likely occurs in a short period of time during the early satellite cell activation suggesting transient *miR-133* antagonism may provide long term benefit. These advantages have been observed previously [31] which are phenotypically mimicked by transient PFTα treatment. As the anti-obesity compounds Quercetin [122], Genistein [123], Metformin [124] and Rofecoxib [125] were identified in the biosensor screen to decrease *miR-133* activity, it would suggest they may also regulate *miR-133* to augment metabolism. Further studies exploring the potential of *miR-133* inhibitors identified in this study or PFTα to augment basal metabolic rate may provide proof of principle evidence that indirect targeting of *miR-133* activity can provide tissue specificity to augment metabolic changes and confer resistance to obesity.

The p53 pathway is well understood to facilitate apoptosis and cell cycle arrest, however, has been implicated in regulating cellular metabolism [144]. and mitochondrial remodelling [136]. Poly(ADP-ribose) polymerases (PARPs) are also well-known cell cycle inhibitors and are major $NAD^+$ consumers in cells and compete with Sirt1 protein for the availability of $NAD^+$. Interestingly, Sirt1 has recently been found to stabilize the Prdm16/PPARγ protein complex critical for brown adipose determination [145], p53 has been found associated in PRDM16 protein complexes [47] and PARP1 and PARP2 are protein interactors of p53 [146]. Therefore, it is conceivable that p53, its interactors (e.g.

PARPs and HSP90) and downstream factors may play a key role in the brown adipose determination by regulating *miR-133* expression or function.

MicroRNA mature through stepwise processes beginning in the nucleus with the transcription of long initial primary transcripts (Pri-miRNA) and subsequent processing by the microprocessor complex forming a ~70nt intermediate precursor miRNA (pre-miRNA) [147]. Pre-miRNA are exported from the nucleus to undergo processing by the endonuclease Dicer to produce ~22nt double-strand mature miRNA to be loaded into the RNA-induced silencing complex (miRISC) to mediate mRNA translational repression, mRNA sequestering or mRNA degradation [147]. The stepwise processing of miRNA and their accumulation within a cell is under tight regulation by tissue-specific miRNA transcription and binding of miRNA regulating proteins [148], the association of sequence-specific dsRNA binding proteins [149] and regulation of miRNA decay [150]. Changes in biosensor activity can be attributed to regulation at any step in this process whereby compounds may inhibit *miR-133* function by decreasing *pri-miR-133* expression level, limiting *miR-133* processing, blocking *miR-133* loading into the miRISC complex or interfering the target recognition of *miR-133* with its target mRNAs. We found that p53 regulates the processing of *miR-133* into its active form likely through specific regulation of a subset of microRNA species. Other studies have identified a putative interaction between p53 and the pri-miRNA processing complex through association with p68[151], however technical limitations including non-specific pre-miRNA RT-qPCR, inappropriate data interpretation regarding pri-miRNA maturation and a lack of insight as to the specificity of p53-p68 mediated regulation of only a subset of miRNA limit the generalisability of results. Nonetheless, co-immunoprecipitations experiments would suggest p53 can associate with p68 and promote miRNA processing in certain cell lines, providing an attractive mechanism to be validated in satellite cells. Understanding the basis of *miR-133* processing and maturation has implications in satellite cell fate decisions but also wide-ranging implications in a

context such as cancer, where p53 is frequently mutated and *miR-133*b can regulate cell invasion and migration [152]. Further studies exploring subcellular fractionation and RNA based imaging techniques such as nuclease protection assays for *pri-miR-133* will better resolve the milieu in which p53 is regulating *miR-133* processing, define *pre-miR-133* abundance and provide insight into potential mechanisms of p53 mediated regulation.

*MiR-133* regulation poses a key thermoregulatory mechanism in cold adaption and augmentation of whole-body energy expenditure. In response to cold, PPARγ coactivator 1A recruits HATs to locally remodel chromatin facilitating mitochondrial biogenesis [153] in tandem with PRDM16 binding to brown adipogenic enhancer regions to establish the thermogenic gene program [154,155]. Cold-induced p53 repression may pose a regulatory step required to promote *PRDM16* stability in both brown adipose and satellite cells [31] to facilitate epigenetic remodelling and increase thermogenic metabolism. As tissue such as limb muscle is resistant to cold-induced UCP1 induction [31] yet exhibit significantly reduced p53 levels in cold (Figure 10B) it would suggest that cell-extrinsic factors *in vivo* such as β-adrenergic innervation [156] or intrinsic factors such as epigenetic permissibility [31,47], heterogeneous niche interactions [5], mitochondrial remodelling potential [136,157] and embryonic origin [47] may attribute to the observed refractory nature of some muscle groups to cold-induced metabolic remodelling.

The tumour suppressor p53 is well-known for its functions in promoting cell cycle arrest and apoptosis. Recently, it was found that p53 also plays an important role in regulating cellular metabolism [144]. Pertinent to obesity, p53 induces insulin resistance in white fat [158] and restricts mitochondrial remodelling in aged mice to limit metabolic “beiging” in white adipose [136]. During myogenesis, activation of p53 promotes the phosphorylation and function of pRb [159], which is known for its pro-myogenic function, regulation of cell cycle and inhibitory action on brown adipose determination [160,161].

Additionally, we show herein that p53 inhibition through PFTα represses *miR-133* activity to facilitate *PRDM16* expression in satellite cells and their progeny to derive brown adipose (Figure 11A-I). It is likely that metabolic changes *in vitro* due to adipogenic induction facilitate the adipogenic conversion of satellite cells, however, the induction of adipogenic cells from Pax7-eYFP cultures (Figure 11A-C), the adipogenic shift in single nGFP colonies (Figure 11D-M), the presence metabolic fibre type changes (Figure 9M) and interstitial brown adipose formation *in vivo* (Figure 11J-P) suggest that p53 inhibition facilitates cell-intrinsic changes amenable for the metabolic and adipogenic conversion of satellite cells. Importantly, mitochondrial function and remodelling can regulate stem cell and cell identity in multiple cell types [136,162] highlighting a complex relationship between cell-intrinsic transcriptional networks, epigenetic permissibility and metabolic status that intersect to regulate cell fate.

Our findings provide proof of principle evidence that indirect targeting of *miR-133* activity through transient p53 inhibition can facilitate satellite cell fate switching towards the brown adipogenic lineage. We envision compounds targeting *miR-133* activity in broad skeletal muscle groups while maintaining *miR-133* activity in cardiac muscle would pose an attractive means to provide long term metabolic benefit for the treatment of obesity and its related disorders.

## ACKNOWLEDGEMENTS

The OICR kinase inhibitor, toolkit libraries were kindly provided by Dr. Mick Bhatia. P.F. is supported by a fellowship from CIHR. M.A.R. holds the Canada Research Chair in Molecular Genetics. These studies were carried out with grant support to M.A.R. from the NIH (R01AR044031), the Canadian Institutes for Health Research (FDN-148387), E-Rare-2: Canadian Institutes of Health Research/Muscular Dystrophy Canada (ERA-132935), the Muscular Dystrophy Association, the Ontario Institute for Regenerative Medicine, and the Stem Cell Network.

## AUTHOR CONTRIBUTION

Conceptualization: P.F., H.Y. and M.A.R.; Methodology: P.F., H.Y., H.M., M.A., and M.A.R.; Investigation: P.F., H.Y., H.M., and M.A.R.; Writing – Original draft: P.F., H.Y. and M.A.R.; Writing – Review and editing: P.F., H.Y., L.M. and M.A.R.; Funding Acquisition: M.A.R.; Resources: L.M. and M.A.R.; Supervision: L.M. and M.A.R.

## DECLARATION OF INTERESTS

No authors declare competing interests.

## STAR METHODS



## SUPPLEMENTAL INFORMATION

Supplemental information includes six figures and one table.

## STAR METHODS

## KEY RESOURCES TABLE

| REAGENT or RESOURCE | SOURCE | IDENTIFIER |
|---|---|---|
| Antibodies | | |
| Chicken anti-GFP | Abcam | Cat# ab13970; RRID: AB_300798 |
| Crystal Violet | Sigma-Aldrich | Cat# C0775 |
| Mouse anti-a-Tubulin | Sigma-Aldrich | Cat# T6199; RRID: AB_477583 |
| Mouse anti-Dicer | Santa Cruz Biotechnology | Cat# sc-393328; RRID: AB_2802128 |
| Mouse anti-GAPDH | Sigma-Aldrich | Cat# G8795; RRID: AB_1078991 |
| Mouse anti-Integrin-a7 APC | Miltenyi Biotech | Cat#130-102-716; RRID: AB_2652464 |
| Mouse anti-MyH3 | DSHB | Cat# F1.652; RRID: AB_528358 |
| Mouse anti-MyH4 | DSHB | Cat# BF-F3; RRID: AB_2266724 |
| Mouse anti-MyH7 | DSHB | Cat# BA-F8; RRID: AB_10572253 |
| Mouse anti-p53 | New England Biolabs | Cat# 2524S; RRID: AB_331743 |
| Mouse anti-Pax7 | DSHB | Cat# Ab 528428; RRID: AB_528428 |
| Mouse anti-Perilipin-A | Vala Sciences | Cat# 4854 |
| Oil Red O | Sigma-Aldrich | Cat# O0625 |
| Rabbit anti-Ago2 | Abcam | Cat# ab156870; RRID: AB_2687492 |
| Rabbit anti-MyoD | Santa Cruz Biotechnology | Cat# sc-304; RRID: AB_631992 |
| Rabbit anti-Myogenin | Santa Cruz Biotechnology | Cat# sc-576; RRID: AB_214908 |
| Rabbit anti-Prdm16 | N/A | Seale et al., 2008. |
| Rabbit anti-UCP1 | EMD Millipore | Cat# 662045 |
| Rat anti-CD11b BV421 | Becton Dickinson | Cat# 562605; RRID: AB_2740930 |
| Rat anti-CD31 BV421 | Becton Dickinson | Cat# 562939; RRID: AB_2665476 |
| Rat anti-CD45 BV421 | Becton Dickinson | Cat# 563890; RRID: AB_2651151 |
| Rat anti-Laminin | Sigma | Cat# L0663; RRID: AB_477153 |
| Rat anti-SCA1 BV421 | Becton Dickinson | Cat# 562729; RRID: AB_2737750 |
| Wheat Germ Agglutinin Alexa 647 conjugate | Life Technologies | Cat# W32466 |
| Chemicals, Peptides and Recombinant Proteins | | |
| Cardiotoxin Gamma from Naja pallida | Cedarlane | Cat# L8102 |
| Chick Embryo Extract | MP Biomedicals | RRID 92850145 |
| Collagenase Type I | Worthington | Cat# LS004169 |
| Cyclic-Pifithrin-α | Cedarlane | Cat# 3843/10 |
| Dexamethasone | Sigma-Aldrich | Cat# D4902 |
| Fibroblast Growth Factor-basic | EMD Millipore | Cat# GF003AFMG |
| IBMX | Sigma-Aldrich | Cat# I5879 |
| Indomethacin | Sigma-Aldrich | Cat# I7378 |
| Insulin | Sigma-Aldrich | Cat# 11376497001 |
| Lipofectamine RNAiMax | Life Technologies | Cat# 13778150 |
| Rosiglitazone | Cedarlane | Cat# 71740 |
| $T_3$ | Sigma-Aldrich | Cat# T6397 |
| Tamoxifen | Sigma-Aldrich | Cat# T5648 |
| Critical Commercial Assays | | |
| Lipofectamine RNAiMax | Life Technologies | Cat# 13778150 |
| miRNEasy miRNA micro isolation kit | Quiagen | Cat# 217084 |
| Ontario Institute for Cancer Research kinase inhibitor and toolkit compound libraries | OICR, Toronto, Canada | N/A |
| SSoFast EvaGreen Supermix | Bio-Rad | Cat# 1725202 |
| Experimental Models: Cell Lines | | |
| C2C12 myoblasts | N/A | CVCL_0188 |
| MiR-133 biosensor | N/A | PAT6926W-90 |
| Experimental Models: Organisms/Strains | | |
| Mouse: C57BL/6 | The Jackson Laboratory | JAX: 000664 |
| Mouse: Myf5-Cre | The Jackson Laboratory | JAX: 007893 |
| Mouse: Myf5-Cre:R26R-eYFP | Kuang et al., 2007 | NA |
| Mouse: p53 | The Jackson Laboratory | JAX: 008462 |
| Mouse: Pax7-CreERT2 | The Jackson Laboratory | JAX: 017763 |
| Mouse: Pax7-nGFP | Rocheteau et al., 2012 | MGI:5449370 |
| Mouse: R26R-eYFP | The Jackson Laboratory | JAX: 006148 |
| Oligonucleotides | | |
| 18s (mtDNA) | F: CGCGGTTCTATTTTGTTGGT | R: AGTCGGCATCGTTTATGGTC |
| ANP | F: GAGGAGAAGATGCCGGTAG | R: CTAGAGAGGGAGCTAAGTG |
| Cidea | F: ATACATCCAGCTCGCCCTTT | R: ACTTACTACCCGGTGTCCAT |
| Cox1 (mtDNA) | F: CCTATCACCCTTGCCATCAT | R: GAGGCTGTTGCTTGTGTGAC |
| GAPDH | F: AGGTCGGTGTGAACGGATTTG | R: TGTAGACCATGTAGTTGAGGTCA |
| LEP | F: ACCAAAACCCTCATCAAGACCATT | R: CTTGGACAAACTCAGAATGGGGT |

| | | |
|---|---|---|
| Let-7 | F: TGAGGTAGTAGGTTGTATAGTT | R: GCATACGAGCTCTTCCGATCT |
| miR-1 | F: TGGAATGTAAAGAAGTATGTAT | R: GCATACGAGCTCTTCCGATCT |
| miR-133a | F: TCCCCTTCAACCAGCTG | R: GCATACGAGCTCTTCCGATCT |
| miR-133b | F: TCCCCTTCAACCAGCTA | R: GCATACGAGCTCTTCCGATCT |
| miR-17 | F: GCTTACAGTGCAGGTAG | R: GCATACGAGCTCTTCCGATCT |
| miR-206 | F: UGGAAUGUAAGGAAGUGUGUGG | R: GCATACGAGCTCTTCCGATCT |
| miR-208 | F: GACGAGCAAAAAGCTTGT | R: GCATACGAGCTCTTCCGATCT |
| Musculin | F: CTATGTGCACCCTGTGAACCT | R: GTTGGCTGCAGAAACGTCTT |
| MyoG | F: AATGCAACTCCCACAGCGC | R: GAGCAAATGATCTCCTGGGTTGG |
| P21 | F: GCAGAATAAAAGGTGCCACAGG | R: CGAAGAGACAACGGCACACT |
| P53 | F: AGGCTTATGGAAACTACTTCCTCC | R: CAGCAACAGATCGTCCATGC |
| Pax7 | F: TACTGCCCACCCACCTACAG | R: GTGTGGACAGGCTCACGTTT |
| Pgc1a | F: GGTCAAGATCAAGGTCCCCA | R: TCATAGCTGTCGTACCTGGG |
| PPARγ | F: GCTTGTGAAGGATGCAAGGG | R: GCCCAAACCTGATGGCATTG |
| PPIA | F: CAGTGCCAAGACTGAATG | R: GTCGGAAATGGTGATCTT |
| PRDM16 | F: CGACTTTGGATGGGAGCAGATG | R: CGCAGAACTTCTCGCTACCC |
| Pri-miR-133a1 | F: GACAGGTATTAGAGGTTCCCACA | R: TAAAGATGCACTGATGTGAGCTG |
| Pri-miR-133a2 | F: TGCATGGGTTCTCAGAGCAG | R: GCTTCTGATCCACTGGGAGG |
| Pri-miR-133b | F: AGCAAGCCATATTTTCGGGGAGCC | R: GGGGTATCCTCTGCTTTCGGCTT |
| RPLP0 | F: GCTTTCTGGAGGGTGTCC | R: GGACGCGCTTGTACCCATTG |
| Sirt1 | F: TTGTGAAGCTGTTCGTGGAG | R: GGCGTGGAGGTTTTTCAGTA |
| Sno202 | F: CCTGTGTACTGACTTGATGAAAG | R: GCATACGAGCTCTTCCGATCT |
| U6snRNA | F: TGGCCCCTGCGCAAGGATG | R: GCATACGAGCTCTTCCGATCT |
| UCP1 | F: ATACTGGCAGATGACGTCCC | R: CGAGTCGCAGAAAAGAAGCC |
| Software and Algorithms | | |
| GraphPad Prism | GraphPad Software Inc | https://www.graphpad.com/scientific-software/prism/ |
| ImageJ | NIH | https://imagej.nih.gov/ij/ |
| SMASH - semi-automatic muscle analysis using segmentation of histology | Smith and Barton, 2014 | http://figshare.com/articles/SMASH_semi_automatic_muscle_analysis_using_segmentation_of_histology_a_MATLAB_application/1247634 |

## CONTACT FOR REAGENT AND RESOURCE SHARING

Information and requests for reagents may be directed to the Lead Contact, Michael A. Rudnicki (mrudnicki@ohri.ca).

## EXPERIMENTAL MODEL AND SUBJECT DETAILS

### Experimental animals

Housing, husbandry, and experimental protocols involving mice in this study were performed in accordance with the guidelines established by the University of Ottawa Animal Care Committee, which is based on the guidelines of the Canadian Council on Animal Care. Mice are housed in ventilated cages with 1/4'' corncob bedding changed every two weeks. Mice are supplied food ad libitum with automated acidified RO water or bottles changed every 7 days. Light cycles are 12h-12h cycle with simulated sunrise and sunset. Health and immune status of experimental mice were normal where Sentinels are routinely monitored (fecal, fur and oral swab) for MNV, MHV, Mouse Parvovirus (MPV/MVM), MRV (EDIM), TMEV/GDVII, Helicobacter, P. pneumotropica-Heyl, P.

pneumotropica-Jawetz, Entamoeba, Mites, Pneumocystis, Pinworm, and Spironucleus muris. No animals were subjected to previous experimental procedures and are test or treatment-naive. For cold exposure, C57BL/6 mice were gradually accustomed to decreasing temperature over 3 days and maintained at 4°C for one week with food and water ad libitum.

The following mouse lines were used: C57BL/6, B6.Cg-Pax7$^{tm1(cre/ERT2)Gaka}$/J (Pax7-CreERT2), B6.129S4-Myf5$^{tm3(cre)Sor}$/J (Myf5-Cre), B6.129X1-Gt(ROSA)26Sor$^{tm1(EYFP)Cos}$/J (R26R-eYFP), B6.SJL-Pax7$^{tm1.2Tajb}$ (Pax7-nGFP), 129P2-Trp53$^{tm1Brn}$ (p53). If not stated differently, 6-8 week old mice were used for all experiments. Myf5-Cre:ROSA26-eYFP mice (Kuang et al., 2007) were F1 progeny from Myf5-Cre x R26R-eYFP breeding pairs. Tamoxifen inducible conditional genetic knockout animals were F2 crosses between the offspring of Pax7-CreERT2 (Cre/+) mice and p53$^{fl/fl}$ generating Pax7-CreERT2:p53$^{(+/+)}$, Pax7-CreERT2;p53$^{(-/+)}$ and Pax7-CreERT2:p53$^{(-/-)}$ mice.

**Cell Lines**

C2C12 cells were used as the parental strain for the *miR-133* biosensor and for follow up analysis as stated. C2C12 were purchased from and authenticated by ATCC. These cells were verified to be free from mycoplasma contamination using the MycoSensor PCR Assay Kit (Agilent Technologies). C2C12 cells were cultured at 37°C in Dulbecco's Modified Eagle's Medium (DMEM) supplemented with 10% fetal bovine serum and 1% penicillin/streptomycin.

**METHOD DETAILS**

**Adipogenic cell culture**

Cells are incubated in adipogenic induction media containing: 10% FBS in DMEM, 1% Pen/strep, 5uM Dexamethasone, 125nM Indomethacin, 1uM Rosiglitazone, 1nM $T_3$, 850nM Insulin, and 0.5mM IBMX for 2 days. Cells media is changed to differentiation

media containing 10% FBS in DMEM, 1% Pen/strep, 1uM Rosiglitazone, 1nM $T_3$, 850nM Insulin, for an additional 6-7 days until adipocytes are visible.

**Biosensor design and screening**

C2C12 myoblasts were infected with lentiviral particles in 293T cells containing both luciferase vectors (Figure 6A) and underwent puromycin selection. Single cells were established by limited dilution. Clones were identified containing both renilla and firefly_133 integration for further dynamic range testing by *miR-133* mimetics/ inhibitors transfection and luciferase assay. Constructs were then tested during differentiation for a *miR-133* response. Biosensor C2C12 cells were cultured in 96-well plates and treated with 560 compounds (400 compounds from OICR Kinase Inhibitor Library and 160 compounds from OICR Tool Compound Library) individually in growth media (DMEM + 20% FBS) for 48 hours. The final concentrations of compounds in each well were 40nM and 1μM. As these compounds were resolved in DMSO, 6 wells of cells on each 96-well plate were treated with correspondingly diluted DMSO as controls. After 48 hours of incubation, luciferase activities were measured and normalized to the protein concentrations for every well. The 560 compounds were sorted based on their normalized luciferase activities at each concentration and presented as two spectrums.

**Cardiotoxin Injury**

I.M. cardiotoxin injections (Latoxan, 50ul of 10 mM solution in saline) were injected directly into the right TA muscle through the skin under general anesthesia. For pharmacological inhibition, PFTα was mixed into the cardiotoxin solution for a final concentration of 50nM, equal dilution of DMSO was used as vehicle control. Supplemental injection of inhibitors (20uL of 50nM in saline) was performed 2 days after cardiotoxin injection. Muscles were harvested 7 days post-injury as a mid-point of regeneration where the number of Myog-expressing cells is above baseline and myofibers are reforming. Time points of 21 days represent full repair.

**Compound Libraries and Small Molecules**

The Ontario Institute for Cancer Research kinase inhibitor and toolkit compound libraries (OICR, Toronto, Canada) consists of 400 specific kinase inhibitors and 160 additional small molecule compounds targeting cellular and developmental pathways. Compound libraries were obtained as 1mM solutions dissolved in DMSO.

**EDL fiber Culture**

EDL were carefully dissected and incubated at 37°C in DMEM with 2% L-glutamine, 4.5% glucose, and 110 mg/mL sodium pyruvate (GIBCO) containing 0.2% collagenase I(Sigma) for 50 min. Myofibers were isolated using gentle trituration in DMEM+ with 2% L-glutamine, 4.5% glucose, and 110 mg/ml sodium pyruvate (GIBCO) containing 20% FBS (Wisent) with a glass pipet. Myofibers were cultured floating in serum coated dishes at 37°C for 40, 48, or 72h or alternatively plated directly onto Matrigel-coated plates and cultured in DMEM+ with 2% L-glutamine, 4.5% glucose, and 110 mg/ml sodium pyruvate (GIBCO) containing 20% FBS (Wisent), 1% chick embryo extract (MP Biomedicals), and 2.5ng/ml bFGF (Cedarlane). For pharmacological inhibition, PFTα (50nM in DMSO, Tocris Bioscience) was added to the culture medium for a final concentration of 50nM, equal dilution of DMSO was used as vehicle control.

**FACS isolation and single-cell culture**

Satellite cells from naïve Pax7nGFP mice or Pax7nGFP mice 3 days post-injury were FACS isolated based on FSC/SSC, CD31/CD11b/CD45/SCA1 (V450), a7-Integrin (APC) and nGFP and either isolated for RNA extraction or sorted into 96-well plates based on single-cell purity settings. Single cells were deposited into each well in 96-well plates coated with Matrigel (1:4 dilution, thin gel coating) with 100ul of 20% FBS, 1% CEE, DMEM in each well. The first and final plate from each mouse was manually validated for single cells, dual nGFP+APC+ single cells and to rule out the presence of doublets. Cells are cultured in 200ul DMEM+ with 2% L-glutamine, 4.5% glucose, and 110 mg/ml sodium

pyruvate (GIBCO) containing 20% FBS (Wisent), 1% chick embryo extract (MP Biomedicals), and 2.5ng/ml bFGF (Cedarlane) with media change every 3 days then as per overview in Figure 11D.

**Histological Analysis of Muscle Section**

For analysis of muscle fibre type, non-fixed samples were blocked in 10% NGS for 1hr at room temperature. Primary antibodies in 10% NGS were applied for 2h at room temperature. Sections were extensively washed in PBS and secondary antibodies were applied diluted in PBS for 1h at room temperature. Sections were washed in PBS and counterstained with DAPI for 10min and mounted with Permafluor. Antibodies were as follows: mouse anti-MyH3 (clone F1.652, DSHB), mouse anti-MyH4 (clone BF-F3, DSHB), mouse anti-MyH7 (BA-F8, DSHB). For minimum myofibre Feret's diameter analysis, non-fixed samples were washed with PBS and stained with Wheat Germ Agglutinin Alexa 647 conjugate (Fisher) for 1h at room temperature. Samples were washed once with PBS and counterstained with DAPI. Samples were mounted with Permafluor. Images were taken immediately following staining. Minimum fiber Feret measurement was performed using the SMASH software in MATLAB 2015a as described previously[163]. The total number of myofibers in each tissue was verified manually.

**Immunoblotting**

Protein was separated on a 10% SDS-PAGE gel and transferred to Immobilon-P PVDF membrane (EMD Millipore) overnight. Membranes were probed with primary antibodies, followed by light chain specific HRP-conjugated secondary antibodies at 1:5000 (Bio-Rad) and developed using Immobilon Western HRP substrate (EMD Millipore). Membranes were exposed to BIOMAX film (Eastman Kodak). The following antibodies were used: Rabbit anti-Ago2 (Abcam Cat# ab156870; RRID: AB_2687492), Mouse anti-a-Tubulin (Sigma-Aldrich Cat# T6199; RRID: AB_477583), Mouse anti-Dicer (Santa Cruz Biotechnology Cat# sc-393328; RRID: AB_2802128), Mouse anti-GAPDH (Sigma-Aldrich

Cat# G8795; RRID: AB_1078991), Mouse anti-Pax7 (DSHB Cat# Ab 528428; RRID: AB_528428), Rabbit anti-MyoD (Santa Cruz Biotechnology Cat# sc-304; RRID: AB_631992), Mouse anti-p53 (New England Biolabs Cat# 2524S; RRID: AB_331743), Rabbit anti-Myogenin (Santa Cruz Biotechnology Cat# sc-576; RRID: AB_214908), Rabbit anti-UCP1 (EMD Millipore Cat# 662045)

**Immunofluorescence staining**

EDL myofibers were fixed for 10 min in warm 2% PFA and washed with PBS. Fibres were permeabilized in 0.5% Triton X-100 for 1h then blocked in 5% NGS in PBS overnight at 4°C. Primary antibodies were applied in blocking solution for 2h at room temperature or at 4°C overnight. Samples were washed in PBS and stained with appropriate secondary Alexa Fluor antibodies for 1h at room temperature in the dark. Samples were washed in DAPI 10min, then PBS and mounted with Permafluor (Fisher). Muscle samples were embedded in OCT and frozen in liquid nitrogen-cooled isopentane and cryosectioned in 10-mm slices. Sections were washed in PBS then fixed in 2% PFA 10min, permeabilized with 0.1% Triton X-100/0.125M Glycine in PBS 10min and extensively washed with PBS. Samples were blocked using M.O.M. Blocking reagent (Vector) 2h followed by additional blocking in 5% NGS at 4° C overnight. Primary antibodies were applied in blocking at 4°C overnight. Samples were washed extensively in PBS and incubated in appropriate secondary Alexa Fluor antibodies for 1h at room temperature in the dark. Samples were washed in DAPI 10min, then PBS and mounted with Permafluor (Fisher).

The following antibodies were used: Chicken anti-GFP (Abcam Cat# ab13970; RRID: AB_300798), Mouse anti-MyH3 (DSHB Cat# F1.652; RRID: AB_528358), Mouse anti-MyH4 (DSHB Cat# BF-F3; RRID: AB_2266724), Mouse anti-MyH7 (DSHB Cat# BA-F8; RRID: AB_10572253), Mouse anti-Pax7 (DSHB Cat# Ab 528428; RRID: AB_528428), Mouse anti-Perilipin-A (Vala Sciences Cat# 4854), Rabbit anti-Myogenin (Santa Cruz Biotechnology Cat# sc-576; RRID: AB_214908), Rabbit anti-Prdm16 (generated in Dr.

Patrick Seale's laboratory), Rat anti-Laminin (Sigma Cat# L0663; RRID: AB_477153), Rabbit anti-UCP1 (EMD Millipore Cat# 662045), Oil Red O (Sigma-Aldrich Cat# O0625), Crystal Violet (Sigma-Aldrich Cat# C0775), Wheat Germ Agglutinin Alexa 647 conjugate (Life Technologies Cat# W32466). Images of immunostainings were taken on an Axio Observer.Z1 microscope equipped with an LSM510 META confocal laser scanner and a plan-Apochromat 63x/1.40 Oil DIC M27 objective or an Axioplan 2 microscope equipped with a plan-Neofluar 40x/1.30 Oil DIC and a plan-Neofluar 100x/1.30 Oil DIC objective. Images were processed and analyzed with Axiovision, Zen, and FIJI software. 3D z stack images were projected by maximum intensity using Fiji software (Http://fiji.sc/).

**Lineage Tracing with Myf5-Cre/R26R-eYFP**

Myf5-Cre/R26R-eYFP transgenic mice, possessing a knock-in of Cre recombinase in the coding-region of the myogenic commitment factor Myf5[164] crossed with the knock-in of Cre-activated yellow fluorescent protein (eYFP) at the ROSA26 locus[165], were used as a lineage reporter model to discriminate committed satellite myogenic cells that have expressed Myf5-Cre ($eYFP^{Pos}$) from satellite stem cells that have never expressed Myf5-Cre ($eYFP^{neg}$)[22]. This transgenic model allows for the visualization of de novo Myf5 expression in committed daughter cells during asymmetric divisions.

**Myoblasts transfection of siRNA, *miR-133* inhibitors and *miR-133* mimetics**

Transfection of myoblasts was performed using lipofectamine RNAiMax (Life Technologies) and validated DsiRNAs (TriFECTa) for p53, Dicer or scramble (SCR). MicroRNA inhibitors or mimics are denatured at 70°C for 10min and mixed in lipofectamine RNAiMax at a final concentration of 500nM *miR-133*a/b PNA inhibitors (Panagene, Korea) and 20nM *miR-133*b Pre-miR™ Precursor (Ambion) per 6-well. Knockdown efficiencies of the siRNA were validated in myoblasts by western blot and qRT-PCR.

**Quantitative reverse transcription PCR**

Total RNA was extracted from cells by TRIzol, Arcturus® PicoPure® RNA Isolation Kit (Applied Biosystems) or miRNEASY RNA micro isolation Kit (Quiagen) following manufactures' recommendations. For RT-qPCR of mRNAs, total RNAs were reverse transcribed into cDNAs by SuperScript III (Invitrogen) and a mixture of oligo dT18-20 primers and random hexamers. MicroRNA RT-qPCRs were performed as previously described (Shi and Chiang, 2005). Locked Nucleic Acid validation of *miR-133*a and *miR-133*b isoform was performed using *miR-133*a and *miR-133*b specific miRCURY LNA miRNA PCR Assays (Quiagen). Sybr Green, real-time PCR analysis (SSoFast EvaGreen Supermix, Bio-Rad) was performed using the CFX384 real-time PCR detection system (Bio-Rad), and results were normalized to *Gapdh, U6snRNA, miR-17, Sno202, RPLP0* or *PPIA* expression and analyzed by Bio-Rad CFX Manager software, Microsoft excel and relative expression ratios were calculated by REST2009 (Qiagen).

**Rat Primary Cardiomyocyte isolation and treatment**

Primary rat cardiomyocytes were isolated by repeated trypsinization of newborn (day 1-3) rat pup hearts followed by washing in serum-containing medium and plating at equal cell quantity. Cells were immediately transfected with the ANP luciferase plasmid. 24h after isolation, primary cardiomyocytes were incubated with pharmacological compounds at 40nM concentration for 48h before Luciferase assay or RNA isolation.

**QUANTIFICATION AND STATISTICAL ANALYSIS**

Compiled data are expressed as mean ± standard deviation (SD) or mean ± standard error of the mean (SEM) as stated. Experiments were performed with a minimum of three biological replicates unless stated otherwise. For statistical comparisons of two conditions, the Student’s t-test was used. For Biosensor screening pathway analysis, a Wilcoxon-Mann-Whitney rank-sum test between grouped drugs and total compounds was used. Paired tests were used for biologically matched samples. Unpaired tests were used to compare unrelated samples. No data were removed as outliers. The experimental design

incorporated user blinding when possible. Statistical analysis was performed in GraphPad Prism or Microsoft Excel. The level of significance is indicated as follows: * $p < 0.05$, ** $p < 0.01$, *** $p < 0.005$.

## Manuscript II: EGF Stimulates Asymmetric Divisions in Muscle Stem Cells and Enhances Regeneration of Dystrophin-Deficient Muscle

AUTHORS: Yu Xin Wang[1,2,4], **Peter Feige[1,2,4]**, Caroline E. Brun[1,2], Bahareh Hekmatnejad[1,2], Nicolas A. Dumont[1,2], Jean-Marc Renaud[2,] Sharlene Faulkes[1,2], Daniel E. Guindon[1,2], and Michael A. Rudnicki [1,2,3,5].

**AUTHOR AFFILIATION**: 1. Sprott Center for Stem Cell Research, Ottawa Hospital Research Institute, Regenerative Medicine Program, Ottawa, ON, Canada. 2. Department of Cellular and Molecular Medicine, Faculty of Medicine, University of Ottawa, Ottawa, ON, Canada. 3. Department of Medicine, Faculty of Medicine, University of Ottawa, Ottawa, ON, Canada. 4. These authors contributed equally

**This manuscript was published in Cell Stem Cell in 2019.**

Yu Xin Wang et al., EGFR-Aurka Signalling Rescues Polarity and Regeneration Defects in Dystrophin-Deficient Muscle Stem Cells by Increasing Asymmetric Divisions. *Cell Stem Cell*. (2019). 24, 419-432. https://doi.org/10.1016/j.stem.2019.01.002

### AUTHOR CONTRIBUTION

Y.X.W. and M.A.R. conceptualized the kinase inhibitor screen. Y.X.W. performed the screening. Y.X.W. and S.F. validated lead compounds. Y.X.W. and P.F. evaluated EGF on mitotic orientation. D.G. performed immunoprecipitation studies. Y.X.W. performed proximity ligation assay. P.F. performed all histological analyses. P.F. evaluated EGFR signalling on myofibres. C.E.B. evaluated the activation of EGFR during muscle regeneration. Y.X.W., P.F. and N.A.D. evaluated in vitro myofibre cultures for the effect of EGF on satellite cell commitment in WT and *mdx* muscle. X.Y.W. and P.F. electroporated

EGF into *mdx* muscle. Y.X.W. and P.F. optimized and performed all *in situ* force measurement. P.F. evaluated satellite cell polarity, EGFR cKO mice and the role of EGF on satellite stem cell commitment through satellite cell transplantation. Y.X.W. wrote the initial manuscript. Y.X.W. and P.F. developed the Figures and edited manuscript drafts. M.A.R. oversaw the experimental design, analysis of results, manuscript editing, and financial support.

**ABSTRACT**

Loss of dystrophin in Duchenne Muscular Dystrophy (DMD) brings about progressive degeneration of skeletal muscle that is exacerbated by reduced rates of asymmetric division of muscle stem cells, resulting in reduced generation of progenitors, and impaired regeneration. Through a small molecule screen, we identified epidermal growth factor receptor (EGFR) and Aurora kinase A (Aurka) as regulators of muscle stem cell asymmetric division. The inhibition of EGFR results in a pronounced shift from asymmetric to symmetric division. Conversely, treatment with EGF stimulates a 2.5-fold increase in asymmetric divisions. Activation of EGFR orients mitotic centrosomes through Aurka, and inhibition of Aurka blocks EGF stimulation of asymmetric division. EGF treatment markedly stimulates asymmetric divisions in dystrophin-deficient muscle stem cells in *mdx* mice, resulting in increased numbers of progenitors, enhanced regeneration, and restoration of muscle strength. Therefore, activating the EGFR polarity pathway stimulates the functional rescue of dystrophin-deficient satellite cells and enhances muscle force generation.

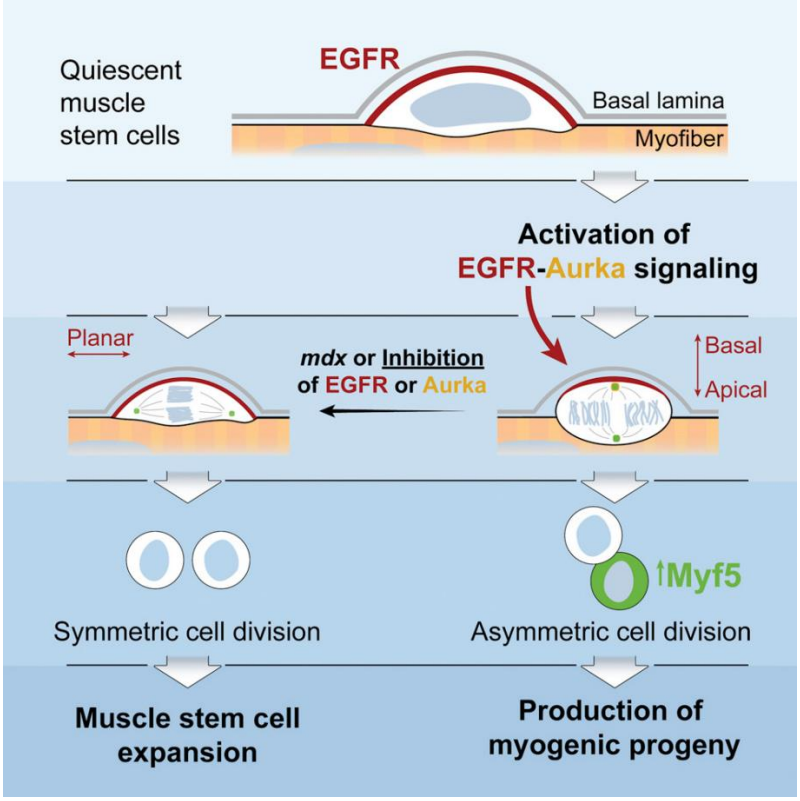


Figure 12: **Graphical abstract for manuscript II.**

**HIGHLIGHTS**

- EGFR expression and activation is polarized in satellite cells
- EGF stimulates asymmetric satellite stem cell division
- Polarized EGFR activation orients mitotic centrosomes through Aurka
- EGF stimulation rescues *mdx* satellite cell function *in vitro* and *in vivo*

**eTOC blurb**

Wang et al., found that EGFR–Aurka signalling in muscle stem cells acts to direct apicobasal oriented mitoses and asymmetric cell division. EGF treatment rescues the reduction of asymmetric divisions in dystrophin-deficient satellite cells in *mdx* mice, resulting in increased numbers of progenitors and enhanced regeneration.

## INTRODUCTION

The balance between stem cell self-renewal and differentiation impacts the kinetics and efficiency of tissue regeneration. Rather than directly undergoing differentiation, stem cells can give rise to progenitors through asymmetric cell divisions. This creates a layer of regulation that allows stem cells to self-renew, as well as imprint the identity of their progeny by asymmetrically segregating fate determinants through polarity, protein trafficking, and cell cycle-dependent mechanisms[166]. While many intrinsic mechanisms of asymmetric divisions are conserved across evolution and in different cell types, extrinsic determinants are dependent on the tissue organization and spatial localization of cell fate determinants [167,168].

Muscle stem cells, or satellite cells, are essential for the growth and regeneration of skeletal muscle [169]. The majority of satellite cells represent a short term repopulating cell[22], while a subset of the satellite cell population is capable of long-term self-renewal and can give rise to committed myogenic progenitors through asymmetric cell divisions [170–172]. We term these cells satellite stem cells. A key feature of satellite stem cells is the lack of the myogenic transcription factor *Myf5*, which can be used to distinguish stem cells from committed progenitors [171].

Stimulating satellite stem cell symmetric expansion results in enhanced and augmented muscle regeneration with a dramatic increase in satellite cell numbers [173]. Conversely, promiscuous activation of JAK2/STAT3 signalling mediates the decline of satellite cell self-renewal in ageing by biasing satellite stem cells toward asymmetric divisions [174,175]. Moreover, cell-autonomous defects leading to a loss of polarized p38MAPK signalling in aged cells further attenuates self-renewal, whereby pharmacological rejuvenation of aged stem cells can restore muscle function [176,177]. Thus, the regulation of satellite stem cell asymmetric division is a key control point that significantly impacts the efficiency of the muscle regenerative program.

We recently discovered that deficits in muscle stem cell asymmetric divisions are a part of the underlying mechanism that results in the progressive wasting of skeletal muscles found in Duchenne Muscular Dystrophy (DMD), an X-linked genetic disease caused by mutations in the Dystrophin gene [178]. Whereas dystrophin-deficiency in muscle fibres makes them susceptible to membrane damage[179,180], dystrophin-deficiency in satellite stem cells results in a loss of polarity determination and reduced asymmetric divisions, ultimately leading to the diminished production of myogenic progenitors and hindered regeneration. The compounding effect of diminished regeneration with the chronic degeneration of fragile myofibres accounts for the eventual replacement of muscle tissue by adipose and fibrotic infiltrates in mouse[14,103] and human muscle[181].

Here we report the identification of the epidermal growth factor receptor (EGFR) and aurora kinase A (Aurka) pathways as determinants of asymmetric satellite stem cell divisions through an *in-niche* muscle stem cell screen. EGF stimulation activates EGFR localized at the basal surface of muscle stem cells and recruits the mitotic spindle assembly protein Aurka to induce apicobasal asymmetric divisions. siRNA mediated knockdown of Aurka abolishes EGF induced asymmetric muscle stem cell divisions. Importantly, the EGFR polarity pathway acts independently of dystrophin and is able to rescue the reduction in the asymmetric division in dystrophin-deficient satellite cells. Treatment with exogenous EGF ligand in *mdx* mice, a mouse model of DMD, enhances the formation of new myofibres resulting in better muscle function while delaying fibrotic accumulation. Therefore, we conclude that the EGFR pathway can be exploited to restore muscle stem cell polarity and function in DMD.

## RESULTS

### In-Niche Screen for Regulators of Satellite Cell Self-Renewal

The satellite cell microenvironment is required to provide necessary niche signals for asymmetric divisions [182]. Therefore, we set out to design a scalable method to quantify satellite stem cell fate decisions without removing them from their native niche. Using *Myf5-Cre*[164] and *R26R-eYFP*[165] alleles, the Cre-mediated recombination at the *R26R-eYFP* allele and expression of yellow fluorescent protein following *Myf5* activation discriminates *Myf5*$^{Neg}$ satellite stem cells and *Myf5*$^{Pos}$ committed satellite cells. Culturing single myofibres from *Myf5-Cre/ROSA26-eYFP* mice for 42h, where 80% of satellite cells have undergone a single round of cell division, we can robustly quantify symmetric and asymmetric satellite stem cell divisions, as well as committed satellite cell divisions through the expression of eYFP (Figure 13A).

The recombination event at the *R26R-eYFP* allele results in individual genotypes for satellite stem cells and committed satellite cells. Therefore, primer combinations designed against the recombination status of the *R26R-eYFP* allele can be used to quantify the numbers of satellite stem cells and committed satellite cells by quantitative real-time PCR (Figure S7A and B). Consistent with the manual enumeration of satellite stem cell numbers by immunofluorescence, qRT-PCR quantification of the recombination state of genomic DNA isolated from myofibre cultures accurately detected a 1.5-fold increase in satellite stem cell numbers after Wnt7a stimulation (Figure S7C). Thus, this method enables us to readily analyze changes in the stem cell population. With that, we adapted this system to a 96-well culture format using myofibres isolated from *Flexor digitorum brevis* (FDB) muscles, which have a higher satellite cell to myonuclei ratio and are amenable for transfer by pipetting [183], to conduct a screen of well-characterized small molecule inhibitors.

Altogether, 640 well-characterized pharmacological compounds were screened against Wnt7a as a positive control [173]. We identified 43 candidate compounds as robust inducers of satellite stem cell expansion (Table S2). Consistent with p38MAPK being a driver of satellite cell commitment [176,177,184,185], several inhibitors of the p38MAPK pathway, including SB203580, were confirmed to increase satellite stem cell numbers in the myofibre screen (Figure 13C), thus further validating that the screening platform reliably identified small molecule compounds capable of driving the symmetric expansion of satellite stem cells.

Several of the compounds effective in stimulating satellite stem cell expansion were inhibitors of EGFR/Erbb or Aurk pathways (Figure 13C). Notably, Lapatinib, an FDA approved and clinically experienced EGFR/Erbb2 inhibitor, was identified as a lead compound for follow-up analysis. Furthermore, the top hit from the screen ZM 449829 and its prodrug ZM 39923 hydrochloride, also have known inhibitory actions on EGFR [186,187]. Of the Aurk inhibitors, ZM447439 and JNJ-7706621 are extensively studied inhibitors against both aurora kinase A (Aurka) and B (Aurkb) [188], whereas TC-A2317 is a variant of VX-680 that exhibits higher specificity for Aurka inhibition [189].

Toward identifying the specific gene targets of the EGFR/Erbb and Aurk inhibitors, we examined gene expression using microarray data [190] to correlate the expression pattern of EGFR/Erbb and Aurk family to a possible regulatory function in satellite cell self-renewal. Only *EGFR* from the EGFR/Erbb family was highly expressed in freshly-isolated satellite cells, whereas *Erbb2*, *Erbb3*, and *Erbb4* were expressed at very low levels (Figure 13D and Figure S7D). This agrees with previously published data where EGFR protein is readily detectable in satellite cells and myoblasts but is lost in differentiation [184,191]. *Aurka*, and *Aurkb* were expressed moderately in satellite cells. However, they were highly expressed in proliferating myoblasts, consistent with their function in regulating the cell cycle [192] (Figure 13D and Figure S7E). *Aurkc*, on the other hand, was only expressed late

in differentiation (Figure 13D). This information suggested that *EGFR*, *Aurka*, and *Aurkb* are likely targets of the inhibitors identified in the myofibre screen.

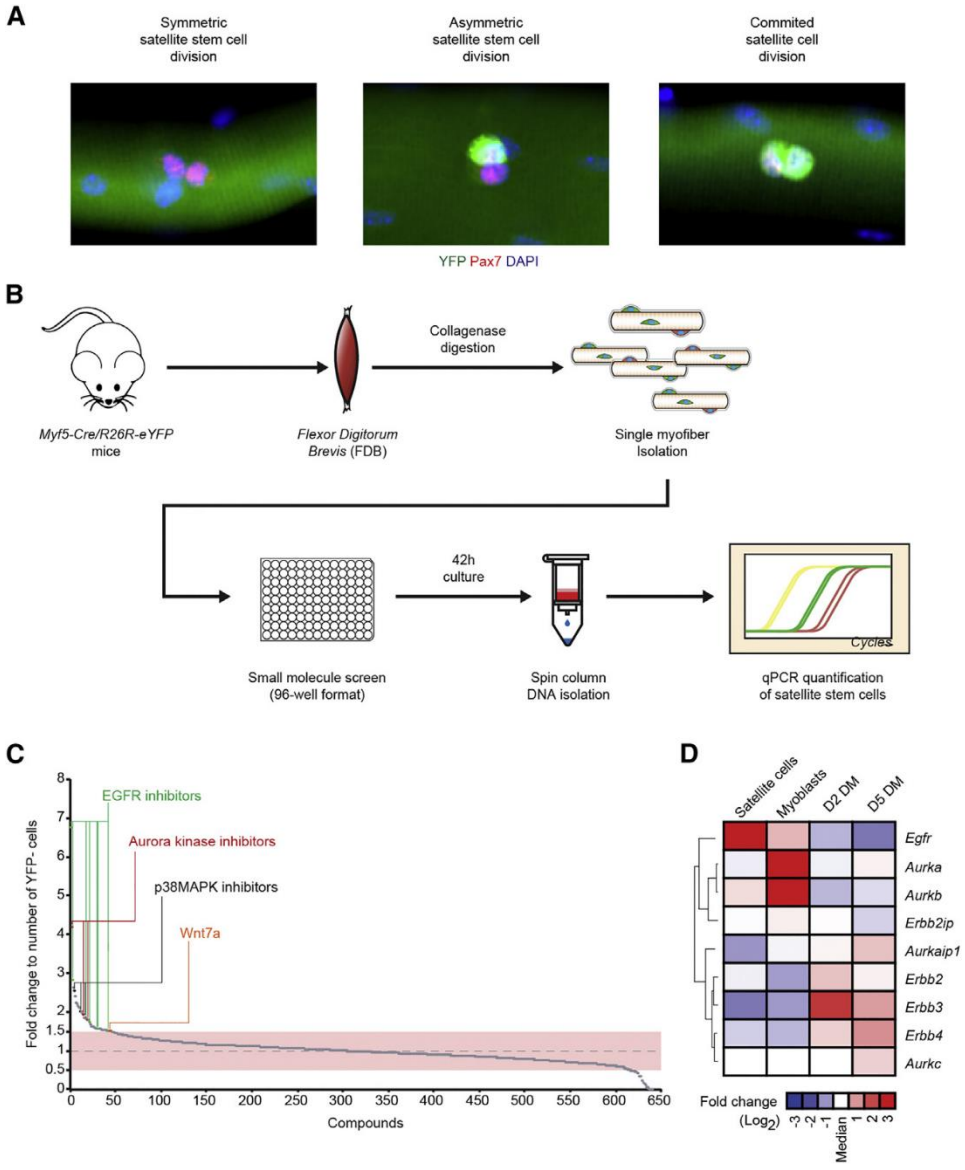


Figure 13: **Identification of Small Molecules that Drive Satellite Stem Cell Symmetric Division.** (A) Symmetric satellite stem cell division, asymmetric satellite stem cell division, and committed satellite cell division on single Myf5-Cre/R26R-eYFP myofibres after 42 h of culture stained with Pax7 (red), eYFP (green), and DAPI (blue). (B) Graphic overview of the myofibre screening protocol. (C) Relative changes to satellite stem cell numbers with small-molecule treatment sorted by changes to $eYFP^{Neg}$ satellite stem cell numbers compared with vehicle (DMSO) controls. Wnt7a was a positive control. Screening hits are listed in Table S2. (D) Microarray heatmap representing genes from the EGFR-Erbb and Aurk family from prospectively isolated satellite cells, cultured myoblasts in vitro, and 2- and 5-day-differentiated myotubes.

**Validation of Activity of Lead Compounds**

To confirm the activity of our lead compounds on satellite cell asymmetric division and to validate our findings are not specific to satellite stem cells of the FDB muscle, we cultured satellite cells in myofibres isolated from *Extensor Digitorum Longus* (EDL) muscles from *Myf5-Cre/R26R-eYFP* mice and monitored for changes to cell proliferation and changes to symmetric or asymmetric cell division. Inhibition of EGFR signalling resulted in a marked shift towards satellite stem cell symmetric divisions as evidenced by a significant 83% decrease in the number of asymmetric divisions observed (Figure 14A–B, and Figure S7A). This change in the mode of satellite stem cell division thus resulted in a 71% increase in the number of satellite stem cells (Figure 14C). Importantly, EGFR inhibition did not change the total numbers of satellite cells (Figure 14D), indicating that EGFR signalling does not impact the rate of cell proliferation.

Similarly, we tested the pharmacological inhibition of Aurka on single EDL myofibres isolated from *Myf5-Cre/R26R-eYFP* following treatment with the specific Aurka inhibitor TC-A2317. Comparable to the effect from EGFR inhibition, TC-A2317 treated samples exhibited a 74% decrease in the rate of asymmetric divisions (Figure 14E and F). This shift to symmetric divisions gave rise to 77% increased numbers of satellite stem cells (Figure 14G). Consistently, inhibition of Aurka with TC-A2317 also did not impact the rate of cell proliferation (Figure 14H). These results suggest that EGFR and Aurka signalling regulates the mode of satellite stem cell division.

To investigate whether the inhibition of EGFR or Aurka prevents myogenic differentiation generally, we treated differentiating primary myoblasts with either Lapatinib, TC-A2317 or vehicle controls. Interestingly, unlike satellite cells on cultured myofibres, inhibition of EGFR signalling with Lapatinib in differentiating primary myoblasts led to a slight, albeit statistically significant, increase in activation of the differentiation marker

Myog (Figure S8B), consistent with previous reports regarding siRNA knockdown of EGFR in mouse and human myoblasts [191,193]. Likewise, Aurka inhibition with TC-A2317 also modestly increased the percentage of cells expressing Myog (Figure S8B). These results suggest that EGFR and Aurka have different roles in satellite cell self-renewal and progenitor differentiation.

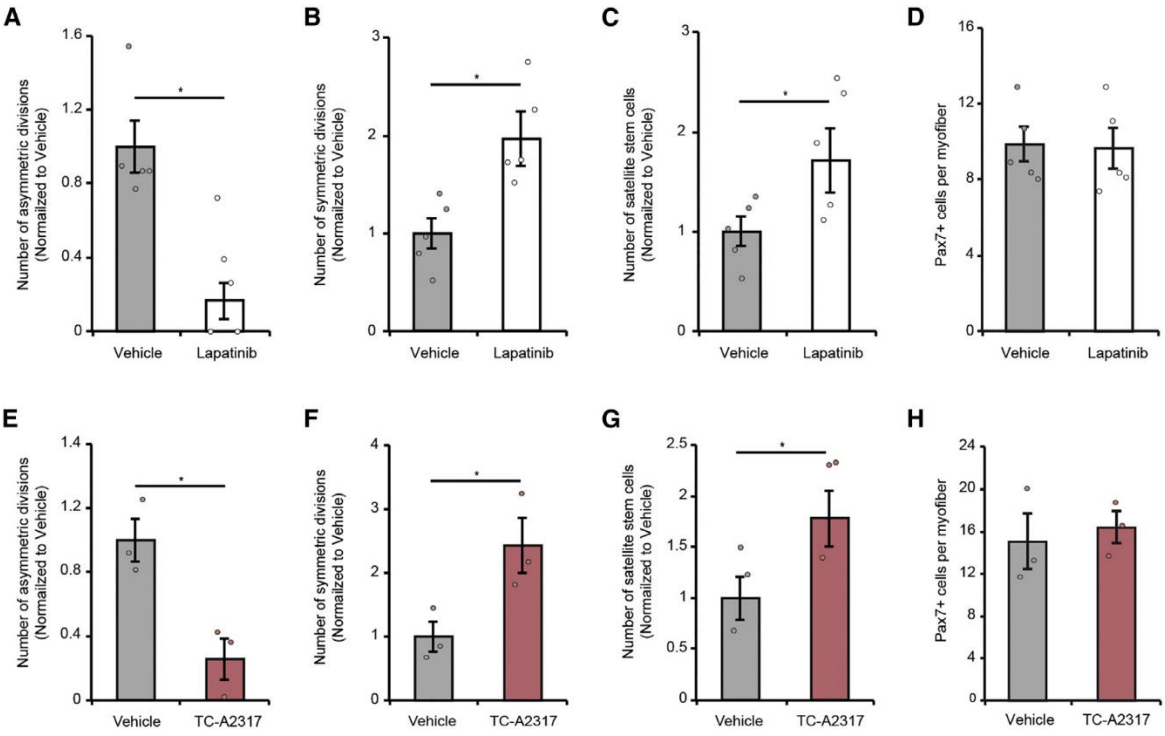


Figure 14: **Lapatinib and TC-A2317 Inhibit Asymmetric Satellite Stem Cell Divisions.** (A and B) Number of (A) asymmetric and (B) symmetric satellite stem cell divisions per myofibre at 42 h of culture in the presence of lapatinib normalized to the DMSO control (vehicle). (C and D) Number of (C) eYFPNeg and (D) total Pax7-expressing satellite stem cells per myofibre at 42 h of culture in the presence of lapatinib normalized to the DMSO control (vehicle). (E and F) Number of (E) asymmetric and (F) symmetric satellite stem cell divisions per myofibre at 42 h of culture in the presence of TC-A2317 normalized to the DMSO control (vehicle). (G and H) Number of (G) eYFPNeg and (H) total Pax7-expressing satellite stem cells per myofibre at 42 h of culture in the presence of TC-A2317 normalized to the DMSO control (vehicle). In (A)–(H), error bars represent means ± SEM; $*p < 0.05$, $**p < 0.01$, $***p < 0.005$. In (A)–(D), n = 5 mice; in (E)–(H), n = 3 mice

**EGFR is polarized in satellite cells and promotes asymmetric division in satellite stem cells**

To gain insight into the function of EGFR in regulating satellite stem cell asymmetric division, we carefully examined EGFR localization and activation at various time points *in vitro* and *in vivo*. Immunofluorescence on frozen muscle sections revealed that EGFR protein is polarized and is localized at the basal surface of quiescent satellite cells (Figure 15A). To examine the signalling status of EGFR, we performed immunostaining of satellite cells on myofibres cultured in serum-free medium with and without EGF stimulation. In quiescent satellite cells, we found that EGFR is inactive by immunostaining for activated EGFR phosphorylated on Tyr 1068 (p-EGFR) (Figure 15B). Following stimulation with recombinant EGF protein for 1h, activated p-EGFR was detected in the majority of satellite cells (Figure 15B and C).

In sublaminar satellite cells, p-EGFR was polarized in 63% of satellite cells (Figure 15C) localized to the basal surface on the opposite cortex to the myofibre (Figure S9B). Surprisingly, p-EGFR was restricted to a streak-like domain, which is even more constrained than the total EGFR observed in quiescent satellite cells (Figure 15B). Furthermore, by tracking satellite cells through their re-entry into the cell cycle, polarized p-EGFR signalling is maintained even as the cells enter M-phase (Figure 15D). P-EGFR is also basal-laterally localized in satellite cells on myofibres isolated then immediately fixed following injury-induced activation *in vivo* (Figure 15E). In whole muscle samples following injury, p-EGFR and Aurka closely followed the expression pattern of Pax7 peaking between 3-7 days of regeneration (Figure 15F). This early activation of EGFR and Aurka correlates with the expansion of the proliferating satellite cell population [178] and the expression of Myog in differentiating myogenic progenitors (Figure 15F). Together, these data suggest the hypothesis that basally localized EGFR primes satellite stem cells for asymmetric divisions.

To investigate whether activation of EGFR signalling acts as a driver of asymmetric division, recombinant EGF protein was supplemented to the culture media of single EDL myofibres isolated from *Myf5-Cre/R26R-eYFP* mice. Strikingly, we observed that EGF treatment led to a 2.5-fold increase in the rate of asymmetric satellite stem cell division (Figure 15G).

Recent studies of polarized epithelial MDCK cells have identified a role for EGFR signalling in orienting the mitotic axis along the apicobasal axis [194]. Moreover, asymmetric satellite cell divisions occur in an apicobasal orientation [171,178]. Therefore, single EDL myofibres were cultured for 36h and satellite cell centrosomes were detected by immunostaining for phosphorylated aurora kinase (p-Aurk). Importantly, EGF treatment resulted in a 50% increase in the proportion of total mitotic satellite cells aligned along the apicobasal axis (Figure 15H). In these experiments, we did not observe any changes to the rate of proliferation of satellite cells, with around 5% of cells undergoing mitosis, marked by p-Aurk staining, at 36h irrespective of EGF treatment (Figure S9C–D). Moreover, there was no change in the rate of S-phase entry in either $eYFP^{Pos}$ or $eYFP^{Neg}$ satellite cell populations following EGF treatment as determined by EdU incorporation over the first 20h of culture (Figure 15I).

To further confirm the specific effects of EGFR signalling, siRNA against *EGFR* (si*EGFR*) was transfected into satellite cells on single EDL myofibres isolated from *Myf5-Cre/R26R-eYFP* mice. Similar to pharmacological inhibition with Lapatinib, si*EGFR* reduced the rate of asymmetric division by 65% compared to transfection with a scrambled siRNA (siSCR) (Figure 15J). Transfection with si*EGFR* also increased the rate of symmetric divisions and led to a 76% increase in satellite stem cell numbers (Figure 15K and L). This data strongly suggests that EGF stimulation of satellite cells stimulates a change in mitotic orientation by the recruitment of centrosomes along the polarized p-EGFR signal.

To test the possibility that EGF is acting independent of cell polarity and leading to the activation of *Myf5* expression or enforcing myogenic commitment in satellite stem cells, we further studied the effect of EGF treatment on satellite cell-derived primary myoblasts in culture. Quantitative real-time PCR showed no change in *Myf5* (*eYFP*) activation in cultured myoblasts derived from $eYFP^{Pos}$ or $eYFP^{Neg}$ satellite cells isolated from *Myf5-Cre/R26R-eYFP* mice (Figure S9H-I). Importantly, EGF was unable to promote eYFP protein expression in myoblasts derived from $eYFP^{Neg}$ satellite cells (Figure S9J). These data strongly support our hypothesis that EGFR is activated in a polarized manner in satellite cells and promotes apicobasal oriented division in satellite cells within the myofibre niche.

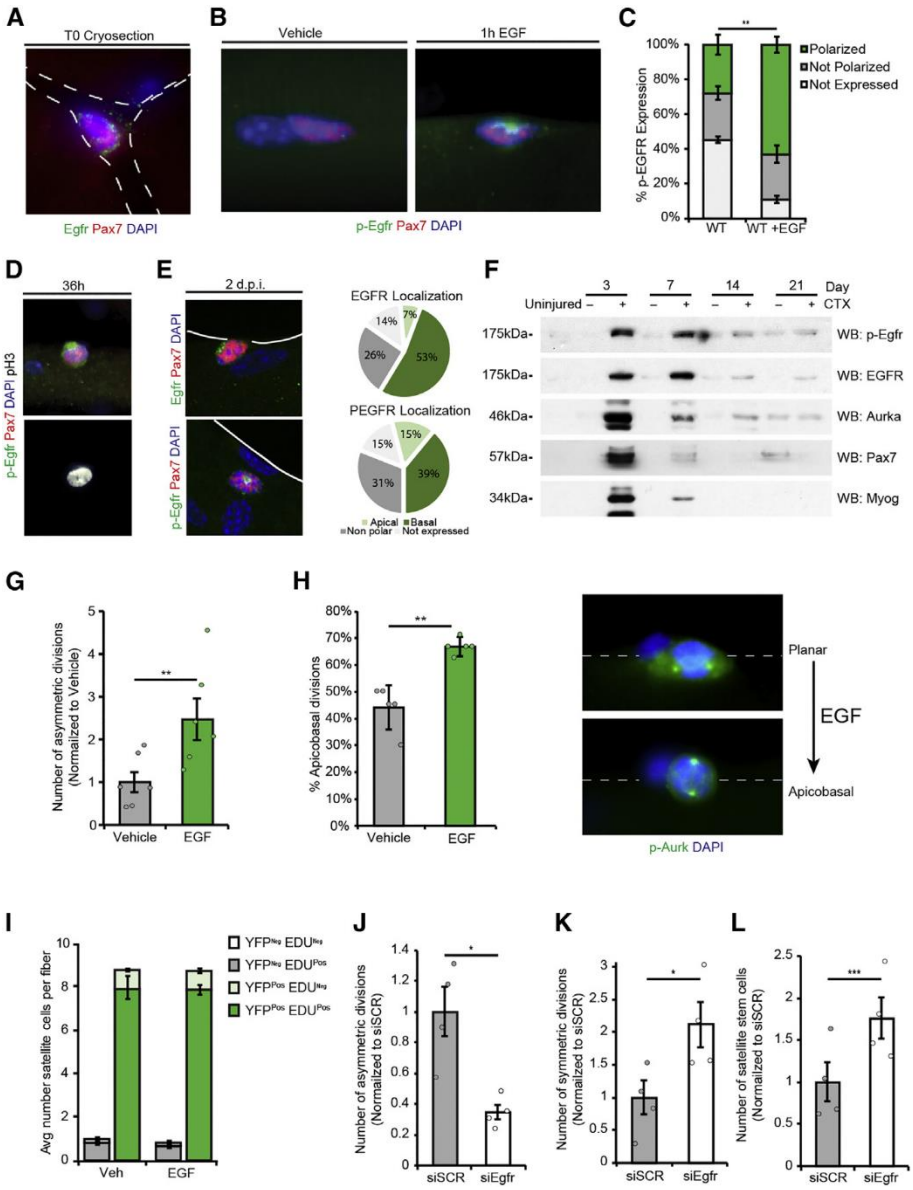


Figure 15: **Polarized Localization and Activation of EGFR in Satellite Cells.** (A) Localization of EGFR (green) in Pax7-expressing (red) satellite cells on an immunostained muscle section. The basal surface of the satellite cell is attached to a basal lamina that surrounds both the cell and its host fibre. Dashed lines are based on autofluorescence of the myofibre sarcolemma. (B) Signalling status of p-EGFR (green) in Pax7-expressing (red) and DAPI-positive (blue) cells on EDL myofibres at 1 h of culture in vehicle or EGF-containing medium. (C) Quantification of p-EGFR staining in satellite cells on EDL myofibres at 1 h of culture in vehicle or EGF-containing medium. (D) Polarized p-EGFR (green) staining in mitotic p-H3-expressing (white) and Pax7-expressing (red) satellite cells on EDL myofibres at 36 h. DAPI is shown in blue. (E) Analysis of EGFR and p-EGFR localization from injured EDL muscle fixed 2 days after injury and manually dissociated and then stained with DAPI (blue), EGFR or p-EGFR (green), and Pax7 (red). (F) Immunoblot analysis of p-EGFR, EGFR, Aurka, Pax7, and Myog expression in uninjured TA muscles or 3, 7, 14, and 21 days after saline or cardiotoxin (CTX) injection. (G) Number

of asymmetric satellite stem cell divisions per myofibre at 42 h of culture in EGF-containing medium normalized to vehicle. (H) Number of apicobasal oriented mitotic satellite cell divisions at 36 h of culture in EGF-containing medium normalized to vehicle stained with p-Aurk (green). The host myofibre is outlined with a dashed line. DAPI is shown in blue. (I) Quantification of EdU-labeled satellite cells on myofibres from Myf5-Cre/R26R-eYFP mice cultured in vehicle or EGF-containing medium supplemented with EdU for 20 h and with a 20-h chase prior to fixation. (J–L) Number of (J) asymmetric satellite stem cell divisions, (K) symmetric satellite stem cell divisions, and (L) eYFPNeg satellite stem cells per myofibre at 42 h of culture after transfection with siRNA against EGFR (siEGFR) normalized to scrambled siRNA (siSCR). In (H), (G), and (J)–(L), error bars represent means ± SD; $*p < 0.05$, $**p < 0.01$, $***p < 0.005$. In (C), n = 3 mice; in (E), n = 43 and n = 46 cells, respectively; in (F), n = 2 mice per time point; in (G), n = 6 mice; in (H), n = 5 mice; in (I), n = 3 mice; in (J)–(L), n = 4 mice.

**EGFR promotes asymmetric division in satellite stem cells *in vivo***

To further explore whether EGFR signalling affects *Myf5*$^{Neg}$ satellite stem cells, *Myf5*$^{Pos}$ committed satellite cells or myoblasts *in vivo*, we crossed the *Myf5-Cre* allele with a *ROSA26R-nTnG* allele [195], which consists of a CMV/β-actin promoter, a loxP flanked nuclear TdTomato (nTdTomato) and nuclear GFP (nGFP) cassette within the ROSA.26(Sor) locus, to generate a *Myf5-Cre nTnG* transgenic reporter mouse model where all *Myf5*$^{Neg}$ cells express nTdTomato and *Myf5*$^{Pos}$ cells express nGFP. Prospective isolation of nTdTomato$^{Pos}$ satellite cells (*Myf5*$^{Neg}$) and nGFP$^{Pos}$ satellite cells (*Myf5*$^{Pos}$) allows us to determine the outcome of asymmetric division following transplantation where nuclear TdTomato satellite cells undergoing asymmetric division give rise to one nGFP$^{Pos}$ myogenic progenitor and one nTdTomato$^{Pos}$ satellite stem cell (Figure S10A–E).

We observed that the nTdTomato$^{Pos}$ satellite cells gave rise to a roughly a three-fold higher engraftment as Pax7-expressing satellite cells compared to nGFP$^{Pos}$ satellite cells (Figure 16B-C), consistent with our previous reports [171]. By contrast, nGFP$^{Pos}$ satellite cell-derived myoblasts from the same donors, cultured for 4 passages, lost all self-renewal capacity and failed to engraft as Pax7-expressing satellite cells, despite injecting a 10-fold higher number of cells (Figure 16D). Strikingly, treatment of nTdTomato$^{Pos}$ satellite cells with EGF for 3 hours following isolation was sufficient to significantly increase the nGFP$^{Pos}$

progeny of donor cells and facilitate their engraftment as nGFP$^{Pos}$ satellite cells (Figure 16B). This effectively enhanced donor cell engraftment as myonuclei by roughly 3-fold while maintaining their capacity to self-renewal. Furthermore, consistent with our findings using *ex vivo* myofibre cultures and primary myoblast cultures, EGF had no effect on transplanted nGFP$^{Pos}$ satellite cells or nGFP$^{Pos}$ myoblasts (Figure 16C-D). This evidence further supports the notion that the role of EGF is specific to the *Myf5*$^{Neg}$ satellite stem cell where it promotes the generation of *Myf5*$^{Pos}$ progenitors that further amplify and differentiate into muscle fibres.

To better understand the effect of EGFR signalling in satellite cells versus other cell types that express EGFR in muscle, we developed a satellite cell-specific *EGFR* conditional knockout (*EGFR cKO*) mouse model by crossing the *Pax7-CreERT2* allele with floxed alleles of EGFR [196]. Excision of *EGFR* in satellite cells by tamoxifen treatment in *EGFR cKO* mice did not change the number of Pax7-expressing satellite cells in resting mice, but when also challenged with injury by intramuscular injection cardiotoxin (CTX) into the *Tibialis Anterior* (TA) muscle, we observed a decreased number of Pax7-expressing cells by day 10 compared to tamoxifen-treated *Pax7-CreERT2* littermates (Figure 16F). Correspondingly, treatment with recombinant EGF protein at early time points after injury (days 0 and 2) led to an increase in the number of Pax7-expressing cells and Myog-expressing cells in regenerating TA muscles of *Pax7-CreERT2* mice at day 10 post-injury (Figure 16G–H). *EGFR cKO* satellite cells did not respond to exogenous stimulation by recombinant EGF protein, treated muscles contained fewer Pax7-expressing cell and Myog-expressing cells compared to regenerating muscles of *Pax7-CreERT2* littermates that were treated with EGF (Figure 16G–H). These experiments suggest that EGFR signalling in satellite cells is crucial during regeneration and supplementation with recombinant EGF proteins can enhance the pool of myogenic progenitors during muscle regeneration.

To further assess the effect of EGF-treatment on other cell types in skeletal muscle, we performed immunofluorescence staining for α-smooth muscle actin (αSMA) and VEGFR2 in EGF treated regenerating TA muscles to quantify potential changes in the muscle vasculature. Neither αSMA nor VEGFR2 showed any change with EGF treatment or when comparing *EGFR cKO* mice and their *Pax7-CreERT2* littermates (Figure S10F-G). These findings further support that difference in Pax7-expressing cells and Myog-expressing cells observed with EGF treatment is not due to EGF promoting vascularization within the muscle.

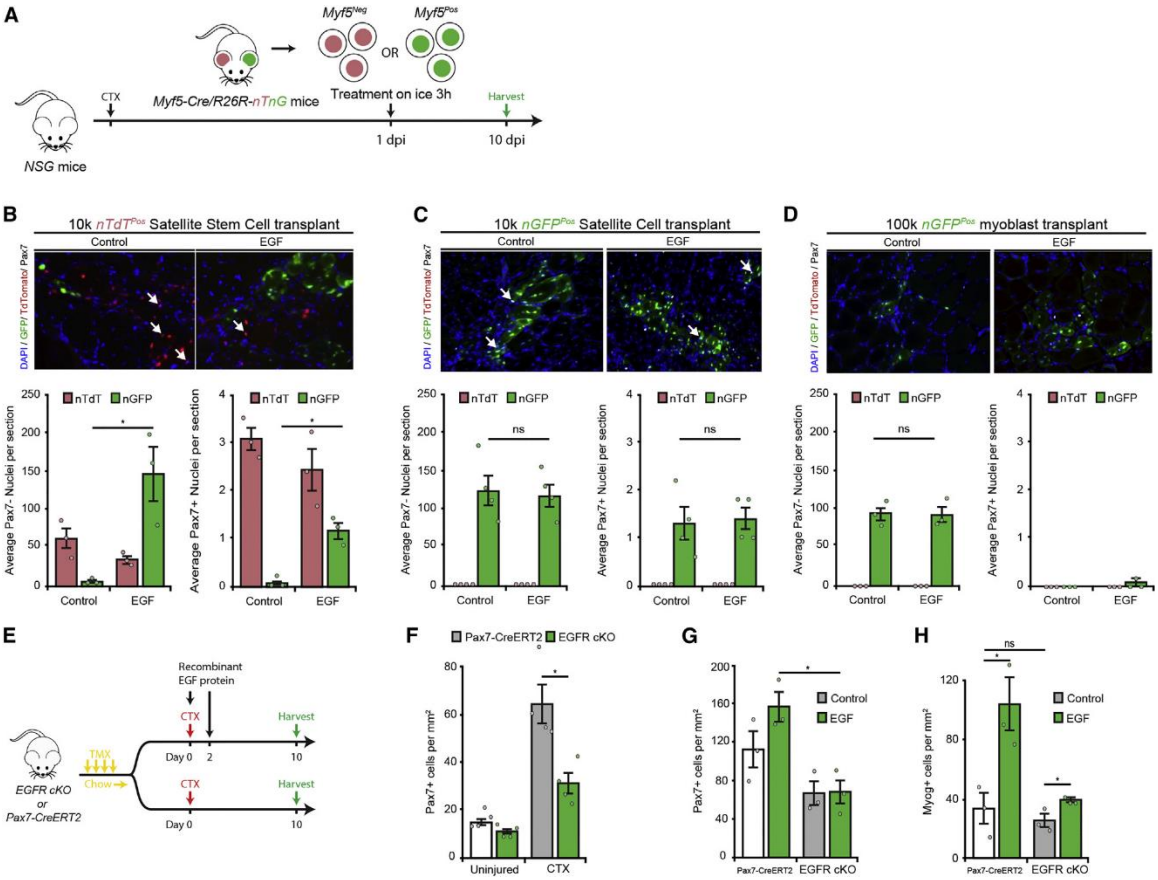


Figure 16: **EGF Promotes Asymmetric Division in Satellite Stem Cells.** (A) Graphic overview of Myf5-Cre/R26R-nTnG satellite cell transplantation into injured NSG mice. (B–D) Representative images of (B) 10,000 nTdT POS transplanted satellite stem cells, (C) 10,000 transplanted nGFP POS satellite cells, or (D) 100,000 transplanted nGFP POS myoblasts stained with DAPI (blue), GFP (green), TdTomato (red), and Pax7 (gray). Arrows indicate donor-derived Pax7+ satellite cells. (E) Graphic overview of CTX-induced injury and treatment with recombinant EGF in EGFR cKO mice. (F) Quantification of Pax7-expressing cells on sections from non-injured and regenerating EGFR cKO or Pax7-

CreERT2 TA muscles 10 days after injury. (G and H) Quantification of (G) Pax7-expressing and (H) Myog-expressing cells on sections from regenerating EGFR cKO or Pax7-CreERT2 TA muscles 10 days after CTX-induced injury treated with control (saline) or EGF protein. In (B)–(D) and (F)–(H), error bars represent means ± SEM; $*p < 0.05$. In (B) and (D), n = 3 donors; in (C), n = 4 donors; in (F), n = 4 mice; in (G) and (H), n = 3 mice.

**Aurka Acts Downstream of EGFR to Orient Asymmetric Divisions**

Our observation that EGF treatment regulates the mitotic orientation of satellite cells suggests that EGFR signalling induces the recruitment of centrosome regulators along the apicobasal axis. We, therefore, hypothesized that aurora kinases, identified as a regulator of asymmetric stem cell divisions in our screen, is an effector of EGFR signalling.

Aurora kinases are a family of kinases that regulate mitosis [192,197]. Aurka and/or Aurkb have been suggested to act with upstream regulators in the determination of mitotic orientation during symmetric and asymmetric cell divisions [198–200]. Consistent with its involvement in organizing mitotic centrosomes, Aurka protein is localized at centrosomes in M-phase myoblasts (Figure 17A). Challenging the idea that Aurka is essential for mitosis, the presence of Aurka at the centrosomes of cycling myoblasts is heterogeneous (Figure 17A).

In support of our hypothesis, Aurka was identified as an EGF-dependent interactor of EGFR in lung cancer cells [201]. Therefore, reciprocal co-immunoprecipitation (co-IP) and proximity ligation assays (PLA) were performed in proliferating primary myoblasts. We observed EGF-dependent binding between endogenous p-EGFR and Aurka by reciprocal co-IP western blot analyses (Figure 17B). In addition, using PLA we detected a strong interaction between p-EGFR and Aurka in cultured myoblasts that was significantly increased by EGF stimulation (Figure 17C and Figure S11A).

Similar to pharmacological inhibition of Aurka, knockdown of *Aurka* by siRNA transfection (si*Aurka*) led to a 59% decrease in asymmetric divisions and a 36% increase in satellite stem cell numbers (Figure 17D–F and Figure S11B). Notably, si*Aurka* did not

decrease the rate of cell cycle as determined by ki67 staining (data not shown) or the number of total satellite cells (Figure S11C). Importantly, EGF stimulation of satellite cell asymmetric division was abolished when *Aurka* expression was knocked down following transfection with si*Aurka* (Figure 17G, Figure S11D–E). Therefore, we conclude that Aurka is a key effector of EGFR regulation of asymmetric division.

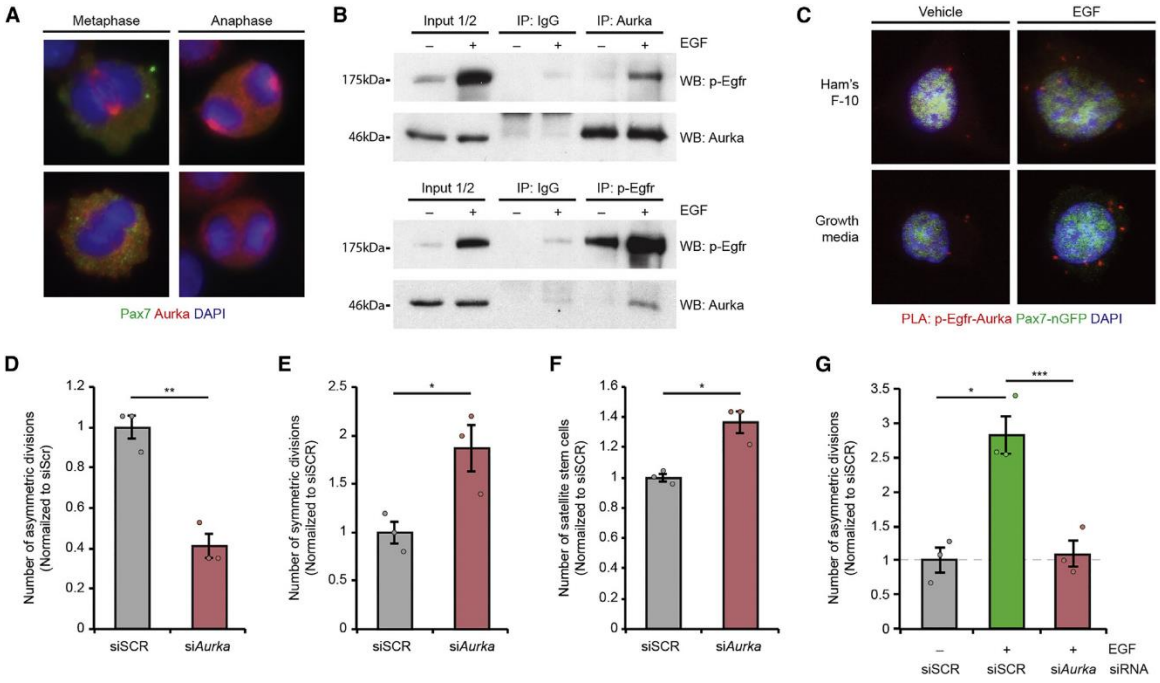


Figure 17: **EGFR Signals through Aurka to Stimulate Asymmetric Divisions.** (A) Immunofluorescence localization of Aurka (red) at centrosomes in mitotic metaphase (left) and anaphase (right) myoblasts. Pax7 is shown in green; DAPI is shown in blue. (B) Immunoblotting of reciprocal co-immunoprecipitation of Aurka and p-EGFR in serum-starved myoblasts refed for 1 h in vehicle or EGF-containing growth medium. (C) Proximity ligation assay for interactions between Aurka and p-EGFR (red) in serum-starved Pax7-nGFP (green) myoblasts refed for 1 h in vehicle or EGF-containing growth medium. DAPI is shown in blue. (D and E) The number of (D) asymmetric and (E) symmetric satellite stem cell divisions per myofibre at 42 h of culture after transfection of siRNA against Aurka (siAurka) normalized to siSCR. (F) Number of eYFPNeg satellite stem cells per myofibre at 42 h of culture after transfection with siAurka normalized to siSCR. (G) Number of asymmetric satellite stem cell divisions per myofibre at 42 h of culture in EGF-containing medium after transfection with siSCR or siAurka normalized to control medium after transfection with siSCR. In (D)–(F) and (G), error bars represent means ± SEM; $*p < 0.05$, $**p < 0.01$, $***p < 0.005$. In (D)–(F), n = 3 mice; in (G), n = 3 mice.

**EGF Treatment Rescues the Polarity Deficits in Dystrophin-Deficient Satellite Cells**

Loss of dystrophin in Duchenne muscular dystrophy (DMD) causes a polarity deficit in satellite cells in *mdx* mice [178]. Satellite stem cells lacking dystrophin exhibit a dramatic reduction in the number of asymmetric divisions resulting in the diminished generation of Myog-expressing myogenic progenitors and delayed regeneration.

To establish whether EGFR localization and activation are affected by the loss of dystrophin, single EDL myofibres from *mdx* mice were immunostained for p-EGFR after 1h with or without recombinant EGF stimulation. P-EGFR was significantly stimulated in *mdx* fibres treated with EGF (Figure 18A-B). Moreover, comparable to WT cells, p-EGFR was similarly localized in streak-like domains on the basal surface of *mdx* cells (Figure 17A). These findings suggest that EGFR localization and activation can occur normally in *mdx* satellite cells.

Similar to WT satellite cells, EGF treatment of *mdx* satellite cells resulted in increased numbers of apicobasal orientated mitotic centrosomes (Figure 18C) and polarized Pard3 (Figure 18D). However, the rate of abnormal cell divisions in *mdx* satellite cells as evidenced by abnormal patterns of p-Aurk staining was unaffected by EGF stimulation. This observation implies that cell cycle dysregulation is not completely rescued by polarity signalling alone, however, EGF signalling through the EGFR/Aurka/Pard3 axis enforces a polarity and facilitates productive asymmetric divisions in dystrophin-deficient satellite cells.

To assess whether EGFR signalling would stimulate the asymmetric division of dystrophin-deficient satellite stem cells, EDL myofibres were isolated from WT and *mdx Myf5-Cre/R26R-eYFP* mice and cultured for 42h with or without recombinant EGF stimulation. The rate of *mdx* satellite stem cells that undergo asymmetric divisions is significantly reduced relative to WT satellite cells (Figure 18E). Despite an expanded stem cell pool in *mdx* muscles, the absolute numbers of asymmetric *mdx* satellite stem cell

divisions are less than half of WT counterparts (Figure 18F and Figure S12B–C). EGF treatment of WT satellite cells resulted in a 29% increase in asymmetric division (Figure 18E and F). Strikingly, EGF stimulation of mdx satellite cells resulted in a 67% increase in the rate of asymmetric division (Figure 18E). Although stimulation with EGF does not completely restore the fate choice between the symmetric and asymmetric division of *mdx* satellite stem cells, we observe that with EGF treatment the absolute number of asymmetric stem cell divisions becomes similar to the numbers in untreated WT samples (Figure 18E–F).

The increased proportion of asymmetric divisions suggests that EGF stimulation has the potential to restore the rate of progenitor production by dystrophin-deficient satellite cells and ameliorate the reduced generation observed in *mdx* muscle (Dumont et al., 2015b). Therefore, to assess whether EGF-driven asymmetric divisions could rescue the reduced generation of myogenic progenitors in *mdx* cultures, single EDL myofibres from *mdx* mice were cultured for 72h and immunostained for the expression of Myog. Notably, EGF stimulation of *mdx* satellite cells led to a significant increase in the number of Myog-expressing cells as well as the total number of myogenic cells (Figure 18G and H).

To assess the effect of EGF treatment on dystrophin-deficient satellite cells *in vivo*, 10ng of recombinant EGF protein was intramuscularly (IM) injected at the time of CTX-induced injury and 2d after the injury (Figure 18G). Previously, we observed that dystrophin- or Dag1-deficient muscles generate reduced numbers of Pax7-expressing and Myog-expressing cells following CTX-injury [178]. By acutely injuring and assessing the recovery of *mdx* muscle, we can measure the functional output of the muscle stem cell population. Notably, EGF-injected *mdx* muscles contained 26% more Pax7-expressing satellite cells and 50% more Myog-expressing differentiating myogenic cells (Figure 18J and K). Moreover, regenerating myofibres in EGF-treated muscles exhibited an increase

in Feret's diameter compared to vehicle-injected controls (Figure S12H). These results suggest that intramuscular supplementation with recombinant EGF restores the productive generation of myogenic progenitors and thus enhances regeneration of *mdx* muscle.

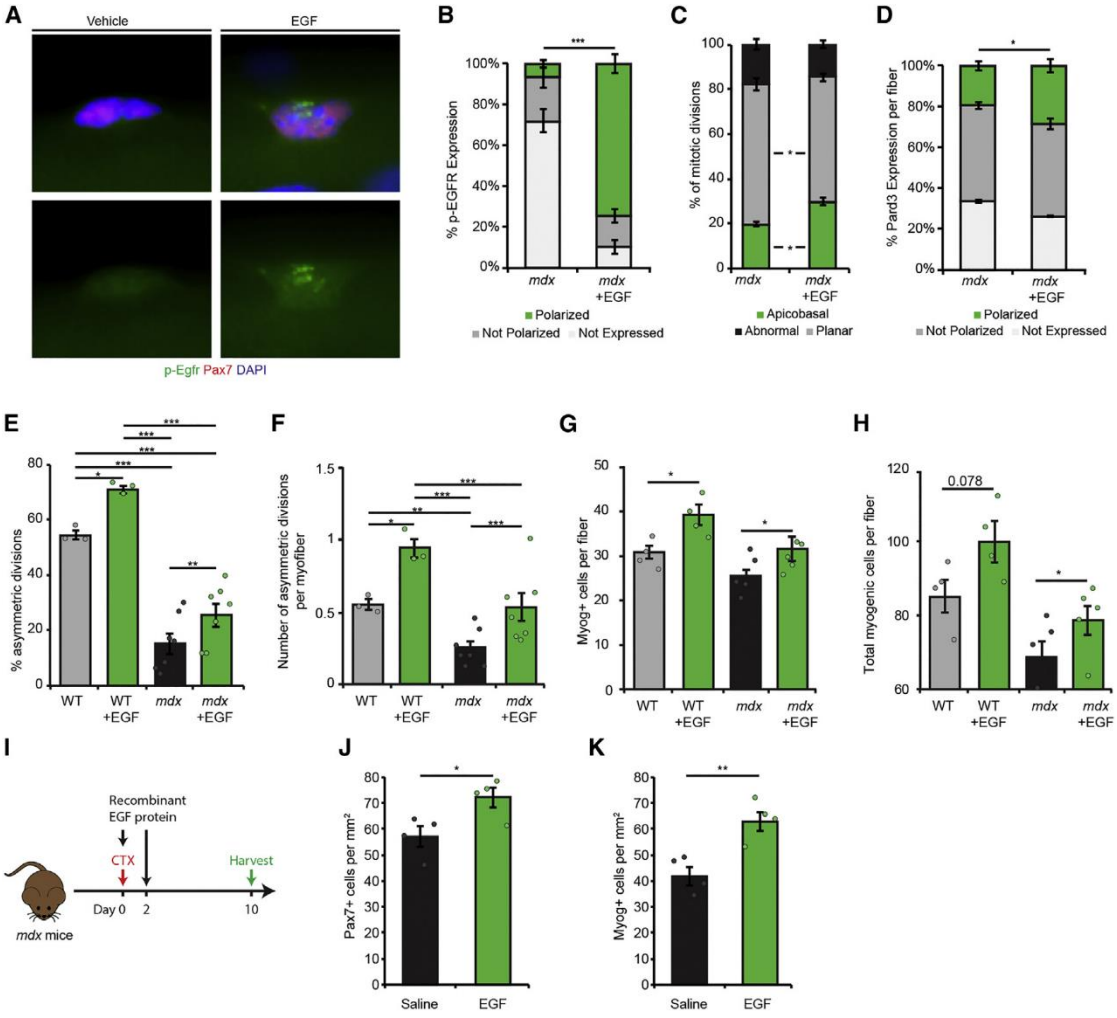


Figure 18: **EGF Stimulation Rescues Polarity Deficits in mdx Satellite Cells.** (A) Signalling status of p-EGFR (green) in Pax7-expressing (red) and DAPI-positive (blue) cells on mdx EDL myofibres at 1 h of culture in vehicle or EGF-containing medium. (B) Quantification of p-EGFR staining in mdx satellite cells on EDL myofibres fixed at 1 h of culture in vehicle or EGF-containing medium. (C and D) Quantification of (C) abnormal, planar, and apicobasal orientated mitotic spindles and (D) Pard3 localization in satellite cells on mdx myofibres at 36 h of culture in vehicle or EGF-containing medium. (E) Quantification of asymmetric divisions relative to total satellite stem cell divisions in WT and mdx myofibres at 42 h of culture in vehicle or EGF-containing medium. (F) The number of asymmetric divisions per myofibre in WT and mdx myofibres at 42 h of culture

in vehicle or EGF-containing medium. (G and H) Quantification of (G) Myog-expressing cells per mdx myofibre and (H) total myogenic cells (Pax7- or Myog-expressing cells) per mdx myofibre at 72 h of culture in vehicle or EGF-containing medium. (I) Graphic overview of CTX-induced injury and treatment with recombinant EGF in mdx mice. (J and K) Quantification of (J) Pax7-expressing and (K) Myog-expressing cells on sections from mdx TA muscles 10 days after injury treated with saline (vehicle) or recombinant EGF. In (B)–(E) and (H)–(J), error bars represent means ± SEM; $*p < 0.05$, $**p < 0.01$, $***p < 0.005$. In (B), n = 3 mice; in (C), (E), and (F), n = 3 WT mice and 7 mdx mice; in (D), n = 3 mice; in (G)–(H), n = 34 WT and 5 mdx mice; in (J) and (K), n = 4 mice for each group.

**EGF Treatment Enhances *mdx* Muscle Function**

While acute damage is a readout of the capacity of muscle stem cells to facilitate regeneration, DMD is a progressive disease that requires the long-term maintenance of muscle tissue against the pressures of chronic myofibre damage. Therefore, to address the effect of long-term EGF treatment, we electroporated an expression plasmid containing the human *EGF* cDNA [202] into *mdx* TA muscles (Figure 19A). The secretion of EGF was validated *in vitro* through transient transfection in HEK 293T cells (Figure S13A).

TA muscles were electroporated at 4 weeks of age, during the onset of muscle degeneration, and collected 30 and 150 days post-intervention (d.p.i.). Strikingly, *mdx* muscles electroporated with the EGF expression vector exhibited an 18% increase in mass by 30 d.p.i. (Figure 19B). This increase in muscle mass is reflected in the overall cross-sectional area of the EGF-electroporated TA muscles compared to the empty vector controls (Figure 19C).

Similar to effects we observed with short-term EGF treatment, electroporation with the EGF vector boosted the number of Myog-expressing myogenic progenitors at 30 d.p.i. and maintained their numbers even 150 d.p.i. whereas fewer Myog-expressing cells were found in the empty vector controls (Figure 19D). We observed a roughly 30% increase in the number of myofibres in the muscles electroporated with the EGF vector consistently at 30 and 150 d.p.i. (Figure 19E–J). EGF electroporated muscles exhibited no change in fibre Feret (Figure 19F-J), which suggests that they are not arising from the survival of

hypertrophic fibres. Consistent with a reduced dystrophic pathology, EGF electroporation reduced the progressive increase in fibrosis and deposition of extracellular matrix proteins as measured by wheat germ agglutinin (WGA) staining (Figure S13C-D).

To determine whether the increase in myofibre number was due to increased myofibre branching, single EDL myofibres from electroporated and non-electroporated muscles at 150dpi were isolated. We observed no significant change in the proportion of non-branched fibres between non-electroporated or electroporated muscles (Figure S13F). However, EGF electroporated muscles exhibited a significant increase in single branched fibres but decreased numbers of double and triple branched fibres over control electroporated muscles (Figure 19F). Together these data support the notion that EGF electroporated *mdx* muscle exhibit delayed progression of the dystrophic phenotype.

To measure the impact of these histological changes at the level of muscle function, we performed *in situ* measurements of TA muscle force generation. Strikingly, TA muscles electroporated with the EGF expression vector generated 32% greater force at tetanus compared to those electroporated with the empty vector at 30 d.p.i. (Figure 19K). Moreover, after normalizing to the physiological cross-sectional area of the muscle, we found that muscles electroporated with the EGF vector exhibited a 25% higher specific force at 30 d.p.i., which remained at 17% higher compared to the empty vector muscles at 150 d.p.i. (Figure 19L and Figure S13K). Normalizing to maximum force, there was no change to the force-frequency response of either group of electroporated muscles at any time point, suggesting that EGF treatment does alter fibre type composition (Figure S13L).

Together, these results indicate that EGF treatment provides long-term enhancement of muscle strength in *mdx* mice by slowing the progression of the dystrophic phenotype. Thus, EGF-stimulation of muscle stem cell asymmetric division results in an increased generation of progenitors, improved regeneration potential, and amelioration of disease progression in a mouse model of DMD.

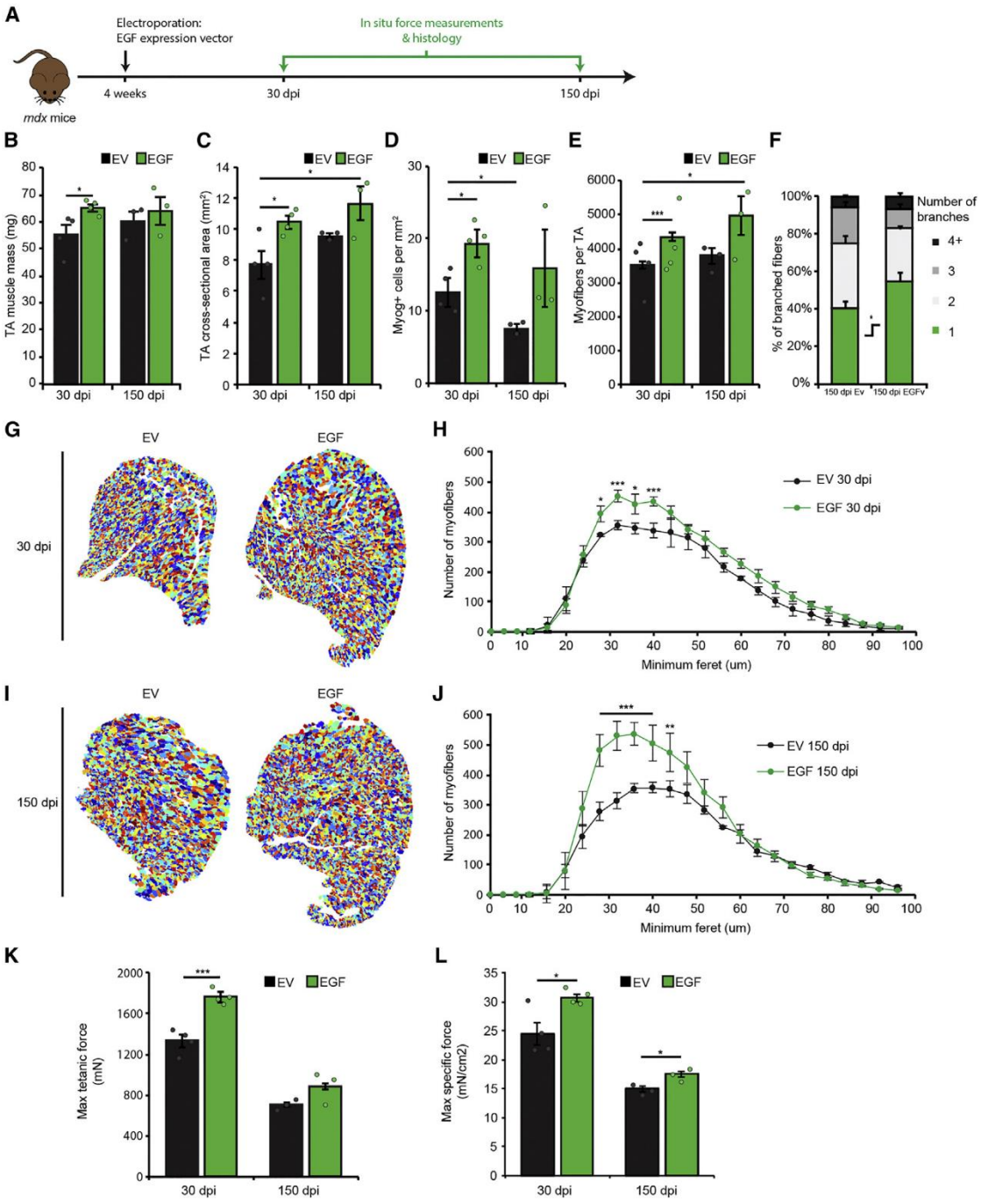


Figure 19: **EGF Enhances Regeneration of Dystrophin-Deficient Skeletal Muscle.** (A) Graphic overview of electroporation of the EGF vector in mdx mice. (B–E) Muscle mass (B), cross-sectional area (C), quantification of Myog-expressing cells (D), and quantification of myofibres (E) from TA muscles of mdx mice 30 or 150 days after electroporation with empty vector (Ev) or EGF expression vector (EGFv). (F) The proportion of branched myofibres isolated from electroporated EDLs of mdx mice 150 days after electroporation with Ev or EGFv. (G and H) Representative mask generated from SMASH (semi-automatic muscle analysis using segmentation of histology) analysis of cross-sections of TA muscles (G) and size distribution of myofibres from TA muscles (H) of mdx mice 30 days after electroporation with Ev or EGFv. (I and J) Representative mask

generated from SMASH analysis of cross-sections of TA muscles (I) and size distribution of myofibres from TA muscles (J) of mdx mice 150 days after electroporation with Ev or EGFv. (K and L) Maximum tetanic force (K) and specific maximum force (L) of TA muscles of mdx mice 30 or 150 days after electroporation with Ev or EGFv. dpi, days post-intervention. In (B)–(K), error bars represent means ± SEM; $*p < 0.05$, $**p < 0.01$, $***p < 0.005$. n = 4 mice for each group at 30 dpi and 3 mice for each group at 150 dpi.

## DISCUSSION

Extrinsic regulation of tissue-specific stem cell fate is critical for balancing regeneration and stem cell maintenance. Effectors acting at the level of long term-engrafting stem cells are amplified through the proliferation of committed progenitors. Here we identified EGFR-Aurka signalling as a polarity regulator in long term-engrafting *Myf5*$^{Neg}$ satellite stem cells through an in-niche small molecule screen (Figure 13C).

EGFR down-regulation occurs during mouse and human myoblast differentiation [191,193], but its role in satellite cells has not been well characterized. Our findings strongly support the notion that EGFR signalling specifically and positively affects the capacity of the *Myf5*$^{Neg}$ satellite stem cells to undergo asymmetric cell divisions and generate committed *Myf5*$^{Pos}$ progeny. Stimulation with recombinant EGF protein increases asymmetric satellite stem cell divisions by 2.5-fold *in vitro* (Figures 15G–H), which translated to a 3-fold increase in the number of progeny that engraft as muscle fibres *in vivo* (Figure 16B–D). Pharmacological inhibition or siRNA knockdown of EGFR reduces asymmetric divisions (Figure 14A–C and Figure 15J–L). Importantly, EGF stimulation or inhibition of EGFR did not impact cell cycle re-entry (Figure 14F), rate of mitosis (Figure S9C-D), or total cell numbers *in vitro* (Figure S9G), which further enforces the assertion that EGFR is a determinant of stem cell fate and is not acting as a mitogen. Moreover, EGF treatment of cultured primary myoblasts-derived from *Myf5*$^{Neg}$ satellite stem cells does not turn on *Myf5* (Figure S9H–I), which further suggests that this effect is stage-specific and/or dependents on polarity mechanisms that are lacking in 2D cultures.

EGFR signalling transiently increases during skeletal muscle regeneration (Figure 15F), which is localized to the basal surface of satellite cells isolated on day 2 post-injury (Figure 15E). This transient EGFR signalling directs the capacity of satellite cells to self-renew or give rise to committed progeny during skeletal muscle regeneration *in vivo*. Specific deletion of EGFR in satellite cells dysregulates the stem cell pool and results in a significant reduction in the number of self-renewing Pax7-expressing cells by 10d post-injury (Figure 16F). Exogenous supplementation with recombinant EGF enhances the numbers of Pax7-expressing satellite cells and Myog-expressing differentiating progenitors, whereas a loss of EGFR expression in satellite cells abrogates the effects of exogenous EGF (Figure 16G-H). Interestingly, despite having reduced numbers of Pax7-expressing cells with the loss of EGFR in satellite cells, we did not observe a change in the number of Myog-expressing cells during regeneration. These data strongly suggest that *EGFR* cKO satellite stem cells are precociously committing to compensate for the demand of differentiating progenitors necessary for differentiation or directly differentiating similar to previous reports of EGFR-downregulation in myoblasts[203,204], resulting in the exhaustion of the stem cell pool.

EGFR is an epithelial polarity regulator [205], which adds to an accumulating body of evidence that suggests quiescent satellite cells share many apicobasal polarity regulators found in epithelial cell types. Unlike polarized epithelial cells, satellite cells do not have a luminal surface. Therefore, the basal surface of satellite cells attaches to the basal lamina and the apical surface attaches to its host myofibre through junctional complexes. M-cadherin (Cdh15), a well-known satellite cell marker, and its partner β-catenin are exclusively localized to the apical surface and form cell-cell adherence junctions with the host myofibre [206–208]. Pard3 (the mouse homologue of *Drosophila* Par-3, also known as Baz or bazooka), a member of the Par complex, is also localized along the apical surface of satellite cells [178,209]. This suggests that the apical surface of satellite cells resemble the

apical-lateral domain of epithelial cells. Indeed, the polarity effector Scribble is also apically distributed in satellite cells and segregates to the committed daughter cell during asymmetric divisions [210]. This distinction makes satellite cells in skeletal muscle a unique system to study polarity effector function in asymmetric stem cell division.

Similar to polarized renal epithelial cells [205] and enterocytes [211], EGFR is localized to the basal surface of quiescent satellite cells (Figure 15A). This basal localization primes the activation of the signalling cascade in a polarized manner (Figure 15B–C and Figure S9B). Surprisingly, phosphorylation of EGFR propagates from an extremely localized 'streak'-like domain in these quiescent satellite cells, suggestive of receptor clustering or localized activation (Figure 15B and Figure 18A). This localized activation likely recruits EGF-dependent interactors and drives the tyrosine phosphorylation of EGFR substrates asymmetrically at the basal surface. Interactions with integrins present at the basal surface can lead to the specific activity of EGFR Basolateral EGFR signalling is able to activate unique effectors, such as focal adhesion kinase, compared to apical or generalized activation [212]. In satellite stem cells, Aurka is recruited to p-EGFR and orients mitotic centrosomes along the apicobasal axis (Figure 15G-H and Figure 17). Aurka directly phosphorylates Pard3 resulting in its release from the Par complex[213]. Thus, EGFR-Aurka signalling establishes a signalling gradient which polarizes the Par complex (Figure 18D). It will be interesting to examine the mechanism of EGFR localization and whether other canonical EGFR signalling effectors are activated in a polarized manner and if these play a role in determining the cell fate of daughters from asymmetric divisions.

Immediately following acute injury, the satellite cell niche undergoes dramatic changes, accumulating infiltrating immune cells and fibroadipogenic progenitors [182]. One possible source of EGF is the large number of neutrophils and macrophages that accumulate in the damaged muscle to clear away necrotic myofibres [214]. Specifically, M2 macrophages have been shown to secrete high levels of EGF [215] and are closely

associated with committed myogenic progenitors during muscle regeneration [216]. However, other ligands including transforming growth factor-β (TGF-β), heparin-binding EGF-like growth factor (HB-EGF), amphiregulin, epiregulin also have the potential to activate EGFR signalling [217]. Interestingly, phosphorylation of EGFR in muscle is reduced in *HB-EGF*$^{-/-}$ mice subjected to arterial ligation [218]. Alternatively, amphiregulin is secreted by specialized Foxp3-expressing and CD3-expressing regulatory T-cells during regeneration, depletion of these cells in *mdx* mice causes accelerated muscle degeneration and increased fibrosis [219]. Thus, further studies will be required to determine the source or sources of EGFR activating ligands in regenerating muscle.

Importantly, EGF treatment was able to rescue asymmetric divisions in dystrophin-deficient satellite stem cells (Figure 18E–F). This suggests that redundancies in overlapping polarity signalling could provide functional compensation toward establishing asymmetric divisions. Moreover, EGF stimulated the productive generation of myogenic progenitors required to form new myofibres (Figure 19E–J). Unlike the mislocalized Par complex proteins in *mdx* satellite cells [178], EGFR is properly localized and activated in response to EGF stimulation (Figure 18A). This suggests that EGFR-mediated polarity can function without dystrophin-dystroglycan signalling.

Interestingly, EGFR signalling was previously identified as a genetic modifier to the loss of dystrophin-dystroglycan in a *Drosophila* phenotypic screen [220]. Loss of *kek1* or *argos*, repressors of EGFR signalling in *Drosophila*, suppressed abnormal wing-vein morphologies of dystrophin-RNAi *Drosophila* phenotype. Therefore, EGFR and dystrophin–dystroglycan signalling likely intersects to establish cell polarity and determine cell fate. Moreover, this evidence suggests that positive modifiers of EGFR signalling could be utilized to compensate for the lack of dystrophin.

Consistent with its effects in myofibre cultures, EGF treatment enhances the regeneration kinetic of *mdx* muscles. Loss of polarity signalling from dystrophin-deficiency

causes cell cycle defects in *mdx* satellite cells [178,221,222]. Therefore, chronic degeneration of dystrophic myofibres in DMD is not fully repaired. Although methods of re-expressing dystrophin are being attempted with AAV viral delivery with great promise in delaying disease progression and reducing myofibre fragility [223–226], a major step toward regaining muscle function in DMD is to restore satellite stem cell function and enhancing regeneration. In short-term regeneration, EGF treatment boosts the number of myogenic cells (Figure 18J-K), suggesting that satellite stem cells could overcome cell-cycle defects to generate additional progenitors to participate in regeneration. This facilitates the recovery of the muscle by producing larger regenerated myofibres compared to the untreated muscles (Figure S12H).

Strikingly, *mdx* muscles electroporated with an EGF-expressing vector are larger, contain more differentiating myogenic progenitors which go on to form new myofibres, and have reduced myofibre branching associated with the mdx phenotype (Figure 19B–J). Nascent myofibres inhibit the adipogenic differentiation of fibroadipogenic progenitors in the muscle, thereby tissue fibrosis is directly impacted by the rate of muscle regeneration [227,228]. In agreement with this idea, EGF-electroporated muscles contained less fibrosis compared to empty vector controls (Figure 19C and D). Importantly, these changes to the muscle architecture are translated to direct enhancements to muscle function, lasting over 150 days after the treatment (Figure 19K–L). The increase in specific force generation observed with EGF-treated TA muscles indicates the presence of additional contractile muscle fibres or increased myofibre cross-sectional area from reduced fibrosis, which provides further evidence of attenuated dystrophic progression.

Importantly, balancing symmetric expansion and asymmetric commitment in satellite stem cells is critical to maintaining muscle regeneration in DMD. Stimulation of satellite cell expansion with compounds such as Wnt7a [229] can boost regenerative outcomes by promoting a larger pool of satellite cells able to offset deficits in

differentiation. Speculatively, prolonged satellite cell expansion may result in proliferative stress and could accelerate telomere shortening leading to stem cell exhaustion [230]. Reorienting satellite cell divisions to promote myogenic commitment with EGF tips the balance to promote an increase in the absolute number of asymmetric division similar to a wild type context (Figure 18F) and improve regenerative outcomes (Figure 19). The effect of EGF stimulation on human satellite cell function is an exciting prospect as the pathological progression of human DMD is more severe than the mdx mouse model [231,232].

Our findings provide proof-of-principle evidence to support the functional rescue of *mdx* satellite cells *in vivo* by stimulating the EGFR-driven polarity pathway. We envision that stimulation of muscle stem cell function can be combined with dystrophin restoration to restore muscle function in Duchenne muscular dystrophy. Future studies will further elucidate the role of EGFR signalling in the regulation of stem cell polarity and the potential for small molecule activation of EGFR signalling as a therapeutic modality for the treatment of DMD.

## METHODS

Key resource table is available in the online version of the article: https://doi.org/10.1016/j.stem.2019.01.002

## STAR METHODS

### CONTACT FOR REAGENT AND RESOURCE SHARING

Information and requests for reagents may be directed to the corresponding author Michael A. Rudnicki (mrudnicki@ohri.ca).

### EXPERIMENTAL MODEL AND SUBJECT DETAILS

#### Experimental animals

Housing, husbandry and all experimental protocols for mice used in this study were performed in accordance with the guidelines established by the University of Ottawa Animal Care Committee, which is based on the guidelines of the Canadian Council on Animal Care. Mice are housed in ventilated cages with 1/4" corncob bedding changed every two weeks. Mice are supplied food *ad libitum* with automated acidified RO water or bottles changed every 7 days. Light cycles are 12h-12h cycle with simulated sunrise and sunset. Health and immune status of experimental mice were normal where Sentinels are routinely monitored (fecal, fur and oral swab) for *MNV, MHV,* Mouse *Parvovirus (MPV/MVM), MRV (EDIM), TMEV/GDVII, Helicobacter, P. pneumotropica-Heyl, P. pneumotropica-Jawetz, Entamoeba,* Mites*, Pneumocystis,* Pinworm*, and Spironucleus muris.* No animals were subjected to previous experimental procedures and are test or treatment naïve. The following mouse lines were used: B10-*Dmd* $^{mdx}$/J *(mdx,* homozygous DMD$^{mdx}$ females and hemizygous DMD$^{mdx}$ males*)*, NOD.*Cg-Prkdc*$^{scid}$*Il2rg*$^{tm1Wjl}$/SzJ (NSG), B6.Cg-*Pax7*$^{tm1(cre/ERT2)Gaka}$/J (*Pax7-CreERT2)*, B6.129S4-*Myf5*$^{tm3(cre)Sor}$/J *(Myf5-Cre),* B6.129X1-*Gt(ROSA)26Sor*$^{tm1(EYFP)Cos}$/J *(R26R-eYFP)*, B6.SJL-Pax7$^{tm1.2Tajb}$ *(Pax7-nGFP),*B6;129S6-*Gt(ROSA)26Sor*$^{tm1(CAG-tdTomato*,-EGFP*)Ees}$/J *(R26R-nTnG),* B6.129S6-

*Egfr*$^{tm1Dwt}$/Mmnc (EGFR$^{fl/fl}$). If not stated differently, 6-8 week old mice were used for all experiments. *Myf5-Cre:ROSA26-eYFP* mice[171] were F1 progeny from *Myf5-Cre* x *R26R-eYFP* breeding pairs. *Myf5-Cre:nTnG* mice were F1 progeny from *Myf5-Cre* x *R26R-nTnG* breeding pairs. Tamoxifen inducible conditional genetic knockout animals were F2 crosses between the offspring of *Pax7-CreERT2 (Cre/+)* mice[233] and EGFR$^{fl/fl}$ mice[234] generating Pax7-CreERT2:EGFR(+/+) and Pax7-CreERT2:EGFR(*fl/fl*) mice.

**Cell Lines**

HEK293T cells were used for validation of EGF expression following transient transfection. HEK293T cells were purchased from and authenticated by ATCC. These cells were verified to be free from mycoplasma contamination using the MycoSensor PCR Assay Kit (Agilent Technologies). HEK293T cells were cultured at 37°C in Dulbecco's Modified Eagle's Medium (DMEM) supplemented with 10% fetal bovine serum and 1% penicillin/streptomycin

**METHOD DETAILS**

**Lineage Tracing with *Myf5-Cre/R26R-eYFP* and *Myf5-Cre/R26R-nTnG***

*Myf5-Cre/R26R-eYFP* transgenic mice, possessing a knock-in of Cre recombinase in the coding-region of the myogenic commitment factor *Myf5* crossed with the knock-in of Cre-activated yellow fluorescent protein (eYFP) at the *ROSA26* locus, were used as a lineage reporter model to discriminate committed satellite myogenic cells that have expressed *Myf5-Cre* (eYFP$^{Pos}$) from satellite stem cells that have never expressed *Myf5-Cre* (eYFP$^{Neg}$). *Myf5-Cre/R26R-nTnG* transgenic mice, possess a CMV/b-actin promoter, a loxP flanked nuclear TdTomato (nTdTomato) and nuclear GFP (nGFP) cassette within the ROSA.26(Sor) locus. When crossed with the *Myf5-Cre* transgenic line, all cells express nTdTomato except those cells that have expressed *Myf5*, which express an nGFP signal.

These transgenic models allow for the visualization of *de novo Myf5* expression in committed daughter cells during asymmetric divisions.

**qPCR Enumeration of eYFP$^{Pos}$ and eYFP$^{Neg}$ Cells**

Recombination of the *R26R-eYFP* allele involves the removal of a genomic segment containing a PKG-neomycin resistance (*Neo*) cassette and three poly-adenylation transcription stop sites flanked by loxP recognition sites. We designed specific primers that amplify either: within the *Neo* coding region, which will only amplify in eYFP$^{Neg}$ cells; spanning the two loxP sites, which will only amplify in eYFP$^{Pos}$ cells; and within the eYFP coding region, which is used to normalize DNA input (Figure S7A). Primer pairs were optimized with purified pBigT plasmid (Addgene) in its native state or recombined by an *in vitro* Cre recombinase (New England BioLabs). DNA isolated from cultured eYFP$^{Pos}$ and eYFP$^{Neg}$ myoblasts were used to validate the detection efficiency of the primer pairs. Real-time PCR analysis (SSoFast EvaGreen Supermix, Bio-Rad) was performed using the CFX384 real-time PCR detection system (Bio-Rad), and results were normalized to e*YFP*. The Z-factor for detecting eYFP$^{Pos}$ cells was 0.935 and eYFP$^{Neg}$ cells were 0.872 (Figure S7B). The primers used for qPCR detection of recombination at the *R26R-eYFP* allele were as follows. *Neo*, GGCCGCTTTTCTGGATTCAT and GGCGATACCGTAAAGCACGA; *LoxP*, TCGCGGTTGAGGACAAACTC and AGCTAGCTTGGGCTGCAGGT; and *eYFP*, GAACTGTTCGCCAGGCTCAA and CACGGGTAGCCAACGCTATG

**Compound Libraries and Small Molecules**

The Ontario Institute for Cancer Research kinase inhibitor and toolkit compound libraries (OICR, Toronto, Canada) consists of 400 specific kinase inhibitors and 160 additional small molecule compounds targeting cellular and developmental pathways. The Tocris kinase inhibitor library (Tocris Bioscience) consists of 80 well-characterized kinase inhibitors. Compound libraries were obtained as 1mM solutions dissolved in DMSO.

**FDB Myofibre Screening Assay**

Single myofibres were isolated from FDB muscles of 6-8 week old *Myf5-Cre*/*R26R-eYFP* mice (adapted from[183]) and cultured at 37°C in suspension in 96-well dishes containing DMEM+ with 2% L-glutamine, 4.5% glucose, and 110 mg/ml sodium pyruvate (Gibco) containing 20% FBS (Wisent) and 1% chick embryo extract (CEE, Accurate Chemicals) and supplemented with either 1:1000-dilution of DMSO (Sigma), DMSO +Wnt7a (50ng/mL; R&D Systems), or 1uM of a small molecule compound. Fibres were collected after 42h of culture and genomic DNA was isolated and purified using the Dneasy 96-well Blood and Tissue kit (Qiagen). qPCR enumeration of $eYFP^{Pos}$ and $eYFP^{Neg}$ cells was performed as described above. Primary screening was performed in biological duplicates, each with technical duplicate qPCR reactions. Results were normalized to DMSO-only controls and averaged between replicates.

**Gene Expression Analysis**

A previously published GEO dataset was used. Expression clustering analysis was performed on normalized gene expression fold change with respect to the median expression value using Cluster 3.0 (http://bonsai.hgc.jp/~mdehoon/software/cluster/software.htm).

**EDL fibre Culture and siRNA Transfection**

Myofibre culture was performed as described previously. Briefly, EDL were carefully dissected and incubated at 37°C in DMEM with 2% L-glutamine, 4.5% glucose, and 110 mg/mL sodium pyruvate (Gibco) containing 0.2% collagenase I (Sigma) for 45 min. Myofibres were isolated using gentle trituration in DMEM+ with 2% L-glutamine, 4.5% glucose, and 110 mg/ml sodium pyruvate (Gibco) containing 20% FBS (Wisent) with a glass pipet. Myofibres were cultured at 37°C for 36, 42, or 72h in DMEM+ with 2% L-glutamine, 4.5% glucose, and 110 mg/ml sodium pyruvate (Gibco) containing 20% FBS (Wisent), 1% chick embryo extract (MP Biomedicals), and 2.5ng/ml bFGF (Cedarlane).

For pharmacological inhibition, Lapatinib ditosylate (1mM in DMSO; Santa Cruz Biotechnology), TC-A2317 hydrochloride (1mM in DMSO; Tocris Bioscience) was added to the culture medium for a final concentration of 1uM, equal dilution of DMSO was used as vehicle control. For EGF treatment, human recombinant EGF (100 ng/ul in PBS with 0.1% BSA, Life Technologies) was added to the culture medium at 100ng/mL. For EdU labelling, EdU was supplemented into the media for the first 20h of culture as per manufactures protocol, followed by extensive washing and replacement of fresh growth media.

To assess the signalling status of EGFR in quiescent satellite cells and 2 days post-injury, EDL muscles were fixed in 4% PFA immediately post-dissection. Myofibre bundles were teased from the fixed muscles by tweezers. For studies pertaining to the activation of EGFR, myofibres were isolated in serum-free conditions with DMEM with 2% L-glutamine, 4.5% glucose, and 110 mg/mL sodium pyruvate (Gibco) and then treated with human recombinant EGF (100 ng/ul in PBS with 0.1% BSA Life Technologies) at 100ng/mL for 1h, equal dilution of 0.1% BSA in PBS was used as vehicle control.

Transfection of satellite cells on myofibres was performed using lipofectamine RNAimax (Life Technologies) and validated Smartpool siRNAs for *EGFR*, *Aurka*, or scramble (SCR) (Dharmacon). To ensure maximal efficiency, two transfections were performed at 4h and 16h after isolation of the myofibres as described previously. Knockdown efficiencies of the siRNA were validated in myoblasts by western blot and qRT-PCR.

To assess myofibre branching in electroporated muscles, EDL muscles were isolated and fixed in 4% immediately post-dissection and washed extensively. Single myofibres were isolated by enzymatic digestion in 0.4% collagenase I (Sigma) for 30 min with trituration. Fibres were incubated in DAPI and imaged in phase. 75 fibres from each mouse per condition were analyzed as per representative images in Figure S13E.

**Characterization of Satellite Cell Divisions**

The orientation of mitotic spindles in satellite cells was measured as described previously [178]. Single myofibres were fixed after 36h of in vitro culture, as described above. Satellite cells were identified by Pax7 expression. Pax7 staining becomes cytoplasmic in mitotic satellite cells after the dissociation of the nuclear envelope but is still discernable. Mitotic satellite cells were identified by positive p-Aurk staining, which labels cells from pro-metaphase to cytokinesis. Mitotic satellite cells with p-Aurk staining patterns that were not observed in WT cells, including monopolar, multipolar (>2), and abscission defects were quantified as abnormal. Mitotic orientations were manually counted according to the angle between the mitotic spindle and the tangential plane of the satellite cell's attachment point to the myofibre. Unless stated, >50 fibres were analyzed per condition.

**Cell Culture and Co-Immunoprecipitation**

Satellite cells isolated from WT or *Pax7-nGFP* mice by fluorescence-activated cell sorting and cultured as primary myoblasts on collagen-coated plates at 37°C in primary myoblast growth media (Ham's F10 media (Gibco) with 20% FBS (Wisent), 1% penicillin-streptomycin (Gibco) and 5 ng/mL bFGF (Cedarlane)). For EGF stimulation, myoblasts were serum-starved for 1h in Ham's F10 media and then refed in primary growth media with or without recombinant human EGF (100ng/mL) for an additional hour. Co-immunoprecipitation experiments were performed as described previously [236], with slight modifications. In short, sub-confluent myoblasts were collected and lysed in lysis buffer (1% NP-40, 0.25% sodium deoxycholate, 150 mM NaCl, 50mM tris-HCL pH7.4) in the presence of protease inhibitors (cOmplete mini, Roche) and phosphatase inhibitors (Nacalai). 2.5uL of primary antibodies were incubated with cell lysates overnight at 4°C. Immunoprecipitations were performed using Dynabeads Protein G (Novex) at 10:1 (v/v) beads to antibody ratio. Beads were then washed 3 times with washing buffer (0.1% NP-40, 150 mM KCl, 25 mM Tris-HCl pH 7.9, 5mM MgCl2, 10% glycerol, 0.3 mM DTT) and

bound proteins were eluted by boiling at 100°C in 50µL of 2X Laemmli buffer for 5 min. Primary antibodies used: mouse IgG (cat# sc-2025, Santa Cruz Biotechnology), rabbit IgG (cat# sc-2027, Santa Cruz Biotechnology), rabbit anti-phospho-EGFR Y1068 (cat# 3777S, Cell Signalling Technology), mouse anti-Aurka (35C1, cat# ab13824, Abcam).

**Immunoblotting**

Proteins were separated on 10% SDS-PAGE and transferred to Immobilon-P PVDF membrane (EMD Millipore). Membranes were probed with primary antibodies, followed by light chain specific HRP-conjugated secondary antibodies at 1:5000 (Bio-Rad) and developed using Immobilon Western HRP substrate (EMD Millipore). EGF levels were detected by dot plots. Conditioned media from transfected 293T cells were concentrated 15x using 3kDa ultrafiltration tubes (Amicon, EMD Millipore). Serial dilution of recombinant EGF protein was used as a standard curve. 2uL of non-denatured protein preparation was loaded directly onto 0.2um nitrocellulose membrane (GE Life Sciences) and allowed to dry. Membranes were blocked in 5% BSA in TBST for 1h and probed with rabbit anti-EGF (cat# ab9695, Abcam), followed by HRP-conjugated secondary antibody at 1:5000 (Bio-Rad) and developed using Immobilon Western HRP substrate (EMD Millipore). Membranes were visualized using FluorChem HD2 (Alpha Innotech) or exposed to BIOMAX film (Eastman Kodak).

**Electroporation and Cardiotoxin Injury**

I.M. cardiotoxin injections (Latoxan, 50ul of 10uM solution in saline) were injected directly into the right TA muscle through the skin under general anesthesia. For pharmacological inhibition, Lapatinib ditosylate (1mM in DMSO; Santa Cruz Biotechnology), TC-A2317 hydrochloride (1mM in DMSO; Tocris Bioscience) was mixed into the cardiotoxin solution for a final concentration of 1uM, equal dilution of DMSO was used as vehicle control. Supplemental injection of inhibitors (20uL of 2.5uM of inhibitors in saline) was performed 2 days after cardiotoxin injection. For recombinant EGF injections, 10ng of human

recombinant EGF (100 ng/ul in saline, Life Technologies) was mixed into 50uL of cardiotoxin solution or 20uL of saline, equal volumes of saline were used as vehicle control. Muscles were harvested 10 days post-injury as a mid-point of regeneration where the number of Myog-expressing cells is above baseline and myofibres are generally reformed. Extended timepoints of 30 days and 150 days post-injury represent full repair and onset of DMD disease progression respectively.

Electroporations were performed as described previously [190]. 30ug of purified endotoxin-free pTT3-CD4d3+4-bio empty vector control (cat #32402, Addgene) [237] or pTT3-EGF-CD4d3+4-bio-His expression plasmid (cat# 53340, Addgene) [202] expression plasmid in saline was injected into the right hind TA muscle of 4-week old mdx mice through the skin under general anesthesia. Immediately after injection, electric stimulation was applied to the TA by a pulse generator (ECM 830, BTX) of 100-150 volts for 6 pulses, with a fixed duration of 20ms and an interval of 200ms using 5mm needle electrodes (BTX).

**Immunostaining, PLA and Antibodies**

EDL myofibres were fixed for 10 min in 2% PFA and washed with PBS. Fibres were blocked and permeabilized in horse serum blocking buffer (5% horse serum, 1% BSA (Sigma), and 0.5% Triton X-100 (Sigma) in PBS) for 1h at room temperature or at 4°C overnight. Primary antibodies were applied in blocking solution for 2h at room temperature or at 4°C overnight. Samples were subsequently washed with PBS and stained with appropriate fluorescently labelled secondary antibodies (Alexafluor 488, 546, or 647) for 1h at room temperature. After washing with PBS, samples were mounted with Permafluor (Fisher).

Muscle samples were embedded in OCT and frozen in liquid nitrogen-cooled isopentane and cryosectioned in 12-□m slices. Cross-sections were washed once with PBS and fixed in 2% PFA 10min, permeabilized with 0.1% Triton X-100/0.15M

Glycine/PBS 10min and extensively washed with PBS. Samples were blocked using M.O.M. Blocking reagent (Vector) 2h followed by additional blocking in 5% NGS/2%BSA at 4°C overnight. Primary antibodies were applied in blocking at 4°C overnight. Samples were washed extensively in PBS and secondary antibodies were applied in PBS (Alexa Flour 546, 647) for 1h at room temperature. Following PBS washes, cross-sections were counterstained with DAPI 10min and mounted with Permafluor (Fisher).

Antibodies were as follows: mouse anti-Pax7 (DSHB), chicken anti-GFP (cat# ab13970, Abcam), rabbit anti-EGFR (cat# 4267S, Cell Signalling technology), rabbit anti-phospho-EGFR Y1068 (cat# 3777S, Cell Signalling technology), mouse anti-Aurka (35C1, cat# ab13824, Abcam), rabbit anti-phospho-Aurk (cat# 2914S, Cell Signalling technology), rabbit anti-Pard3 (cat# 07-330, Millipore), rat anti-laminin (cat# L0663, Sigma), rabbit anti-myogenin (M225, cat# sc-576, Santa Cruz).

Proximity ligation assays (PLA) were performed as described previously using Duolink (Sigma) PLA probes mouse and rabbit (Dumont et al., 2015b). Images of immunostainings were taken on an Axio Observer.Z1 microscope equipped with an LSM510 META confocal laser scanner and a plan-Apochromat 63x/1.40 Oil DIC M27 objective or an Axioplan 2 microscope equipped with a plan-Neofluar 40x/1.30 Oil DIC and a plan-Neofluar 100x/1.30 Oil DIC objective. Images were processed and analyzed with Axiovision, Zen, and FIJI software. 3D z-stack images were projected by maximum intensity using Fiji software (http://fiji.sc/Fiji).

For grey value measurements, images of cells were collected with fixed exposures or confocal z-stacks as stated. Fiji software was used to generate masks of satellite cells based on Pax7 staining on raw images. Due to the highly localized staining for p-EGFR and variable epifluorescent background intensity based on the plane of focus, grey values for p-EGFR staining were calculated as “staining intensity = max intensity – average intensity”. Three-dimensional analysis of p-EGFR staining was performed on confocal z-

stacks taken at 1um resolution on a Zeiss 510 confocal microscope. Z-stacks were analyzed for pixel intensity in the apical vs basal side of the cell following measured bi-section along the apical-basal axis. Satellite cells from EGFR cKO mice treated with EGF were used as a biological negative control.

**Histological Analysis of Muscle Sections**

For Fibre type analysis, non-fixed samples were washed with PBS and blocked in 10% NGS for 1hr at room temperature. Primary antibodies were applied in 10% NGS for 2h at room temperature. Sections were washed extensively with PBS and secondary antibodies were applied in PBS for 1h at room temperature. Following PBS washes, sections were counterstained with DAPI 10min and mounted with Permafluor. Antibodies were as follows: mouse anti-MyH3 (clone F1.652, DSHB), mouse anti-MyH4 (clone BF-F3, DSHB).

For analysis of myofibre Feret's diameter and CNF, non-fixed samples were washed with PBS and stained with Wheat Germ Agglutinin Alexa 647 conjugate (Fisher) for 1h at room temperature. Samples were washed once with PBS and counterstained with DAPI. Samples were washed with PBS and mounted with Permafluor. Images were taken immediately following staining. Minimum fibre Feret measurement was performed using the SMASH software in MATLAB 2015a as described previously [238]. Samples with significant staining artifacts were excluded from automated analyses. The total number of myofibres in each tissue was verified manually. >95% of myofibres were quantified across each section in its entirety.

**Satellite cell transplantation and analysis**

Satellite cells from *Myf5-Cre/R26R-nTnG* transgenic mice were FACS isolated based on FSC/SSC, CD31/CD11b/CD45/SCA1 (V450), a7-Integrin (APC) and nGFP/nTdT (Figure S10A). Mice were processed independently to allow one donor per experimental replicate. Satellite cells were isolated, spun down and fractioned into 10,000 cell aliquots. Satellite cells are treated with EGF or saline on ice for 3h, washed twice and resuspended. 10,000

cells from the same donor (nTdT control or nTdT + EGF) were injected into the left and right TA muscle of 8-12 week NOD.*scid*.gamma mice injured with cardiotoxin one day prior to transplantation. Mice were allowed to recover for 10 days post-injury followed by perfusion fixation. Isolated muscles were frozen and sectioned at 20um with ~200um spacing between consecutive sections. 100,000 cultured nGFP myoblast (passage 4) from the same initial donors were transplanted under the same experimental plan to determine the role of EGF on committed myogenic cells.

### *In situ* Force Measurements

Force measurements were performed on a custom setup in accordance with experimental protocols outlined previously [239]. Briefly, mice were anesthetized with 2-5% vaporized Isoflurane mixed with $O_2$. Mice were position on top of a heated surface in order to maintain the body and muscle temperature to 30°C. Knees were secured to a fixed steel post using surgical suture and their feet were pinned to a platform to prevent movement from the contraction of other muscle groups. The distal tendon of both TA muscles, electroporated and contralateral, was attached to separate FT03 force transducers connected to a 79E physiograph (Grass Technologies, Warwick, U.S.A.), which in turn was connected to a KCP13104 data acquisition system (Keithley, U.S.A.). Data were sampled at recorded at 5 kHz. Exposed muscles were kept from drying with physiological saline solution (118.5 mM NaCl, 4.7 mM KCl, 2.4 mM CaCl2, 3.1 mM MgCl2, 25 mM NaHCO3, 2 mM NaH2PO4, and 5.5 mM D-glucose). Electrical stimulations were applied across two needle electrodes, placed through the skin just above and below the knee to stimulate the tibial nerve. The electrodes were connected to a Grass S88 stimulator and a Grass SIU5 isolation unit (Grass Technologies). Tetanic contractions were elicited every 100 s with 200 ms trains of 0.3 ms, 5 V (supramaximal voltage) pulses at frequencies varying between 1 and 200 Hz. The tetanic force was defined as the force generated upon stimulation and calculated

as the difference in force at the maximum height of contraction and the force just prior to the stimulation. The tetanic force was normalized as follows:

$$F_{Normalized} = F_{Measured} / CSA * CF$$

$$CSA = Le / We * M_{Density}$$

where $F_{Normalized}$ was the normalized force in N/cm2; $F_{Measured}$, the measured force in g; CF, the converting factor 0.00980665 N/g; CSA, the cross-sectional area in $cm^2$; Le, the experimental muscle length in cm; We, the muscle weight in g; and $M_{Density}$, the muscle density taken as 1.06 $g/cm^3$.

**Real-Time PCR**

Total RNA was isolated (NucleoSpin RNA II, Macherey-Nagel). Reverse transcription was carried out using a mixture of oligodT and random hexamer primers (iScript cDNA Synthesis Kit, Bio-Rad). Sybr Green, real-time PCR analysis (SSoFast EvaGreen Supermix, Bio-Rad) was performed using the CFX384 real-time PCR detection system (Bio-Rad), and results were normalized to *Gapdh* and *Tbp* or *PPIA* and *18s* expression and analyzed by Bio-Rad CFX Manager software. The following primers were used (5'-3'): *Aurka*, GAGTTGGCAAACGCTCTGTC and TTCTCCTGGAAGATGGAGCA; *EGFR*, GGGGATGTGATCATTTCTGG and AAGGATTGCAGACGTGGTTC; *Pax7, TACTGCCCACCCACCTACAG and GTGTGGACAGGCTCACGTTT; eYFP*, CACGACTTCTTCAAGTCCGCCATG and GCGGATCTTGAAGTTCACCTTGAT; PPIA, CACTGCCAAGACTGAATG and GTCGGAAATGGTGATCTTC; 18s, CGCGGTTCTATTTTGTTGGT and AGTCGGCATCGTTTATGGTC; *Gapdh*, CCCAGAAGACTGTGGATGG and ACACATTGGGGGTAGGAACA; and *Tbp*, AGAACAATCCAGACTAGCAGCA and GGGAACTTCACATCACAGCTC.

**QUANTIFICATION AND STATISTICAL ANALYSIS**

Compiled data are expressed as mean ± standard error of the mean (SEM). Experiments were performed with a minimum of three biological replicates. For statistical comparisons of two conditions, the Student's t-test was used. Paired tests were used for biologically matched samples. Unpaired tests were used to compare unrelated samples. Feret's size and force measurements were analyzed using two-way ANOVA with a two-stage set up to control for false discovery rate. No data was removed as outliers, with data point representation graphically where appropriate. The experimental design incorporated user blinding when possible. Statistical analysis was performed in GraphPad Prism or Microsoft Excel. The level of significance is indicated as follows: * $p < 0.05$, ** $p < 0.01$, *** $p < 0.005$.

**SUPPLEMENTAL ITEMS**

Supplemental information contains 7 figures, one table and one movie.

## Manuscript III: Isolation of satellite cells and transplantation into mice for lineage tracing in muscle

AUTHORS: **Peter Feige**[1,2,3] and Michael A. Rudnicki[1,2,3,4]

AUTHOR AFFILIATION: 1. Sprott Center for Stem Cell Research, Ottawa Hospital Research Institute, Regenerative Medicine Program, Ottawa, ON, Canada. 2. Department of Cellular and Molecular Medicine, Faculty of Medicine, University of Ottawa, Ottawa, ON, Canada. 3. Department of Medicine, Faculty of Medicine, University of Ottawa, Ottawa, ON, Canada. Faculty of Medicine University of Ottawa Ottawa, ON, Canada

**This manuscript was published in Nature Protocols in 2020.**

Feige, P., Rudnicki, M.A. Isolation of satellite cells and transplantation into mice for lineage tracing in muscle. Nat Protoc 15, 1082–1097 (2020). https://doi-org/10.1038/s41596-019-0278-8

### AUTHOR CONTRIBUTION

P.F. conceptualized the study, experimental design and performed all experiments herein. M.A.R. oversaw the experimental design, analysis of results, manuscript editing, and financial support.

**ABSTRACT**

Limited methods exist to assay the direct effects of therapeutic intervention on muscle stem cell fate, proliferation or differentiation in an *in vivo* context. Here we provide an optimized protocol for muscle stem cell isolation and transplantation into mice to deconvolute heterogeneity within isolated stem cell populations. Viable and pure cell populations are isolated within 2h and can then be used for therapeutic intervention or transplantation to uncover the repopulating and differentiation potential in mice, a physiologically relevant *in vivo* context. Effects can be assessed 9 days following transplantation. This methodology analyzes cell and sort purity prior to transplantation to improve reproducibility and outlines novel blocking steps to improve tissue staining and analysis. Experience with surgical procedures in mice is recommended before attempting this protocol. Our system is widely applicable to explore stem cell dynamics within muscle and has already been used to study heterogeneity within muscle stem cell populations and the efficacy of the therapeutic intervention on isolated stem cell populations.

## INTRODUCTION AND DISCUSSION

Muscle satellite cells represent a heterogeneous population composed of stem cells and committed cells that facilitate muscle regeneration during homeostasis and disease. Satellite cell heterogeneity has a significant role in muscle regeneration, where the satellite stem cells maintain muscle stem cell homeostasis by undergoing asymmetric division to give rise to a committed satellite cell and a self-renewing satellite stem cell[171]. The asymmetric division plays a critical role in balancing satellite cell homeostasis and tissue regeneration[5].

The heterogeneity within the satellite cell pool can be observed based on the kinetics of cell cycle entry, gene expression and repopulation potential[5]. Defining stem cell hierarchies is fundamental in understanding stem cell identity and stem cell potential. The satellite stem cell is defined by its expression of the protein Pax7 whereupon spontaneous differentiation or asymmetric division results in expression of the protein Myf5 and commitment to the myogenic lineage. Committed satellite cells then undergo multiple rounds of division to produce enough cells for muscle repair. Recent single-cell mass spectrometry experiments suggest some myogenic cells and other resident cells within skeletal muscle traverse unique trajectories[34,240], demanding novel methods to isolate and assay cellular potential.

Here we provide a methodology to examine muscle stem cell hierarchy through transplantation of satellite stem cells, committed satellite cells or muscle progenitor cells to advance our understanding of muscle stem cell hierarchy. This protocol uses expedited enzymatic digestion of muscle that allows robust isolation of satellite cell populations through flow-cytometry based sorting techniques based on cell-surface markers and endogenous genetic reporters for functional lineage tracing. We provide instructions on analyzing cell purity prior to transplantation, methods to assess transplantation efficiency

and self-renewal capacity of transplanted cells as well as guidelines on appropriate experimental and biological controls. We further outline novel tissue processing techniques to improve the imaging of endogenous reporters and reduce biases in analysis. Our protocol involves terminal assessment of cell engraftment but can be adapted for long term non-invasive monitoring employed by others[89,241,242]. This protocol has been used successfully in our lab[101] and provides the framework to standardize stem cell transplantation in muscle across research groups. Individuals with working surgical skills and flow cytometry knowledge should be able to complete the protocol.

**Advantages of this protocol compared to other methods to evaluate satellite cells**

Isolation of satellite cells based on well-characterized cell surface markers[9] allows causative outcomes to be determined for lineage tracing, transplantation potential and repopulation kinetics in an *in vivo* context. Similarly, our transplantation protocol allows direct intervention on defined satellite cell subtypes prior to transplantation to define causal relationships in satellite cell fate and heterogeneity. Our protocol is amenable to pharmacological or genetic manipulation of satellite cell populations to assess lineage commitment, repopulation kinetics and transplantation potential. The protocol allows for redundancy in quality control of cell and sort purity prior to transplantation and the expedited protocol reduces processing times to promote viability, resulting in cells more representative of endogenous states.

Our protocol combines novel tissue processing steps and blocking procedures that are advantageous over existing methods and allow imaging of endogenous fluorescent markers, reducing the requirement for antibody labelling. These blocking steps significantly improve the signal to noise for immunofluorescence labelling in resting and injured skeletal muscle. The nuclear-bound reporter systems used in this protocol allow for discrete quantification of satellite cell commitment as cytoplasmic and membrane

reporters are shared among differentiated myofibres[241,242]. Additionally, we outline methods to ensure tissues are processed to allow comparable repeat staining among serial sections appropriate for archiving and to reduce random sampling bias during analysis.

Although *in vitro* culture of myogenic progenitors allows for flexibility in interrogating and analyzing commitment or self-renewal in isolated populations derived from satellite cells, it does not recapitulate the stem cell niche nor the complexity of the muscle fibre environment or its dynamics in response to injury[182,243]. Importantly, *in vitr*o propagation of satellite cells results in the clonal selection, loss of stemness and inability to engraft as stem cells following transplantation[244,245]. Although technically challenging, culturing myofibres harbouring satellite cells maintains endogenous niche interactions[171], extracellular matrix composition[182] and myofibre rigidity[243] to provide a more relevant *ex-vivo* culture paradigm[5]. However, cultured myofibres lack nervous system innervation, cardiovascular circulation and the three-dimensional regenerative environment associated with *in vivo* muscle repair.

Inducible lineage tracing models exploring satellite cell heterogeneity have provided significant insight in stem cell dynamics[172,246], however, these models are not conducive to monitor the isolated effect of pharmacological intervention on satellite cell signalling or heterogeneity without also impacting adjacent tissue. Most commonly, pharmacological interventions are injected directly into regenerating muscle to understand their effect on satellite cell-driven muscle repair. Although these methods address the regenerative consequence of injecting a therapeutic intramuscularly, it does not causatively address the influence of the therapeutic on satellite cells but rather its influence on signalling within whole muscle tissue. Isolated treatment of pure satellite cell

populations allows causal relationships to be identified and interrogated to functionally define the role of novel cell types or signalling pathways on regenerative outcomes.

Our protocol outlines good practices in stem cell transplantation. Quality control steps allow researchers to monitor cell viability and identity prior to transplant and steps to quantify accurate numbers of engrafted cells allow for a robust measure of engraftment efficiency. Our tissue processing steps outline measures to avoid random sampling bias and improve transparency by reporting absolute engrafted cell numbers and representative images of whole transplanted muscle sections. Adopting these guidelines should help improve reproducibility and transparent reporting among researchers.

**Applications of the protocol**

Exploring stem cell heterogeneity and stem cell fate is critical to define stem cell identity and hierarchy. Given the importance of satellite cells in muscle regeneration[247,248], our protocol has wide-ranging applications for the study of The mechanisms involved in satellite cell self-renewal and commitment; The pathways regulating satellite stem cell identity and multi-lineage commitment; The transplantation and self-renewal potential of novel satellite cell subtypes, and; The efficacy of regenerative therapies targeting muscle stem cells

We have previously demonstrated that satellite stem cells specifically integrate EGF signalling to promote asymmetric division and form committed satellite cell progeny[8]. In myopathies such as Duchenne's Muscular Dystrophy, satellite stem cells are impeded in the ability to undergo asymmetric division, resulting in hyperplasia of the stem cell pool and poor myogenic regeneration[178]. By isolating pure populations of satellite stem cells, we were able to show that treating satellite stem cells but not committed satellite cells or progenitors with EGFR ligand, resulted in an augmented asymmetric division *in vivo* to

give rise to myogenic progenitors[101]. Exploring cell signalling in isolated rare stem cell types is critical to understand complex tissue homeostasis and regeneration following injury.

Our protocol will be of interest to researchers exploring stem cell heterogeneity, therapeutic interventions targeting stem cells and muscle regeneration. Our guidelines for biological and technical controls provide the framework for robust experimental design and the means for causative relationships to be explored. Optimized staining procedures are applicable to both transplantation experiments and other techniques examining rare populations in tissue with high autofluorescence background. Researchers can expand their analysis of satellite cell potential by engrafting into immunocompromised *mdx* mice to evaluate the therapeutic potential of treated cells in the context of muscular dystrophy[5]. Researchers isolating other cell types from muscle such as fibroblasts, mesenchymal stem cells or fibroadipogenic precursors and analyzing their lineage commitment following transplantation may find our protocol useful for their experiments.

**Limitations of the protocol**

There are limitations to our protocol. Foremost, isolation of stem cells from tissue results in stem cell activation in a similar but not identical manner to injury[249–251]. This limits homeostatic assays to timepoints following transplantation and tissue regeneration, where transplanted satellite stem cells have taken up the niche position and are contributing to the resident satellite cell pool.

Our protocol examines the lineage commitment in treated satellite cells and can be adapted for early or long-term timelines, however, our protocol is a terminal procedure. Other labs have explored strategies to examine the therapeutic effects of satellite cell transplantation over the long term through non-invasive monitoring[89,241,242]. These

methods allow routine monitoring of satellite cell commitment, even following re-injury however the use of non-nuclear bound reporters limits the ability to discretely quantify numbers of committed progeny following transplantation. In our protocol, we have used the immunocompromised NOD.*Cg-Prkdc*$^{scid}$*Il2rg*$^{tm1Wjl}$/SzJ (NSG) mouse model, which may be cost-prohibitive in some experiments. Alternative methods rely on chemical immunosuppressants using transplanted Alzet pumps, however, we strongly suggest the use of NSG mice as they reduce experimental complexity and variability.

In our hands' cell viability has been optimized, however, gene and pharmacological intervention require extended experimental timelines which can affect cell viability, activation states and cell function. Care should be taken in the selection of experimental controls (outlined in **Experimental design**) and quality control of prospective populations (outlined in **Experimental design, Steps 32-43**) to reduce interpretation of technical artifact or variability.

Our protocol has been optimized using donor reporter mice bred on the C57/BL6 genetic background and recipient NSG mice, therefore transplantation efficiency may differ when using other mouse strains. Differences in background strain transplantation efficiency are controlled for by using the suggested controls contained within this protocol.

**Experimental design**

***Muscle injury in recipient immunocompromised mice.*** Isolation of satellite cells requires enzymatic digestion and results in the activation of satellite cells similar to injury[249–251]. It is important that isolated cells are grafted into an environment akin to their activation state to allow cells to progress under relevant regenerative timelines. Recipient *Tibialis Anterior* muscles from NSG mice are injured the day prior to isolating donor satellite cells (Figure 20) using myotoxin isolated from Cobra (*Naja pallida*). Researchers

may choose to limit the regeneration of endogenous satellite cells as is routine in other labs[241,252], however, researchers should assess if these conditions and methods are appropriate for their research question. Age of donor mice is also important to consider as yield, self-renewal and engraftment potential in aged satellite cells is impaired[174]. For experiments involving gene or pharmacological intervention, we advise control and treated cells to be isolated from one donor and transplanted into one recipient's adjacent injured *Tibialis Anterior* muscles to reduce experimental variability within recipient animals.

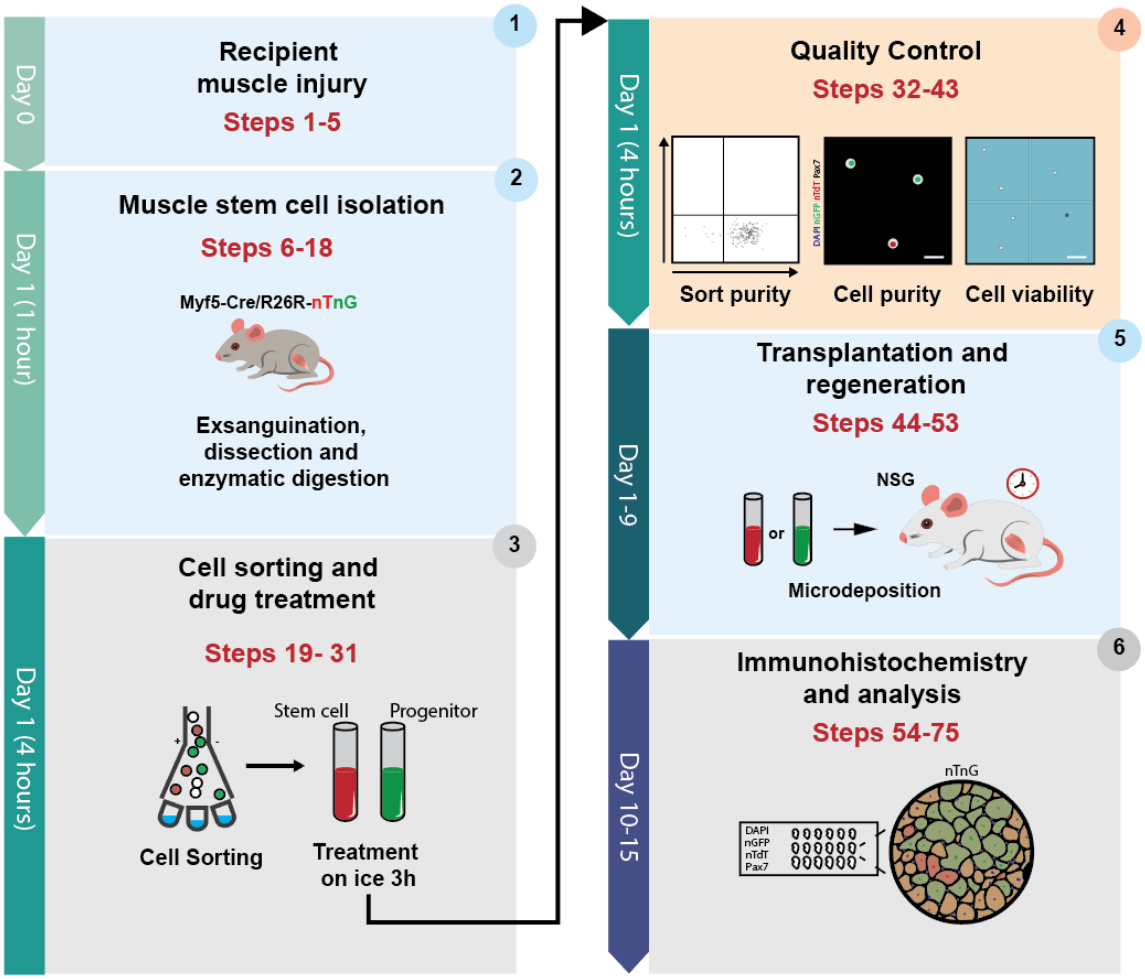


Figure 20: **Overview of the protocol for satellite cell isolation and transplantation.** Recipient muscle is injured (Steps 1–5) the day prior to isolating muscle stem cells (Steps 6–18). Muscle stem cells are labelled for cell sorting and treated with pharmacological interventions (Steps 19–31) concurrent to quality control analysis (Steps 32–43). Subpopulations of satellite stem cells committed satellite cells or cultured myoblasts are transplanted into immunocompromised mice (Steps 44–54) and allowed to grow in vivo prior to immunohistochemistry analysis (Steps 54–75).

***Isolation of satellite stem cells committed satellite cells and myogenic progenitors.***

Quiescent Muscle stem cells reside in a specialized niche located between the myofibre and the basal lamina[182]. Dissociation of satellite cells requires careful mechanical and enzymatic digestion to isolate satellite cells quickly and without compromising viability. Hindlimb muscle is isolated from mice previously exsanguinated by perfusion of isotonic

saline following a lethal dose of barbiturate (Figure 21). Exsanguination is critical to reduce immune and red blood cell content, reduce saturating antibody concentrations, avoid the need to use cytotoxic compounds for red blood cell lysis and reduce total cell content in samples allowing faster sorting rates at lower differential pressure thereby reducing shear forces on cells. Excised muscles are placed in Miltenyi GentleMACS tubes along with digestion buffer and minced until a rough slurry. We recommend automated dissociation techniques to reduce variability in tissue processing. Minced tissue is placed on a Miltenyi OctoMACS Separator and processed using our expedited protocol (**step 14**). Filtered FBS is added to the slurry to inhibit over digestion and samples are filtered to remove non-digested tissue. Samples are pelleted to remove interstitial adipose and other debris. Satellite cells are then isolated by unique cell surface-marker expression and satellite stem cells and committed satellite cells are isolated by labelling of Myf5. We use a simplified 4 colour sorting strategy, with fluorescence-minus-one (FMO) controls and negative selection using violet excitable dyes thereby minimizing fluorescence compensation to effectively isolate satellite cells. Antibody clones and concentrations are provided in **step 20** and in the reagents section. Cell sorting knowledge or assistance by a FACS operator is recommended to establish gating and validate sort purity (Figure 22). Researchers adopting alternate reporter system or selection markers may have to optimize their gating, however, this strategy is adaptable for most commercial cell sorters. Isolated satellite stem cells and committed satellite cells are fractioned, where known cell quantities are treated with a gene or pharmacological intervention or control. As cells rapidly lose self-renewal capacity in culture[244,245], a fraction of isolated cells is cultured *in vitro* to establish lines of committed myogenic progenitors from the same donor to assess satellite cell-specific effects of treatment on engraftment. Researchers may leverage this paradigm to explore pathways promoting engraftment and self-renewal following in vitro expansion of myogenic progenitors[88,89]. We advise that transplants are conducted using a single donor

for control or treated cells for each replicate to reduce the effect of genetic influences on causative outcomes in satellite stem cells, committed satellite cells and myogenic progenitors. Immediately prior to transplantation, a subset of treated cells is isolated to assess cell viability and an expedited immunofluorescence protocol is used to validate cell purity (Figure 22, Figure S14). It is critical to assess the sorting purity, cell viability and identity prior to transplantation to accurately determine their effect on cell lineage following transplantation and to avoid transplanting low purity or non-viable cells.

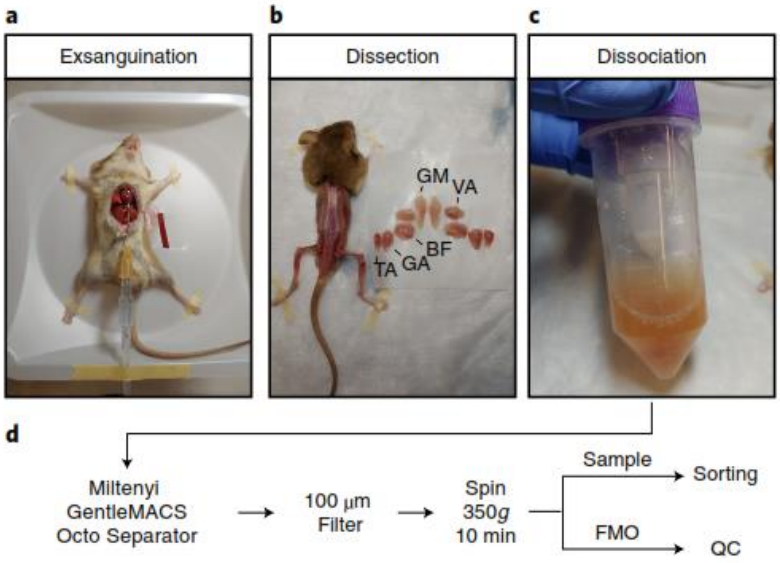


Figure 21: **Muscle stem cell isolation from hindlimb muscle.** a, Mice are mounted to a platform suspended over a collection vessel after euthanasia, and the thoracic cavity is exposed for cardiac perfusion. A 25G syringe is inserted into the left ventricle, and the right atria are perforated to allow exsanguination with isotonic saline. b, A transverse incision is made in the skin, and the mouse is degloved to expose the muscles of the hindlimb. TA (*Tibialis Anterior*), GA (gastrocnemius), BF (bicep femoris), GM (gluteus medius) and VA (vastus lateralis) are dissected. c, The muscle is placed into 5-ml of digestion buffer and minced into a rough slurry using clean scissors. d, The sample is then loaded onto the Miltenyi GentleMACS Octo Separator and dissociated with heating. Samples are filtered and pelleted prior to labelling for cell sorting and quality control. Experimental protocols for mice used in this study were performed in accordance with the guidelines established by the University of Ottawa Animal Care Committee, which is based on the guidelines of the Canadian Council on Animal Care. QC, quality control.

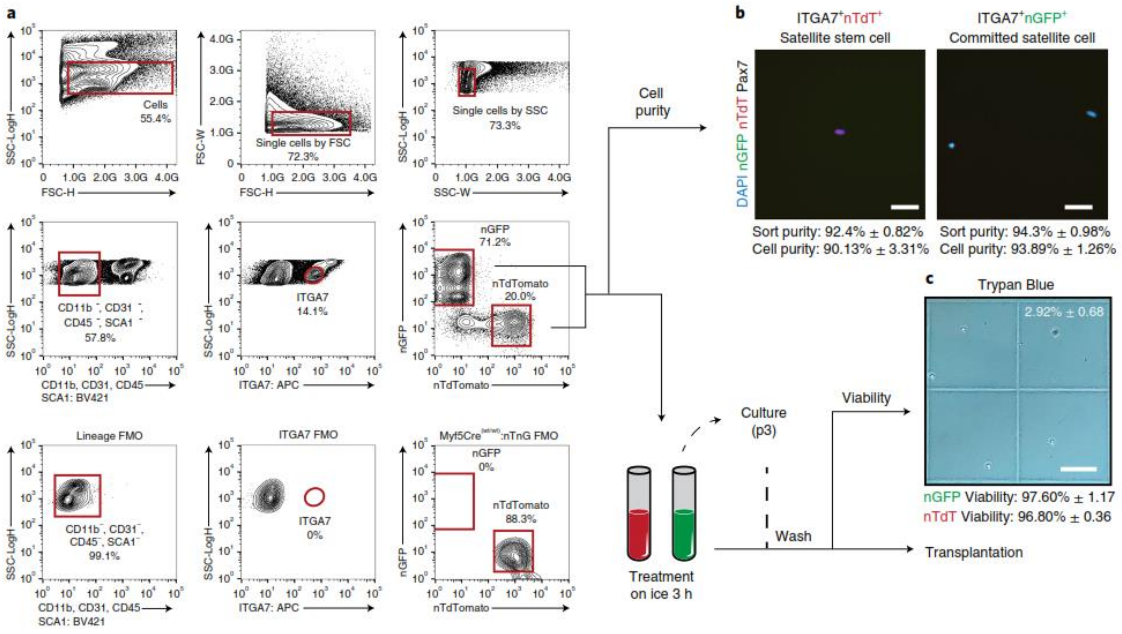


Figure 22: **Muscle stem cell lineage gating and quality control strategy.** a, Representative FACS plots generated on the MoFlo XPD and analyzed by FlowJo V10 for sequential gating of satellite stem cells and committed satellite cells. FMO controls are used to identify the true negative signal for a given marker and dictate gate placement. The percentage of each population in reference to the parent is shown. b, Representative immunofluorescence images of isolated satellite stem cells and committed satellite cells pelleted onto cytospin slides and stained for the satellite cell marker Pax7 and either nTdTomato or nGFP to identify stem or progenitor lineages. Average sort purity, measured as the percentage of events from re-sorted populations falling within the lineage gate, and average cell purity, measured as the percentage of cells from a given lineage over total counted cells, are given for each population. Blue, DAPI; green, nGFP; red, nTdTomato; white, Pax7. Scale bars, 25 µm. n = 3, mean ± s.d. c, Prior to cell transplantation, the viability of FACS sorted or cultured cells at passage 3 (p3) is measured by Trypan Blue staining, with the average percentage of Trypan Blue–positive cells given. Scale bar, 100 µm. n = 3, mean ± s.d. Experimental protocols for mice used in this study were performed in accordance with the guidelines established by the University of Ottawa Animal Care Committee, which is based on the guidelines of the Canadian Council on Animal Care.

***Satellite cell transplantation.*** Transplanting genetically labelled satellite cell populations into a non-labelled immunocompromised environment allows tracing of cell fate, where pharmacological or genetic interventions allow causative relationships on cell lineage to be developed. Transplantation into a newly injured muscle presents a regeneration context to isolated cells, similar to their isolation-induced activation state to maintain regenerative dynamics *in vivo*.

Treated cells are washed extensively to remove excess serum, drug or protein intervention and transplanted in minimal volume to improve retention and reduce cell leakage. When working with small volumes of concentrated cells, we advise an excess of cells are resuspended to reduce the risk of volume loss during transplantation and allow quantification of remaining cells. Cells are transplanted with sterile Hamilton syringes using a “micro-deposition” protocol (outlined in steps 46-50, Figure 23) which improves transplantation efficiency by depositing small volumes of cells within the tissue and reduces cell leakage by decreasing volumes along the main needle tract. Exact numbers of transplanted cells are easily assessed by counting the number of cells in the remaining cell suspension following transplantation. Minimal cell leakage along with the discrete assessment of numbers of grafted cells allows robust quantification of engraftment efficiency. Grafts are allowed to regenerate for 9 days, which represents an early regenerative timepoint where satellite cells have returned to the niche and engrafted myofibres are newly formed[8,10]. Grafts may be allowed to grow for extended time points to assess homeostatic stability of grafts, graft competitive advantage following re-injury or physiological improvements in grafted tissues. We recommend the use of NSG mice over immunosuppression to reduce experimental variables and inter-mouse transplant variability.

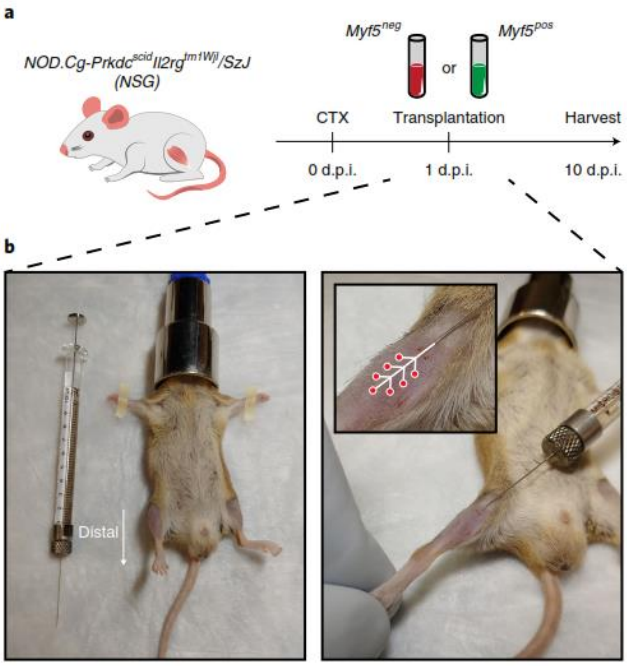


Figure 23: **Microdeposition of muscle stem cells into recipient muscle.** a, Overview of the transplantation timeline into cardiotoxin (CTX) injured NSG mice. b, Mice are anesthetized with isoflurane, and the hindlimbs are shaved using sterile clippers. The foot is positioned to place the *Tibialis Anterior* muscle under stretch and parallel to the working surface facing upward. A 10-µl Hamilton syringe is used to deposit a sequential bolus of cells throughout the muscle to improve engraftment. Mice are monitored and allowed to recover for 10 d post-injury (d.p.i.). Experimental protocols for mice used in this study were performed in accordance with the guidelines established by the University of Ottawa Animal Care Committee, which is based on the guidelines of the Canadian Council on Animal Care.

***Tissue processing, staining and analysis.*** Careful analysis of grafted tissue is required to reduce analytical biases and robustly assess fate decisions in transplanted cells. Skeletal muscle is a dense tissue containing multiple cell types including adipocytes, interstitial cells, immune cells, nerves, connective tissue, muscle fibres and satellite cells. Skeletal muscle has a high level of autofluorescence, including lipofuscin granules, requiring careful preparation to improve the immunofluorescence signal. Lipofuscin is an accumulation of indigestible lipid and oxidized macromolecules. In post-mitotic cells, lipofuscin accumulates due to poor exocytotic clearance[253] and is present within muscle interstitium as a by-product of injury. Careful blocking using lipofuscin quenchers can critically improve imaging of endogenous markers and reduce autofluorescent tissue artifacts by blocking lipofuscin emission in the green to far-red channels (Figure S15). Critically, some non-membrane or nuclear bound genetic reporter systems result in soluble fluorescent reporters contained within the cytoplasm. As mature muscle fibres share cytoplasmic contents, sectioning non-perfusion fixed samples results in loss of the

genetic reporter upon incubation with aqueous buffer, limiting experimental validity. Perfusion fixation of transplanted animals maintains endogenous protein localization, reduces background by removing blood and immune cells from tissues and improves antigenicity of target proteins. Blocking with monovalent anti-mouse FAB fragments improves antigenicity of mouse-on-mouse antibody labelling by reducing non-specific binding of secondary antibodies to endogenous mouse IgG by pre-occupying sites with the FAB fragment. Blocking electrostatic interactions on tissue sections with Image-iT FX signal enhancer help reduce non-specific background staining from secondary antibodies harbouring excess charge. These steps are critical to reduce the non-specific reactivity of secondary antibodies and improve image quality. Careful analysis and experimental planning are critical to robustly assess differences in transplanted cell fates. It is important to reduce experimental degrees of freedom to minimize experimental variability. Timelines should be strictly maintained from recipient injury to transplantation in order to reduce environmental influences between animals. Tissue processing and sectioning for analysis should be equivalent across tissues, where ideally the whole transplanted tissue is analyzed (see troubleshooting, Figure 24), and sequential sections are averaged to reduce variability in graft location. Researchers should aim to report absolute numbers of engrafted cells and present representative images of whole muscle sections to improve transparency in data reporting. Adherence to this protocol will allow robust analysis of the role of an experimental intervention on stem cell fate.

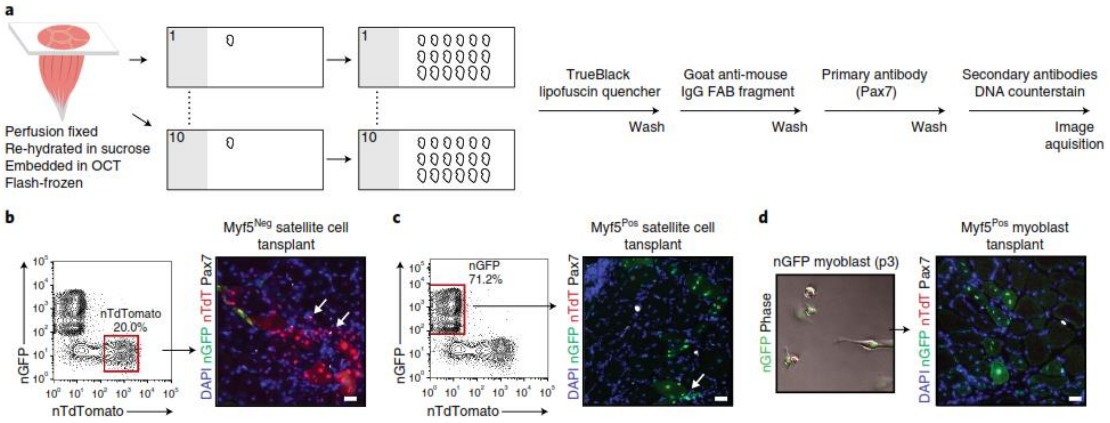


Figure 24: **Graft processing and immunohistochemistry strategy.** a, Overview of the processing strategy to obtain slides with sufficient histological coverage to analyze cell engraftment and processing steps for imaging. Lipofuscin quenching is critical for robust analysis of engrafted cells. b–d, Representative immunofluorescence images of transplants from satellite stem cells, committed satellite cells and cultured myoblasts. White arrows denote engrafted satellite cells. Blue, DAPI; green, nGFP; red, nTdTomato; white, Pax7. Scale bars, 50 µm. Experimental protocols for mice used in this study were performed in accordance with the guidelines established by the University of Ottawa Animal Care Committee, which is based on the guidelines of the Canadian Council on Animal Care.

## METHODS
## REAGENTS

Mice: ♂/♀ Myf5-Cre/R26R-nTnG mice were F1 progeny from Myf5-Cre x R26R-nTnG breeding pairs (B6.129S4-Myf5$^{tm3(cre)Sor}$/J (Myf5-cre) (JAX, Cat. no. 007893) and B6;129S6-Gt(ROSA)26Sor$^{tm1(CAG-tdTomato*,-EGFP*)Ees}$/J (R26R-nTnG) (JAX, Cat. no. 023035)). The isolation of muscle stem cells was performed on 8wk Myf5-Cre:nTnG mice, however, the isolation is amenable to any mouse strain with possible changes to yields. ♂ NOD.*Cg-Prkdc$^{scid}$Il2rg$^{tm1Wjl}$*/SzJ (JAX, cat no. 005557) mice aged 8-12 weeks were used as recipients in all cases, and transplantation is recommended using fluorescently labelled cells to identify host vs donor cells. **!CAUTION** Experiments involving live animals must conform to **appropriate international, national and institutional regulatory board guidelines.** Housing, husbandry and all experimental protocols for mice used in this study were performed in accordance with the guidelines established by the University of Ottawa

Animal Care Committee, which is based on the guidelines of the Canadian Council on Animal Care.

- FBS (Fisher, Cat. no. SH30396)
- EDTA (Thermo, Cat. no. 17892)
- Sodium Pentobarbital **!CAUTION** Sodium pentobarbital is a potent barbiturate and should be handled with care. The use and purchase of Sodium pentobarbital must conform with appropriate regulatory guidelines.
- Chlorohexidine 2%
- Ham's-F10 media (Wisent, Cat. no. 318-051-CL)
- Collagenase B powder (Sigma, Cat. no. 11088831001)
- Dispase II powder (Sigma, Cat. no. 04942078001)
- Round bottom polystyrene tubes (Fisher, Cat. no. 14-959-1A)
- Mouse anti-Pax7 (DSHB, Cat. no. Ab528428; RRID: AB_528428)
- Goat anti-mouse IgG FAB fragments (Jackson Immuno, Cat. no. 115-007-003)
- Rat anti-CD11b-BV421 (Becton Dickinson, Cat. no. 562605; RRID: AB_2740930)
- Rat anti-CD31-BV421(Becton Dickinson, Cat. no. 562939; RRID: AB_2665476)
- Rat anti-CD45-BV421 (Becton Dickinson, Cat. no. 563890; RRID: AB_2651151)
- Rat anti-SCA1-BV421 (Becton Dickinson, Cat. no. 562729; RRID: AB_2737750)
- Mouse anti-Integrin-a7-APC (Miltenyi, Cat. no. 130-102-716; RRID: AB_2652464)
- Cardiotoxin Gamma from Naja pallida (Cedarlane, Cat. no. L8102) **!CAUTION** Cardiotoxin is a myotoxin and should be handled with care. Protect the eyes and skin by wearing gloves and working in a biosafety hood.
- Trypan Blue (Sigma, Cat. no. T8154)
- 1% penicillin-streptomycin (Wisent, Cat. no. 450-201-EL)
- bFGF, 5ng/ml (Fisher, Cat. no. GF003AFMG)

- Collagen (VWR, Cat. no. CACB354236)
- Hamilton 10ul syringe (Hamilton, Cat. no. 7635-01)
- Hamilton 28g needle 30° angle, tip type 4 (Hamilton, Cat. no. 7803-02)
- Insulin syringe (Fisher, Cat. no. 36-104-1352)
- Perfusion pump (Boading Shenchen Precision Pump, Cat. no. LabV1/MC4(10))
- PFA powder (Sigma, Cat. no. p6148)
- Sucrose (Fisher, Cat. no. S5-500)
- OCT compound (VWR, Cat. no. 25608-930)
- Isopentane (Fisher, Cat. no. O35514)
- Triton X-100 (Sigma, Cat. no. T8787)
- Glycine (Fisher, Cat. no. BP3815)
- Donkey Serum (Sigma, Cat. no. S30)
- TrueBlack Lipofuscin autofluorescence quencher (Biotium, Cat. no. 23007)
- Image-iT FX signal enhancer (Fisher, Cat. no. I36933)
- Vectashield (Vector Labs, Cat. no. H-1400)

**EQUIPMENT**

- 30um cell strainer (Miltenyi, Cat. no. 130-041-407)
- Shandon Double Cytoslides (Fisher, Cat. no. 5991055)
- Shandon Double Cytofunnel (Fisher, Cat. no. 5991039)
- Hydrophobic pen (Vector labs, Cat. no. H-4000)
- 100um cell strainer (Fisher, Cat. no. 22363549)
- 1.5ml tubes (Beckman Coulter, Cat. no. 357448)
- 15ml conical centrifuge tubes (Falcon, Cat. no. 352098)
- 50ml conical centrifuge tubes (Falcon, Cat. no. 352098)

- 5ml round-bottom tubes (Becton Dickinson, Cat. no. 352063)
- GentleMACS Octo separator (Miltenyi, Model. no. 130-095-937)
- GentleMACS C Tubes (Miltenyi, Cat. no. 130-096-334)
- Floor model centrifuge with a rotor (Thermo Fisher, Cat. no. 75004509)
- CytoSpin centrifuge (Thermo Fisher, Cat. no. A78300003)
- Flow cytometer (Beckman Coulter, Model. no. MoFlo XPD)

**REAGENT SETUP**

**Cell-culture media:** Cell culture media contains 20% (vol/vol) FBS, 1% (vol/vol) penicillin-streptomycin and 5ng/ml bFGF in Ham's F-10 media. Store media up to 1 month at 4°C.

**Cell-suspension buffer**: Cell suspension buffer contains 10% (vol/vol) FBS, and 3mM EDTA in PBS. Adjust pH to 7.4. Filter the buffer through a 0.22um pore sized membrane. Store at 4°C for up to 1 week.

**Cell-treatment buffer**: Cell treatment buffer contains 10% (vol/vol) FBS, and 1mM EDTA in Ham's-F10 media. Adjust pH to 7.4. Filter the buffer through a 0.22um pore sized membrane. Store at 4°C for up to 1 week.

**Digestion buffer**: Digestion buffer contains 10g/l collagenase B and 4g/l dispase I in Hams F-10 media. Adjust pH to 7.4. Filter the buffer through a 0.22um pore sized membrane. Store buffer up to 1 week at 4°C or freeze for up to 2 months.

**Cardiotoxin solution**: Cardiotoxin solution contains 10uM cardiotoxin dissolved in saline. **CRITICAL** Make fresh prior to use.

**Blocking buffer**: Blocking buffer contains 5% (vol/vol) normal donkey serum in phosphate-buffered saline. Filter buffer through 0.22-um pore sized membrane. Store at 4°C for up to 1 week.

**Sucrose gradient**: Sucrose gradient contains alternating 10% (wt/vol), 20% (wt/vol) and 30% (wt/vol) sucrose in PBS. Layer 5ml of each solution into a 15ml conical centrifuge tube using a wide bore pipette. Store gradients on a non-vibrating work surface at 4°C and use within 2 days.

**Perfusion fixative**: Perfusion fixative contains 4% PFA (wt/vol) in PBS. Heat to 60°C and adjust pH to 7.4. Filter buffer through 0.22-um pore sized membrane. Store at 4°C and use within 3 weeks.

## EQUIPMENT SETUP

MoFlo XPD Sorter setup

| Fluorophore | Laser (nm) | Filter (nm) |
|---|---|---|
| BV421 | 405 | 450/65 |
| GFP | 488 | 530/40 |
| TdTomato | 561 | 580/30 |
| APC | 640 | 670/40 |

## PROCEDURE

### Injury of transplant recipient muscle (TIMING 30min)

**1|** Acquire a suitable number of 8-week old *NOD.Cg-Prkdc$^{scid}$Il2rg$^{tm1Wjl}$/SzJ* (NSG) or equivalent immunocompromised mice to be recipients for satellite cell transplants.

**2|** In a sterile environment, anesthetize a mouse using isoflurane (1L/min, 2% isoflurane) until recumbent and non-reflexive to gentle pressure on the toes. Provide subcutaneous 0.1mg/kg buprenorphine or similar analgesia as required by the institutional animal oversight committee.

**3|** With the mouse supine, shave the hindlimb of the mouse and clean with chlorohexidine.

**4|** Holding the foot parallel to the work surface, inject 35ul cardiotoxin solution distal to the kneecap ~2mm into the *Tibialis Anterior* muscle of both legs.

**5|** Allow animals to recover and monitor for 24h providing 0.1mg/kg buprenorphine as required or similar analgesia as approved by the institutional animal oversight committee.

**Mouse donor muscle dissection (TIMING 40min)**

**6|** Acquire a suitable number of 8-week old *Myf5-cre/R26R-nTnG* or equivalent for adult satellite cell isolation.

**!CRITICAL STEP** A single 8-week old mouse is sufficient to acquire enough cells for two satellite stem cell transplants (10 000 cells per transplant) and enough cells for up to 7 committed satellite cell transplants (10 000 cells per transplant). Sorted satellite cells can be cultured to yield enough cells for multiple myoblast transplants (100 000 cells per transplant).

**7|** Euthanize by intra-peritoneal Sodium Pentobarbital injection (200mg/kg) and monitor until recumbent and non-reflexive to gentle pressure on the toes.

**!CRITICAL STEP** This is done one day after injection of cardiotoxin into recipient NSG mice.

**8|** Surgically open the thoracic cavity and exsanguinate by perfusing 30ml of cold isotonic saline at a rate of 5ml per minute into the left ventricle.

**!CRITICAL STEP** Perfusion of saline removes red blood cells and immune cells from excised tissue, improving flow cytometry speeds and cell viability by reducing the need for red blood cell lysis.

**9|** Using scissors, cut the skin perpendicular to the midline around the abdomen and de-glove the skin. Anatomical images to aid dissection can be found in Figure 21.

**10|** Using scissors, remove the skeletal muscle of the hindlimb, and place it on ice in a dish with cold PBS.

**11|** Remove all non-skeletal muscle tissue in the dish using scissors.

**Tissue dissociation (TIMING 30min)**

**12|** Transfer skeletal muscle tissue into a Miltenyi GentleMACS C tube and add 5ml of digestion buffer.

**13|** Using scissors, mince tissue for 30 seconds until a rough slurry.

**14|** Mount the tubes to the Miltenyi GentleMACS Octo Separator and run the following: Temp ON 37°C, 90rpm 5min, -90rpm 5min, loop 10x (360rpm 5s, -360rpm 5s), 90rpm 5min, -90rpm 5min, end.

**15|** Transfer Miltenyi GentleMACS C tubes to a sterile hood and add 5ml FBS to inhibit over-digestion

**16|** Collect the digests in a 50ml conical centrifuge tube through a 100-um pore membrane.

**17|** Wash the membrane with 20ml cell-suspension buffer and aliquot filtrates to three 15ml conical centrifuge tubes

**!CRITICAL STEP** recovery of satellite cells is greater in 15ml tubes and will improve yields.

**18|** Centrifuge 10min 350*g* for 10min at 4°C. Aspirate the supernatant and resuspend the pellet in 500ul of cold cell suspension buffer on ice.

**Antibody staining (TIMING 25min)**

**19|** Transfer 10ul of the cell suspension to 5 Fluorescence-minus-one (FMO) control tubes containing 160ul cell suspension buffer on ice.

**20|** Stain the FMO controls and experimental samples based on the below table for 10min on ice in the dark.

| Antibody | Clone | Fluorophore | Concentration |
|---|---|---|---|
| Anti-Cd11b | M1/70 | BV421 | 1:500 |
| Anti-CD31 | MEC 13.3 | BV421 | 1:500 |
| Anti-CD45 | 30-F11 | BV421 | 1:500 |
| Anti-Sca1 | D7 | BV421 | 1:500 |
| Anti-Integrin-α7 | 3C12 | APC | 1:100 |

**21|** Wash samples in 10ml cell suspension buffer.

**22|** Centrifuge tubes at *350g* for 10 min at 4°C and resuspend the pellet in 1ml cell suspension buffer.

**23|** Collect the cells in 5ml round bottom tubes through a 30um pore membrane, washing the membrane with an additional 3ml of cold cell suspension buffer on ice.

**Flow Cytometry (TIMING 30 min per mouse)**

**24|** Using a 70-um nozzle, calculate drop-delay, adjust stream alignment and maintain the collection stage at 4°C for your machine.

**25|** Run the FMO samples to establish the gating strategy required for sorting. Generate the following plots for optimal gating: (i) SSC-LogH versus FSC-H to select single cells, (ii) FSC-W versus FSC-H to isolate single cells by FSC, (iii) SSC-LogH versus SSC-W to isolate single cells by SSC, (iv) SSC-LogH versus BV421 to select BV421

negative cells, (v) SSC-logH versus APC to select satellite cells, (vi) GFP-LogH versus TdTomato-LogH to select TdTomato positive satellite stem cells and GFP positive committed satellite cells. Examples of typical cytometry plots are shown in **Figure 22.** Expected yields are shown in Table 1.

**?Troubleshooting**

**26|** Sort desired cells into 200ul cell suspension buffer in FBS coated tubes on 'purity' setting.

**27|** Resuspend 5ul of sorted cells in 500ul cell suspension buffer in a round bottom tube and re-sort to analyze sort purity.

**28|** Centrifuge sorted cells at *350g* for 10min at 4°C and resuspend in 200ul cell-suspension buffer.

**Pharmacological intervention and quality control (optional) (TIMING 3h)**

**29|** Aliquot cell suspensions into desired fractions for drug or protein treatment, respective controls as well as cell culture for myogenic progenitors.

**!CRITICAL STEP** In-donor controls are suggested by treating cells from one donor with the intervention of interest or control to minimize biological variability in donor-derived cells. Experiments should be planned with a minimum of 3 cell donors and recipients as required.

Treatment uptake should be empirically tested prior to proceeding.

**30|** Culture donor-derived cells on collagen-coated dishes in cell-culture media to establish lines of myogenic progenitors for treatment and transplantation at a later date.

**31|** Add protein or drug to cell suspensions and maintain on ice for 3h with frequent agitation. **!CRITICAL STEP** Dosage of protein or drug of interest should be previously validated in primary cell culture.

**!PAUSE POINT** 3h during incubation if not proceeding with quality control staining described in steps 32 - 42.

**32|** Dilute 10ul aliquots from each initial donor into 100ul and load into assembled Double Cytoslide and Double Cytofunnel.

**33|** Centrifuge the Cytoslide in a Cytospin centrifuge 55g *(700r.p.m.)* for 10min at medium acceleration.

**!CRITICAL STEP** Cytoslides allow for centrifugation of cells onto slides to allow adherence without culturing.

**34|** Add 100ul pre-warmed perfusion fixative for 8min.

**35|** Wash with 100ul PBS containing 0.1% Triton-X100 (vol/vol) and 125mM Glycine for 5min, twice.

**36|** Add 10ug Goat anti-mouse IgG Fab Fragments in 100ul PBS to each sample for 10min.

**37|** Remove buffer, add 100ul blocking buffer for 10min.

**38|** Remove buffer, add Pax7 primary antibody diluted 1:2 in 100ul blocking buffer for 45min.

**39|** Wash in 500ul blocking buffer for 5min, add 2 drops of Image iT-FX signal enhancer 5min

**40|** Remove buffer, add secondary antibodies diluted 1:1000 in 100ul blocking buffer for 30min.

**41|** Wash in 500ul DAPI for 5min, twice.

**42|** Image and quantify cell purity.

**?Troubleshooting**

**Transplantation and micro-deposition (TIMING 1h)**

**43|** Aliquot a small quantity of cells from step 31 for Trypan Blue staining to assess the viability and concurrently centrifuge total cell fractions from step 31 at *350g* for 10min at 4°C and resuspend the cell pellet in 10ul cold saline per 10,000 cells.

**44|** In a sterile environment, anesthetize a previously injured NSG mouse (from step 5) using isoflurane (1L/min, 2% isoflurane) until recumbent and non-reflexive to gentle pressure on the toes.

**45|** With mouse supine, clean the Hindlimb with chlorohexidine.

**46|** Draw 10ul of cell suspension into a sterile 10ul Hamilton syringe with a 28g needle.

**47|** Holding the foot parallel to the work surface, position the tip of the syringe immediately distal to the kneecap and move the needle ~3mm into the *Tibialis Anterior* muscle angled slightly dorsally to reach the center of the muscle.

**48|** Depress the Hamilton syringe to deposit 4ul of cell suspension.

**49|** Gently remove the Hamilton 1/5$^{th}$ of the injection depth, angle slightly caudally, depresses 1ul, move the tip back to midline and angle slightly dorsally, depress 1ul. Repeat until 2/5$^{th}$ injection depth remains. Anatomical images to aid micro-deposition can be found in Figure 23.

**!CRITICAL STEP** Micro-deposition of cells significantly improves cell survival, engraftment and reduces cell leakage compared to injecting a single cell bolus.

**?Troubleshooting**

**50|** Slowly remove the needle over a span of 5-10 seconds to prevent cell leakage.

**51|** Inject contralateral limb with control-treated cells following the above methodology.

**52|** Allow animals to recover and monitor for 24h providing 0.1mg/kg buprenorphine as required or similar analgesia as approved by the institutional animal oversight committee.

**53|** Allow tissue regeneration of 9-21 days or longer as required.

**Transplant analysis and processing (TIMING 5 days)**

**54|** Euthanize transplant recipient mice by intra-peritoneal Sodium Pentobarbital injection (200mg/kg) and monitor until recumbent and non-reflexive to gentle pressure on the toes.

**55|** Exsanguinate by perfusing 30ml of cold isotonic saline followed by 30ml cold perfusion fixative at a rate of 5ml per minute.

**56|** Using scissors, cut the skin around the ankles and remove fur to expose the *Tibialis Anterior* muscle.

**57|** Using scissors, remove the *Tibialis Anterior* muscle and place in cold perfusion fixative diluted 1:10 in 10ml of PBS for 12h at 4°C.

**!CRITICAL STEP** fixation times in 0.4% PFA are critical and should not be circumvented or extended.

**58|** Place transplanted *Tibialis Anterior* muscles into individual sucrose gradients and allow the tissue to sink at 4°C, this usually takes 24h.

**59|** Submerge tissues in OCT compound in small tinfoil cups and freeze in liquid nitrogen-cooled isopentane.

**!PAUSE POINT** Samples can be stored long term (>1yr) at -80°C in a frost-free freezer.

**60|** Cut cross-sections of tissue in a cryostat at 20um depth placing sequential tissues on 10 slides and repeating until the tissue is processed. Images to aid in processing can be found in Figure 24.

**!CRITICAL STEP** Each slide will contain 20-30 sections across the tissue and represent a 200um resolution within the tissue to reduce variability in graft location.

**61|** Outline slides with hydrophobic pen and wash in excess PBS.

**62|** Wash slides with 0.4% Triton-X100 (vol/vol) and 125mM Glycine for 10min.

**63|** Wash slides extensively in PBS until no trace of detergent remains.

**!CRITICAL STEP** All detergent must be washed from the slide prior to proceeding

**64|** Dilute TrueBlack reagent 1:20 in 70% ethanol as per manufacturers' suggestion and add 100ul per slide with gentle rocking for 1min.

**!CRITICAL STEP** Detergents should not be used in the following steps.

**65|** Wash slides extensively in PBS until no hydrophobicity is apparent.

**66|** Add 10ug Goat anti-mouse IgG Fab Fragments in 200ul PBS to each sample for 30min, wash slides in excess PBS.

**67|** Remove buffer, add 200ul blocking buffer for 1h, wash slides in excess PBS.

**68|** Remove buffer, add Pax7 primary antibody diluted 1:4 in 200ul blocking buffer for 1h-overnight at 4°C.

**69|** Wash slides extensively in excess PBS.

**70|** Apply 4-5 drops of Image-iT FX signal enhancer for 10min, wash slides in excess PBS.

**71|** Add secondary antibodies diluted 1:1000 in 200ul blocking buffer for 1h.

**72|** Wash slides extensively in excess PBS.

**73|** Apply DAPI counterstain for 10min.

**74|** Aspirate most liquid from the slide and mount using Vectashield mounting media.

**75|** Image sections and quantify donor-derived satellite cells and myofibres, averaging counts over 5 consecutive sections.

**?Troubleshooting**

**Troubleshooting**

Table 1: **Transplantation troubleshooting guidance**

| Step | Problem | Possible reason | Possible solution |
|---|---|---|---|
| 25 | Red blood cells present in samples | (i) Inefficient or no exsanguination | (i) Incubate pellet in 2ml Versalyse (Beckman, Cat. no. A09777) to lyse red blood cells |

| | | | |
|---|---|---|---|
| | | | (ii) Slower sorts speeds should be used to reduce shear stress on cells<br>(iii) Ensure viability is tested in step 43 |
| 25 | Contaminating cell populations present | (i) Supernatant carryover from step 18 | (i) Gently overlay 10ml of buffer onto the pellet, do not resuspend and centrifuge for 5min at 350*g*, aspirate supernatant and continue |
| 25 | Poor cell yield | (i) Cell density is too high | (i) Dilute cells in cell suspension buffer to maintain adequate sorting efficiency |
| 42 | Poor target signal | (i) Prolonged fixation time<br>(ii) Excess antibody labelling for FACS<br>(iii) Poor cell purity<br>(iv) Inadequate liquid handling on CytoSpin slides | (i) Prepare fresh warm (37°C) fixative prior to proceeding<br>(ii) Reduce the concentration of FACS antibodies to balance gating and signal to noise in quality control<br>(iii) Ensure sort purity by resorting cells, ensure proper FACS gating using FMO controls<br>(iv) Ensure stained slides do not dry, wash with excess PBS as described |
| | Low cell purity after flow cytometry | (i) Improper drop delay for FACS<br>(ii) Use of different antibody clone | (i) Work with flow cytometry expert to establish drop delay and monitor throughout sorting<br>(ii) Ensure the antibodies listed in the reagents section are used |
| | Low cell viability | (i) Over-digestion<br>(ii) Excessive processing times<br>(iii) FACS differential pressure too high | (i) Batch to batch variability can change digestion times, ensure digests are processed until a fine slurry and immediately add FBS as directed<br>(ii) Cells should be transplanted as soon as possible; treatment timelines can be empirically decreased as required<br>(iii) Maintain low differential pressures, if speeds are too low, decrease dilution volume in **step 23** |
| 47 | Difficulty transplanting cells | (i) Dull Hamilton syringe<br>(ii) Incision point too low or high on *Tibialis Anterior*<br>(iii) Incision depth is too deep | (i) Use new or sharpened needles<br>(ii) Depress the skin using sterile tools to identify the edge of the kneecap as reference<br>(iii) Prior to autoclaving, mark Hamilton needles at 1mm intervals as a guide |
| 75 | No graft 10 days post-transplantation | (i) Cell leakage during transplantation<br>(ii) Too few cells transplanted<br>(iii) Poor perfusion fixation<br>(iv) Cells did not pass quality control<br>(v) Aged donor satellite cells | (i) Remove syringes slowly from tissue and observe for leakage following transplant<br>(ii) Harvest more hindlimb muscle, validate cell numbers prior to transplant and quantify cell quantity in residual cell suspensions following transplant<br>(iii) Prepare fresh fixative and ensure efficient perfusion by observing pallor in the hindlimb<br>(iv) Ensure cells are viable and pure as per instruction, assess viability in cultured myogenic progenitors<br>(v) Ensure satellite cells are harvested from ~8wk old donor mice |

| | | | |
|---|---|---|---|
| | Variability in graft efficiency | (i) Incomplete sectioning of transplanted tissue<br>(ii) Excessive or inadequate host injury | (i) Transplanted tissues must be completely sectioned to identify graft location.<br>(ii) Confirm adequate injury by observing centrally located nuclei in host tissue and ensure all tools are autoclaved prior to use to avoid surgical infections |

**RESULTS**

An average 8wk mouse should yield roughly 1.71g ± 0.021 (n=3) of hindlimb muscle and roughly 100 000 total sorted satellite cells (Table 1). Aged donors yield significantly less satellite cells[174]. Isolated cells should be viable, and consistently pure (Figure 22) as measured by the proportion of trypan blue negative cells and cell identity by immunofluorescence. Cell viability should be above 95% (average Trypan Blue negative 97.2**%** ±0.56, n=3), sort purity above 90% and cell purity above 90%. If viability is below 80% use **?Troubleshooting** guidance to improve viability. Some carryover of FACS labelling is possible during quality control, we recommend Pax7 as a purity marker due to its specificity and nuclear localization. Expected purity values, representative images and yields can be found in Figure 22, Table 1 and Figure S14. Gating for sorting should always be based on FMO controls. Researchers exploring cell type-specific FACS panels should empirically validate staining and saturation using FMO and genetic controls.

Successful grafts should span an area of 0.5-1mm in length within the muscle and typically there is a normal distribution of cells within the graft. It is important to analyze and average counts from at least 5 consecutive sections (spaced ~200um apart as per Figure 24) within the belly of the graft in order to reduce biases in graft location and random sampling biases. Reporting absolute numbers of engrafted cells helps reduce data ambiguity and presenting images of whole muscle sections improves transparency and allows researchers to objectively assess graft efficiency. Careful treatment of sections and adequate blocking (Figure 24**,** Figure S15) is critical to avoid interpreting endogenous

artifacts as transplanted cells. Host myofibres should contain centrally located nuclei due to injury, whereas grafted cells should contribute to both the satellite cell pool and the central myonuclei participating in the repair process. A quantification of graft efficiency has been previously published[101]. Briefly, transplanted satellite stem cells (nTdTomato+ sorted satellite cells) resulted in augmentation of the stem cell pool and gave rise to both nTdTomato satellite cells and nGFP satellite cells, while transplantation of myogenic satellite cells resulted in augmented myogenic commitment (nGFP+ sorted satellite cells). Transplanted cultured myoblasts are less prolific that satellite cells and require a 10-fold higher number for transplantation which results in contribution exclusively to the myonuclei (Pax7 negative). Analyzing the number and flux of nTdT satellite cells to nGFP satellite cells and myonuclei post-transplantation enables evaluation of self-renewal, satellite cell commitment and terminal differentiation respectively. Transplantation of treated cultured myoblasts can be used as an internal control to evaluate if the treatment of interest is satellite cell-specific. Grafts can be analyzed at 10 days post-injury for rapid assessment of cell lineage or allowed to regenerate for 30 days or longer to see physiological effects on measurements of isometric muscle force. Grafts can be re-injured following **steps 1-5** in order to observe the competitive advantage of grafted cells or the repopulation potential of the cell to generate satellite cells and myonuclei.

## Manuscript IV: Muscle regeneration is impaired in the *mdx* mouse

AUTHORS: Caroline E. Brun[1,2*], **Peter Feige[1,2*],** Marie-Claude Sincennes[1,2], Michael A. Rudnicki[1,2,3,4]

AUTHOR AFFILIATION: 1. Sprott Center for Stem Cell Research, Ottawa Hospital Research Institute, Regenerative Medicine Program, Ottawa, ON, Canada. 2. Department of Cellular and Molecular Medicine, Faculty of Medicine, University of Ottawa, Ottawa, ON, Canada. 3. Department of Medicine, Faculty of Medicine, University of Ottawa, Ottawa, ON, Canada. * These authors contributed equally.

**This manuscript is in preparation for Nature Communications**.

### AUTHOR CONTRIBUTION:

C.B. and M.A.R. conceptualized the study. C.B. and P.F. conceptualized experimental design. P.F. optimized and performed all *in situ* force measurements. P.F. performed all chemical histological staining. C.B. and P.F. performed all immunofluorescence staining. P.F. performed minimum fibre Feret analysis and analysis of collagen deposition. C.B. and P.F. performed all quantitative and statistical analyses. M.C.S. performed RNA sequencing and quality control and P.F. performed g:Profiler analysis. P.F. wrote the initial draft. M.A.R. oversaw the experimental design, analysis of results, manuscript editing, and financial support.

**HIGHLIGHTS**

- Dystrophin loss leads to increased muscle fibre number following injury
- Gross morphological changes compensate for the loss of physiological muscle strength in *mdx* mice
- Satellite cell hyperplasia becomes reduced with repetitive injury and age
- Delays in *mdx* muscle regeneration contribute to impaired repair

**eTOC blurb**

Brun et al., thoroughly evaluate the *mdx* mouse model of Duchenne's Muscular Dystrophy and the regenerative consequence of dystrophin loss in acute injury, repetitive injury and age. Mice lacking Dystrophin have increased myofibre numbers, reduced myofibre calibre, delayed satellite cell activation and decreased muscle-specific force with injury and ageing.

**ABSTRACT**

Duchenne's muscular dystrophy (DMD) is characterized by progressive muscle wasting and limitation of life in affected patients. DMD is commonly modelled using the *mdx* mouse model. In this study, we document dystrophic disease progression in *mdx* mouse skeletal muscle focusing on the *tibialis anterior* and the *diaphragm* muscle. We find *mdx* skeletal muscle undergoes progressive changes with age and in response to injury resulting in a compensatory increase in myofibre number with a concomitant loss in muscle stem cells, reduction in myofibre calibre and impaired physiological force. We provide evidence that delays in regeneration in dystrophin-deficient satellite cells contribute to *mdx* disease progression. This study highlights the impact of dystrophin-deficiency in satellite cells on disease progression in *mdx* mice and provides perspective for current and future studies targeting muscle repair in DMD.

## INTRODUCTION

Duchenne's Muscular Dystrophy (DMD) is a debilitating childhood muscle disorder characterized by progressive muscle wasting and death in the second decade of life[8]. DMD is the most common muscular dystrophy affecting 1:3600 male births and is caused by loss of function mutation in the dystrophin gene. The dystrophin protein acts to connect the extracellular matrix of the muscle to the myofibre cytoskeleton and helps guide muscle stem cell (satellite cell) polarity during stem cell commitment. In the absence of dystrophin protein, muscle fibre integrity is compromised[6] and satellite cell homeostasis is perturbed[7].

Muscle regeneration is facilitated by satellite cells that are normally quiescent and reside within the satellite cell niche between the basal lamina and myofibre sarcolemma[5]. Interactions between satellite cells and the niche maintain quiescence, where the loss of Notch[19] or Collagen V[20] expression from satellite cells results in impaired adhesion and precocious exit from quiescence. Additionally, the polarized satellite cell niche establishes internal cell polarity by spatially restricting cell fate determinants prior to mitotic division[5]. Following an apical-basal oriented cell division, polarized cell fate determinants facilitate divergent daughter cell fate through asymmetric chromatin remodelling[24], kinase activtity[25] and niche interactions[7,22,27]. The establishment of apical-basal polarity can impact the efficiency of myogenic progenitor production[5] where the loss of Par polarity complex localization in *mdx* satellite cells can impact muscle repair[7].

Previous studies have implicated impaired satellite cell function as a potential cause of disease progression in DMD as regeneration is impaired in patients despite increased satellite cell numbers[103,254]. Studies exploring telomere length in DMD suggest telomere shortening may be a contributing cause of disease progression, however, elevated satellite cell numbers would suggest satellite cell depletion is not a normal consequence[254,255]. Additionally, specific deletion of dystroglycan in mature mouse

myofibres does not recapitulate the entire *mdx* disease phenotype[14] and dystrophin expression in satellite cells facilitates internal cell polarity[7]. These studies implicate impaired satellite cell signalling and the production of myogenic progeny as a cause of DMD disease progression.

Satellite cells express high levels of dystrophin and dystroglycan which can be polarized to the basal surface of a subset of satellite cells prior to division to facilitate internal cell polarity[7,14]. Prior to an asymmetric division, dystrophin associates with Par1b, where in dystrophin-deficient satellite cells Par1b becomes downregulated resulting in loss of the PAR complex polarity and in turn impaired orientation of mitotic divisions[7]. Additionally, the methyltransferase Carm1 can bind the dystroglycan complex which limits its nuclear translocation in one daughter cell, where methylation of Pax7 epigenetically induces *Myf5* expression in the committed daughter cell[256]. The epigenetic changes occurring during asymmetric division facilitate satellite cell commitment and production of myogenic progeny where the loss of internal cell polarity in dystrophin-deficient satellite cells reduces the rate of asymmetric division, reduces the production of myogenic progenitors and delays muscle regeneration[5,7]. Additional epigenetic changes facilitating programmed cell death are required for clearance of a subset of presumably abnormal *mdx* satellite cells to facilitate muscle regeneration during dystrophy progression[257].

Improving regenerative outcomes in *mdx* disease progression can be facilitated by improving endogenous satellite cell-mediated repair by altering the balance of stem[10,87–90] and progenitor cells[101] in a given context. Our lab has recently shown that the intrinsic polarity defects in *mdx* satellite cells and decreased formation of myogenic progenitors[7] can be directly targeted to improve muscle repair[101]. Strategies targeting endogenous repair mechanisms in conjunction with gene-mediated therapeutics are an attractive combinatorial approach, able to target whole body muscle regeneration and theoretically

promote long term repair. Robust modelling of the DMD phenotype and understanding the underlying disease etiology is critical to translate research findings into the clinical arena. Multiple DMD animals have been developed from non-mammalian systems, small animal as well as large animal models which reflect varying disease phenotypes[102]. The *mdx* mouse remains widely used and has provided critical insight into the progression and treatment of DMD[7,99,103–105].

Here we provide insight into the physiological and histological consequence of dystrophin-deficiency in the *mdx* mouse and the role of satellite cell-intrinsic defects to this impaired repair process. We show impaired regeneration in *mdx* muscle results in increased myofibre number, reduced myofibre calibre, collagen deposition and impaired physiological force generation. Additionally, we observe hyperplasia in dystrophin-deficient satellite cells with a concomitant delay in myogenic differentiation in response to injury. This study provides strong evidence to support the role of impaired satellite cell-intrinsic mechanisms in the progression of DMD.

## RESULTS

### Progressive degeneration in *mdx* muscle impairs physiological force generation

We hypothesized that *mdx* muscle regeneration is impaired due in part by changes to intrinsic *mdx* satellite cell signalling with age. To address this aim, we assessed histological and physiological consequences of ageing in *mdx* mice from three to twelve months in age. Monitoring wildtype (WT) and *mdx* mouse weight gain during ageing revealed *mdx* mice maintain a 12%-34% reduced weight gain (Figure S16A) with a significant 30%-41% increase in *Tibialis Anterior* (TA) muscle mass (Figure S16B-C).

We monitored histological changes in muscle with age, where *mdx* TA muscle had apparently undergone progressive regeneration as indicated by myofibres with centrally located nuclei labelled with Hoechst (Figure 25A). Additionally, muscle cross-sections

stained with Laminin showed mixed myofibre hypertrophy and atrophy by twelve months in age (Figure 25A). Quantification of total myofibres per TA muscle shows a significant and progressive 9%-47% increase in myofibre number per aged *mdx* TA muscle compared to WT counterparts (Figure 25B). Increased myofibre numbers did not result in changes to the average minimum fibre Feret in aged *mdx* TA muscle (Figure 25C) however does represent a general leftward shift in minimum fibre Feret distribution suggesting a general reduction in myofibre calibre (Figure S16D). Additionally, staining of aged TA muscle from WT and *mdx* mice with Masson's Trichrome show a significant 1.7-4.9-fold increase in collagen deposition within whole TA cross-sections (Figure 25A, D). We did observe a significant increase in lipid deposition within *mdx* TA muscle, however at levels that are unlikely to have a functional consequence (Figure S16E-F).

To address the physiological consequences of increased myofibre number and collagen deposition in *mdx* TA muscle, we measured *in situ* physiological force in aged *mdx* TA muscle. Both WT and *mdx* mice maintained maximum tetanic force generation from 3 to 12 months in age (Figure 25E) however when normalizing to TA displacement volume, *mdx* mice show significantly 18%-38% decreased specific force with age compared to WT counterparts (Figure 25F, Figure S16G). Taken together this data reinforces that *mdx* mouse muscle undergoes progressive degeneration and regeneration that impair physiological force generation.

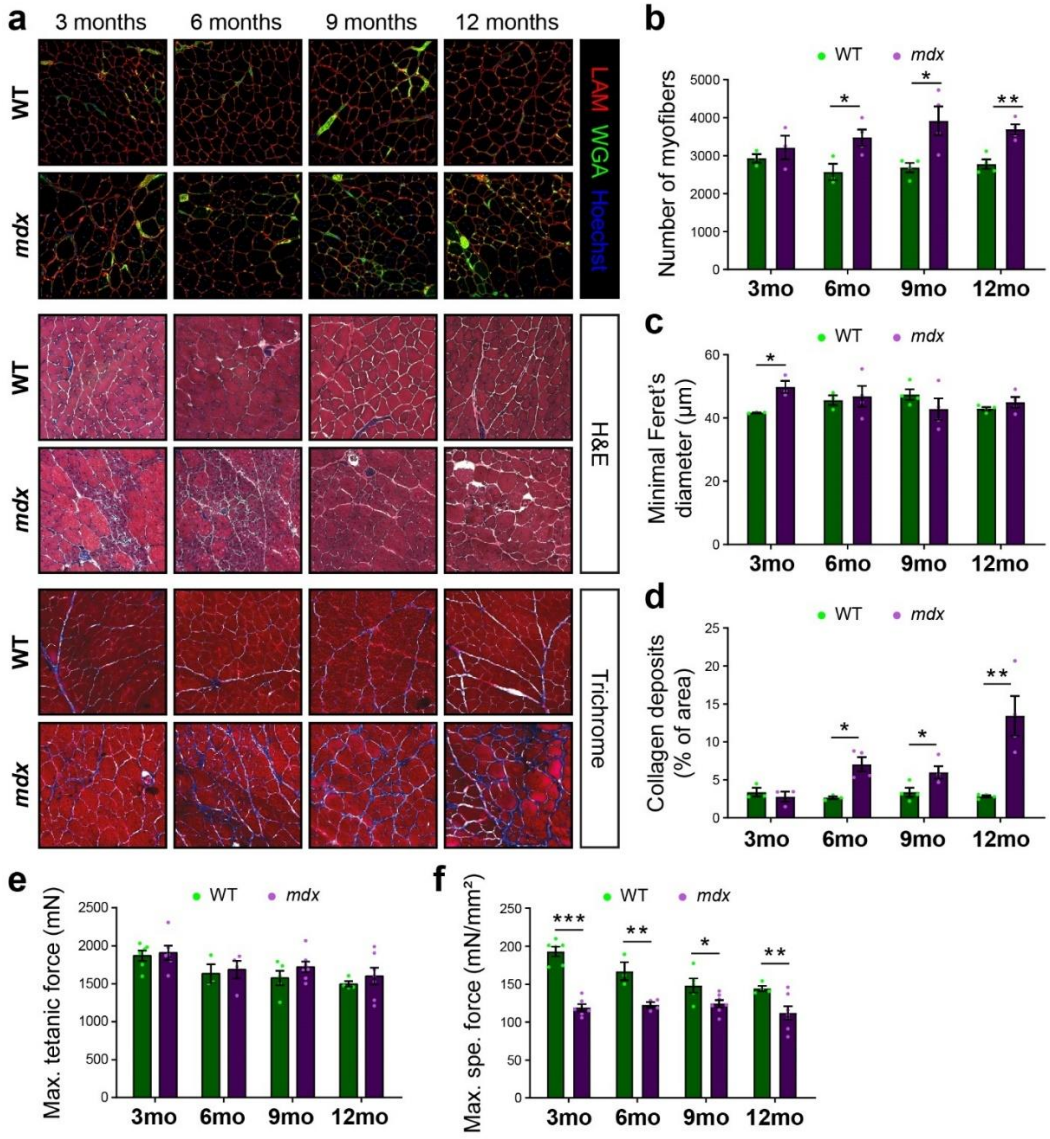


Figure 25: **Progressive degeneration in mdx muscle impairs physiological force generation.** A) Representative images of wild-type (WT) and *mdx* TA muscle cross-sections labelled by immunofluorescence for Laminin (Red), Wheat germ agglutinin (Green) and Hoechst (Blue) (Top panel), Hematoxylin and Eosin (Middle panel) and Trichrome (Bottom panel) from 3-12 month aged mice. B) Quantification of myofibre numbers from TA cross-sections in aged WT and *mdx* muscle from 3-12 months in age. C) Quantification of average minimum fibre Feret from TA muscles from 3-12 months in age mice as measured by SMASH software. D) Quantification of collagen content in muscle cross-sections from trichrome stained TA cross sections from 3-12 months in age mice. Quantification of E) max tetanic force and F) max specific force from TA muscles of WT and *mdx* mice from 3-12 months in age. (B-F) Error bars represent mean ±SEM; p-values: *=<0.05, **=<0.01; ***=<0.005. (B-D) n= 3 for 3mo, n=4 6-12mo, (E-F) n= 3-7 mice, where individual data points represent independent animals.

**Diaphragm muscle is acutely impacted in mdx mice**

As the diaphragm muscle is fundamental for respiration and is significantly impacted in patients with DMD[258], we wished to assess degeneration occurring in *mdx* diaphragm muscle with age. To address this, we monitored histological changes in Diaphragm muscle from WT and *mdx* mice from three to twelve months in age.

Aged *mdx* diaphragm muscle shows apparent histological differences to WT mice as early as six months in age as apparent Wheat germ agglutinin staining of interstitial deposits containing sialic acid and glucosamine (Figure 26A) and increased myofibre spacing as apparent in Hematoxylin and Eosin stained diaphragm muscle (Figure S17A). Quantification of minimum myofibre Feret from diaphragm muscle shows a progressive and significant 13%-22% decrease in minimum Feret compared to WT counterparts (Figure 26B) and a leftward shift in minimum myofibre Feret proportion with age (Figure S17B).

Staining of diaphragm muscle with Masson's Trichrome shows a striking and progressive 1.2-9.5-fold increase in interstitial collagen deposition within the diaphragm of *mdx* mice with age compared to WT counterparts, representing up to 51% of total diaphragm area (Figure 26A, C). We did observe a variable increase in lipid deposition within the Diaphragm of *mdx* mice however the levels remained low (Figure S17C-D). Taken together, the Diaphragm in *mdx* mice is significantly impacted by progressive deposition of interstitial collagen.

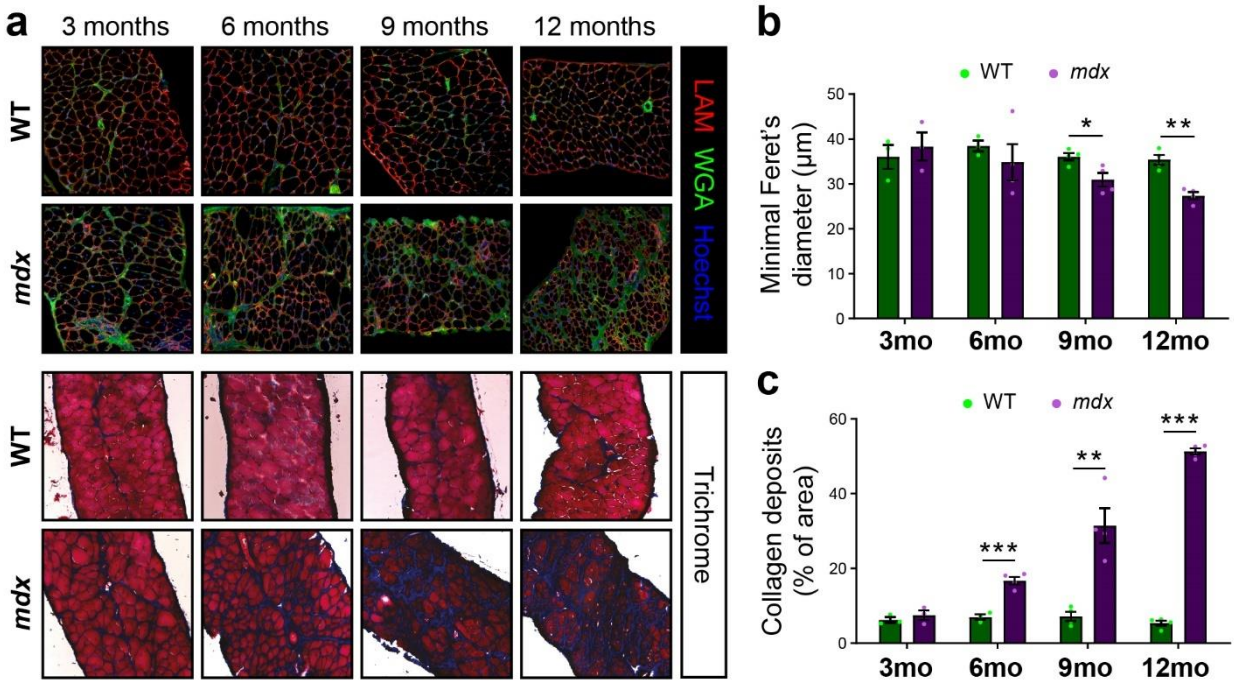


Figure 26: **Diaphragm muscle is acutely impacted in mdx mice.** A) Representative images of wild-type (WT) and *mdx* Diaphragm muscle cross-sections labelled by immunofluorescence for Laminin (Red), Wheat germ agglutinin (Green) and Hoechst (Blue) (Top panel) and Trichrome (Bottom panel) from 3-12 month aged mice. B) Quantification of average minimum fibre Feret from Diaphragm from 3-12 months in age mice as measured by SMASH software. C) Quantification of collagen content in muscle cross-sections from trichrome stained TA cross sections from 3-12 months in age mice. (B-C) Error bars represent mean ±SEM; p-values: *=<0.05, **=<0.01; ***=<0.005. (B-C) n= 3-4 mice, where individual data points represent independent animals.

**Dystrophin-deficiency impacts satellite cell signalling**

To explore the effect of dystrophin-deficiency in satellite cells from *mdx* mice, we monitored satellite cell expansion in aged *mdx* muscle. Immunofluorescence staining of aged *mdx* TA muscle with Pax7 antibody (Figure 27A) showed a significant 68-230% increase in the quantity of Pax7-expressing satellite cells from *mdx* mice compared to WT counterparts three to twelve months in age with a general decrease in total satellite cell quantity over time (Figure 27B). Quantifying immunofluorescence stained Pax7-expressing cells in the Diaphragm muscle from *mdx* mice show a striking 3.3-fold increase

in satellite cell quantity to that of WT mice at three months in age with a progressive decline satellite cell numbers by twelve months (Figure S18B). We did observe the appearance of revertant fibres expressing dystrophin protein in *mdx* TA muscle (Figure 27C) with a significant 3.1-3.9-fold increase with age (Figure 27D). Revertant fibres represent a small (~0.5-2%) proportion of total myofibres and have a clonal appearance (Figure 27C), suggesting myofibre repair propagated from a restorative dystrophin mutation from a single satellite cell.

We hypothesized that since *mdx* satellite cells exhibit significantly altered dynamics under resting conditions that altered gene expression may contribute to the different kinetics in dystrophin-deficient satellite cells. Therefore, we performed RNA sequencing on freshly isolated satellite cells in biological triplicate isolated from *WT*;*Pax7-nGFP* and *mdx:Pax7-nGFP* transgenic mice to ensure pure satellite cell isolation by FACS. We identified 1691 differentially regulated genes, representing 827 upregulated and 370 downregulated genes with greater than 1.5-fold differential gene expression between WT and *mdx* satellite cells.

To determine altered biological processes in quiescent *mdx* satellite cells, we subjected genes with greater than 1.5-fold differential gene expression to GO term analysis using g:Profiler (Figure 27E-F). Of the upregulated genes in quiescent *mdx* satellite cells, overrepresented GO terms included integrin binding ($p=1.4E^{-5}$), epidermal growth factor receptor binding (p=0.025), where 4 of the top 5 overrepresented biological processes related to cell migration ($p=4.8E^{-36}$-$9.7E^{-44}$) and 30 of the 53 cellular components GO terms relate to changes in the extracellular membrane and cell projections ($p=0.02$-$3.2E^{-14}$)(Figure 27E). Of the downregulated genes in quiescent *mdx* satellite cells, overrepresented GO terms included protein tyrosine phosphatase activity (p=0.006) where 6 of 25 biological processes represent catabolic metabolism (p=0.04-

0.002) and 10 of 14 molecular functions GO terms represented changes in ion channel activity (p=0.02-0.001)(Figure 27F). Taken together, this data suggests that quiescent dystrophin-deficient satellite cells are maintained in an activated state with altered interactions with the niche.

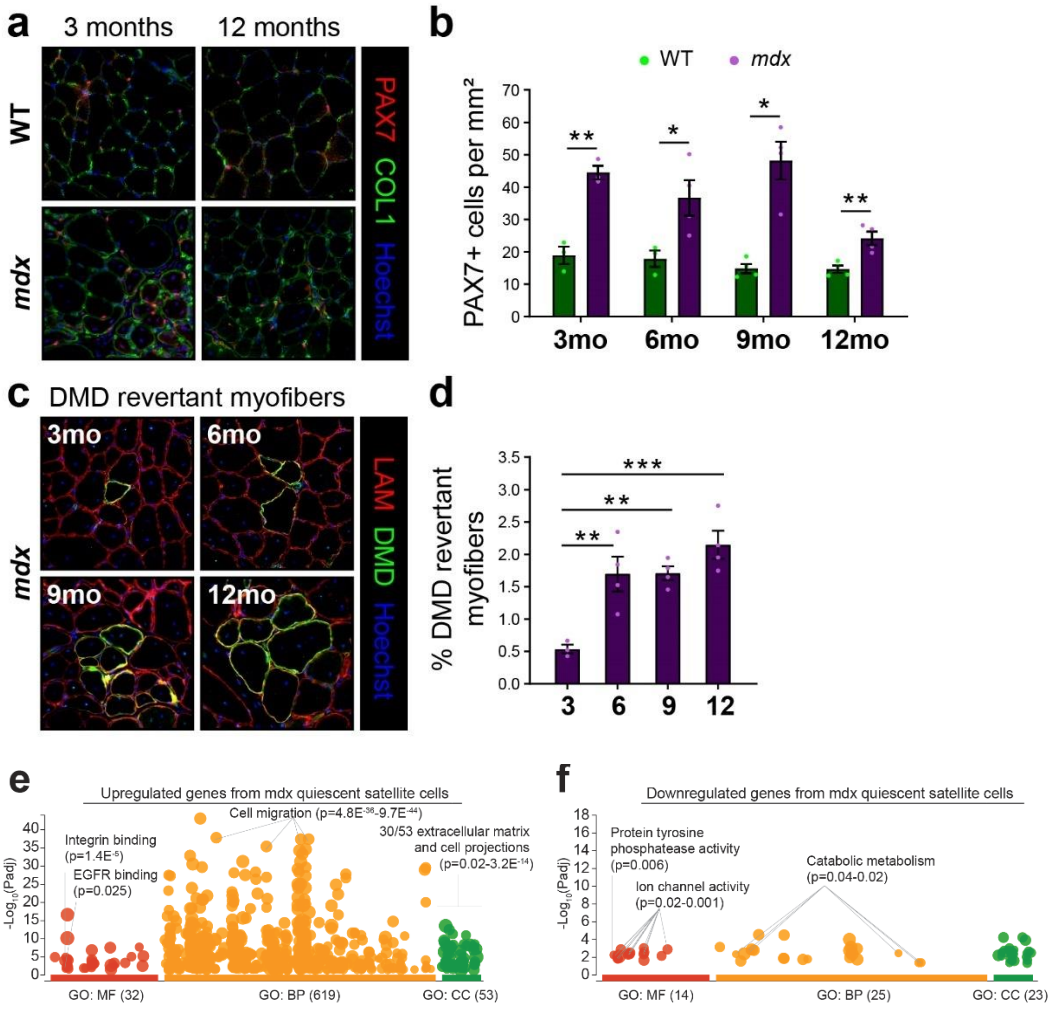


Figure 27: **Dystrophin-deficiency impacts satellite cell signalling.** A) Representative images of WT and *mdx* TA cross-sections stained by immunofluorescence for Hoechst (Blue), Collagen (Green), and Pax7 (Red). B) Quantification of Pax7-expressing cell quantity per $mm^2$ in WT and *mdx* mice TA cross sections from 3-12 months in age. C) Representative images of *mdx* mice TA cross-sections stained by immunofluorescence for Hoechst (Blue), Dystrophin (Green), and Laminin (Red). D) Quantification of Dystrophin-expressing myofibres in *mdx* mice TA cross sections from 3-12 months in age. GO term enrichment and g:Profiler output of E) upregulated and F) downregulated genes from transcriptome sequencing of quiescent *mdx;Pax7-nGFP* satellite cells compared to *WT;Pax7-nGFP* controls. (B, D) Error bars represent mean ±SEM; p-values: *=<0.05,

**=<0.01; ***=<0.005 (B,D) n= 3-4 mice, where individual data points represent independent animals, (E-F) n = 3 independent animals from each genotype.

**Regeneration is impaired following injury in *mdx* muscle**

To determine if the changes we observed in resting satellite cell quantity and intrinsic signalling impacted acute regenerative outcomes in *mdx* muscle, we injured the TA muscle of WT and *mdx* mice by intramuscular injection of cardiotoxin (CTX). By performing acute injury and assessing regeneration at early (3-10dpi) and late time points (21-90dpi) we can monitor the effect of dystrophin loss on the kinetics of muscle repair and the histological and physiological consequences of injury. We additionally subjected a subset of mice to a triple cardiotoxin injury (Figure S19A) to assess the regenerative potential of satellite cells from WT and *mdx* mice following repetitive acute injury. Notably, acute injury in *mdx* muscle did not result in increased relative muscle weight (Figure S19C) and following immunofluorescence labelling of Laminin (Figure 28A) *mdx* TA muscle exhibit a significant 128% increase in myofibre numbers 90dpi and a 51% increase following triple injury (Figure 28B). Quantification of myofibre minimum fibre Feret shows that while resting muscle *mdx* mice have a 20% increase in minimum fibre Feret, injury results in an 18% decrease at 90dpi, a 10% decrease in minimum myofibre Feret following triple injury (Figure 28C) and a general leftward shift in min Feret proportion at 90dpi in *mdx* mice compared to WT counterparts (Figure S19D). Quantification of collagen deposition following Masson's Trichrome staining in injured TA muscle shows a 1.8-fold increase in collagen deposition following 90dpi without an increase following triple injury in *mdx* mice compared to WT counterparts (Figure 28D), suggesting *mdx* regeneration in response to acute injury differs from progressive changes with age (Figure 26C).

To determine the physiological consequences increased myofibre number observed in injured *mdx* TA muscle we measured *in situ* physiological force production in

injured WT and *mdx* mice. Notably, WT and *mdx* mice maintain max tetanic force generation following injury (Figure 28E) while normalizing to displacement volume shows a significant 38% reduction in resting specific force and a 24%-26% reduction in specific force generation in *mdx* TA muscle following injury compared to WT counterparts (Figure 28F, Figure S19E). Taken together, this data suggests that in response to acute injury, *mdx* muscle exhibits increased myofibre number and impaired physiological force generation without an increase in interstitial collagen deposition.

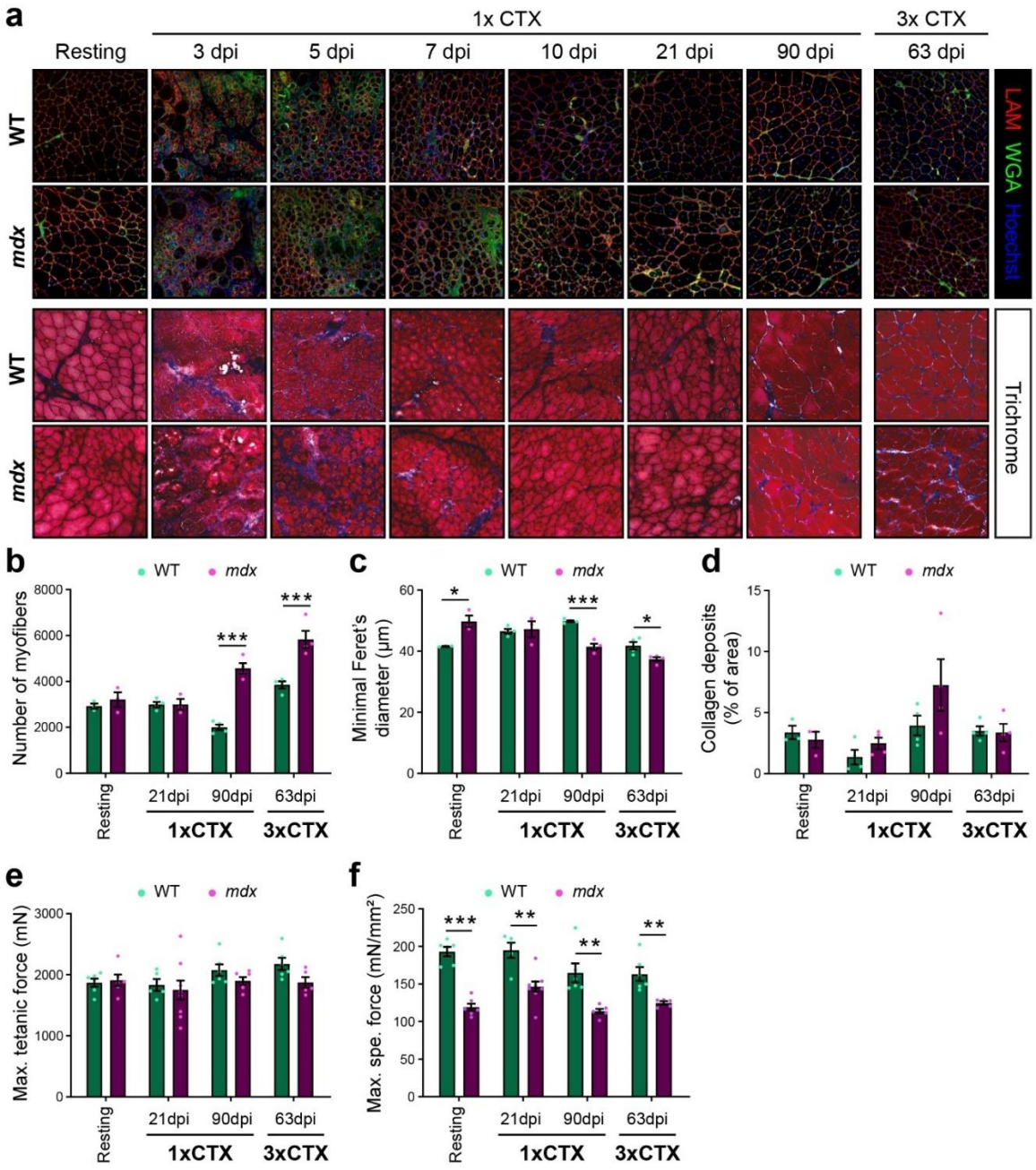


Figure 28: **Regeneration is impaired following injury in mdx muscle.** A) Representative images of wild-type (WT) and *mdx* TA muscle cross-sections labelled by immunofluorescence for Laminin (Red), Wheat germ agglutinin (Green) and Hoechst (Blue) (Top panel) and Trichrome (Bottom panel) from resting and injured muscle from 3-90 days post-injury (dpi) and from triple injured muscle (3x CTX). B) Quantification of myofibre numbers from TA cross-sections in injured WT and *mdx* muscle. C) Quantification of average minimum fibre Feret from injured WT and mdx TA muscles as measured by SMASH software. D) Quantification of collagen content from injured WT and mdx TA muscles from trichrome stained TA cross-sections. Quantification of E) max tetanic force and F) max specific force from injured WT and mdx TA muscles. (B-F) Error

bars represent mean ±SEM; p-values: *=<0.05, **=<0.01; ***=<0.005. (A-F) n= 3-8 mice, where individual data points represent independent animals.

**Injured *mdx* muscle has delayed satellite cell activation**

To determine the effect of acute injury on dystrophin deficient-satellite cell activation we stained injured TA muscle from WT and *mdx* mice with Pax7 (Figure 29A). Notably, CTX induced injury results in a significant increase in satellite cell numbers in both WT and *mdx* at 5dpi with a progressive decrease in satellite cell numbers to 21dpi (Figure 29B). As *mdx* satellite cells have increased resting satellite cell numbers (Figure 27B, Figure 29B) yet exhibit similar induction in satellite cell numbers at 5dpi, we calculated the fold change in satellite cell numbers following injury. Notably, *mdx* muscle exhibits a marked decrease in satellite cell fold-change (14.4-fold vs 7.9-fold) compared to WT counterparts at 5dpi (Figure 29C).

To further explore the consequence of acute injury on satellite cell dynamics we quantified satellite cell numbers at 90dpi and in triple injured WT and *mdx* muscle. Importantly, satellite cell numbers were decreased 16% and 52% in *mdx* muscle 90dpi and following triple injury (Figure 29D) compared to WT counterparts, suggesting an impairment in satellite cell expansion following repetitive acute injury. Quantifying fold change in satellite cell expansion at late injury timepoints show a marked decrease in satellite cell induction following 21dpi (2.7-fold vs 1.2-fold), 90dpi (1.6-fold vs 0.75-fold), and triple injury (2.2-fold vs 0.65-fold) compared to WT counterparts (Figure 29E). Taken together, this data suggests that dystrophin-deficient satellite cells have impaired expansion in response to acute injury.

As we observed *mdx* satellite cells exhibited delayed expansion in response to injury (Figure 29C-E) we hypothesized that altered gene expression may contribute to the

impaired expansion of the *mdx* satellite cell pool in response to injury. We therefore subjected early activated satellite cells isolated from 3dpi cardiotoxin injured *WT*;*Pax7-nGFP* and *mdx:Pax7-nGFP* muscle by FACS to RNA sequencing in biological triplicate. We identified 5974 differentially regulated genes, representing 2646 upregulated and 1501 downregulated genes with greater than 1.5-fold differential gene expression between activated WT and *mdx* satellite cells. We subjected genes with greater than 1.5-fold differential gene expression to GO term analysis using g:Profiler (Figure 29F-G). Of the upregulated genes in activated *mdx* satellite cells, overrepresented GO terms include pathways associated with adhesion including fibronectin-binding (p=0.0005), proteoglycan binding ($p=7.1E^{-5}$), Collagen binding ($p=1.5E^{-5}$), glycosaminoglycan binding ($p=6.5E^{-6}$), integrin-binding ($p=1.6E^{-7}$) where upregulated biological processes include cell migration ($p=5.6E^{-18}$-$9.8E^{-27}$) and cell adhesion ($p=3.8E^{-31}$-$4.3E^{-32}$)(Figure 29F). Of the downregulated genes in activated *mdx* satellite cells, there is a striking overrepresentation of GO terms relating to biological processes regulating cell cycle ($p=1.2E^{-18}$), DNA replication ($p=1.8E^{-35}$), cellular metabolic processes ($p=2.7E^{-52}$), RNA processing ($p=9.3E^{-66}$) and ribonucleoprotein complex biogenesis ($p=8.7E^{-89}$)(Figure 29G). Taken together, this data suggests that activated dystrophin-deficient satellite cells have a delay in myogenic progression likely reflecting an impaired flux from the stem cell compartment to the progenitor compartment due to loss of polarity and reduced asymmetric division.

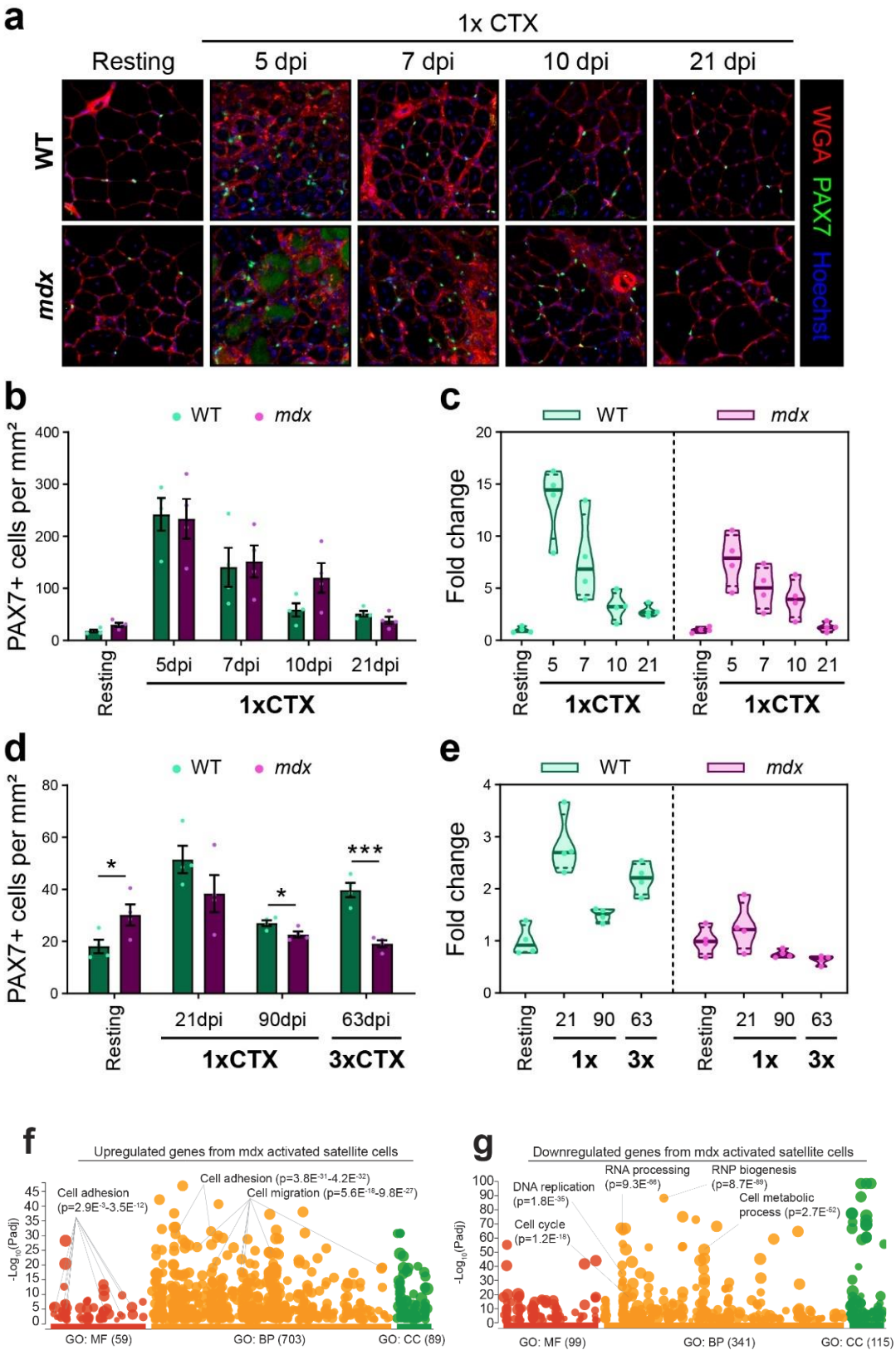


Figure 29: **Injured mdx muscle has delayed satellite cell activation.** Representative images of injured TA cross-sections from WT and *mdx* mice stained with Hoechst (Blue),

Pax7 (Green) and Wheat germ agglutinin (Red). B) Quantification of Pax7-expressing cells per $mm^2$ in injured WT and *mdx* TA muscle cross-sections. C) Quantification of Fold change of Pax7-expressing cells from injured WT and *mdx* TA muscle cross-sections relative to the resting state. D) Quantification of Pax7-expressing cells per $mm^2$ in 21 dpi, 90 dpi and triple injured WT and *mdx* TA muscle cross-sections. E) Quantification of Fold change of Pax7-expressing cells from 21 dpi, 90 dpi and triple injured WT and *mdx* TA muscle cross-sections relative to the resting state. GO term enrichment and g:Profiler output of F) upregulated and G) downregulated genes from transcriptome sequencing of activated (3dpi) *mdx;Pax7-nGFP* satellite cells compared to *WT;Pax7-nGFP* controls. (B-E) Error bars represent mean ±SEM; p-values: *=<0.05; ***=<0.005. (A-G) n= 4 mice, where individual data points represent independent animals. (F-G) n = 3 independent animals from each genotype.

## DISCUSSION

Balancing satellite cell self-renewal and commitment is required for efficient regeneration over a lifetime[5]. In conditions such as DMD, loss of dystrophin leads to myofibre fragility[259] and repeated cycles of injury and repair due to weight-bearing or exercise. These regenerative cycles are further exacerbated due to satellite cell-intrinsic deficits in *mdx* mice leading to satellite stem cell hyperplasia, poor myogenic progenitor formation and in turn inefficient repair[7]. Understanding the complex nature of DMD disease progression will help design pathways, or cell type-specific therapeutics to restore dystrophin expression in myofibres and promote satellite cell-mediated muscle repair.

Our findings contribute to a large body of evidence exploring impaired muscle regeneration in the *mdx* mouse model[260]. We show specifically that collagen deposition in *mdx* TA and more specifically Diaphragm muscle is a major histopathological complication with age, where in conjunction with increased myofibre number result in muscles with decreased specific force generation. We provide evidence that dystrophin-deficient satellite cells in *mdx* mice maintain a state of activation compared to WT counterparts where in response to injury results in increased myofibre number, reduced myofibre calibre and impaired force generation without increased deposition of collagen. Specifically, we provide evidence that dystrophin-deficient satellite cells have a delay in

expansion in response to injury, potentially facilitated by altered niche interactions and impaired cell cycle progression.

We observed gross morphological changes in *mdx* TA muscle following age and in response to injury which reflected impaired physiological force generation (Figure 25, Figure 28). Muscle from *mdx* mice maintained similar max tetanic force production to WT mice despite increased myofibre number, reduced myofibre calibre, increased collagen deposition and increased mass where normalizing to muscle volume revealed impaired specific force. Previous reports have highlighted the consequence of myofibre branching present in *mdx* myofibres as a contributor to myofibre weakness[261,262], however, significant impairments in Diaphragm muscle function may also contribute weakness through limiting oxygen availability in *mdx* muscle. Additionally, as injured *mdx* muscle exhibit similar morphological changes and impaired physiological force to aged *mdx* muscle without an increase in collagen deposition, additional factors such as impaired mitochondrial function[263] may contribute to muscle weakness in *mdx* mice.

We made the observation that in response to injury, *mdx* TA muscle has impaired specific force generation compared to WT muscle (Figure 28). Interestingly, force generation in acute injured *mdx* muscle does not decrease from the level at a resting state suggesting that compensation through increased myofibre number but reduced myofibre calibre maintains similar physiological output. Increases in myofibre number taken together with the reduction in satellite cell numbers following triple injury in *mdx* mice (Figure 29) would suggest that compensation in response to injury in *mdx* mice would result in eventual exhaustion of the satellite cell pool and regenerative failure.

Our observation that *mdx* satellite cells exhibit downregulated cell cycle genes following early activation (Figure 29) could be attributed to deficits in spindle assembly checkpoints[264] or aberrant centrosome amplification[7] resulting in delayed cell cycle

progression in *mdx* satellite cells. Alternatively, these differences could be attributed to an altered ratio of stem cells, rapidly amplifying progenitors and differentiating myocytes between WT and *mdx* mice from impaired flux of the satellite stem cell compartment to the production of amplifying progenitors due to reduced asymmetric division. Future studies delineating the replicative kinetics of *mdx* satellite cells during early activation would better resolve the cause or consequence of delayed cell cycle progression on myogenic differentiation.

Importantly, our study focused on the cellular, histological and physiological changes that occur in *mdx* skeletal muscle during regeneration and disease progression with age with a focus on satellite cell-mediated repair. Other groups have highlighted additional cell types such as fibroadipogenic precursors[265] that are integral players in orchestrating the regenerative environment within skeletal muscle in response to injury. The crosstalk between satellite cells and their environment maintains the efficiency of muscle repair[266–268] where a lack of regeneration due to *mdx* satellite cell deficiencies may lead to a permissive state where other cell types such as fibroblast can become opportunistic and contribute to disease pathology. As others have observed the secretome of *mdx* satellite cells can epigenetically reprogram healthy satellite cells[257] it may suggest that intrinsic changes to the satellite cell secretome may contribute to the dystrophic environment and impact muscle homeostasis. There has yet to be supported arguments suggesting a lack of dystrophin in other cell types such as fibroadipogenic precursors or similar ECM secreting cells can contribute to pathological conditions. Taken together, this may suggest that the altered timelines in satellite cell proliferation and progenitor formation may alter signalling within the regenerative context[268] resulting in fibrotic progression, highlighting the complex nature of *mdx* skeletal muscle regeneration.

Together, our findings demonstrate that muscle wasting in DMD is not solely the consequence of myofibre fragility but also a by-product of deficient satellite cell activity. These results add to a growing body of evidence that function is impaired *mdx* satellite cells due to a delay in myogenic progenitor production[7,103,254]. This study provides insight into the dynamics of *mdx* muscle regeneration, age-related changes to the satellite cell pool and regenerative outcomes in response to acute injury. This study provides useful insight into DMD disease progression and highlights the need for future studies addressing molecular therapeutics targeting satellite cells for the treatment of DMD.

## METHODS

### Animals and Animal Care

The following mouse lines were used: ♂ C57BL/10ScSn-Dmd$^{mdx}$/J (*mdx*, JAX# 001801) and ♂ C57BL/10ScSnJ (WT, JAX# 000476). All experiments were initiated at 6-8 weeks old unless stated otherwise. Housing, husbandry and all experimental protocols for mice used in this study were performed in accordance with the guidelines established by the University of Ottawa Animal Care Committee, which is based on the guidelines of the Canadian Council on Animal Care.

### Cardiotoxin Injury

Mice were anesthetized using isoflurane (1L/min, 2% isoflurane) and injected with 50ul of 10uM cardiotoxin solution (Latoxan) through the skin directly into the tibialis anterior muscle. Mice were provided 0.1mg/kg buprenorphine and maintained on analgesic regimes as required. For repetitive injury, mice were allowed to regenerate for 21 days between cardiotoxin injections into the same muscle. Experimental protocols for mice used in this study were performed in accordance with the guidelines established by the University of Ottawa Animal Care Committee, which is based on the guidelines of the Canadian Council on Animal Care.

### Histological staining of Muscle Cross Sections

For Haemotoxylin and Eosin staining, samples were incubated in Haematoxylin for 30 seconds with agitation and washed extensively in running water for 45 seconds. Samples were incubated in 70% ethanol for 3 minutes and exchanged with 1% Eosin for 15 seconds with agitation. Samples were dehydrated in a 70-100% graded ethanol series. Samples were washed three times in xylene for 3 minutes each wash. Samples were mounted using DPX mounting media.

For Masson Trichrome staining, samples were fixed in warm 4% PFA for 1h and washed extensively in PBS. Samples were re-fixed in Bouin's solution overnight and washed in excess water for 2 minutes. Samples were incubated in Weigert's Hematoxylin solution and washed under warm running tap water for 10 minutes. Samples were incubated in Biebrich Scarlet-acid Fuchsin solution for 5 minutes. Samples were washed in excess water for 3 minutes. Samples were stained in a glass container containing a 1:1:2 part solution of Phosphotungstic Acid, Phosphomolybdic Acid and ddH2O solution for 10 minutes. Samples were decanted and immediately incubated with Aniline Blue solution for 5 minutes. Samples were washed in excess water and incubated in 1% Glacial Acetic Acid for 30 seconds. Samples were washed in excess water and dehydrated in a 70-100% graded ethanol series and terminally in xylene for 5 minutes. Samples were mounted using DPX mounting media.

**Histological Analysis of Muscle Cross Sections**

Minimum fibre Feret measurements were performed using the semi-automated SMASH software plugin for MATLAB 2015a described previously [238]. Total myofibre count per cross-section was verified by manual validation of SMASH myofibre masks and original images. >95% of myofibres were quantified for Feret diameter for each cross-section studied. The total cross-sectional area was measured using the trace tool in ImageJ. The fibrotic area was analyzed using either Wheat Germ Agglutinin staining or Masson Trichrome staining and measuring the % area of thresholded pixels in Wheat Germ Agglutinin single-channel images or images extracted from the red channel in trichrome staining. The positively stained tissue was calculated as a fraction of the total measured surface area. Embryonic myosin fibre number was counted manually across each cross-section studied.

**Immunostaining and Antibodies**

Tibialis anterior cross-sections were fixed for 10 min in warm 4% PFA and washed in excess PBS. Sections were permeabilized in 0.1% Triton X-100 for 10 min and incubated in 125mM glycine for 10 min for antigen retrieval. Samples were washed in excess PBS and blocked using 5% donkey serum (Sigma). Primary antibodies were applied for 2h at room temp or overnight at 4°C. Samples were washed in excess PBS and stained with appropriate fluorescent secondary antibodies (Life Tech, Alexa flour 488, 546, or 647). Samples were washed in excess PBS, counterstained with DAPI and mounted with Permaflour (Fisher). All manipulations were carried out at room temperature unless stated otherwise. To minimize random sampling bias, cell counts were performed on whole cross-sections as described.

For fibre type staining, non-fixed samples were washed briefly in PBS and blocked for 1h in 10% donkey serum. Samples were incubated in primary antibodies for 2h and washed extensively in PBS. Samples were incubated in secondary antibody for 1h and washed extensively in PBS. Samples were counterstained with DAPI and mounted with Permaflour. Images were acquired immediately following staining.

For myofibre Feret analysis, non-fixed samples were washed with excess PBS and incubated with Wheat Germ Agglutinin Alexa 647 conjugate for 1h. Images were acquired immediately following staining.

Antibodies used in the study are as follows: mouse anti-Pax7 (1:2, DSHB, Cat. no. Ab528428; RRID: AB_528428), rat anti-Laminin (1:1000, Sigma, Cat. no. L0663; RRID: AB_477153), rabbit anti-Myogenin (1:1000, Santa Cruz, Cat. no. sc-576; RRID: AB_2148908), rabbit anti-Dystrophin (1:1000, Abcam, Cat. no. ab85302, RRID: AB_85302), rabbit-anti-Collagen I (1:1000, Abcam, Cat. no. ab34710; RRID: AB_731684), Wheat Germ Agglutinin Alexa 647 conjugate (1:1000, Fisher, Cat. no. W32466).

### *In Situ* Force Measurements

Muscle force measurements were performed on an Aurora Scientific 300C-LR-FP dual-mode muscle lever system equipped with a 1N force transducer and 1cm lever arm (Cat. no. 300C-LR-FP). Electrical stimulation was performed using monopolar needle electrodes (Chalgren, Cat# 111-725TP) attached to an Aurora Scientific 701C High-Power, Bi-Phase Stimulator (Cat# 701C). Force transducers were calibrated prior to the study using precision weights.

Mice were anesthetized using isoflurane (2% isoflurane, 1L/min) until recumbent and non-reflexive to pressure on the paw. Mice were positioned supine and hindlimb was shaved. A small incision was made above the hallux and the foot was partially degloved to expose the distal insertion of the *tibialis anterio*r tendon up to the *tibialis anterior* muscle. The cruciate crural ligament was severed to release the *tibialis anterior* tendon from the foot.

A pre-tied loop of waxed 3.5 metric suture was attached to the tibialis anterior tendon using a series of double thumb knots above, below and through the loop. The suture was secured to the tendon using minimal cyanoacrylate glue. The skin of the hindlimb was removed up to mid *vastus lateralis* to expose the *tibialis anterior* and the kneecap. The fascia of the *tibialis anterio*r is cut using spring scissors. The distal insertion of the *tibialis anterior* tendon was severed and the *tibialis anterior* is gently lifted to release it from the *extensor digitorum longus* muscle and connective tissue. Muscles were kept from drying using physiological saline. Mice were placed supine on the 37°C pre-warmed measurement stage. The measured hindlimb was secured between the limb clamp and the stage using a 40mm long 27g needle inserted through the epiphysis of the femur immediately proximal the kneecap and directly into a receiving hole in the stage. Clamping was verified by observing no movement of the kneecap following manipulation of the foot

and the needle was secured by a hand screw. The pre-tied loop was attached to the hook on the force transducer lever arm and maintained without tension.

Two monopolar needle electrodes were positioned adjacent to the tibial nerve proximal to the kneecap and distal the kneecap adjacent to the *extensor digitorum longus* muscle. The transducer was retracted to maintain 20mN of measured tension for an initial 15-minute stretching period with 100ms trains of 0.3ms, 5V supramaximal voltage pulses at 1Hz stimulation every 100 seconds. Following stretching, muscles were maintained at 20mN tension and tetanic contractions were measured every 100 seconds following 200ms trains of 0.3ms, 5V supramaximal voltage pulses at serial frequencies from 1Hz to 200Hz. The maximal force was defined by the difference in maximal force measured during stimulation to that of the tension immediately prior to stimulation.

Following force measurement, muscle mass was measured. Muscle volume was measured in saline-filled PCR tubes by removing 100ul of liquid and measuring the volumetric displacement of dissected muscle using precision pipettes.

The specific force of muscles was calculated as follows:

$$F_{measured}/PCSA$$

$$PCSA = (M_{displacement}/M_{FL})*Cos(M_{PA})$$

Where $F_{measured}$ was the force measured in mN, PCSA is the physiological cross-sectional area in $mm^2$, $M_{displacement}$ is the measured muscle displacement in µl ($mm^3$), $M_{FL}$ is the experimentally determined muscle fibre length in mm, $M_{PA}$ is the experimentally determined muscle pennation angle in °. For non-volumetric analysis, muscle mass was related to the assumed density of mammalian tissue ($1.06g/cm^3$). Muscle fibre length and pennation angles were determined previously (Charles et al., 2016).

**Statistical Analysis**

Data are expressed as mean ± standard error of the mean (SEM) unless stated otherwise. Statistical analysis of two conditions was evaluated by Student's t-test where paired tests were used for biologically matched samples and unpaired testing was used for unrelated samples. P-values are provided for each statistical test performed. All experiments were performed on a minimum of three biological replicated with biological replicate numbers described in figure legends.

**ACKNOWLEDGEMENTS**

C.E.B. is supported by a Postdoctoral Fellowship from the Ontario Institute for Regenerative Medicine. P.F. is supported by a fellowship from CIHR. These studies were carried out with the support of grants to M.A.R. from the US National Institutes for Health [R01AR044031], E-Rare-2: Canadian Institutes of Health Research/Muscular Dystrophy Canada [ERA-132935], Canadian Institutes for Health Research [FDN-148387], the Muscular Dystrophy Association, and the Stem Cell Network.

**AUTHOR CONTRIBUTIONS**

Conceptualization, C.E.B. and M.A.R.; Methodology, C.E.B., P.F., M.C.S., and M.A.R.; Investigation, C.E.B., P.F., M.C.S., and M.A.R; Writing an original draft, P.F., and M.A.R; Funding acquisition, M.A.R.; Resources, M.A.R.; Supervision, M.A.R.

**COMPETING INTERESTS**

No authors declare competing interests.

**MATERIALS & CORRESPONDENCE**

Information and requests for reagents may be directed to the corresponding author Michael A. Rudnicki (mrudnicki@ohri.ca).

## Manuscript V: Analysis of Human Satellite Cell Dynamics on Cultured Adult Skeletal Muscle Myofibres

AUTHORS: **Peter Feige**[1,2,3], Eve Tsai[4] Michael A. Rudnicki[1,2,3,5]

AUTHOR AFFILIATION: 1. Sprott Center for Stem Cell Research, Ottawa Hospital Research Institute, Regenerative Medicine Program, Ottawa, ON, Canada. 2. Department of Cellular and Molecular Medicine, Faculty of Medicine, University of Ottawa, Ottawa, ON, Canada. 3. Department of Medicine, Faculty of Medicine, University of Ottawa, Ottawa, ON, Canada. 4. University of Ottawa Heart Institute. 5. Faculty of Medicine University of Ottawa Ottawa, ON, Canada

This manuscript formatted for the anticipation of submission in **Skeletal Muscle**.

This study was approved by the Ottawa Hospital Research Ethics Board and informed consent was obtained prior to proceeding. Samples were harvested from patients consented for organ donation through the Trillium Gift of Life Network following cardiac death in compliance with guidelines from The Ottawa Hospital Research Ethics Board.

### AUTHOR CONTRIBUTION

P.F. conceptualized the study, experimental design, performed all experiments herein and wrote the initial draft. E.T. oversaw the experimental design and sample acquisition. M.A.R. oversaw the experimental design, analysis of results, manuscript editing, and financial support.

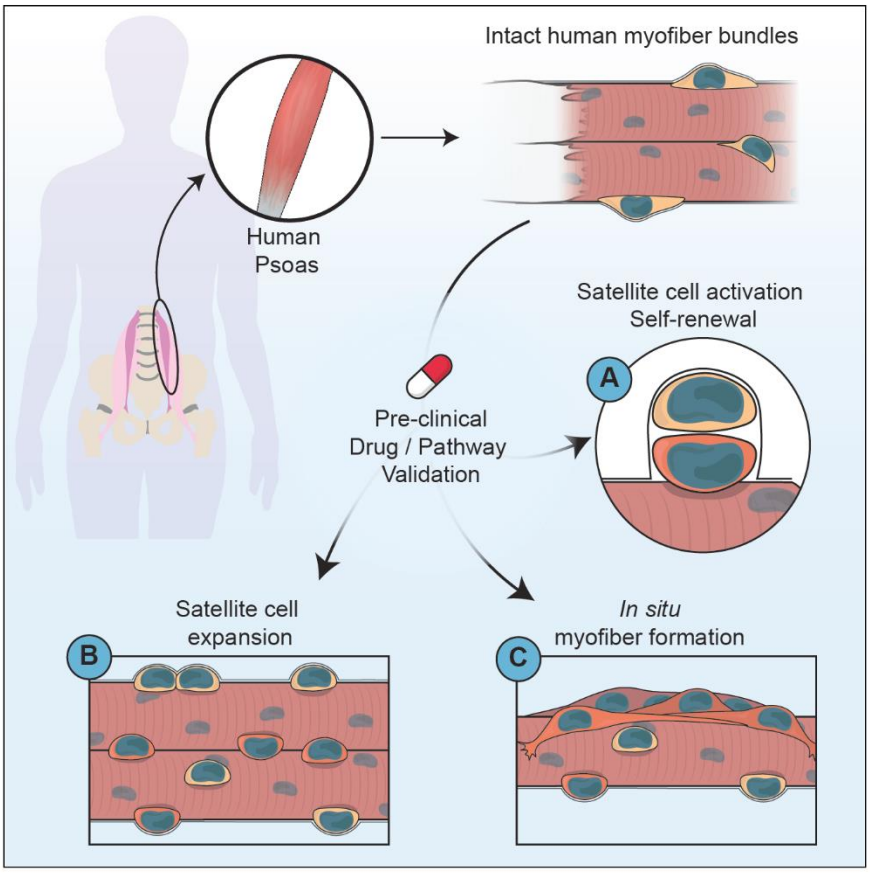


Figure 30: **Graphical abstract for Manuscript V**

**HIGHLIGHTS**

- Intact primary human muscle fibres can be cultured following surgical excision
- Human myofibres maintain the relevant structural, chemical and cellular composition of regenerating muscle
- Human satellite cells activate and differentiate in culture
- EGFR stimulation augments human satellite cell expansion and differentiation

**eTOC blurb**

Feige et al., establish a novel method to culture intact human muscle fibres ex vivo and observe direct interventions on muscle resident stem cell fate. The study outlines a straightforward method to culture human myofibres with widespread implications in pre-clinical therapeutic testing, disease modelling and regenerative medicine.

**SUMMARY**

Maintaining stem cells in physiologically relevant states is necessary to understand cell and context-specific signalling paradigms and understand complex interfaces between cells *in situ*. Understanding human stem cell function is largely based on tissue biopsies, cell culture and transplantation into model organisms. Here we describe a method to isolate post-mortem intact human muscle myofibres and culture muscle stem cells within the niche microenvironment to assay cellular dynamics, stem cell identity, stem cell hierarchy, as well as differentiation potential. We show human myofibre culture maintains complex cell-cell contacts and extracellular niche composition during culture. Human satellite cells can be cultured at least 8 days, which represents a timepoint of activation, differentiation and *de novo* human myofibre formation. We validate stimulation of the EGFR pathway augments human satellite cell expansion and myogenic differentiation. This method has widespread applications in pre-clinical therapeutic testing, muscle disease modelling and regenerative medicine.

## INTRODUCTION

Skeletal muscle is a complex tissue, responsible for mobility, thermoregulation and breathing. Skeletal muscle maintenance, growth, and repair are facilitated by muscle resident stem cells (satellite cells) that reside within skeletal muscle, resting within a specialized cleft underneath the basal lamina [269]. Muscle homeostasis requires a balance between satellite cell self-renewal and differentiation to facilitate efficient repair over time and in response to injury [5]. Changes to satellite cell-intrinsic signalling, satellite cell-niche interactions or the regenerative context in conditions such as ageing or muscular dystrophy alter the kinetics of muscle repair (reviewed in[5]). Improved modelling of human satellite cell dynamics in a physiologically relevant context will improve our understanding of signalling pathways pertinent to muscle repair in humans.

With age, progressive loss of satellite cell number is observed with a functional decline in skeletal muscle [3,4]. In aged mice, extrinsic changes to soluble ligands in the niche [23,270,271], increased fibrosis [272], and intrinsic changes in satellite cells such as constitutively active p38a-b signalling, or elevated JAK-STAT signalling alter cell fate, reduces regenerative capacity in muscle [9,10,26,27] and biases aged satellite cells to asymmetric modes of division producing committed progenitors and exhausting the muscle stem cell pool [10]. Chemical and physical cues present in young and healthy muscle act to balance satellite cell quiescence, self-renewal and asymmetric division to maintain the satellite cell pool in a sate amenable to rapid activation in response to injury [9–11]. Understanding if these processes are conserved or altered in human satellite cells is important to develop methods improving endogenous satellite cell-mediated repair.

Applying laboratory insights to human disease is failure-prone, where roughly one in ten pharmaceuticals entering clinical trials gain approval by the FDA [273] with efficacy being a major concern [274]. The value of animal models for predicting clinical responses to therapy remains controversial and partially explained by publication biases,

methodological flaws in animal experiments, non-transparent data reporting and fundamental differences in human and animal physiology limiting generalisability of results [106,275]. Improved methods investigating satellite cell biology such as satellite cell isolation [276], satellite cell transplantation[135,277] and myofibre culture[278] have significantly improved our understanding of satellite cell heterogeneity[31,101,171], hierarchy[31,47,247], regenerative capacity [10,90,279] and the therapeutic potential of augmenting muscle stem cell repair [88,101,280].

Development of novel 3D culture systems [281], bioengineering approaches modelling human muscle [282,283], humanized mouse models of muscular dystrophy [102] and advancements in iPSC derived myogenic cells [284,285] have uncovered unique aspects of human muscle disease, however, no system robustly recapitulates the complexity in the human myofibre chemical composition, physical composition, or cellular composition [283]. In model organisms, culturing myofibres harbouring satellite cells maintains extracellular matrix composition [269], myofibre rigidity [243] and endogenous niche interactions [171] to provide a more relevant *ex-vivo* culture paradigm [5].

Understanding the satellite cell-intrinsic changes occurring with disease provides important insight into treatments addressing the etiology of muscle disease. Our lab made the seminal discovery that intrinsic satellite cell signalling through the protein dystrophin is perturbed in mouse models of Duchenne's Muscular Dystrophy (DMD) altering cell polarity and resulting in inefficient satellite cell-mediated repair [7]. Clinically, current therapeutics target myofibre instability associated with dystrophin loss [6], but do not directly address satellite cell-mediated repair mechanisms. The development of novel methods to assess dystrophin signalling in human satellite cells will provide important insight into the progression of DMD.

Myofibre culture [278] has led to multiple seminal discoveries in mouse satellite cell biology[7,10,101,171,279]. We hypothesized human myofibre isolation could provide insight into

fundamental differences in human and mouse satellite cell biology. Common methods of isolating human muscle such as punch biopsy are not suitable to culture as sarcolemma membrane damage results in calcium overload and fibre hypercontraction[286]. Maintaining healthy myofibres amenable for culture requires tendon to tendon isolation followed by enzymatic digestion of the extracellular matrix to release single muscle fibres [278].

Here we report that by utilizing primary human myofibres, we can model human muscle stem cell dynamics in a chemically, physically and cellularly relevant context. This method is amendable to model human muscle resident stem cells including satellite cells and feasibly other resident cell types in muscle such as fibroadipogenic precursors, mesenchymal cells, fibroblast, pericyte, endothelial cells and tenocytes [240,287]. Myofibres can be prepared within 3 hours of surgical excision and can be cultured *ex vivo* for at least 8 days which reflects satellite cell expansion, differentiation and *de novo* human myofibre formation. The ability to directly assay genetic pathways in human satellite cells in a relevant context provides an exciting opportunity for pre-clinical testing and to develop causative relationships in human satellite cell signalling. As a proof of principle, we show stimulation of the EGFR pathway augments satellite cell expansion and production of myogenic progenitors in culture. This method holds the potential to accelerate therapeutic development and translation into viable clinical options. We expect method refinement will allow a personalized approach where a non-essential muscle is excised from patients and therapeutics are tested ex-vivo to determine clinical efficacy and treatment direction.

## RESULTS

### Human *Psoas* muscle is amenable for satellite cell culture *in situ*

To evaluate our hypothesis that human myofibres could be cultured in a laboratory setting, we decided to isolate primary human tissue from cardiorespiratory deceased organ donors following ethics approval and informed consent. We evaluated muscle

groups for suitability in myofibre culture where surgical access to both tendinous insertions is feasible and where myofibres are short to facilitate manipulation in a laboratory setting with common plasticware and reasonable reagent volumes. We identified the small muscles of the hand, including the *Abductor* or *Flexor Pollicis Brevis*, the *Flexor Digitorum Brevis* of the foot or the *Pronator Quadratus* of the forearm would be ideal candidates due to their size and accessibility, however availability of these muscles limited laboratory testing. We reasoned that an alternative strategy would involve isolating muscle with large angles of pennation, where individual myofibres are aligned at an angle oblique to the longitudinal angle of muscle contraction. These muscles provide a mechanical advantage over shorter contraction distances and possess shorter myofibre fascicles attaching to fibrous aponeuroses running along the periphery of the muscle. These muscle types would also allow myofibre isolation from partial muscle dissections.

We identified the human *Psoas* minor muscle as a moderately pennate muscle attached to the T12 vertebrae and the Lacunar ligament (Figure 31A) as a good candidate to isolate myofibres. We obtained muscle samples from neurologically determined deceased organ donors ranging from 61±9.4yr in age. Muscle samples were 24.35 ±13.56g in mass and 11.42±2.15cm in length.

Mouse myofibre isolation requires enzymatic digestion of the extracellular components from isolated mouse *Extensor Digitorum Longus* muscle in order to release single myofibres amenable for culture. To test if human *Psoas* myofibres could be prepared in a similar manner, we subjected myofibre isolated *Psoas* minor biopsies to collagenase digestion. Isolated *Psoas* minor muscle was resistant to digestion using collagenase Type 1, Type 2, Type 3, Type 4, Type 5, Type 6, Type 7 or Elastase buffers due to the thick perimysium, endomysium, extracellular matrix (ECM) and vascular

networks present (data not shown). Thus, the established methods of myofibre isolation from mouse studies are not appropriate to human myofibre isolation.

To further evaluate if human myofibres could be maintained in culture we manually dissected myofibre bundles from *Psoas minor* samples from tendon to tendon (Figure S20A). Manually dissected myofibril bundles contained 220 ±63 myofibres (Figure 31C) and were 1.9±0.5mm in diameter (Figure 31D). Myofibre bundles displayed heterogeneous viability, where excess tension during surgical excision or processing resulted in samples containing hyper contracted myofibres which were excluded from further analysis (Figure S20A). Successful myofibre preparations contained intact myofibres where 83±5% of myofibres within a bundle did not exhibit any signs of hyper contraction or injury (Figure 31E). Injured myofibres can be distinguished into hypercontracted myofibres, moderately injured and minor injured subgroups. Hypercontracted myofibres (Figure S20B) show bisected myofibre segmentation within an extracellular matrix scaffold while myofibres with moderate damage (Figure S20C) exhibit widespread disorganization of sarcomeric banding and significant autofluorescence. Myofibres with minor damage (Figure S20D) exhibit focal autofluorescence and invagination of the extracellular matrix but maintain myofibre-cell-ECM contact. Quantification of sarcomere spacing through α-Actinin staining (Figure 31F, Figure S20E-F) showed significantly shorter sarcomere banding in contracted myofibres, where healthy myofibres can be maintained in culture for at least 8 days without myofibre contraction or loss of sarcomere disorganization. Together this data suggests that human *Psoas* myofibre bundles can be isolated and maintained in culture without consequence to myofibre integrity.

Mouse and human myofibres exhibit different histological characteristics, where human skeletal muscle generally lack glycolytic myosin heavy chain type IIb (MyHC IIb)

muscle fibres in favour of type IIx [288]. Additionally, myofibre type has an impact on satellite cell response to exercise, where satellite cells resident to oxidative MyHC type I human muscles show augmented expansion following aerobic training [289]. We hypothesized that myofibre type would influence satellite cell fate in human *Psoas* myofibre cultures and could confound translating signalling pathways identified in mice to human satellite cells. We evaluated myofibre type and histological profiles of human *Psoas* myofibre bundles, mouse *Extensor Digitorum Longus* (EDL) and mouse *Psoas* myofibres to better correlate difference in rodent and human satellite cell biology. Isolated human *Psoas* myofibre bundles were composed of mixed 36.5±3.1% slow (Type I) and 63.5±6% fast (Type IIa, IIx) myofibres compared to 14.4±2% Type IIa and 62.5±1.2% Type IIb fast twitch mouse *Psoas* or 11±1.2% Type IIa and 72.9±0.7% Type IIb EDL muscles (Figure S20G). Human *Psoas* myofibres do not significantly differ in minimum fibre Feret (Figure 31H) or myofibre surface area (Figure S20I) compared to mouse *Psoas* or EDL fibres where a subset of human *Psoas* myofibres are hypertrophic (Figure 31I, Figure S20J). Human myofibres however are roughly 10-fold longer than mouse *Psoas* or EDL myofibres (Figure 31J-K) (36.4±0.4mm vs 3.34±0.05mm and 3.60±0.12mm). Taken together, this data suggests that human *Psoas* myofibres display distinct histological characteristics from mouse *Psoas* or EDL muscle.

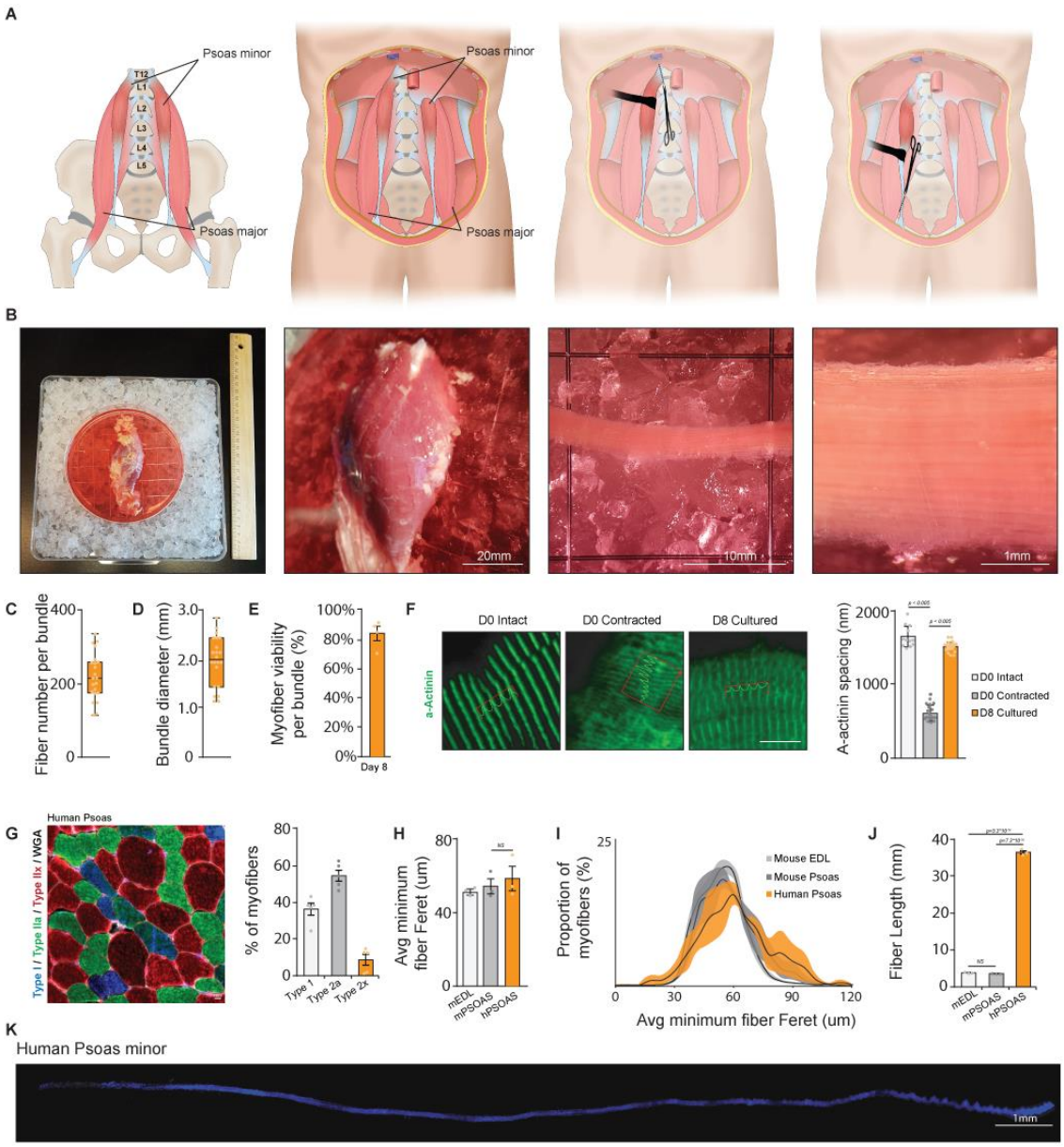


Figure 31: **Human *Psoas minor* muscle is amenable for myofibre culture.** A) Graphic overview of anatomical dissection of *Psoas minor* muscle from organ donors. B) Photographic overview of myofibre bundle isolation from surgically removed human *Psoas minor* muscle. Quantification of C) single myofibres per bundle and D) myofibre bundle diameter, whiskers represent min and max values. E) Myofibre viability as quantified by the presence of hypercontracted myofibres. F) Representative images and quantification of myofibre sarcomere spacing from intact, contracted and cultured myofibres stained with α-Actinin (Green). G) Representative image and quantification of human *Psoas* fibre type stained for Type I myofibres (Blue), Type IIa myofibres (Green), Type IIx myofibres (Red) and Wheat germ agglutinin (White). H) Quantification of average minimum fibre Feret and I) minimum myofibre Feret proportion of myofibres from human *Psoas* myofibres compared to mouse *Extensor Digitorum Longus* and mouse *Psoas* muscles using SMASH software. J) Quantification of human *Psoas* myofibre length compared to mouse *Extensor*

*Digitorum Longus* and mouse *Psoas* muscles. K) Representative image of a single isolated human *Psoas minor* myofibre stained with DAPI (Blue). (C-D, F) Error bars represent means ±SD, (E, G-J) Error bars represent means ± SEM; p-values are listed. (C-D) n= 22 myofibre bundles, (E) n=4 biological replicates, (F) n= averages from 12-19 myofibres per condition, (G) n=5 biological replicates. (H-J) n = 3 biological replicates.

**Human satellite cells expand in myofibre culture**

Satellite cells remain mitotically quiescent but are poised to activate and enter the cell cycle in response to extrinsic cues such as exercise or trauma [5]. In rodents, this can be achieved by experimental models of injury, muscle digestion for stem cell isolation [249,250] or in the case of myofibre preparation, digestion with collagenase and exposure to growth factors in cell culture [278]. To evaluate if human satellite cells from *Psoas* myofibre cultures spontaneously activate in vitro, we evaluated basal satellite cell numbers immediately following surgical excision and during culture where we analyzed an average 1.8±1.1mm length of myofibres per experiment (Figure S21A).

Human *Psoas* muscle has generally more satellite cells per $mm^2$ (15.7 ±3.0) compared to mouse *Psoas* (9.5 ±0.5) or EDL myofibre cross-sections (10.0 ±0.36) following immunofluorescence staining for Pax7 (Figure 32A). We observed by immunofluorescence staining for Pax7 that human *Psoas* myofibres with centrally located nuclei possess significantly increased (75.1%, 8.67±1.6 vs 15.2±3.1) satellite cells per mm of myofibre (Figure S21B-C) possibly due to prior injury.

Human *Psoas* satellite cells reside within the niche at isolation (Figure 32B) where 88.0±3.8% of human satellite cells express the cell surface marker Syndecan-4 (Figure 32C, Figure S21D-E) and 34.5±10.2% heterogeneously express M-Cadherin (Figure 32D, Figure S21F). Most satellite cells maintain Syndecan-4 expression in culture (93.0 ±5.2%) (Figure S21E) and do not express the apoptotic marker Annexin-5 (Figure S21D). To evaluate myofibre integrity and maintenance of cell-cell and ECM interactions throughout

culture, myofibre bundles were subject to scanning electron microscopy. Electron micrographs (Figure 32E) show myofibre bundles exhibit no apparent tearing or porosity and maintain complex cell-cell and cell-ECM interactions following 8 days in culture. This data suggests human satellite cells expand locally in response to prior trauma and express and maintain Syndecan-4 expression throughout culture.

To directly assess satellite cell expansion in culture, we quantified satellite cell numbers throughout culture and double labelled with Pax7 and Ki67 to assess human satellite cell proliferation. We observed no change in total nuclei per mm of myofibre following 8 days in culture (Figure 32G) with a concomitant increase in proliferating satellite cells (0.017± 0.02 vs 22.7±3.4 per mm myofibre day 8) (Figure 32H) and other cell types (0.65±0.3 vs 6.9±0.5 per mm myofibre day 8) (Figure S21H). Following 8 days in culture, human satellite cells make up 30±3.7% of total nuclei along myofibres (Figure 32I). As the number of activated satellite cells heterogeneously increases at day 4 (Figure 32H, Figure S21I), the first satellite cell divisions likely occur between day 3 and day 4 in culture (Figure 32H-I), where the biological variance between samples is greater than that between myofibres (Figure S21J). Following 8 days in culture, most satellite cells (91.8±2.1%) express Ki67 (Figure 32J). Taken together, this data suggests satellite cells actively proliferate in culture along with other resident cell types.

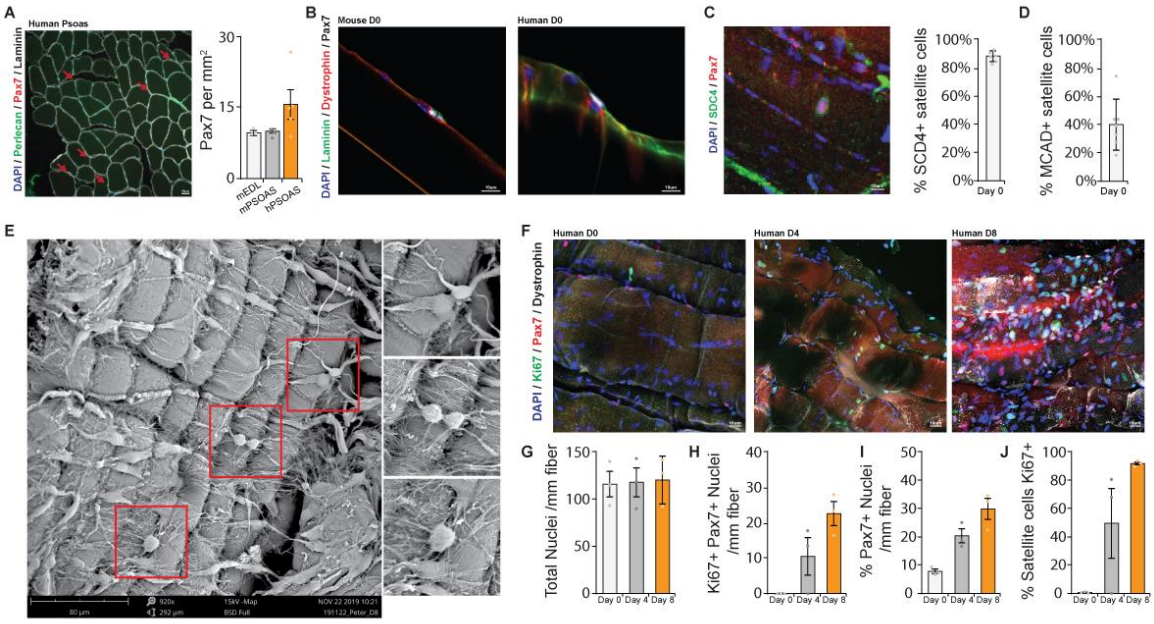


Figure 32: **Human satellite cells expand in culture.** A) Representative image and quantification of satellite cell density from human *Psoas* minor muscle cross-sections stained with DAPI (Blue), Perlecan (Green), Pax7 (Red) and Laminin (White). B) Representative images of mouse and human satellite cells in the niche at isolation stained for DAPI (Blue), Laminin (Green), Dystrophin (Red) and Pax7 (White). C) Representative image and quantification of human satellite cells expressing Syndecan-4 (SDC4) at isolation stained with DAPI (Blue), Syndecan-4 (Green) and Pax7 (Red). D) Quantification of human satellite cells expressing M-Cadherin (MCAD) at isolation. E) Representative scanning electron micrograph of cultured human myofibres (day 8) showing maintenance of myofibre extracellular matrix composition and cell-cell contacts. F) Representative images of human myofibres in culture from day 0, day 4 and day 8 stained with DAPI (Blue), Ki67 (Green), Pax7 (Red) and Dystrophin (White). Quantification of G) total nuclei per mm of myofibre, H) satellite cells expressing Ki67 per mm of myofibre, I) the percentage of satellite cells per total nuclei per mm of myofibre, J) proportion of satellite cells expressing Ki67 on myofibres. (C-D) Error bars represent mean ±SD. (A, G-J) Error bars represent mean ±SEM; (A) n = 3 biological replicates for mEDL, m*Psoas*, n=5 biological replicates from h*Psoas*. (C) n = averages from 6 myofibres. (D) n = averages from 7 myofibres. (G-J) n = 3 biological replicates.

**Satellite cell expansion and production of differentiated progeny can be tuned *in situ***

To evaluate the possibility of human satellite cells undergoing apical-basal oriented asymmetric division, we examined myofibres by immunofluorescence staining throughout culture. Interestingly we observed rare apicobasal and planar oriented satellite cell

doublets expressing Pax7 and residing in the niche from samples fixed at isolation and stained with Pax7, Perlecan and Dystrophin (Figure S22A-B) suggesting homeostatic repair mechanisms may undergo either mode of division. We additionally examined culture day 3 to day 4, a time point reflecting the first division in human satellite cells in culture. Strikingly, staining for the protein Dystrophin (DMD), which can be polarized in mouse satellite cells to facilitate asymmetric division [7], shows strong expression and polarity on the basal surface of a subset of cultured satellite cells (Figure 33A, Figure S22C). This suggests that human satellite cells can polarize dystrophin to their basal surface interfacing with the extracellular matrix.

To evaluate myogenic differentiation in *Psoas* myofibre culture, we examined myofibres by immunofluorescence staining for Myogenin (MyoG). Culturing *Psoas* myofibres for 8 days results in significant presence of MyoG-expressing cells (20.8 ±1.8 per mm myofibre), where 13.5±1.3% of all cells express MyoG (Figure 33B, Figure S22D). We found an average of 95.4±6.2 myogenic cells per mm expressing either Pax7 or MyoG (Figure 33D) where MyoG-expressing differentiating satellite cell progeny represent 21.8%±0.6 of the myogenic cell population (Figure 33D). Additionally, by 8 days in culture we can observe de novo myofibre formation occurring characterized by multiple aligned small myofibres expressing MyoG (Figure S22E-F) suggesting human *Psoas* myofibre culture may represent a paradigm to model human satellite cell activation, differentiation and myofibre formation. This data suggests that by 8 days in culture, human *Psoas* satellite cells expand in number and express differentiation markers including MyoG.

We have previously established that mouse satellite cells express EGFR that is polarized prior to an asymmetric cell division to orient the satellite cell mitotic spindle in an apical-basal orientation [101]. To evaluate if human *Psoas* satellite cells integrate EGFR signalling, cultures were treated with EGF ligand to stimulate EGFR activation. Following

EGFR stimulation, myofibres were stained for the presence of phosphorylated EGFR, where most satellite cells express p-EGFR (Figure 33E-F). This data suggests that the EGFR signalling pathway is activated following EGF treatment in human satellite cells.

To evaluate if EGFR augmented production of myogenic progeny through the promotion of asymmetric division as shown previously [101], we examined fibres by immunofluorescence for Pax7, MyoG and Ki67. Quantifying total nuclei per mm of fibre show no significant change following 8 days of EGF treatment (Figure S22G), however, treatment with EGF results in an appreciable increase in the number of proliferating satellite cells per mm of myofibre (56.7% paired, 78% unpaired, n=3 control, n=2 EGF) (Figure 33G, Figure S22H) and an increased proportion of satellite cells per myofibre (29% increase unpaired, 15% increase paired, n=3 control, n=2 EGF) (Figure S22I). Interestingly, EGF treatment resulted in an increased the number of Ki67 negative satellite cells per mm of myofibre (161% increase unpaired, 118% increase paired, n=3 control, n=2 EGF) following 8 days in culture treated with EGF or vehicle control (Figure 33H, Figure S22J). Concomitant with an increase in proliferating satellite cells, EGF treatment resulted in an appreciable increase in MyoG-expressing cells per mm of myofibre (69% increase unpaired,78% increase paired n=3 control, n=2 EGF) (Figure 33I, Figure S22L).

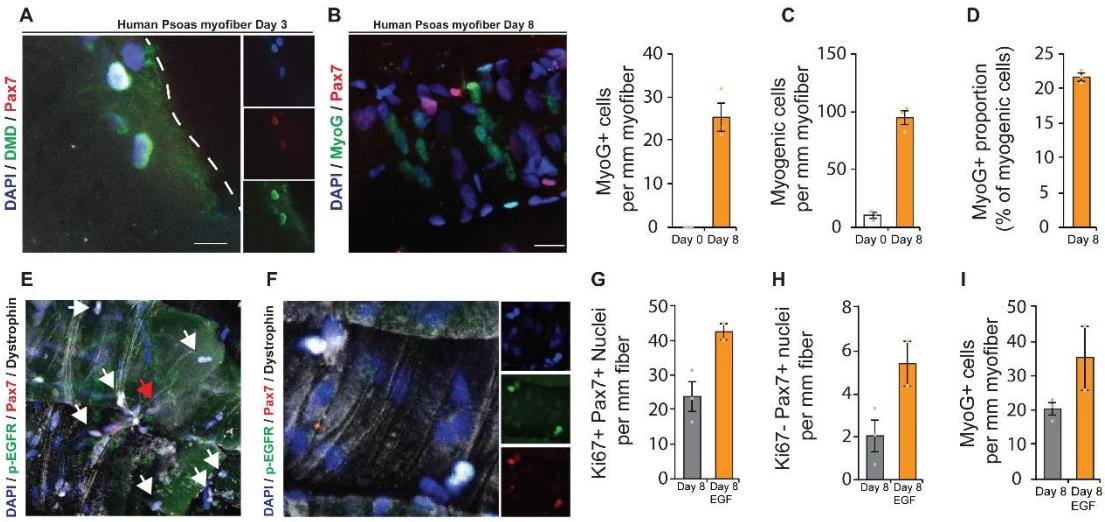


Figure 33: **Human satellite cell expansion and differentiation can be tuned in situ.** A) Representative image of human satellite cells cultured for three days and stained with DAPI (Blue), Dystrophin (Green) and Pax7 (Red). B) Representative image and quantification of human satellite cells and Myogenin (MyoG) expressing differentiating progenitors cultured on human *Psoas* minor myofibre cultures stained with DAPI (Blue), MyoG (Green) and Pax7 (Red). Quantification of C) number of Pax7 or MyoG-expressing myogenic cells per mm of myofibre and D) proportion of MyoG+ myogenic cells. E-F) Representative images of human satellite cells expressing phosphorylated active EGFR (p-EGFR) stained with DAPI (Blue), p-EGFR (Green), Pax7 (Red) and Dystrophin (White). Quantification of G) satellite cells expressing Ki67 per mm of myofibre and H) Ki67 negative satellite cells per mm of myofibre following EGF treatment or vehicle control of human myofibres. H) Quantification of the number of MyoG-expressing cells per mm of myofibre following EGF treatment of human myofibres. (B-D, G-I) Error bars represent means ± SD (EGF) and means ± SEM (Control); (B-D) n = 3 biological replicates. (E-H) n = 3 biological replicates control, n = 2 biological replicates EGF. (I) n = 3 biological replicates control, n = 2 biological replicate EGF.

## DISCUSSION

Evaluating human stem cell dynamics in a physiologically relevant context is critical to model biological phenomena and generalize results to benefit human health. New methods to improve the evaluation of pre-clinical therapeutics in augmenting endogenous stem cell activity hold promise to improve regenerative medicine outcomes in conditions such as Duchenne's Muscular Dystrophy. Here we developed a novel system to evaluate human satellite cell fate choices in a physiologically relevant context to interrogate human

satellite cell biology and evaluate pre-clinical therapeutics in improving muscle regeneration.

A balance in satellite cell proliferation, production of myogenic progeny and return to quiescence is critical to maintaining muscle repair over a lifetime. Asymmetric stem cell division is one method to balance stem cell maintenance and production of myogenic progeny, where following division one daughter cell maintains its stem cell state and one differentiates down the myogenic lineage. Asymmetric cell division is established through cells integrating extrinsic environmental ques to restrict cell fate determinants in a polarized manner such that when oriented parallel with the angle of division, daughter cells will receive discrete cellular contents [5]. Typically, in mouse satellite cells, the daughter cell maintaining niche interactions with the basal lamina maintains its stem cell nature. Establishment of an apical-basal oriented mitotic spindle is in part facilitated by the PAR polarity complex, where we have previously shown EGFR is spatially restricted prior to mitotic divisions to orient centrosomes through recruitment of Aurora kinase A and spindle assembly [101]. We hypothesized that as human *Psoas* myofibres maintain myofibre and extracellular matrix composition that human satellite cells in culture could integrate three-dimensional external cues to influence cell fate.

Our findings support that human *Psoas* myofibre cultures provide a unique opportunity to culture human satellite cells to explore fate choices during satellite cell activation and differentiation. In our system, myofibre integrity is maintained (Figure 31, Figure S20) as well as cell polarity cues (Figure 32B, E, Figure 33A, Figure S22C) where treatment with EGF results in augmented production of myogenic progeny (Figure 33G-I). As EGF treatment also increases the number of non-satellite cells expressing Ki67 (Figure S22K), it is possible that EGF influences cell survival or is acting as a mitogen on the varied cell populations within myofibre cultures. Further studies exploring other resident

cell types such as fibroblast, pericyte and fibroadipogenic precursor cells will better evaluate the specificity of EGF in culture. Additionally, studies exploring growth factor and oxygen penetration in myofibre bundles through staining of growth factors and incubation in oxygen sensing compounds such as Hypoxy Probe labels would further evaluate the potential effect of nutrient availability on heterogeneity in satellite cell activity within bundles.

Small sample sizes (Figure S22H, L) limit the generalizability of drawn conclusions however the data could be interpreted that an increase in the number of non-proliferative satellite cells following EGF treatment is not due to EGF acting as a general mitogen. Additionally, increased proliferating satellite cells and increased formation of myogenic progeny could be interpreted as stimulated asymmetric division resulting in a larger pool of non-cycling stem cells and a more efficient production of proliferative myogenic progeny. Further studies are required to increase biological sample sizes and delineate the role of EGF on human satellite cells. Taken together, the human *Psoas* muscle provides an exciting tool to explore in niche satellite cell biology and facilitate translation of pre-clinical therapeutics from studies in model organisms to humans.

Previous studies have developed methods to assess human satellite cell expansion in vitro from primary tissue [290] through the culture of human myofibre fragments from punch biopsies. Myofibre fragments contained 1-8 bisected myofibres 2-3mm in length and by 10 days in culture 80% of nuclei were Pax7+ with a significant amount of Desmin expressing cells within the myofibre [290]. Transplantation of whole myofibre fragments resulted in limited engraftment into mouse recipients. Differences in timepoints and muscle groups assessed between our study and others [290] limit comparisons, however in our hand's injury to the myofibre through hyper contraction or bisection results in disorganized myofibre sarcomeres (Figure 1F) and altered myofibre-ECM interactions

(Figure S20B-C) where only minor focal damage is tolerated along myofibres to maintain myofibre-cell-ECM interactions (Figure S20D). Additionally, cell polarity is maintained in *Psoas* myofibre culture (Figure 33A, Figure S22C) and by 8 days ~50% of cells express Pax7 and ~14% represent committed progeny. Differences between the models could be attributed to differential activation ques, non-satellite cell survival or differential activation in different muscle groups. This suggests human *Psoas* myofibre culture may reflect a model of homeostatic turnover or response to minor injury such as load induced trauma or de-innervation, while human myofibre fragments may represent a paradigm of rapid satellite cell activation in response to widespread myofibre damage. Both human myofibre bundles and myofibre fragments present powerful tools to asses human satellite cell biology, however further studies are required to evaluate each model's generalizability to human muscle repair in conditions of acute injury (volumetric muscle loss, trauma, sports injury), homeostasis (ageing, muscle hypertrophy) and disease such as DMD.

Assessing human muscle stem cells directly in a physiologically relevant context improves the generalizability in preclinical efficacy studies however a lack of human genetic models and inter-donor biological variability limit the establishment of causative relationships. Early time points in human *Psoas* culture harbour the potential for genetic modification using CRISPR-Cas9 or electroporation-based strategies to genetically modify human satellite cells and develop causative signalling relationships during satellite cell activation and differentiation. Expanding our studies, human *Psoas* culture poses and exciting opportunity to test transduction efficiencies of different AAV serotypes in quiescent and activated human muscle stem cells to help refine gene editing and replacement strategies targeting long term muscle repair in conditions such as DMD [99].

Isolating primary tissue from human patients for laboratory testing holds the potential for exciting interdisciplinary advancements in regenerative medicine. In 2018,

532 neurologically determined and 230 cardiorespiratory determined deceased organ donations were procured across 9 organ procurement organizations in Canada[291] with an additional 10,721 deceased organ donors in the United States [292]. Deceased organ donors can significantly improve the lives of others, where tissue isolation provides an additional method for patients to benefit medical research and translation posthumously. Future studies exploring routine surgical procedures exposing muscle groups appropriate for culture would establish a renewable source of human muscle to assess satellite cell physiology and therapeutic responses. We envision this method to be refined to be used as a personalized medicine approach for patients with muscular dystrophy and act as a tool for clinical decision making as DMD therapeutics become available. Additionally. applying this protocol to disease context such as DMD will provide a valuable avenue to better understand the consequence of dystrophin loss on the cellular dynamics of the satellite cells within the muscle environment.

We are currently pursuing methods to evaluate human satellite cell fate decisions in a highly multiplexed manner through iterative labelling of antibody-DNA conjugates [293]. This technique will provide a unique opportunity to validate known signalling pathways and explore the impact of pharmacological intervention on human satellite cell dynamics.

We are currently pursuing further studies evaluating satellite cell activation kinetics through pulsed EdU labelling, assessing the proportion of apical-basal oriented divisions during culture (Figure 33A, Figure S22C), clonal expansion through pulsed CellTrace labelling, and further evaluation of EGF stimulating de novo myofibre formation and muscle repair (Figure S22E-F), will better delineate the role of EGF on human satellite cell activation, division orientation and mitogenic activity in myofibre cultures. Evaluating pre-clinical lead compounds to augment satellite cell-mediated intrinsic repair in human myofibre cultures remains an exciting avenue for continued studies.

Our findings provide proof-of-principle evidence to support human muscle fibre culture as a novel paradigm to explore human satellite cell differentiation and self-renewal while also providing an opportunity to evaluate pre-clinical drug efficacy in a physiologically relevant manner. This method provides an opportunity to assay satellite cell heterogeneity, stem cell potential, stem cell hierarchy and activation kinetics in a physiologically relevant context with the potential to therapeutically interrogate pathways of interest. Additionally, this method provides a platform to validate phenomena observed in other model organisms, validate lead compounds for drug discovery and testing, reduce animal model use, and accelerate the evaluation of therapeutics improving human health. We envision this technique will aid in generalizing pre-clinical strategies into the clinical arena and may in the long term be appropriate as a personalized therapeutic tool.

## STAR METHODS

## KEY RESOURCE TABLE

| REAGENT or RESOURCE | SOURCE | IDENTIFIER |
|---|---|---|
| Antibodies | | |
| Mouse anti-Dystrophin | DSHB | Cat# MANEX1011B; RRID:AB_1157876 |
| Mouse anti-M-Cadherin | BD Biosciences | Cat# 611101, RRID:AB_398414 |
| Mouse anti-MHC | DSHB | Cat# MF 20; AB_2147781 |
| Mouse anti-MyH1 | DSHB | Cat# 6H1; AB_2314830 |
| Mouse anti-MyH2 | DSHB | Cat# SC-71; AB_2147165 |
| Mouse anti-MyH4 | DSHB | Cat# BF-F3; RRID: AB_2266724 |
| Mouse anti-MyH7 | DSHB | Cat# BA-F8; RRID: AB_10572253 |
| Mouse anti-MyoG | Novus | Cat# MAB66861; RRID:AB_10973343 |
| Mouse anti-Pax7 | DSHB | Cat# Ab528428; RRID: AB_528428 |
| Mouse anti-Syndecan-4 | Santa Cruz Biotechnology | Cat# sc-12766; RRID:AB_628314 |
| Mouse anti-α-Actinin | Sigma | Cat# A7732; RRID:AB_2221571 |
| Rabbit anti-Annexin-5 | Abcam | Cat# ab14196, RRID:AB_300979 |
| Rabbit anti-Ki67 | Abcam | Cat# ab15580; RRID:AB_443209 |
| Rabbit anti-MyoD | Abcam | Cat# ab133627 |
| Rabbit anti-p-EGFR | Cell Signalling technology | Cat# 3777S; RRID: AB_2096270 |
| Rat anti-Laminin | Sigma | Cat# L0663; RRID: AB_477153 |
| Rat anti-Perlecan | NSU Bioreagents | Cat# V2600; RRID:AB_2119238 |
| Wheat Germ Agglutinin Alexa 488 conjugate | Fisher | Cat# W11261 |
| Chemicals, Peptides and Recombinant Proteins | | |
| Chick Embryo Extract | MP Biomedicals | RRID 92850145 |
| Collagenase Type I | Worthington | Cat# LS004196 |
| Collagenase Type 2 | Worthington | Cat# LS004176 |
| Collagenase Type 3 | Worthington | Cat# LS004182 |
| Collagenase Type 4 | Worthington | Cat# LS004188 |
| Collagenase Type 5 | Worthington | Cat# LS005282 |
| Collagenase Type 6 | Worthington | Cat# LS005319 |
| Collagenase Type 7 | Worthington | Cat# LS005333 |
| Elastase | Worthington | Cat# LS006365 |
| Fibroblast Growth Factor-basic | EMD Millipore | Cat# GF003AFMG |
| ProClin950 | Sigma | Cat# 46879-U |
| Critical Commercial Assays | | |
| Human recombinant Epidermal Growth Factor | Miltenyi Biotech | Cat# 130-093-825 |
| TrueBlack | Biotium | Cat# 23007 |
| Software and Algorithms | | |
| GraphPad Prism | GraphPad Software Inc | https://www.graphpad.com/scientific-software/prism/ |
| ImageJ | NIH | https://imagej.nih.gov/ij/ |
| SMASH - semi-automatic muscle analysis using segmentation of histology | Smith and Barton, 2014 | http://figshare.com/articles/SMASH_semi_automatic_muscle_analysis_using_segmentation_of_histology_a_MATLAB_application/1247634 |

## CONTACT FOR REAGENT AND RESOURCE SHARING

Information and requests for reagents may be directed to the Lead Contact, Michael A. Rudnicki (mrudnicki@ohri.ca).

## EXPERIMENTAL MODEL AND SUBJECT DETAILS

### Experimental subjects

This study was approved by the Ottawa Hospital Research Ethics Board and informed consent was obtained prior to proceeding. Samples were harvested from patients consented for organ donation through the Trillium Gift of Life Network following cardiac death in compliance with guidelines from The Ottawa Hospital Research Ethics Board.

## METHOD DETAILS

### Histological Analysis of Muscle Cross Sections

Minimum fibre Feret and myofibre surface area measurements were performed using the semi-automated SMASH software plugin for MATLAB 2015a described previously [238]. Total myofibre count per cross-section was verified by manual validation of SMASH myofibre masks and original images. Myofibre types were counted manually across each cross-section studied.

### Human *Psoas* minor isolation

With the patient supine, the heart, lungs and kidneys are removed for organ donation as per standard operating procedures. A graphic overview of the procedure is provided in Figure 1A. *Psoas* minor muscle is exposed using Deaver retractors to visualize tendinous insertions into the T12 vertebrae. Tendinous insertion are cut immediately adjacent to the vertebra using a scalpel. The free proximal end of the *Psoas* minor is lifted, and connective tissue on the dorsal side is removed using blunt scissors to free the muscle. It is critical to minimize tension on the *Psoas* minor during dissection. Deaver retractors are used to expose the distal *Psoas* minor tendon insertion into the iliopectineal arch. The distal tendon is cut using scissors. The free *Psoas* minor is placed into sterile, cold transport media (DMEM, 110mg/ml Pyruvate) and maintained on ice during transport.

### Human myofibre preparation

In a sterile environment, *Psoas* muscle is placed in an appropriate vessel buffered with ice and containing enough transport media to submerge. A photographic overview of the procedure is presented in Figure 31A, Figure S20A. Using a dissecting microscope and blunt micro scissors, adipose tissue and free epimysium is dissected to visualize muscle fascicle tendon-tendon organization. Using blunt-tipped micro scissors and blunt-tipped tweezers fascicle boundaries are gently retracted and perimysium is cut to free fascicle bundles continuing along the fascicle boundaries without freeing bundles from the tendon. Fascicles are further dissociated to bundles containing ~200 muscle fibres by measuring with a precision micro ruler (TDI) to ensure ~2mm in diameter bundles are prepared. Using sharp micro scissors, tendons are cut to release free myofibre bundles avoiding injury to myofibres. Myofibre bundles are then placed in excess filtered myofibre culture media (DMEM, 110mg Pyruvate, 20% FBS, 25ng/ml bFGF, 1% Chicken Embryo extract - 25ml/bundle) and cultured at 37°C in normoxia. Media is changed every day. Following culture, myofibres are fixed by placement in excess warmed 4% paraformaldehyde for 5 minutes where excess 4% paraformaldehyde is then injected directly within myofibre bundles using an insulin syringe. Bundles are fixed for 30minutes in 4% paraformaldehyde. Bundles are then moved to 0.4% paraformaldehyde for 12h followed by extensive washing. Samples are maintained in PBS containing ProClin950 at 4°C for long term storage. For analysis of full-length bundles, individual myofibres may be isolated by retraction using blunt-tipped tweezers along the length of a myofibre bundle. For cross-sectional analysis of cultured bundles, bundles are frozen whole prior to fixing or fixed bundles are segmented, hydrated for 12h in a sucrose gradient and frozen by imbedding in OCT and freezing by nitrogen-cooled isopentane. For bundle analysis, fixed cultured myofibre bundles are manually dissociated to 5-15 myofibre bundles and segmented to length amendable to microscopic analysis and to improve antibody penetration.

**Immunostaining and Antibodies**

Myofibres and myofibre bundles are processed by identical means. Fixed myofibre samples are washed in PBS and permeabilized in 0.4% Triton-X100 for 1h with rocking. Samples are washed in PBS containing 125mM glycine 3x in the excess buffer until no appearance of detergent remains. Samples are blocked using TrueBlack as per manufactures instructions. Samples are then blocked in blocking buffer containing 5% normal donkey serum for 3h at room temperature to overnight at 4°C with rocking. Samples are washed in PBS and primary antibodies are applied for 24h at room temperature with rocking. Samples are washed in excess PBS 5x 30min each with rocking. Secondary antibodies are applied 24h at room temperature with rocking in the dark. Samples are washed in excess PBS for 30min with rocking and DAPI is applied for 1h with rocking. Samples are washed in excess PBS 5x 30min each with rocking in the dark. Samples are then passed through a serial 20-80% glycerol series and mounted onto slides in glycerol mounting media containing 0.1M n-propyl gallate.

Antibodies used in the study are as follows: Mouse anti-Pax7 (1:2, DSHB, Cat. no. Ab528428; RRID: AB_528428), rat anti-Laminin (1:1000, Sigma, Cat. no. L0663; RRID: AB_477153), Mouse anti-Dystrophin (1:500, DSHB, Cat. no. MANEX1011B; RRID:AB_1157876), Rabbit anti-p-EGFR (1:250, Cell Signalling technology, Cat. no. 3777S; RRID: AB_2096270), Mouse anti-M-Cadherin (1:500, BD Biosciences Cat. no. 611101, RRID:AB_398414), Rabbit anti-MyoD (1:500, Abcam, Cat. no, ab133627), Mouse anti-Syndecan-4 (1:500, Santa Cruz Biotechnology Cat. no. sc-12766; RRID:AB_628314), Rabbit anti-Annexin-5 (1:500, Abcam, Cat. no. ab14196, RRID:AB_300979), Mouse anti-MyoG (1:500, Novus, Cat. no. MAB66861; RRID:AB_10973343), Mouse anti-α-Actinin (1:1000, Sigma, Cat. no. A7732; RRID:AB_2221571), Mouse anti-MHC (1:1000, DSHB, Cat. no. MF 20; AB_2147781), Mouse anti-MyH2 (1:100, DSHB, Cat. no. SC-71;

AB_2147165), Mouse anti-MyH1 (1:100, DSHB, Cat. no. 6H1; AB_2314830), Mouse anti-MyH4 (1:100, DSHB, Cat. no. BF-F3; RRID: AB_2266724), Mouse anti-MyH7 (1:100, DSHB, Cat. no. BA-F8; RRID: AB_10572253), Rat anti-Perlecan (1:500, NSU Bioreagents, Cat. no. V2600; RRID:AB_2119238), Rabbit anti-Ki67 (1:1000, Abcam, Cat. no. ab15580; RRID:AB_443209), Wheat Germ Agglutinin Alexa 488 conjugate (1:1000, Fisher, Cat. no. W11261).

**Scanning Electron Microscopy**

Samples were washed with water prior to dehydration in a 35%-100% graded series of ethanol. Samples were critical point dried in dry 100% ethanol using liquid CO2 as transition fluid. CO2 was exchanged at 5-minute intervals for 8 rounds followed by a final 3h release. Samples were maintained under dust-free desiccation following critical point drying. Samples were mounted on aluminum stages using double-sided carbon tape. Mounted samples were sputter-coated with gold for 1min (~10nm) and stored under dust-free desiccation prior to imaging on a phenom Pro-X scanning electron microscope at an accelerating voltage of 15kV.

**Imaging and analysis**

Human *Psoas* myofibre bundles were analyzed on a Leica TCS SP8 confocal microscope equipped with HC PL APO 20x IMM CORR objective with HyD and PMT detectors. Filters and detectors were set to maximal bandwidth and sensitivity to limit bleed-through between channels. Tile scans were stitched directly following acquisition using the Leica LAS AF software. Manual image analysis was performed using ImageJ and presented images that represent maximum intensity projections unless stated otherwise. Myofibres partially encompassed in Z-stacks were excluded form analysis.

**QUANTIFICATION AND STATISTICAL ANALYSIS**

Compiled data are expressed as mean ± standard deviation (SD) or mean ± standard error of the mean (SEM) as stated. Experiments were performed with a minimum of three biological replicates unless stated otherwise. For statistical comparisons of two conditions, the Student's t-test was used for biologically matched samples and unpaired testing was used for unrelated samples. P-values are provided for each statistical test performed. No data were removed as outliers. The experimental design incorporated user blinding when possible. Statistical analysis was performed in GraphPad Prism or Microsoft Excel. The level of significance is indicated as follows: * $p < 0.05$, ** $p < 0.01$, *** $p < 0.005$.

## General discussion

These studies aimed to explore the regulation and mechanisms governing satellite cell fate choices to the myogenic or adipogenic lineage. We show that cell fate is actively maintained by microRNA-mediated translational silencing and that the stem cell niche regulates the fate of activated satellite stem cells. Improving our understanding of the molecular mechanisms governing satellite cell fate will help identify new therapeutics improving endogenous muscle repair and metabolic health in humans.

The balance in satellite cell fate choices impacts regenerative outcomes, where over or inactive self-renewal mechanisms can lead to hyper- or hypoplasia of the stem cell pool and impairments in muscle repair. Satellite cell homeostasis is maintained by a balance in the symmetric expansion of the satellite stem or satellite myogenic cell pool, asymmetric division of satellite stem cells producing self-renewing and myogenic progeny as well as cell-intrinsic differentiation processes in myogenic progenitors. We are beginning to understand the processes regulating satellite cell fate, their relationship with the satellite cell niche and its feedback on satellite cell homeostasis (Reviewed in [5]). These studies highlight the complex networks of intrinsic and extrinsic signals exposed to satellite cells and their integration of fate determinants in a spatial and temporal manner.

### Manuscript 1: General discussion

In manuscript I, we set to identify key regulators of *miR-133* activity to better understand the regulation of satellite cell adipogenic differentiation. We identified the p53 pathway as a potent regulator of *miR-133* activity in satellite cells and their myogenic progeny. We observed that p53 activity promotes *miR-133* processing to facilitate myogenic differentiation through a currently unknown mechanism. Transient p53 inhibition using the drug Pifithrin-α resulted in satellite cell fate switching to the brown adipogenic lineage. Our

report represents a previously unknown function for p53 in regulating satellite cell fate through the processing of *miR-133*.

Interestingly, p53 expression has been observed to be asymmetrically activated in myofibre cultures and suggested to promote stem cell quiescence[294]. In these studies, improper comparisons between myofibre cultures and myoblasts, microarray analysis of mixed populations and a lack of correlation between p53 levels and markers of differentiation limit interpretation. One possible explanation could be that p53 dosing within the cell may result in discrete cellular responses, where p53 induction by Nutlin-3 treatment results in super-physiological levels of p53 to induce cell cycle exit and senescence thereby limiting myogenic differentiation[295]. We show transient p53 inhibition results in mild repression of myogenic differentiation through altered processing of *miR-133* similar to mild repression in differentiation observed in $p53^{-/-}$ myoblasts[159]. Future studies exploring molecular partners of p53 during myogenic differentiation will better evaluate its role during normal cell processes.

Previous reports have highlighted the importance of p53 during brown adipogenic differentiation[296] where $p53^{-/-}$ mice generally have less interscapular BAT with roughly half the level of thermogenic gene expression and protein. In C2C12 cultures overexpressing a PRDM16 expression vector, p53 knockdown resulted in blunted brown adipogenic differentiation[296]. We believe this highlights the importance of p53 for terminal brown adipocyte differentiation, where transient p53 inhibition (Manuscript I) can facilitate a myogenic to brown adipogenic fate change whereupon p53 activity facilitates terminal differentiation and cell cycle exit.

The p53 inhibitor Pifithrin-α rapidly undergoes a condensation reaction at 37°C in culture into Pifithrin-β which remains thermostable[297]. Our observed effects *in vitro* and *in vivo* studies, therefore, are likely due to a mixture of both Pifithrin-α and -β however our

studies using *si-p53* and the Pax7Cre$^{ER}$;p53 mouse model highlight the role of the p53 pathway in regulating *miR-133* activity *in vitro* and *in vivo*. Future studies exploring the metabolic improvements in mice treated with Pifithrin-α will better evaluate its potential as a therapeutic improving weight loss.

The tumour suppressor p53 has wide-ranging functions with context and cell type-specific outcomes[298]. The p53 pathway plays an important role in cell commitment, where p53 deletion improves spontaneous reversion to multipotency in germline stem cells and enhances reprogramming rates 100-fold during iPSC generation through multiple mechanisms[299]. Due to the pleiotropic effects of p53, speculating to its mechanistic role a myogenic context can be misleading. Nonetheless, as we observed p53 inhibition resulted in no change in *pri-miR-133* isoforms but a striking reduction in mature *miR-133* (Figure 8), it would suggest that the processing of *pri-miR-133* to its precursor or *pre-miR-133* to mature form is promoted by p53 activity under normal conditions. The regulation of *miR-133* processing therefore could be dependent on p53 activity during pri-miRNA processing, pre-miRNA export to the cytoplasm, pre-miRNA processing to mature miRNA, or *miR-133* half-life in the cytoplasm (Figure 34). It is reasonable to assume that as the main role of p53 is to act as a transcription factor[300], together with the observation that p53 inhibition does not alter other miRNA levels such as *miR-206* (Figure 6), and that p53 can bind RNA in a base independent manner [301], that p53 is likely acting through a sequence-specific RNA binding protein (RBP) intermediate to regulate *miR-133* processing. By the principle of *lex parsimoniae*, it is likely p53 directly promotes or represses the transcription of an RBP that regulates *miR-133* processing.

Identification of precursor RNA binding partners is possible *in silico* using RBPmap[302] where *pri-miR-133a1, pri-miR-133a2* and *pri-miR-133b* share multiple RNA binding proteins including the serine/arginine-rich splicing factor 3 (SRSF3), RNA Binding

Motif Protein 46 (RBM46), Polypyrimidine tract-binding protein 1 (PTBP1), Muscleblind Like Splicing Regulator 1 (MBNL1) and CUG-BP, Elav-like family 1 (CELF1) (data not shown). These RNA binding proteins have known roles in mRNA splicing where SRSF3 promotes splicing of the iron-sulphur cluster assembly (ISCU) gene important in the TCA cycle[303], PTBP1 represses aberrant ISCU splicing in muscle[304], MBNL1 blocks *pre-miR-1* and *pre-miR-206* processing in myotonic dystrophy[305] and CELF1 hyperphosphorylation contributes to RNA toxicity in myotonic dystrophy[306]. Interestingly, CELF1 inhibition in non-disease states resulted in a mild regenerative phenotype and an increased proportion of slow-twitch myofibres[306], similar to our observations (Manuscript I). Additionally, RBM46 is a nuclear RNA-binding protein highly enriched in brown pre-adipocytes compared to myoblasts or mature adipocytes[307]. Analyzing the putative promoters of these RBP using the JASPAR database[308], shows promoters from RBM46, CELF1 and MBNL1 possess at least one high confidence putative p53 response element (data not shown). The potential of these RBP to alter *miR-133* processing and their potential regulation by p53 is yet to be determined however future studies correlating biotinylated precursor *miR-133* pulldowns from control or PFTα treated myoblasts followed by mass spectroscopy will better identify a mechanistic link between p53 and binding partners in an unbiased manner. Additionally, studies exploring the direct role of p53 on *miR-133* maturation through northern blotting of pri-, pre- and mature *miR-133* and subcellular fractionation will better identify the subcellular loci affected by p53 inhibition.

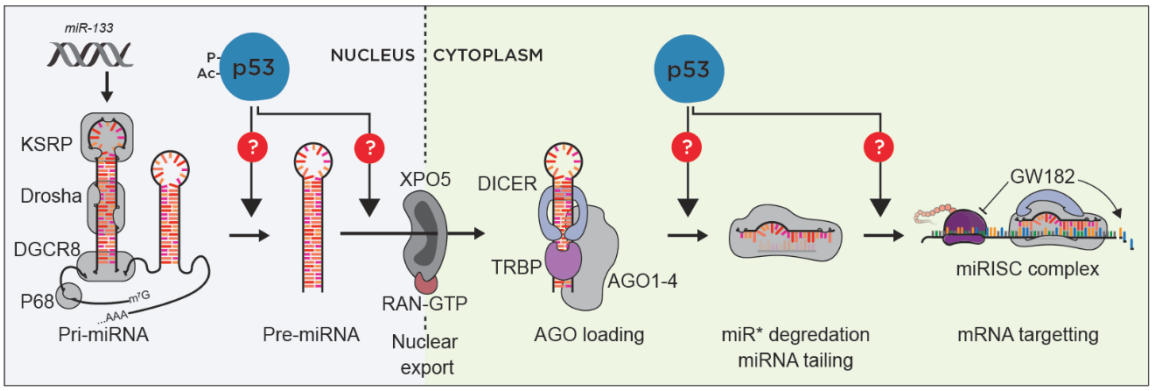


Figure 34: **Theoretical schema of p53 method of action on *miR-133* processing.**

**Manuscript II-IV: General discussion**

Muscle diseases such as DMD can be targeted therapeutically through gene therapy or augmentation of endogenous repair (Figure 4). Current strategies restoring dystrophin expression show some clinical efficacy[93,95] and advancements in AAV mediated delivery of CRISPR-Cas9 constructs show re-expression of dystrophin in mice with some repair in satellite cells[100,225]. Viral mediated delivery of micro-dystrophin constructs also show years-long restoration of dystrophin into satellite cells and muscle[309] however truncation of the DMD gene for packaging into AAV vectors[310] resulted in the loss of Par1b binding sites. Micro-dystrophin constructs would, therefore, restore myofibre integrity however would not rescue polarity deficits in dystrophin-deficient satellite cells and therefore only partially rescue the underlying cause of DMD. Therapeutics promoting endogenous repair such as Stat3 inhibition[175], p38MAPK inhibitors[176], Wnt7a treatment[280] or EGF[101] (Manuscript II) can partially rescue regeneration in dystrophic muscle by promoting alternative cell polarity pathways or by rescuing asymmetric division in satellite cells. Implementing multi-faceted approaches to restore myofibre integrity and improve satellite cell-mediated repair would likely improve clinical outcomes.

During the temporal process of muscle regeneration, satellite cells exit quiescence and enter the cell cycle to facilitate the production of myogenic progeny. The mode of

satellite cell division can impact the kinetics and efficiency of muscle repair. During the initial stages of repair, satellite cells undergo asymmetric division stimulated by EGFR ligands[101] and the dystroglycan complex[178] to form a large number of amplifying progenitors to facilitate repair. Upon reaching a critical mass, myoblasts differentiate to form new muscle. Evidence suggests that Myf5$^{Neg}$ satellite stem cells then integrate ques including Wnt7a from newly formed myofibres to expand their numbers symmetrically to enlarge the stem cell pool[279]. Changes to the initial fate decisions in satellite cells can impact regenerative outcomes in an exponential manner through symmetric expansion producing more stem cells able to generate more amplifying progenitors in subsequent divisions or asymmetric division facilitating a balanced production of stem and progenitor cells. A balance between these two processes maintains efficient long-term muscle repair (Figure 35).

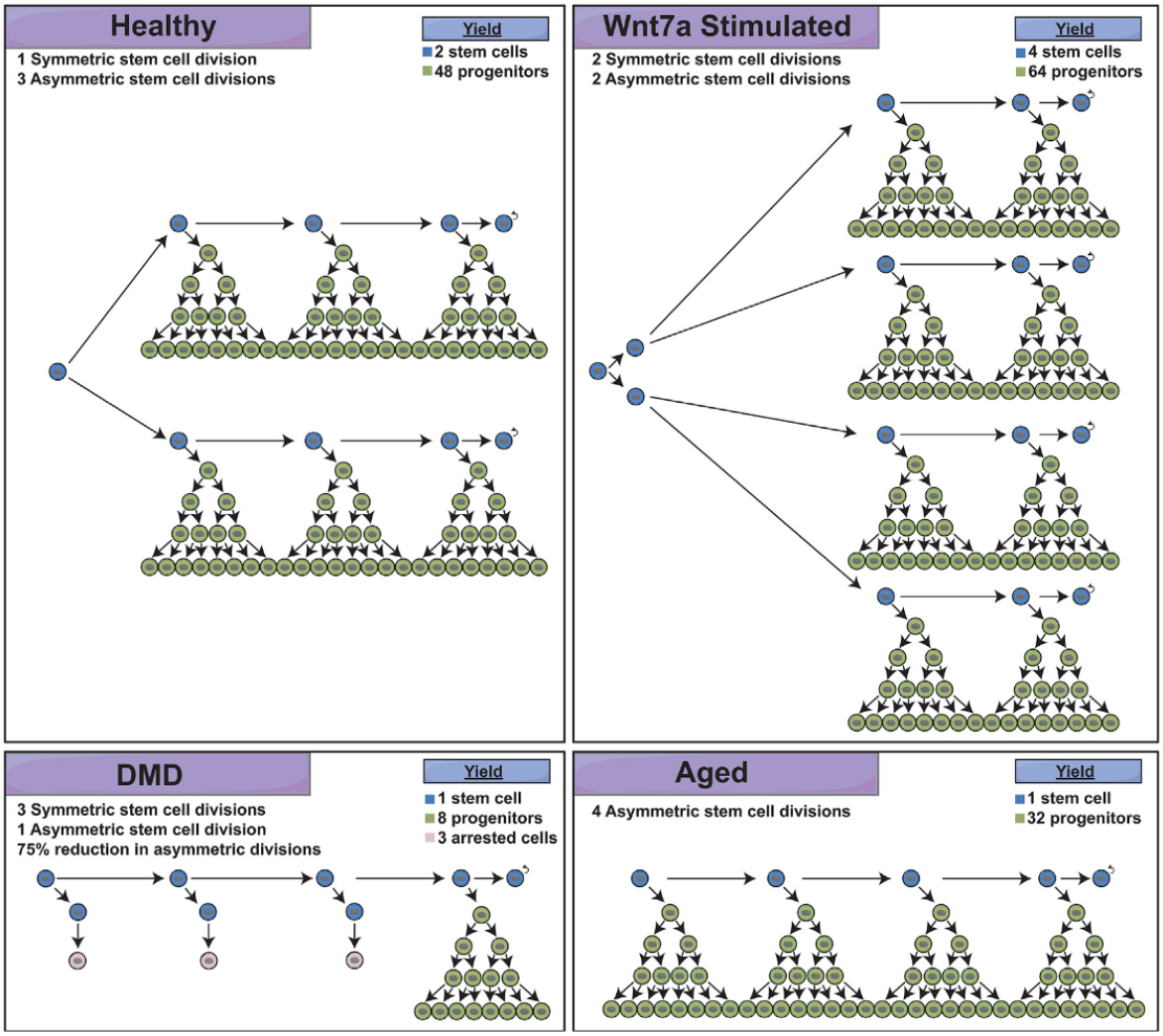


Figure 35: **The Balance between Symmetric and Asymmetric Division Significantly Impacts the Efficiency of Muscle Regeneration.** Schematic depicting changes in self-renewal and myogenic commitment in youthful muscle, Wnt7a stimulated muscle, and aged and dystrophic muscle. Following injury, satellite cells balance self-renewal and commitment through the symmetric expansion of the satellite cell pool and asymmetric commitment, forming progenitors that repair the myofibers and stem cells to facilitate progenitor formation. Increasing self-renewal augments the repair process by increasing the number of satellite cells available to contribute to progenitor formation. Intrinsic and extrinsic changes in satellite cell signalling with age promote cell commitment at the expense of satellite cell self-renewal. Myopathy, such as Duchenne muscular dystrophy (DMD), significantly impairs the regenerative process due to reduced progenitor formation from mdx satellite cells. Yields are hypothetical based upon 4 initial stem cell divisions. Adapted from Feige et al., 2018.

Although mobility is severely restricted in patients with DMD, ventilation failure is the main complication in late-stage DMD[258]. We show that in *mdx* mice, the diaphragm is severely affected during disease progression compared to limb muscles (Manuscript IV), as shown previously[311]. In adult muscle, diaphragm satellite cells differ from limb muscle due to maintained Pax7 and Pax3 expression[312,313] where *in vitro* cultured diaphragm myoblasts show varied proliferation and differentiation potential compared to limb muscle-derived myoblasts[314]. *In vivo* studies show Pax7 is dispensable for diaphragm remodelling following exercise[315] and lineage tracing suggests higher rates of homeostatic turnover in diaphragm compared to limb muscle[316]. Many promising studies exploring satellite cell-mediated repair in skeletal muscle have yet to explore their efficacy on repair in the diaphragm muscle. The development of a novel means to evaluate repair or slow disease progression in the diaphragm of DMD patients could improve the preclinical testing of therapeutics.

The crosstalk between satellite cells, muscle and other muscle resident cells such as fibroadipogenic precursors maintains efficient myogenic differentiation[228,267] while repressing adipose infiltration[228] and excess ECM deposition from fibroblast[268]. In the *mdx* context, delays in myofibre growth are apparent prior to disease symptoms[231] and *mdx* satellite cells produce fewer MyoG expressing cells following injury[178]. The progressive nature of muscle degeneration in the *mdx* mouse requires continual satellite cell turnover, where small changes in the efficiency of myogenic differentiation can have compounding consequences on muscle repair and fibrotic deposition (Manuscript IV, Figure 35).

We made the observation in Manuscript IV that although as a consequence of CTX induced injury *mdx* muscles show improved histological characteristics such as decreased fibrosis, physiological force is still impaired. This data suggests intrinsic changes to

myofibres such as mitochondrial dynamics[317], or increased myofibre branching[261] may also contribute to physiological impairment in muscle force of *mdx* mice.

Although the importance of the loss of dystrophin in satellite cell-mediated repair may remain in controversy, the identification of the EGFR pathway to regulate asymmetric division in *mdx* mice to improve muscle regeneration (Manuscript II) and further validation in human satellite cells (Manuscript V) suggest that conserved pathways regulating muscle repair may retain function across mouse and man. EGFR can be activated by multiple cytokines in the circulation including EGF, epiregulin, amphiregulin, heparin-binding EGF-like growth factor, transforming growth factor-α[217], where the myofibre can also be a source of EGF[318]. During an injury, growth factor release from the ECM[319] can act as a signal for satellite cell activation where infiltrating immune cells can also secrete high levels of EGF[215]. As quiescent satellite cells are exposed to vascular circulation, myofibre derived EGF, and express high levels of *Egfr* yet do not activate EGFR signalling, would suggest that additional mechanisms are required to activate EGFR signalling. In other tissues, the sensitivity of EGFR to ligands can be spatially regulated through protein tyrosine phosphatases (PTPs)[320] and spatial restriction of PTPs within the cell can lead to localized and dosed responses in EGFR phosphorylation and recycling through endosomal trafficking[321]. Complex responses of EGFR can emerge through interactions with PTPs and autocatalytic activation[322] where we made the observation that phosphorylated EGFR is spatially restricted to the basal surface in activated satellite cells (Manuscript II). Furthermore, as we observe both Myf5$^{pos}$ and Myf5$^{neg}$ satellite cells can localize phosphorylated EGFR to the basal cortex prior to division (Manuscript II), it would suggest they may share EGFR regulators including PTPs where in addition to establishing an apical-basal axis of division, factors such as epigenetic permissibility and internal cell polarity facilitate asymmetric divisions in Myf5$^{neg}$ satellite cells. Future studies exploring

the effect of EGFR signalling on primary satellite cells from patients would provide insight into the regulators of EGFR activity and better evaluate the clinical potential of modulating satellite cell polarity to augment repair in a dystrophic context.

**Manuscript V: General discussion**

In manuscript V we developed a novel system to model human satellite cell dynamics *in situ* to better evaluate signalling pathways regulating human satellite cell quiescence, activation, polarity and differentiation. This provides an exciting proof of principle, however, *Psoas* myofibre cultures lack innervation or circulatory blood flow which can impact satellite cell activation, proliferation and differentiation[2]. Nonetheless, our system holds the potential to model satellite cell-intrinsic signalling pathways, interactions of satellite cells with their immediate microenvironment and soluble niche factors. It remains unclear if satellite cell activation in *Psoas* fibre culture is due to mechanical stretching associated with isolation, denervation or high serum conditions present in culture.

To expand our study, the use of genetic tools to develop causative signalling relationships is an attractive strategy. Introducing lineage tracing constructs or CRISPR-Cas9 based gene editing strategies through viral infection of early cultured fibres could provide significant clarity on satellite stem cell hierarchy in the human context. Further studies exploring additional muscle groups and in larger patient populations may expand the potential of the method to additional clinical areas such as modelling age-related changes to satellite cell activity. Identification and culture of myofibres from living donors would further extend the potential of evaluating personalized medicine strategies targeting muscle repair.

## Concluding Remarks

The presented studies provide insight into the molecular events governing myogenic and adipogenic fate decisions in satellite cells and new methods to uncover molecular pathways regulating human muscle stem cell fate. These studies highlight the prolific nature of satellite cells in facilitating muscle repair and the clinical potential of therapeutics augmenting satellite cell-mediated endogenous repair. A better understanding of the specific mechanisms governing muscle repair will develop our understanding of human satellite cell dynamics and define pathways amenable for therapeutic intervention in muscle disorders such as Duchenne's Muscular Dystrophy and sarcopenia.

## References


1. Dumont, N. A., Bentzinger, C. F., Sincennes, M.-C. & Rudnicki, M. A. Satellite Cells and Skeletal Muscle Regeneration. in *Comprehensive Physiology* 1027–1059 (American Cancer Society, 2015). doi:10.1002/cphy.c140068.
2. Yin, H., Price, F. & Rudnicki, M. A. Satellite Cells and the Muscle Stem Cell Niche. *Physiol Rev* **93**, 23–67 (2013).
3. Carlson, M. E. & Conboy, I. M. Loss of stem cell regenerative capacity within aged niches. *Aging Cell* **6**, 371–382 (2007).
4. Shefer, G., Van de Mark, D. P., Richardson, J. B. & Yablonka-Reuveni, Z. Satellite-cell pool size does matter: defining the myogenic potency of aging skeletal muscle. *Dev Biol* **294**, 50–66 (2006).
5. Feige, P., Brun, C. E., Ritso, M. & Rudnicki, M. A. Orienting Muscle Stem Cells for Regeneration in Homeostasis, Aging, and Disease. *Cell Stem Cell* **23**, 653–664 (2018).
6. Ervasti, J. M., Ohlendieck, K., Kahl, S. D., Gaver, M. G. & Campbell, K. P. Deficiency of a glycoprotein component of the dystrophin complex in dystrophic muscle. *Nature* **345**, 315–319 (1990).
7. Dumont, N. A. *et al.* Dystrophin expression in muscle stem cells regulates their polarity and asymmetric division. *Nat Med* **21**, 1455–1463 (2015).
8. Koeks, Z. *et al.* Clinical Outcomes in Duchenne Muscular Dystrophy: A Study of 5345 Patients from the TREAT-NMD DMD Global Database. *J Neuromuscul Dis* **4**, 293–306.
9. Bernet, J. D. *et al.* P38 MAPK signaling underlies a cell autonomous loss of stem cell self-renewal in aged skeletal muscle. *Nat Med* **20**, 265–271 (2014).
10. Price, F. D. *et al.* Inhibition of JAK/STAT signaling stimulates adult satellite cell function. *Nat Med* **20**, 1174–1181 (2014).

11. Cosgrove, B. D. *et al.* Rejuvenation of the aged muscle stem cell population restores strength to injured aged muscles. *Nat Med* **20**, 255–264 (2014).
12. Tierney, M. T. *et al.* STAT3 signaling controls satellite cell expansion and skeletal muscle repair. *Nat Med* **20**, 1182–1186 (2014).
13. Blanco-Bose, W. E., Yao, C. C., Kramer, R. H. & Blau, H. M. Purification of mouse primary myoblasts based on alpha 7 integrin expression. *Exp. Cell Res.* **265**, 212–220 (2001).
14. Cohn, R. D. *et al.* Disruption of DAG1 in differentiated skeletal muscle reveals a role for dystroglycan in muscle regeneration. *Cell* **110**, 639–648 (2002).
15. Chargé, S. B. P. & Rudnicki, M. A. Cellular and molecular regulation of muscle regeneration. *Physiol. Rev.* **84**, 209–238 (2004).
16. Cornelison, D. D., Filla, M. S., Stanley, H. M., Rapraeger, A. C. & Olwin, B. B. Syndecan-3 and syndecan-4 specifically mark skeletal muscle satellite cells and are implicated in satellite cell maintenance and muscle regeneration. *Dev. Biol.* **239**, 79–94 (2001).
17. Pisconti, A., Cornelison, D. D. W., Olguín, H. C., Antwine, T. L. & Olwin, B. B. Syndecan-3 and Notch cooperate in regulating adult myogenesis. *J Cell Biol* **190**, 427–441 (2010).
18. Xian, X., Gopal, S. & Couchman, J. R. Syndecans as receptors and organizers of the extracellular matrix. *Cell Tissue Res.* **339**, 31–46 (2010).
19. Bröhl, D. *et al.* Colonization of the satellite cell niche by skeletal muscle progenitor cells depends on Notch signals. *Dev. Cell* **23**, 469–481 (2012).
20. Baghdadi, M. B. *et al.* Reciprocal signalling by Notch-Collagen V-CALCR retains muscle stem cells in their niche. *Nature* **557**, 714–718 (2018).

21. Fujimaki, S. *et al.* Notch1 and Notch2 Coordinately Regulate Stem Cell Function in the Quiescent and Activated States of Muscle Satellite Cells. *Stem Cells* **36**, 278–285 (2018).
22. Kuang, S., Kuroda, K., Le Grand, F. & Rudnicki, M. A. Asymmetric Self-Renewal and Commitment of Satellite Stem Cells in Muscle. *Cell* **129**, 999–1010 (2007).
23. Conboy, I. M. & Rando, T. A. The regulation of Notch signaling controls satellite cell activation and cell fate determination in postnatal myogenesis. *Dev. Cell* **3**, 397–409 (2002).
24. Kawabe, Y., Wang, Y. X., McKinnell, I. W., Bedford, M. T. & Rudnicki, M. A. Carm1 Regulates Pax7 Transcriptional Activity Through MLL1/2 Recruitment During Asymmetric Satellite Stem Cell Divisions. *Cell Stem Cell* **11**, 333–345 (2012).
25. Troy, A. *et al.* Coordination of Satellite Cell Activation and Self-Renewal by Par-Complex-Dependent Asymmetric Activation of p38α/β MAPK. *Cell Stem Cell* **11**, 541–553 (2012).
26. Chakkalakal, J. V., Jones, K. M., Basson, M. A. & Brack, A. S. The aged niche disrupts muscle stem cell quiescence. *Nature* **490**, 355–360 (2012).
27. Rozo, M., Li, L. & Fan, C.-M. Targeting β1-Integrin Signaling Enhances Regeneration in Aged and Dystrophic Muscle in Mice. *Nat Med* **22**, 889–896 (2016).
28. Webster, M. T., Manor, U., Lippincott-Schwartz, J. & Fan, C.-M. Intravital Imaging Reveals Ghost Fibers as Architectural Units Guiding Myogenic Progenitors During Regeneration. *Cell Stem Cell* **18**, 243–252 (2016).
29. Gurevich, D. B. *et al.* Asymmetric division of clonal muscle stem cells coordinates muscle regeneration in vivo. *Science* **353**, (2016).
30. Bischoff, R. & Heintz, C. Enhancement of skeletal muscle regeneration. *Developmental Dynamics* **201**, 41–54 (1994).

31. Yin, H. *et al.* MicroRNA-133 Controls Brown Adipose Determination in Skeletal Muscle Satellite Cells by Targeting Prdm16. *Cell Metab* **17**, 210–224 (2013).
32. Buckingham, M. & Relaix, F. The role of Pax genes in the development of tissues and organs: Pax3 and Pax7 regulate muscle progenitor cell functions. *Annu. Rev. Cell Dev. Biol.* **23**, 645–673 (2007).
33. Cho, D. S. & Doles, J. D. Single cell transcriptome analysis of muscle satellite cells reveals widespread transcriptional heterogeneity. *Gene* **636**, 54–63 (2017).
34. Porpiglia, E. *et al.* High-resolution Myogenic Lineage Mapping by Single-Cell Mass Cytometry. *Nat Cell Biol* **19**, 558–567 (2017).
35. Chakkalakal, J. V. *et al.* Early forming label-retaining muscle stem cells require p27kip1 for maintenance of the primitive state. *Development* **141**, 1649–1659 (2014).
36. Nicholls, D. G. & Locke, R. M. Thermogenic mechanisms in brown fat. *Physiological Reviews* **64**, 1–64 (1984).
37. Haman, F. & Blondin, D. P. Shivering thermogenesis in humans: Origin, contribution and metabolic requirement. *Temperature (Austin)* **4**, 217–226 (2017).
38. Periasamy, M. & Huke, S. SERCA Pump Level is a Critical Determinant of Ca2+Homeostasis and Cardiac Contractility. *Journal of Molecular and Cellular Cardiology* **33**, 1053–1063 (2001).
39. Meis, L. de *et al.* The Thermogenic Activity of Rat Brown Adipose Tissue and Rabbit White Muscle Ca2 + -ATPase. *IUBMB Life* **57**, 337–345 (2005).
40. Nowack, J., Giroud, S., Arnold, W. & Ruf, T. Muscle Non-shivering Thermogenesis and Its Role in the Evolution of Endothermy. *Front. Physiol.* **8**, (2017).
41. Bal, N. C. *et al.* Sarcolipin is a newly identified regulator of muscle-based thermogenesis in mammals. *Nat Med* **18**, 1575–1579 (2012).

42. Mitchell, P. Vectorial Chemistry and the Molecular Mechanics of Chemiosmotic Coupling: Power Transmission by Proticity. *Biochemical Society Transactions* **4**, 399–430 (1976).
43. Kazak, L. *et al.* A Creatine-Driven Substrate Cycle Enhances Energy Expenditure and Thermogenesis in Beige Fat. *Cell* **163**, 643–655 (2015).
44. Shapira, S. N. & Seale, P. Transcriptional Control of Brown and Beige Fat Development and Function. *Obesity* **27**, 13–21 (2019).
45. Sharp, L. Z. *et al.* Human BAT Possesses Molecular Signatures That Resemble Beige/Brite Cells. *PLoS One* **7**, (2012).
46. Smorlesi, A., Frontini, A., Giordano, A. & Cinti, S. The adipose organ: white-brown adipocyte plasticity and metabolic inflammation. *Obes Rev* **13 Suppl 2**, 83–96 (2012).
47. Seale, P. *et al.* PRDM16 controls a brown fat/skeletal muscle switch. *Nature* **454**, 961–967 (2008).
48. Harms, M. & Seale, P. Brown and beige fat: development, function and therapeutic potential. *Nat Med* **19**, 1252–1263 (2013).
49. Lidell, M. E. *et al.* Evidence for two types of brown adipose tissue in humans. *Nat Med* **19**, 631–634 (2013).
50. Sturkenboom, M., Franssen, E., Berkhof, J. & Hoekstra, O. Physiological uptake of [18F]fluorodeoxyglucose in the neck and upper chest region: are there predictive characteristics? *Nuclear Medicine Communications* **25**, 1109–1111 (2004).
51. Cypess, A. M. *et al.* Identification and importance of brown adipose tissue in adult humans. *N. Engl. J. Med.* **360**, 1509–1517 (2009).
52. Orava, J. *et al.* Blunted metabolic responses to cold and insulin stimulation in brown adipose tissue of obese humans. *Obesity (Silver Spring)* **21**, 2279–2287 (2013).

53. Lepper, C. & Fan, C.-M. Inducible lineage tracing of Pax7-descendant cells reveals embryonic origin of adult satellite cells. *Genesis* **48**, 424–436 (2010).
54. Walden, T. B., Timmons, J. A., Keller, P., Nedergaard, J. & Cannon, B. Distinct expression of muscle-specific MicroRNAs (myomirs) in brown adipocytes. *Journal of Cellular Physiology* **218**, 444–449 (2009).
55. Timmons, J. A. *et al.* Myogenic gene expression signature establishes that brown and white adipocytes originate from distinct cell lineages. *Proc Natl Acad Sci U S A* **104**, 4401–4406 (2007).
56. Forner, F. *et al.* Proteome Differences between Brown and White Fat Mitochondria Reveal Specialized Metabolic Functions. *Cell Metabolism* **10**, 324–335 (2009).
57. Tharp, K. M. *et al.* Actomyosin-mediated tension orchestrates uncoupled respiration in adipose tissues. *Cell Metab* **27**, 602-615.e4 (2018).
58. Kopecky, J., Clarke, G., Enerbäck, S., Spiegelman, B. & Kozak, L. P. Expression of the mitochondrial uncoupling protein gene from the aP2 gene promoter prevents genetic obesity. *J Clin Invest* **96**, 2914–2923 (1995).
59. Yoneshiro, T. *et al.* Brown Adipose Tissue, Whole-Body Energy Expenditure, and Thermogenesis in Healthy Adult Men. *Obesity* **19**, 13–16 (2011).
60. Kajimura, S. & Saito, M. A new era in brown adipose tissue biology: molecular control of brown fat development and energy homeostasis. *Annu. Rev. Physiol.* **76**, 225–249 (2014).
61. Ghorbani, M., Claus, T. H. & Himms-Hagen, J. Hypertrophy of brown adipocytes in brown and white adipose tissues and reversal of diet-induced obesity in rats treated with a β3-adrenoceptor agonist. *Biochemical Pharmacology* **54**, 121–131 (1997).
62. Lowell, B. B. *et al.* Development of obesity in transgenic mice after genetic ablation of brown adipose tissue. *Nature* **366**, 740–742 (1993).

63. Rousseau, C. *et al.* Brown fat in breast cancer patients: analysis of serial 18F-FDG PET/CT scans. *Eur J Nucl Med Mol Imaging* **33**, 785–791 (2006).
64. van Marken Lichtenbelt, W. D. *et al.* Cold-activated brown adipose tissue in healthy men. *N. Engl. J. Med.* **360**, 1500–1508 (2009).
65. Engin, A. The Definition and Prevalence of Obesity and Metabolic Syndrome. in *Obesity and Lipotoxicity* (eds. Engin, A. B. & Engin, A.) 1–17 (Springer International Publishing, 2017). doi:10.1007/978-3-319-48382-5_1.
66. Afshin, A., Reitsma, M. B. & Murray, C. J. L. Health Effects of Overweight and Obesity in 195 Countries. *N. Engl. J. Med.* **377**, 1496–1497 (2017).
67. Iida, S., Chen, W., Nakadai, T., Ohkuma, Y. & Roeder, R. G. PRDM16 enhances nuclear receptor-dependent transcription of the brown fat-specific Ucp1 gene through interactions with Mediator subunit MED1. *Genes Dev.* **29**, 308–321 (2015).
68. Kajimura, S. *et al.* Regulation of the brown and white fat gene programs through a PRDM16/CtBP transcriptional complex. *Genes Dev.* **22**, 1397–1409 (2008).
69. Cohen, P. *et al.* Ablation of PRDM16 and Beige Adipose Causes Metabolic Dysfunction and a Subcutaneous to Visceral Fat Switch. *Cell* **156**, 304–316 (2014).
70. Roh, H. C. *et al.* Warming Induces Significant Reprogramming of Beige, But Not Brown, Adipocyte Cellular Identity. *Cell Metab* **27**, 1121-1137.e5 (2018).
71. Inagaki, T., Sakai, J. & Kajimura, S. Transcriptional and epigenetic control of brown and beige adipose cell fate and function. *Nat Rev Mol Cell Biol* **17**, 480–495 (2016).
72. Chen, Q., Huang, L., Pan, D., Zhu, L. J. & Wang, Y.-X. Cbx4 Sumoylates Prdm16 to Regulate Adipose Tissue Thermogenesis. *Cell Reports* **22**, 2860–2872 (2018).
73. Boettger, T., Wüst, S., Nolte, H. & Braun, T. The miR-206/133b cluster is dispensable for development, survival and regeneration of skeletal muscle. *Skelet Muscle* **4**, 23 (2014).

74. Rao, P. K., Kumar, R. M., Farkhondeh, M., Baskerville, S. & Lodish, H. F. Myogenic factors that regulate expression of muscle-specific microRNAs. *Proc. Natl. Acad. Sci. U.S.A.* **103**, 8721–8726 (2006).
75. Sweetman, D. *et al.* Specific requirements of MRFs for the expression of muscle specific microRNAs, miR-1, miR-206 and miR-133. *Developmental Biology* **321**, 491–499 (2008).
76. Wystub, K., Besser, J., Bachmann, A., Boettger, T. & Braun, T. miR-1/133a Clusters Cooperatively Specify the Cardiomyogenic Lineage by Adjustment of Myocardin Levels during Embryonic Heart Development. *PLOS Genetics* **9**, e1003793 (2013).
77. Chen, J.-F. *et al.* microRNA-1 and microRNA-206 regulate skeletal muscle satellite cell proliferation and differentiation by repressing Pax7miRNAs in skeletal muscle satellite cells. *J Cell Biol* **190**, 867–879 (2010).
78. Dey, B. K., Gagan, J. & Dutta, A. miR-206 and -486 induce myoblast differentiation by downregulating Pax7. *Mol. Cell. Biol.* **31**, 203–214 (2011).
79. Chen, J.-F. *et al.* The role of microRNA-1 and microRNA-133 in skeletal muscle proliferation and differentiation. *Nat Genet* **38**, 228–233 (2006).
80. Gloss, D., Moxley, R. T., Ashwal, S. & Oskoui, M. Practice guideline update summary: Corticosteroid treatment of Duchenne muscular dystrophy. *Neurology* **86**, 465–472 (2016).
81. Case, L. E. *et al.* Rehabilitation Management of the Patient With Duchenne Muscular Dystrophy. *Pediatrics* **142**, S17–S33 (2018).
82. Maffioletti, S. M., Noviello, M., English, K. & Tedesco, F. S. Stem Cell Transplantation for Muscular Dystrophy: The Challenge of Immune Response. *Biomed Res Int* **2014**, (2014).

83. Guérette, B., Asselin, I., Skuk, D., Entman, M. & Tremblay, J. P. Control of inflammatory damage by anti-LFA-1: increase success of myoblast transplantation. *Cell Transplant* **6**, 101–107 (1997).
84. Miller, R. G. *et al.* Myoblast implantation in Duchenne muscular dystrophy: the San Francisco study. *Muscle Nerve* **20**, 469–478 (1997).
85. Price, F. D., Kuroda, K. & Rudnicki, M. A. Stem cell based therapies to treat muscular dystrophy. *Biochim. Biophys. Acta* **1772**, 272–283 (2007).
86. del Carmen Ortuño-Costela, M., García-López, M., Cerrada, V. & Gallardo, M. E. iPSCs: A powerful tool for skeletal muscle tissue engineering. *J Cell Mol Med* **23**, 3784–3794 (2019).
87. Charville, G. W. *et al.* Ex Vivo Expansion and In Vivo Self-Renewal of Human Muscle Stem Cells. *Stem Cell Reports* **5**, 621–632 (2015).
88. Judson, R. N. *et al.* Inhibition of methyltransferase Setd7 allows the in vitro expansion of myogenic stem cells with improved therapeutic potential. *Cell Stem Cell* **22**, 177-190.e7 (2018).
89. Zismanov, V. *et al.* Phosphorylation of eIF2α Is a Translational Control Mechanism Regulating Muscle Stem Cell Quiescence and Self-Renewal. *Cell Stem Cell* **18**, 79–90 (2016).
90. Bentzinger, C. F. *et al.* Wnt7a stimulates myogenic stem cell motility and engraftment resulting in improved muscle strength. *J Cell Biol* **205**, 97–111 (2014).
91. Search of: Duchenne Muscular Dystrophy - List Results - ClinicalTrials.gov. https://www.clinicaltrials.gov/ct2/results?term=Duchenne+Muscular+Dystrophy&Search=Search.
92. Welch, E. M. *et al.* PTC124 targets genetic disorders caused by nonsense mutations. *Nature* **447**, 87–91 (2007).

93. McDonald, C. M. *et al.* Ataluren in patients with nonsense mutation Duchenne muscular dystrophy (ACT DMD): a multicentre, randomised, double-blind, placebo-controlled, phase 3 trial. *The Lancet* **390**, 1489–1498 (2017).

94. Mendell, J. R. *et al.* Eteplirsen for the treatment of Duchenne muscular dystrophy. *Ann. Neurol.* **74**, 637–647 (2013).

95. Mendell, J. R. *et al.* Longitudinal effect of eteplirsen versus historical control on ambulation in Duchenne muscular dystrophy. *Ann. Neurol.* **79**, 257–271 (2016).

96. Aartsma-Rus, A. *et al.* Theoretic applicability of antisense-mediated exon skipping for Duchenne muscular dystrophy mutations. *Hum. Mutat.* **30**, 293–299 (2009).

97. Bladen, C. L. *et al.* The TREAT-NMD DMD Global Database: Analysis of More than 7,000 Duchenne Muscular Dystrophy Mutations. *Hum Mutat* **36**, 395–402 (2015).

98. Chamberlain, J. R. & Chamberlain, J. S. Progress toward Gene Therapy for Duchenne Muscular Dystrophy. *Mol Ther* **25**, 1125–1131 (2017).

99. Tabebordbar, M. *et al.* In vivo gene editing in dystrophic mouse muscle and muscle stem cells. *Science* **351**, 407–411 (2016).

100. Ousterout, D. G. *et al.* Multiplex CRISPR/Cas9-based genome editing for correction of dystrophin mutations that cause Duchenne muscular dystrophy. *Nature Communications* **6**, 1–13 (2015).

101. Wang, Y. X. *et al.* EGFR-Aurka Signaling Rescues Polarity and Regeneration Defects in Dystrophin-Deficient Muscle Stem Cells by Increasing Asymmetric Divisions. *Cell Stem Cell* **24**, 419-432.e6 (2019).

102. Yucel, N., Chang, A. C., Day, J. W., Rosenthal, N. & Blau, H. M. Humanizing the mdx mouse model of DMD: the long and the short of it. *NPJ Regen Med* **3**, (2018).

103. Irintchev, A., Zweyer, M. & Wernig, A. Impaired functional and structural recovery after muscle injury in dystrophic mdx mice. *Neuromuscular Disorders* **7**, 117–125 (1997).

104. Blau, H. M., Webster, C. & Pavlath, G. K. Defective myoblasts identified in Duchenne muscular dystrophy. *PNAS* **80**, 4856–4860 (1983).

105. Sacco, A. *et al.* Short Telomeres and Stem Cell Exhaustion Model Duchenne Muscular Dystrophy in mdx/mTR Mice. *Cell* **143**, 1059–1071 (2010).

106. van der Worp, H. B. *et al.* Can Animal Models of Disease Reliably Inform Human Studies? *PLoS Med* **7**, (2010).

107. Govoni, A. *et al.* Ongoing therapeutic trials and outcome measures for Duchenne muscular dystrophy. *Cell. Mol. Life Sci.* **70**, 4585–4602 (2013).

108. McKinnell, I. W. *et al.* Pax7 activates myogenic genes by recruitment of a histone methyltransferase complex. *Nat Cell Biol* **10**, 77–84 (2008).

109. Soleimani, V. D. *et al.* Transcriptional Dominance of Pax7 in Adult Myogenesis is Due to High-Affinity Recognition of Homeodomain Motifs. *Dev Cell* **22**, 1208–1220 (2012).

110. Hausburg, M. A. *et al.* Post-transcriptional regulation of satellite cell quiescence by TTP-mediated mRNA decay. *eLife* **4**,.

111. de Morrée, A. *et al.* Staufen1 inhibits MyoD translation to actively maintain muscle stem cell quiescence. *Proc Natl Acad Sci U S A* **114**, E8996–E9005 (2017).

112. Crist, C. G., Montarras, D. & Buckingham, M. Muscle satellite cells are primed for myogenesis but maintain quiescence with sequestration of Myf5 mRNA targeted by microRNA-31 in mRNP granules. *Cell Stem Cell* **11**, 118–126 (2012).

113. Cheung, T. H. *et al.* Maintenance of muscle stem cell quiescence by microRNA-489. *Nature* **482**, 524–528 (2012).

114. Sharma, M., Juvvuna, P. K., Kukreti, H. & McFarlane, C. Mega roles of microRNAs in regulation of skeletal muscle health and disease. *Front. Physiol.* **5**, (2014).

115. Alteri, A. *et al.* Cyclin D1 is a major target of miR-206 in cell differentiation and transformation. *Cell Cycle* **12**, 3781–3790 (2013).

116. Bartness, T. J., Vaughan, C. H. & Song, C. K. Sympathetic and sensory innervation of brown adipose tissue. *Int J Obes (Lond)* **34 Suppl 1**, S36-42 (2010).

117. Cannon, B. & Nedergaard, J. Brown Adipose Tissue: Function and Physiological Significance. *Physiological Reviews* **84**, 277–359 (2004).

118. Liu, Y., Fu, W., Seese, K., Yin, A. & Yin, H. Ectopic brown adipose tissue formation within skeletal muscle after brown adipose progenitor cell transplant augments energy expenditure. *The FASEB Journal* **33**, 8822–8835 (2019).

119. Zhu, Z. *et al.* Enhanced sympathetic activity in mice with brown adipose tissue transplantation (transBATation). *Physiol. Behav.* **125**, 21–29 (2014).

120. Bowman, W. C. & Nott, M. W. Actions of Sympathomimetic Amines and Their Antagonists on Skeletal Muscle. *Pharmacol Rev* **21**, 27–72 (1969).

121. Chuikov, S., Levi, B. P., Smith, M. L. & Morrison, S. J. Prdm16 promotes stem cell maintenance in multiple tissues, partly by regulating oxidative stress. *Nat Cell Biol* **12**, 999–1006 (2010).

122. Ahn, J., Lee, H., Kim, S., Park, J. & Ha, T. The anti-obesity effect of quercetin is mediated by the AMPK and MAPK signaling pathways. *Biochemical and Biophysical Research Communications* **373**, 545–549 (2008).

123. Behloul, N. & Wu, G. Genistein: a promising therapeutic agent for obesity and diabetes treatment. *Eur. J. Pharmacol.* **698**, 31–38 (2013).

124. Levri, K. M. *et al.* Metformin as treatment for overweight and obese adults: a systematic review. *Ann Fam Med* **3**, 457–461 (2005).

125. Lijnen, H. R., Van Hoef, B., Lu, H. R. & Gallacher, D. J. Rofecoxib impairs adipose tissue development in a murine model of nutritionally induced obesity. *Thromb. Haemost.* **100**, 338–342 (2008).

126. Liu, Y., Liang, Y., Zhang, J. & Fu, W. MicroRNA-133 mediates cardiac diseases: Mechanisms and clinical implications. *Experimental Cell Research* **354**, 65–70 (2017).

127. Li, N., Zhou, H. & Tang, Q. miR-133: A Suppressor of Cardiac Remodeling? *Front Pharmacol* **9**, (2018).

128. Matkovich, S. J. *et al.* MicroRNA-133a protects against myocardial fibrosis and modulates electrical repolarization without affecting hypertrophy in pressure overloaded adult hearts. *Circ Res* **106**, 166–175 (2010).

129. Carè, A. *et al.* MicroRNA-133 controls cardiac hypertrophy. *Nat. Med.* **13**, 613–618 (2007).

130. Callis, T. E. *et al.* MicroRNA-208a is a regulator of cardiac hypertrophy and conduction in mice. *J. Clin. Invest.* **119**, 2772–2786 (2009).

131. Boutz, P. L., Chawla, G., Stoilov, P. & Black, D. L. MicroRNAs regulate the expression of the alternative splicing factor nPTB during muscle development. *Genes Dev.* **21**, 71–84 (2007).

132. Sambasivan, R. *et al.* Distinct regulatory cascades govern extraocular and pharyngeal arch muscle progenitor cell fates. *Dev. Cell* **16**, 810–821 (2009).

133. Beauchamp, J. R. *et al.* Expression of Cd34 and Myf5 Defines the Majority of Quiescent Adult Skeletal Muscle Satellite Cells. *J Cell Biol* **151**, 1221–1234 (2000).

134. Schultz, E. Satellite cell proliferative compartments in growing skeletal muscles. *Dev. Biol.* **175**, 84–94 (1996).

135. Collins, C. A. *et al.* Stem cell function, self-renewal, and behavioral heterogeneity of cells from the adult muscle satellite cell niche. *Cell* **122**, 289–301 (2005).

136. Fu, W., Liu, Y., Sun, C. & Yin, H. Transient p53 inhibition sensitizes aged white adipose tissue for beige adipocyte recruitment by blocking mitophagy. *FASEB J* **33**, 844–856 (2019).

137. Muzik, O. *et al.* 15O PET measurement of blood flow and oxygen consumption in cold-activated human brown fat. *J. Nucl. Med.* **54**, 523–531 (2013).

138. U Din, M. *et al.* Human brown adipose tissue [(15)O]O2 PET imaging in the presence and absence of cold stimulus. *Eur. J. Nucl. Med. Mol. Imaging* **43**, 1878–1886 (2016).

139. Carpentier, A. C. *et al.* Brown Adipose Tissue Energy Metabolism in Humans. *Front. Endocrinol.* **9**, (2018).

140. Kajimura, S., Spiegelman, B. M. & Seale, P. Brown and Beige Fat: Physiological Roles beyond Heat Generation. *Cell Metab.* **22**, 546–559 (2015).

141. Nahon, K. J. *et al.* Lower critical temperature and cold-induced thermogenesis of lean and overweight humans are inversely related to body mass and basal metabolic rate. *J. Therm. Biol.* **69**, 238–248 (2017).

142. Pfannenberg, C. *et al.* Impact of Age on the Relationships of Brown Adipose Tissue With Sex and Adiposity in Humans. *Diabetes* **59**, 1789–1793 (2010).

143. Cypess, A. M. & Kahn, C. R. Brown fat as a therapy for obesity and diabetes. *Curr Opin Endocrinol Diabetes Obes* **17**, 143–149 (2010).

144. Vousden, K. H. & Ryan, K. M. p53 and metabolism. *Nature Reviews Cancer* **9**, 691–700 (2009).

145. Qiang, L. *et al.* Brown Remodeling of White Adipose Tissue by SirT1-Dependent Deacetylation of Pparγ. *Cell* **150**, 620–632 (2012).

146. Bai, P. & Cantó, C. The role of PARP-1 and PARP-2 enzymes in metabolic regulation and disease. *Cell Metab.* **16**, 290–295 (2012).

147. Shukla, G. C., Singh, J. & Barik, S. MicroRNAs: Processing, Maturation, Target Recognition and Regulatory Functions. *Mol Cell Pharmacol* **3**, 83–92 (2011).

148. McCarthy, J. J. The MyomiR Network in Skeletal Muscle Plasticity. *Exerc Sport Sci Rev* **39**, 150–154 (2011).

149. King, I. N. *et al.* The RNA-binding Protein TDP-43 Selectively Disrupts MicroRNA-1/206 Incorporation into the RNA-induced Silencing Complex. *J. Biol. Chem.* **289**, 14263–14271 (2014).

150. Reichholf, B. *et al.* Time-Resolved Small RNA Sequencing Unravels the Molecular Principles of MicroRNA Homeostasis. *Molecular Cell* **75**, 756-768.e7 (2019).

151. Suzuki, H. I. *et al.* Modulation of microRNA processing by p53. *Nature* **460**, 529–533 (2009).

152. Tao, J. *et al.* microRNA-133 inhibits cell proliferation, migration and invasion in prostate cancer cells by targeting the epidermal growth factor receptor. *Oncology Reports* **27**, 1967–1975 (2012).

153. Puigserver, P. *et al.* Activation of PPARgamma coactivator-1 through transcription factor docking. *Science* **286**, 1368–1371 (1999).

154. Hondares, E. *et al.* Peroxisome proliferator-activated receptor α (PPARα) induces PPARγ coactivator 1α (PGC-1α) gene expression and contributes to thermogenic activation of brown fat: involvement of PRDM16. *J. Biol. Chem.* **286**, 43112–43122 (2011).

155. Harms, M. J. *et al.* Prdm16 Is Required for the Maintenance of Brown Adipocyte Identity and Function in Adult Mice. *Cell Metabolism* **19**, 593–604 (2014).

156. Yang, Y. T. & McElligott, M. A. Multiple actions of beta-adrenergic agonists on skeletal muscle and adipose tissue. *Biochem J* **261**, 1–10 (1989).

157. Deng, J. *et al.* Autophagy inhibition prevents glucocorticoid-increased adiposity via suppressing BAT whitening. *Autophagy* **16**, 451–465 (2020).

158. Minamino, T. *et al.* A crucial role for adipose tissue p53 in the regulation of insulin resistance. *Nat. Med.* **15**, 1082–1087 (2009).

159. Porrello, A. *et al.* p53 regulates myogenesis by triggering the differentiation activity of pRb. *J. Cell Biol.* **151**, 1295–1304 (2000).

160. Scimè, A. *et al.* Rb and p107 regulate preadipocyte differentiation into white versus brown fat through repression of PGC-1α. *Cell Metabolism* **2**, 283–295 (2005).

161. Calo, E. *et al.* Rb regulates fate choice and lineage commitment in vivo. *Nature* **466**, 1110–1114 (2010).

162. Khacho, M. *et al.* Mitochondrial Dynamics Impacts Stem Cell Identity and Fate Decisions by Regulating a Nuclear Transcriptional Program. *Cell Stem Cell* **19**, 232–247 (2016).

163. Smith, L. R. & Barton, E. R. SMASH – semi-automatic muscle analysis using segmentation of histology: a MATLAB application. *Skeletal Muscle* **4**, 1–16 (2014).

164. Tallquist, M. D., Weismann, K. E., Hellstrom, M. & Soriano, P. Early myotome specification regulates PDGFA expression and axial skeleton development. *Development* **127**, 5059–5070 (2000).

165. Srinivas, S. *et al.* Cre reporter strains produced by targeted insertion of EYFP and ECFP into the ROSA26 locus. *BMC Developmental Biology* **1**, 4 (2001).

166. Knoblich, J. A. Mechanisms of Asymmetric Stem Cell Division. *Cell* **132**, 583–597 (2008).

167. Arsenio, J., Metz, P. J. & Chang, J. T. Asymmetric Cell Division in T Lymphocyte Fate Diversification. *Trends in Immunology* **36**, 670–683 (2015).

168. Matsuzaki, F. & Shitamukai, A. Cell Division Modes and Cleavage Planes of Neural Progenitors during Mammalian Cortical Development. *Cold Spring Harb Perspect Biol* **7**, a015719 (2015).

169. Dumont, N. A., Bentzinger, C. F., Sincennes, M.-C. & Rudnicki, M. A. Satellite Cells and Skeletal Muscle Regeneration. *Compr Physiol* **5**, 1027–1059 (2015).

170. Gurevich, D. B. *et al.* Asymmetric division of clonal muscle stem cells coordinates muscle regeneration in vivo. *Science* (2016) doi:10.1126/science.aad9969.

171. Kuang, S., Le Grand, F. & Rudnicki, M. A. Asymmetric self-renewal and commitment of satellite stem cells in muscle. *Cell* **129**, 999–1010 (2007).

172. Rocheteau, P., Gayraud-Morel, B., Siegl-Cachedenier, I., Blasco, M. A. & Tajbakhsh, S. A subpopulation of adult skeletal muscle stem cells retains all template DNA strands after cell division. *Cell* **148**, 112–125 (2012).

173. Le Grand, F., Jones, A. E., Seale, V., Scimè, A. & Rudnicki, M. A. Wnt7a activates the planar cell polarity pathway to drive the symmetric expansion of satellite stem cells. *Cell Stem Cell* **4**, 535–547 (2009).

174. Price, F. D. *et al.* Inhibition of JAK-STAT signaling stimulates adult satellite cell function. *Nat Med* **advance online publication**, (2014).

175. Tierney, M. T. *et al.* STAT3 signaling controls satellite cell expansion and skeletal muscle repair. *Nat Med* **20**, 1182–1186 (2014).

176. Bernet, J. D. *et al.* p38 MAPK signaling underlies a cell-autonomous loss of stem cell self-renewal in skeletal muscle of aged mice. *Nat Med* **advance online publication**, (2014).

177. Cosgrove, B. D. *et al.* Rejuvenation of the aged muscle stem cell population restores strength to injured aged muscles. *Nat Med* **20**, 255–264 (2014).

178. Dumont, N. A. *et al.* Dystrophin expression in muscle stem cells regulates their polarity and asymmetric division. *Nat Med* **advance online publication**, (2015).

179. Anderson, M. S. & Kunkel, L. M. The molecular and biochemical basis of Duchenne muscular dystrophy. *Trends Biochem. Sci.* **17**, 289–292 (1992).

180. Cohn, R. D. & Campbell, K. P. Molecular basis of muscular dystrophies. *Muscle Nerve* **23**, 1456–1471 (2000).

181. Bell, C. D. & Conen, P. E. Histopathological changes in Duchenne muscular dystrophy. *Journal of the Neurological Sciences* **7**, 529–544 (1968).

182. Bentzinger, C. F., Wang, Y. X., Dumont, N. A. & Rudnicki, M. A. Cellular dynamics in the muscle satellite cell niche. *EMBO Rep.* **14**, 1062–1072 (2013).

183. Shefer, G. & Yablonka-Reuveni, Z. Isolation and Culture of Skeletal Muscle Myofibers as a Means to Analyze Satellite Cells. *Methods Mol Biol* **290**, 281–304 (2005).

184. Charville, G. W. *et al.* Ex Vivo Expansion and In Vivo Self-Renewal of Human Muscle Stem Cells. *Stem Cell Reports* (2015) doi:10.1016/j.stemcr.2015.08.004.

185. Jones, N. C. *et al.* The p38α/β MAPK functions as a molecular switch to activate the quiescent satellite cell. *J Cell Biol* **169**, 105–116 (2005).

186. Brown, G. R. *et al.* Naphthyl ketones: a new class of Janus kinase 3 inhibitors. *Bioorg. Med. Chem. Lett.* **10**, 575–579 (2000).

187. Gross, E. R., Hsu, A. K. & Gross, G. J. The JAK/STAT pathway is essential for opioid-induced cardioprotection: JAK2 as a mediator of STAT3, Akt, and GSK-3β. *American Journal of Physiology - Heart and Circulatory Physiology* **291**, H827–H834 (2006).

188. Kollareddy, M. *et al.* Aurora kinase inhibitors: Progress towards the clinic. *Invest New Drugs* **30**, 2411–2432 (2012).

189. Ando, R. *et al.* 3-Cyano-6-(5-methyl-3-pyrazoloamino)pyridines: selective Aurora A kinase inhibitors. *Bioorg. Med. Chem. Lett.* **20**, 4709–4711 (2010).

190. Bentzinger, C. F. *et al.* Fibronectin regulates Wnt7a signaling and satellite cell expansion. *Cell Stem Cell* (2013) doi:(In Press).

191. Olwin, B. B. & Hauschka, S. D. Cell surface fibroblast growth factor and epidermal growth factor receptors are permanently lost during skeletal muscle terminal differentiation in culture. *J. Cell Biol.* **107**, 761–769 (1988).

192. Meraldi, P., Honda, R. & Nigg, E. A. Aurora kinases link chromosome segregation and cell division to cancer susceptibility. *Curr. Opin. Genet. Dev.* **14**, 29–36 (2004).

193. Leroy, M. C., Perroud, J., Darbellay, B., Bernheim, L. & Konig, S. Epidermal growth factor receptor down-regulation triggers human myoblast differentiation. *PLoS ONE* **8**, e71770 (2013).

194. Bañón-Rodríguez, I. *et al.* EGFR controls IQGAP basolateral membrane localization and mitotic spindle orientation during epithelial morphogenesis. *The EMBO Journal* **33**, 129–145 (2014).

195. Prigge, J. R. *et al.* Nuclear double-fluorescent reporter for in vivo and ex vivo analyses of biological transitions in mouse nuclei. *Mamm. Genome* (2013) doi:10.1007/s00335-013-9469-8.

196. Lee, T.-C. & Threadgill, D. W. Generation and validation of mice carrying a conditional allele of the epidermal growth factor receptor. *Genesis* **47**, 85–92 (2009).

197. Cowley, D. O. *et al.* Aurora-A Kinase Is Essential for Bipolar Spindle Formation and Early Development. *Mol Cell Biol* **29**, 1059–1071 (2009).

198. Bell, G. P., Fletcher, G. C., Brain, R. & Thompson, B. J. Aurora kinases phosphorylate Lgl to induce mitotic spindle orientation in Drosophila epithelia. *Curr. Biol.* **25**, 61–68 (2015).

199. Johnston, C. A., Hirono, K., Prehoda, K. E. & Doe, C. Q. Identification of an Aurora-A/PinsLINKER/Dlg spindle orientation pathway using induced cell polarity in S2 cells. *Cell* **138**, 1150–1163 (2009).

200. Wirtz-Peitz, F., Nishimura, T. & Knoblich, J. A. Linking cell cycle to asymmetric division: Aurora-A phosphorylates the Par complex to regulate Numb localization. *Cell* **135**, 161–173 (2008).

201. Chen, T.-C. *et al.* Protein phosphorylation profiling using an in situ proximity ligation assay: phosphorylation of AURKA-elicited EGFR-Thr654 and EGFR-Ser1046 in lung cancer cells. *PLoS ONE* **8**, e55657 (2013).

202. Sun, Y. *et al.* A Human Platelet Receptor Protein Microarray Identifies the High Affinity Immunoglobulin E Receptor Subunit α (FcεR1α) as an Activating Platelet Endothelium Aggregation Receptor 1 (PEAR1) Ligand. *Mol Cell Proteomics* **14**, 1265–1274 (2015).

203. Leroy, M. C., Perroud, J., Darbellay, B., Bernheim, L. & Konig, S. Epidermal Growth Factor Receptor Down-Regulation Triggers Human Myoblast Differentiation. *PLOS ONE* **8**, e71770 (2013).

204. Olwin, B. B. & Hauschka, S. D. Cell surface fibroblast growth factor and epidermal growth factor receptors are permanently lost during skeletal muscle terminal differentiation in culture. *J Cell Biol* **107**, 761–769 (1988).

205. Goodyer, P. R., Kachra, Z., Bell, C. & Rozen, R. Renal tubular cells are potential targets for epidermal growth factor. *Am. J. Physiol.* **255**, F1191-1196 (1988).

206. Goel, A. J., Rieder, M.-K., Arnold, H.-H., Radice, G. L. & Krauss, R. S. Niche Cadherins Control the Quiescence-to-Activation Transition in Muscle Stem Cells. *Cell Reports* **21**, 2236–2250 (2017).

207. Irintchev, A., Zeschnigk, M., Starzinski-Powitz, A. & Wernig, A. Expression pattern of M-cadherin in normal, denervated, and regenerating mouse muscles. *Dev. Dyn.* **199**, 326–337 (1994).

208. Marti, M. *et al.* M-cadherin-mediated intercellular interactions activate satellite cell division. *J Cell Sci* **126**, 5116–5131 (2013).

209. Troy, A. *et al.* Coordination of Satellite Cell Activation and Self-Renewal by Par-Complex-Dependent Asymmetric Activation of p38α/β MAPK. *Cell Stem Cell* **11**, 541–553 (2012).

210. Ono, Y. *et al.* Muscle Stem Cell Fate Is Controlled by the Cell-Polarity Protein Scrib. *Cell Reports* **10**, 1135–1148 (2015).

211. Playford, R. J. *et al.* The epidermal growth factor receptor (EGF-R) is present on the basolateral, but not the apical, surface of enterocytes in the human gastrointestinal tract. *Gut* **39**, 262–266 (1996).

212. Kuwada, S. K. *et al.* Differential signaling and regulation of apical vs. basolateral EGFR in polarized epithelial cells. *Am. J. Physiol.* **275**, C1419-1428 (1998).

213. Khazaei, M. R. & Püschel, A. W. Phosphorylation of the par polarity complex protein Par3 at serine 962 is mediated by aurora a and regulates its function in neuronal polarity. *J. Biol. Chem.* **284**, 33571–33579 (2009).

214. Goswami, S. *et al.* Macrophages Promote the Invasion of Breast Carcinoma Cells via a Colony-Stimulating Factor-1/Epidermal Growth Factor Paracrine Loop. *Cancer Res* **65**, 5278–5283 (2005).

215. Xiao, X. *et al.* M2 macrophages promote beta-cell proliferation by up-regulation of SMAD7. *PNAS* **111**, E1211–E1220 (2014).

216. Saclier, M. *et al.* Differentially Activated Macrophages Orchestrate Myogenic Precursor Cell Fate During Human Skeletal Muscle Regeneration. *STEM CELLS* **31**, 384–396 (2013).

217. Schneider, M. R. & Wolf, E. The epidermal growth factor receptor ligands at a glance. *J. Cell. Physiol.* **218**, 460–466 (2009).

218. Chalothorn, D. *et al.* Heparin-binding epidermal growth factor-like growth factor, collateral vessel development, and angiogenesis in skeletal muscle ischemia. *Arterioscler. Thromb. Vasc. Biol.* **25**, 1884–1890 (2005).

219. Burzyn, D. *et al.* A Special Population of Regulatory T Cells Potentiates Muscle Repair. *Cell* **155**, 1282–1295 (2013).

220. Kucherenko, M. M. *et al.* Genetic Modifier Screens Reveal New Components that Interact with the Drosophila Dystroglycan-Dystrophin Complex. *PLoS ONE* **3**, (2008).

221. Blau, H. M., Webster, C. & Pavlath, G. K. Defective myoblasts identified in Duchenne muscular dystrophy. *Proc. Natl. Acad. Sci. U.S.A.* **80**, 4856–4860 (1983).

222. Stuelsatz, P. *et al.* Extraocular muscle satellite cells are high performance myo-engines retaining efficient regenerative capacity in dystrophin deficiency. *Dev. Biol.* **397**, 31–44 (2015).

223. Long, C. *et al.* Postnatal genome editing partially restores dystrophin expression in a mouse model of muscular dystrophy. *Science* **351**, 400–403 (2016).

224. Nelson, C. E. *et al.* In vivo genome editing improves muscle function in a mouse model of Duchenne muscular dystrophy. *Science* **351**, 403–407 (2016).

225. Tabebordbar, M. *et al.* In vivo gene editing in dystrophic mouse muscle and muscle stem cells. *Science* **351**, 407–411 (2016).

226. Zhang, Y. *et al.* Dual AAV therapy ameliorates exercise-induced muscle injury and functional ischemia in murine models of Duchenne muscular dystrophy. *Hum Mol Genet* **22**, 3720–3729 (2013).

227. Sambasivan, R. *et al.* Pax7-expressing satellite cells are indispensable for adult skeletal muscle regeneration. *Development* **138**, 3647–3656 (2011).

228. Uezumi, A., Fukada, S., Yamamoto, N., Takeda, S. 'ichi & Tsuchida, K. Mesenchymal progenitors distinct from satellite cells contribute to ectopic fat cell formation in skeletal muscle. *Nat. Cell Biol.* **12**, 143–152 (2010).

229. von Maltzahn, J., Renaud, J.-M., Parise, G. & Rudnicki, M. A. Wnt7a treatment ameliorates muscular dystrophy. *PNAS* **109**, 20614–20619 (2012).

230. Sacco, A. *et al.* Short telomeres and stem cell exhaustion model Duchenne muscular dystrophy in mdx/mTR mice. *Cell* **143**, 1059–1071 (2010).

231. Duddy, W. *et al.* Muscular dystrophy in the mdx mouse is a severe myopathy compounded by hypotrophy, hypertrophy and hyperplasia. *Skelet Muscle* **5**, 16 (2015).

232. Yucel, N., Chang, A. C., Day, J. W., Rosenthal, N. & Blau, H. M. Humanizing the mdx mouse model of DMD: the long and the short of it. *NPJ Regen Med* **3**, 4 (2018).

233. Nishijo, K. *et al.* Biomarker system for studying muscle, stem cells, and cancer in vivo. *FASEB J.* **23**, 2681–2690 (2009).

234. Lee, T.-C. & Threadgill, D. W. Generation and validation of mice carrying a conditional allele of the epidermal growth factor receptor. *genesis* **47**, 85–92 (2009).

235. Tallquist, M. D., Weismann, K. E., Hellström, M. & Soriano, P. Early myotome specification regulates PDGFA expression and axial skeleton development. *Development* **127**, 5059–5070 (2000).

236. Marcon, E. *et al.* Assessment of a method to characterize antibody selectivity and specificity for use in immunoprecipitation. *Nat. Methods* **12**, 725–731 (2015).

237. Bushell, K. M., Söllner, C., Schuster-Boeckler, B., Bateman, A. & Wright, G. J. Large-scale screening for novel low-affinity extracellular protein interactions. *Genome Res.* **18**, 622–630 (2008).

238. Smith, L. R. & Barton, E. R. SMASH - semi-automatic muscle analysis using segmentation of histology: a MATLAB application. *Skelet Muscle* **4**, 21 (2014).

239. Hakim, C. H., Wasala, N. B. & Duan, D. Evaluation of muscle function of the extensor digitorum longus muscle ex vivo and tibialis anterior muscle in situ in mice. *J Vis Exp* (2013) doi:10.3791/50183.

240. Giordani, L. *et al.* High-Dimensional Single-Cell Cartography Reveals Novel Skeletal Muscle-Resident Cell Populations. *Mol. Cell* **74**, 609-621.e6 (2019).

241. Sacco, A., Doyonnas, R., Kraft, P., Vitorovic, S. & Blau, H. M. Self-renewal and expansion of single transplanted muscle stem cells. *Nature* **456**, 502–506 (2008).

242. Bar-Nur, O. *et al.* Direct Reprogramming of Mouse Fibroblasts into Functional Skeletal Muscle Progenitors. *Stem Cell Reports* **10**, 1505–1521 (2018).

243. Gilbert, P. M. *et al.* Substrate Elasticity Regulates Skeletal Muscle Stem Cell Self-Renewal in Culture. *Science* **329**, 1078–1081 (2010).

244. Beauchamp, J. R., Morgan, J. E., Pagel, C. N. & Partridge, T. A. Dynamics of Myoblast Transplantation Reveal a Discrete Minority of Precursors with Stem Cell–like Properties as the Myogenic Source. *J Cell Biol* **144**, 1113–1122 (1999).

245. Qu, Z. *et al.* Development of Approaches to Improve Cell Survival in Myoblast Transfer Therapy. *J Cell Biol* **142**, 1257–1267 (1998).

246. Tierney, M. T., Stec, M. J., Rulands, S., Simons, B. D. & Sacco, A. Muscle stem cells exhibit distinct clonal dynamics in response to tissue repair and homeostatic aging. *Cell Stem Cell* **22**, 119-127.e3 (2018).

247. Seale, P. *et al.* Pax7 Is Required for the Specification of Myogenic Satellite Cells. *Cell* **102**, 777–786 (2000).

248. Maltzahn, J. von, Jones, A. E., Parks, R. J. & Rudnicki, M. A. Pax7 is critical for the normal function of satellite cells in adult skeletal muscle. *PNAS* **110**, 16474–16479 (2013).

249. Machado, L. *et al.* In Situ Fixation Redefines Quiescence and Early Activation of Skeletal Muscle Stem Cells. *Cell Rep* **21**, 1982–1993 (2017).

250. van Velthoven, C. T. J., de Morree, A., Egner, I. M., Brett, J. O. & Rando, T. A. Transcriptional Profiling of Quiescent Muscle Stem Cells In Vivo. *Cell Rep* **21**, 1994–2004 (2017).

251. van den Brink, S. C. *et al.* Single-cell sequencing reveals dissociation-induced gene expression in tissue subpopulations. *Nature Methods* **14**, 935–936 (2017).

252. Lepper, C., Partridge, T. A. & Fan, C.-M. An absolute requirement for Pax7-positive satellite cells in acute injury-induced skeletal muscle regeneration. *Development* **138**, 3639–3646 (2011).

253. Moreno-García, A., Kun, A., Calero, O., Medina, M. & Calero, M. An Overview of the Role of Lipofuscin in Age-Related Neurodegeneration. *Front Neurosci* **12**, (2018).

254. Reimann, J., Irintchev, A. & Wernig, A. Regenerative capacity and the number of satellite cells in soleus muscles of normal and mdx mice. *Neuromuscul. Disord.* **10**, 276–282 (2000).

255. Kottlors, M. & Kirschner, J. Elevated satellite cell number in Duchenne muscular dystrophy. *Cell Tissue Res* **340**, 541–548 (2010).

256. Chang, N. C. *et al.* The Dystrophin Glycoprotein Complex Regulates the Epigenetic Activation of Muscle Stem Cell Commitment. *Cell Stem Cell* **22**, 755-768.e6 (2018).

257. Sreenivasan, K. *et al.* Attenuated Epigenetic Suppression of Muscle Stem Cell Necroptosis Is Required for Efficient Regeneration of Dystrophic Muscles. *Cell Reports* **31**, 107652 (2020).

258. Mead, A. F. *et al.* Diaphragm remodeling and compensatory respiratory mechanics in a canine model of Duchenne muscular dystrophy. *J Appl Physiol (1985)* **116**, 807–815 (2014).

259. Claflin, D. R. & Brooks, S. V. Direct observation of failing fibers in muscles of dystrophic mice provides mechanistic insight into muscular dystrophy. *American Journal of Physiology-Cell Physiology* **294**, C651–C658 (2008).

260. Partridge, T. A. The mdx mouse model as a surrogate for Duchenne muscular dystrophy. *FEBS J.* **280**, 4177–4186 (2013).

261. Pichavant, C. & Pavlath, G. K. Incidence and severity of myofiber branching with regeneration and aging. *Skeletal Muscle* **4**, 9 (2014).

262. Chan, S., Head, S. I. & Morley, J. W. Branched fibers in dystrophic mdx muscle are associated with a loss of force following lengthening contractions. *Am. J. Physiol., Cell Physiol.* **293**, C985-992 (2007).

263. Kuznetsov, A. V. *et al.* Impaired mitochondrial oxidative phosphorylation in skeletal muscle of the dystrophin-deficient mdx mouse. *Mol Cell Biochem* **183**, 87–96 (1998).

264. Kollu, S., Abou-Khalil, R., Shen, C. & Brack, A. S. The Spindle Assembly Checkpoint Safeguards Genomic Integrity of Skeletal Muscle Satellite Cells. *Stem Cell Reports* **4**, 1061–1074 (2015).

265. Fiore, D. *et al.* Pharmacological blockage of fibro/adipogenic progenitor expansion and suppression of regenerative fibrogenesis is associated with impaired skeletal muscle regeneration. *Stem Cell Res* **17**, 161–169 (2016).

266. Uezumi, A., Fukada, S., Yamamoto, N., Takeda, S. & Tsuchida, K. Mesenchymal progenitors distinct from satellite cells contribute to ectopic fat cell formation in skeletal muscle. *Nature Cell Biology* **12**, 143–152 (2010).

267. Joe, A. W. B. *et al.* Muscle injury activates resident fibro/adipogenic progenitors that facilitate myogenesis. *Nat. Cell Biol.* **12**, 153–163 (2010).

268. Fry, C. S., Kirby, T. J., Kosmac, K., McCarthy, J. J. & Peterson, C. A. Myogenic Progenitor Cells Control Extracellular Matrix Production by Fibroblasts during Skeletal Muscle Hypertrophy. *Cell Stem Cell* **20**, 56–69 (2017).

269. Bentzinger, C. F., Wang, Y. X., Dumont, N. A. & Rudnicki, M. A. Cellular dynamics in the muscle satellite cell niche. *EMBO Rep* **14**, 1062–1072 (2013).

270. Conboy, I. M., Conboy, M. J., Smythe, G. M. & Rando, T. A. Notch-mediated restoration of regenerative potential to aged muscle. *Science* **302**, 1575–1577 (2003).

271. Brack, A. S. *et al.* Increased Wnt Signaling During Aging Alters Muscle Stem Cell Fate and Increases Fibrosis. *Science* **317**, 807–810 (2007).

272. Brack, A. S. & Rando, T. A. Intrinsic changes and extrinsic influences of myogenic stem cell function during aging. *Stem Cell Rev* **3**, 226–237 (2007).

273. Hay, M., Thomas, D. W., Craighead, J. L., Economides, C. & Rosenthal, J. Clinical development success rates for investigational drugs. *Nature Biotechnology* **32**, 40–51 (2014).

274. Van Norman, G. A. Phase II Trials in Drug Development and Adaptive Trial Design. *JACC Basic Transl Sci* **4**, 428–437 (2019).

275. Hackam, D. G. & Redelmeier, D. A. Translation of Research Evidence From Animals to Humans. *JAMA* **296**, 1727–1732 (2006).

276. Pasut, A., Oleynik, P. & Rudnicki, M. A. Isolation of Muscle Stem Cells by Fluorescence Activated Cell Sorting Cytometry. in *Myogenesis: Methods and Protocols* (ed. DiMario, J. X.) 53–64 (Humana Press, 2012). doi:10.1007/978-1-61779-343-1_3.

277. Feige, P. & Rudnicki, M. A. Isolation of satellite cells and transplantation into mice for lineage tracing in muscle. *Nature Protocols* **15**, 1082–1097 (2020).

278. Shefer, G. & Yablonka-Reuveni, Z. Isolation and Culture of Skeletal Muscle Myofibers as a Means to Analyze Satellite Cells. in *Basic Cell Culture Protocols* (eds. Helgason, C. D. & Miller, C. L.) 281–304 (Humana Press, 2005). doi:10.1385/1-59259-838-2:281.

279. Le Grand, F., Jones, A. E., Seale, V., Scimè, A. & Rudnicki, M. A. Wnt7a Activates the Planar Cell Polarity Pathway to Drive the Symmetric Expansion of Satellite Stem Cells. *Cell Stem Cell* **4**, 535–547 (2009).

280. Maltzahn, J. von, Renaud, J.-M., Parise, G. & Rudnicki, M. A. Wnt7a treatment ameliorates muscular dystrophy. *PNAS* **109**, 20614–20619 (2012).

281. Kasper, A. M., Turner, D. C., Martin, N. R. W. & Sharples, A. P. Mimicking exercise in three-dimensional bioengineered skeletal muscle to investigate cellular and molecular mechanisms of physiological adaptation. *Journal of Cellular Physiology* **233**, 1985–1998 (2018).

282. Afshar Bakooshli, M. *et al.* A 3D culture model of innervated human skeletal muscle enables studies of the adult neuromuscular junction. *eLife* **8**,.

283. Li, E. W., McKee-Muir, O. C. & Gilbert, P. M. Chapter Five - Cellular Biomechanics in Skeletal Muscle Regeneration. in *Current Topics in Developmental Biology* (ed. Sassoon, D.) vol. 126 125–176 (Academic Press, 2018).

284. Shelton, M., Kocharyan, A., Liu, J., Skerjanc, I. S. & Stanford, W. L. Robust generation and expansion of skeletal muscle progenitors and myocytes from human pluripotent stem cells. *Methods* **101**, 73–84 (2016).

285. Piga, D. *et al.* Human induced pluripotent stem cell models for the study and treatment of Duchenne and Becker muscular dystrophies. *Ther Adv Neurol Disord* **12**, (2019).

286. Gissel, H. The Role of Ca2+ in Muscle Cell Damage. *Annals of the New York Academy of Sciences* **1066**, 166–180 (2006).

287. Tedesco, F. S., Moyle, L. A. & Perdiguero, E. Muscle Interstitial Cells: A Brief Field Guide to Non-satellite Cell Populations in Skeletal Muscle. in *Muscle Stem Cells: Methods and Protocols* (eds. Perdiguero, E. & Cornelison, D.) 129–147 (Springer, 2017). doi:10.1007/978-1-4939-6771-1_7.

288. Harrison, B. C., Allen, D. L. & Leinwand, L. A. IIb or not IIb? Regulation of myosin heavy chain gene expression in mice and men. *Skelet Muscle* **1**, 5 (2011).

289. Fry, C. S. *et al.* Fibre type-specific satellite cell response to aerobic training in sedentary adults. *J Physiol* **592**, 2625–2635 (2014).

290. Marg, A. *et al.* Human satellite cells have regenerative capacity and are genetically manipulable. *J Clin Invest* **124**, 4257–4265 (2014).

291. CIHI. Annual Statistics on Organ Replacement in Canada: Dialysis, Transplantation and Donation, 2009 to 2018. 9 (2019).

292. HRSA. National Data - OPTN. https://optn.transplant.hrsa.gov/data/view-data-reports/national-data/# (2020).

293. Saka, S. K. *et al.* Immuno-SABER enables highly multiplexed and amplified protein imaging in tissues. *Nat Biotechnol* **37**, 1080–1090 (2019).

294. Flamini, V. *et al.* The Satellite Cell Niche Regulates the Balance between Myoblast Differentiation and Self-Renewal via p53. *Stem Cell Reports* **10**, 970–983 (2018).

295. Yang, Z. J. P. *et al.* p53 suppresses muscle differentiation at the myogenin step in response to genotoxic stress. *Cell Death & Differentiation* **22**, 560–573 (2015).

296. Molchadsky, A. *et al.* p53 is required for brown adipogenic differentiation and has a protective role against diet-induced obesity. *Cell Death Differ* **20**, 774–783 (2013).

297. Walton, M. I., Wilson, S. C., Hardcastle, I. R., Mirza, A. R. & Workman, P. An evaluation of the ability of pifithrin-α and -β to inhibit p53 function in two wild-type p53 human tumor cell lines. *Mol Cancer Ther* **4**, 1369–1377 (2005).

298. Kastenhuber, E. & Lowe, S. Putting p53 in context. *Cell* **170**, 1062–1078 (2017).

299. Tapia, N. & Schöler, H. R. p53 connects tumorigenesis and reprogramming to pluripotency. *J Exp Med* **207**, 2045–2048 (2010).

300. Sullivan, K. D., Galbraith, M. D., Andrysik, Z. & Espinosa, J. M. Mechanisms of transcriptional regulation by p53. *Cell Death Differ* **25**, 133–143 (2018).

301. Riley, K. J.-L. & Maher, L. J. p53–RNA interactions: New clues in an old mystery. *RNA* **13**, 1825–1833 (2007).

302. Paz, I., Kosti, I., Ares, M., Cline, M. & Mandel-Gutfreund, Y. RBPmap: a web server for mapping binding sites of RNA-binding proteins. *Nucleic Acids Research* **42**, W361–W367 (2014).

303. Rawcliffe, D. F. R., Österman, L., Lindsten, H. & Holmberg, M. The High Level of Aberrant Splicing of ISCU in Slow-Twitch Muscle May Involve the Splicing Factor SRSF3. *PLOS ONE* **11**, e0165453 (2016).

304. Rawcliffe, D. F. R., Österman, L., Nordin, A. & Holmberg, M. PTBP1 acts as a dominant repressor of the aberrant tissue-specific splicing of ISCU in hereditary myopathy with lactic acidosis. *Mol Genet Genomic Med* **6**, 887–897 (2018).

305. Rau, F. *et al.* Misregulation of miR-1 processing is associated with heart defects in myotonic dystrophy. *Nat. Struct. Mol. Biol.* **18**, 840–845 (2011).

306. Dasgupta, T. & Ladd, A. N. The importance of CELF control: molecular and biological roles of the CUG-BP, Elav-like family of RNA binding proteins. *Wiley Interdiscip Rev RNA* **3**, 104–121 (2012).

307. Wang, W. *et al.* Ebf2 is a selective marker of brown and beige adipogenic precursor cells. *Proc Natl Acad Sci USA* **111**, 14466–14471 (2014).

308. Fornes, O. *et al.* JASPAR 2020: update of the open-access database of transcription factor binding profiles. *Nucleic Acids Res* **48**, D87–D92 (2020).

309. Kimura, E., Li, S., Gregorevic, P., Fall, B. M. & Chamberlain, J. S. Dystrophin delivery to muscles of mdx mice using lentiviral vectors leads to myogenic progenitor targeting and stable gene expression. *Mol. Ther.* **18**, 206–213 (2010).

310. Harper, S. Q. *et al.* Modular flexibility of dystrophin: implications for gene therapy of Duchenne muscular dystrophy. *Nat. Med.* **8**, 253–261 (2002).

311. Stedman, H. H. *et al.* The mdx mouse diaphragm reproduces the degenerative changes of Duchenne muscular dystrophy. *Nature* **352**, 536–539 (1991).

312. Relaix, F. *et al.* Pax3 and Pax7 have distinct and overlapping functions in adult muscle progenitor cells. *J. Cell Biol.* **172**, 91–102 (2006).

313. Stuelsatz, P., Keire, P., Almuly, R. & Yablonka-Reuveni, Z. A contemporary atlas of the mouse diaphragm: myogenicity, vascularity, and the Pax3 connection. *J. Histochem. Cytochem.* **60**, 638–657 (2012).

314. Ippolito, J., Arpke, R. W., Haider, K. T., Zhang, J. & Kyba, M. Satellite cell heterogeneity revealed by G-Tool, an open algorithm to quantify myogenesis through colony-forming assays. *Skelet Muscle* **2**, 13 (2012).

315. Murach, K. A. *et al.* Depletion of Pax7+ satellite cells does not affect diaphragm adaptations to running in young or aged mice. *J. Physiol. (Lond.)* **595**, 6299–6311 (2017).

316. Keefe, A. C. *et al.* Muscle stem cells contribute to myofibers in sedentary adult mice. *Nat Commun* **6**, 7087 (2015).

317. Allen, D. G., Whitehead, N. P. & Froehner, S. C. Absence of Dystrophin Disrupts Skeletal Muscle Signaling: Roles of Ca2+, Reactive Oxygen Species, and Nitric Oxide in the Development of Muscular Dystrophy. *Physiol Rev* **96**, 253–305 (2016).

318. Lazure, F. *et al.* Myf6/MRF4 is a Myogenic Niche Regulator Required for the Maintenance of the Muscle Stem Cell Pool. *bioRxiv* 691386 (2019) doi:10.1101/691386.

319. Chen, X. & Li, Y. Role of matrix metalloproteinases in skeletal muscle. *Cell Adh Migr* **3**, 337–341 (2009).

320. Tonks, N. K. Protein tyrosine phosphatases: from genes, to function, to disease. *Nature Reviews Molecular Cell Biology* **7**, 833–846 (2006).

321. Stanoev, A. *et al.* Interdependence between EGFR and Phosphatases Spatially Established by Vesicular Dynamics Generates a Growth Factor Sensing and Responding Network. *Cell Systems* **7**, 295-309.e11 (2018).

322. Hubbard, S. R., Mohammadi, M. & Schlessinger, J. Autoregulatory Mechanisms in Protein-tyrosine Kinases. *J. Biol. Chem.* **273**, 11987–11990 (1998).

# Appendices

## Appendix A supplemental data for manuscript I

### Satellite Cell Specification into Brown Adipose is Regulated by p53

AUTHORS: Peter Feige[1,2,3], Hang Yin[1,4], Hong Ming[1], Mohammad Abdul-Ghani[1,2,3], Lynn Megeney[1,2,3], and Michael. A. Rudnicki[1,2,3].

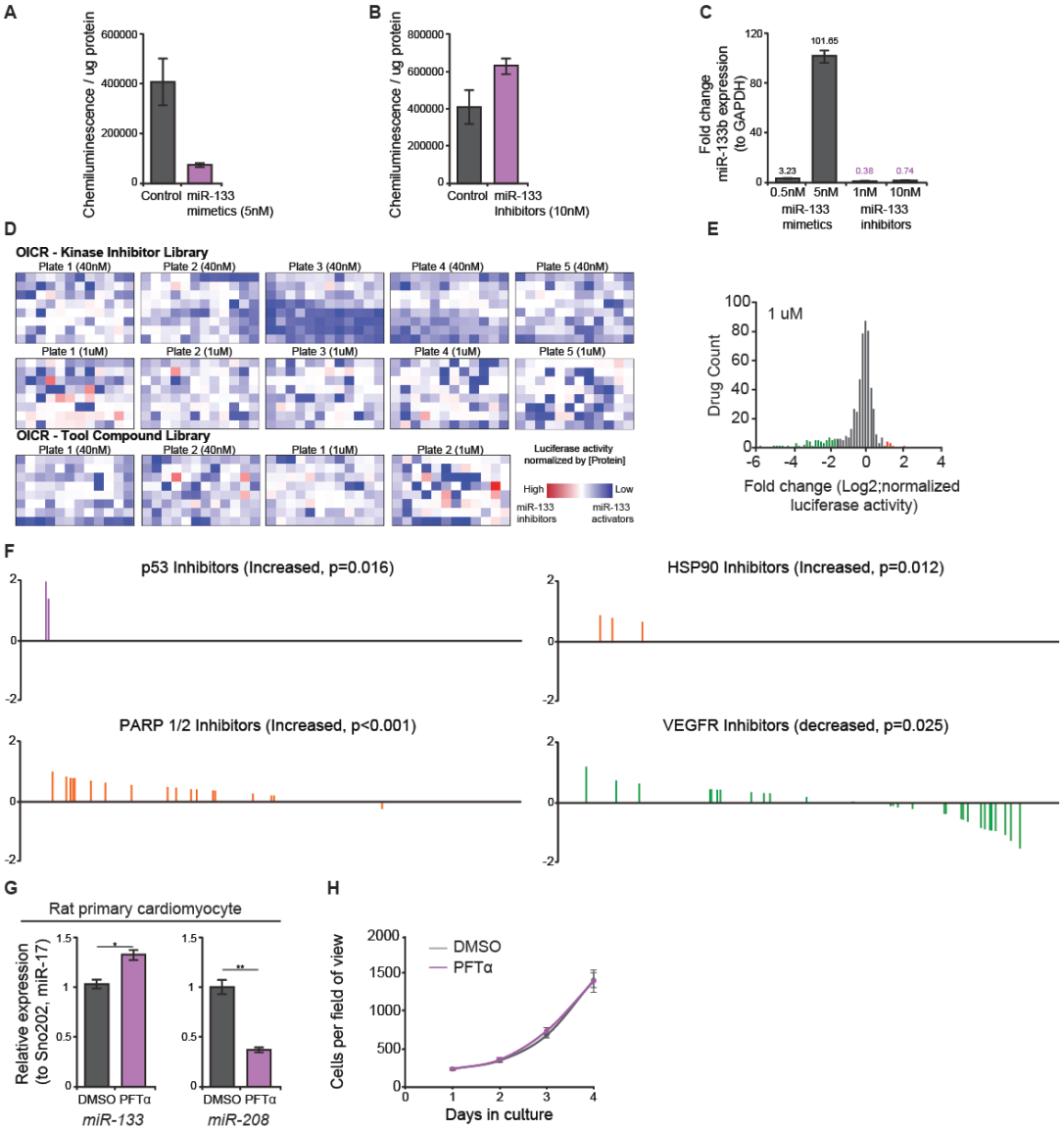


Figure S1: ***MiR-133* biosensor design and validation, Related to Figure 6.** Luciferase assay validation through transfection of A) *miR-133* mimetics and B) *miR-133* inhibitors into the Biosensor line. C) Quantitative Real-time PCR for *miR-133*b in Biosensor cells treated with *miR-133* mimetic or inhibitors. D) Biosensor screening result heatmap representing compounds from the OICR Kinase inhibitor library and OICR Tool compound library at listed concentrations with high (Red) and low (Blue) *miR-133* inhibition. E) Relative change in luciferase activity of biosensor following small molecule screening at 1uM concentration. F) Compounds targeting the same pathway are grouped where statistical significances were calculated based on Wilcoxon-Mann-Whitney rank-sum tests between grouped drugs and total 560 compounds with p-values in parenthesis. G) Quantitative Real-time PCR for *miR-133* and miR-208 in cultured rat primary cardiomyocytes treated with PFTα. H) Quantification of cell numbers per field in mouse primary myoblast seeded at equal densities and cultured in the presence of PFTα or equal volume DMSO control. (A-C) Error bars represent means ±SD; (G-H) Error bars represent mean ±SEM; p-values: *=<0.05, **=<0.01. (A-C) n=6 technical replicate; (G-H) n=3 biological replicates.

| Drug | Target/Function | 40nM | 1uM | ANP Luc |
|---|---|---|---|---|
| Niclosamide | STAT3 inhibitor | 5.80 | 2.20 | 23.8 |
| Irestatin 9389 | IRE1 inhibitor | 4.81 | 0.87 | 2.7 |
| Pifithrin-alpha | P53 inactivator | 3.80 | 2.15 | 2.2 |
| Kenpaullone, alsterpaullone | CDK1, GSK-3b inhibitor | 2.92 | 2.64 | 2.1 |
| Ryuvidine | CDK4 inhibitor | 2.79 | 1.80 | 2.6 |
| Cyclic Pifithrin-alpha hydrobromide | P53 inhibitor | 2.57 | 1.91 | 1.4 |
| Axitinib, AG-013736 | PDGFR, VEGFR1, VEGFR2, VEGFR3, c-FMS inhibitor | 2.28 | 2.87 | 12.2 |
| GTP 14564 | ITD-FLT3 inhibitor | 2.05 | 2.17 | 1.8 |
| Vinorelbine, ANX-530, KW-2307, NVB, SDP-012, Navelbine, Eunades, Exelbine | Tubulin polymerization inhibitor | 2.03 | 1.40 | 0.9 |
| PERK inhibitor | PERK inhibitor | 2.00 | 0.73 | 2.2 |
| 3-Aminobenzamide, 3-ABA, INO-1001 | PARP inhibitor | 1.97 | 1.07 | 2.4 |
| PD-98059 | MEK1, MEK2, ERK1 inhibitor | 1.91 | 2.54 | 4.8 |
| Bexarotene, Targretin, Targretyn, Targrexin, LGD-1069, LG 1069, LG100069, SR-11247 | Retinoid X receptor agonist, RXRs agonist | 1.90 | 0.96 | 3.5 |
| Sal003 | eIF2a inhibitor | 1.87 | 0.97 | 1.9 |
| 17-(Allylamino) Geldanamycin, 17-AAG, Telatinib, Tanespimycin, 17-(Allylamino)-17-demethoxygeldanamycin | Hsp90 inhibitor | 1.80 | 0.35 | 4.2 |
| Quercetin | PI3K inhibitor | 1.78 | 0.97 | 2.8 |
| 6-bromoindirubin-3'-oxime, BIO, Indirubin | GSK-3 inhibitor | 1.76 | 2.28 | 1.1 |
| 5-AIQ hydrochloride | PARP inhibitor | 1.75 | 1.10 | 2.8 |
| Rofecoxib, Vioxx, Ceoxx, Ceeoxx | Cyclooxygenase (COX-2) inhibitor | 1.75 | 0.99 | 3.1 |
| INH2BP | PARP inhibitor | 1.71 | 1.12 | 9 |
| EB-47 | PARP inhibitor | 1.69 | 0.71 | 1.6 |
| 17-DMAG, Alvespimycin, KOS-1022, NSC 07545, 17-(Dimethylaminoethylamino)-17-demethoxygeldanamycin Hydrochloride | Hsp90 inhibitor | 1.68 | 0.04 | 5.3 |
| BMS-345541 | IKK inhibitor | 1.68 | 1.77 | 2.6 |
| XAV-939 | Tankyrase inhibitor | 1.63 | 1.18 | 1.4 |
| IWR-1 | Tankyrase inhibitor | 1.61 | 1.09 | 1.8 |
| 4-HQN | PARP inhibitor | 1.60 | 1.09 | 1.6 |
| NVP-AUY922, AUY922, VER-52296 | Hsp90 inhibitor | 1.53 | 0.03 | 3.2 |
| GSK 4716 | Estrogen-Related Receptor beta (ERRBeta, ERR2) agonist | 1.50 | 1.13 | 3.4 |
| Docetaxel, Taxotere, RP-56976 | Microtubule disassembly inhibitor | 1.44 | 1.46 | 3.1 |
| Wortmannin, KY 12420 | PI3K (covalent) | 1.40 | 1.32 | 0.7 |

Table S1**: Candidate list of compounds identified in the Biosensor screen.** Compounds that increased biosensor activities (Green) at 40 nM concentration and 1 µM concentration, were chosen for ANP luciferase assay. Compounds that significantly increased ANP luciferase activity are in yellow.

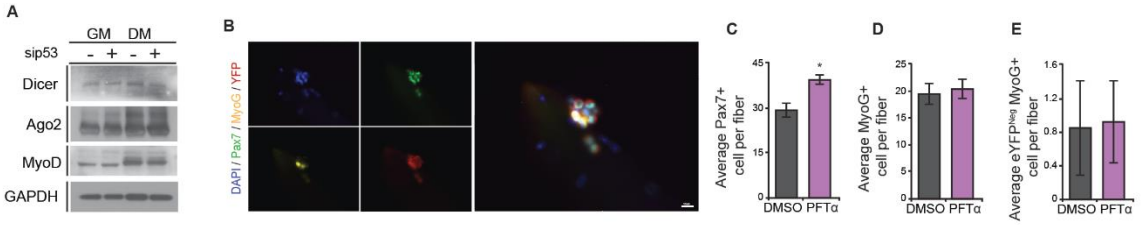


Figure S2: **PFTα promotes muscle stem cell hyperplasia, Relating to Figure 7.** A) Immunoblotting analysis of Dicer, Ago2, MyoD in primary mouse myoblast harvested 48 hours after transfection or 48h after transfection in differentiation medium with scrambled control siRNA (siSCR) or siRNA against p53 (sip53). GAPDH was used as the loading control. B) Single-channel images showing a representative image of myofibres cultured for 72h and stained for DAPI (Blue), Pax7 (Green), MyoG (Yellow) and eYFP (Red). Quantification of C) average total Pax7-expressing cells per myofibre, D) average MyoG-expressing cell per myofibre and E) average eYFPNeg MyoG-expressing cells per myofibre at 72h from Myf5Cre-eYFP EDL fibre cultures treated with 50nM PFTα or equal DMSO control. (C-E) Error bars represent mean ±SEM; p-values: *=<0.05, **=<0.01. (A-E,) n=3 biological replicates.

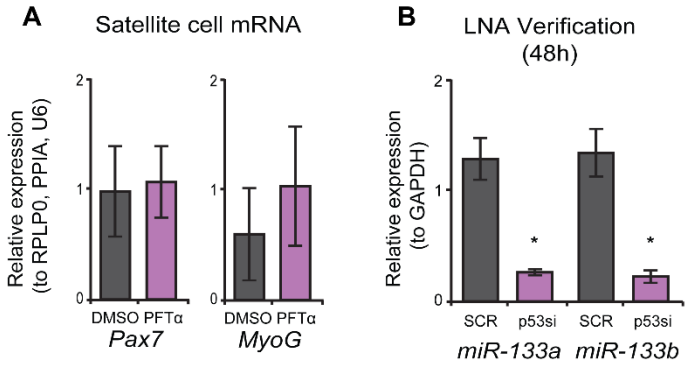


Figure S3: **Tumor suppressor p53 regulates *miR-133* maturation, Relating to Figure 8.** A) Quantitative Real-time PCR for Pax7 and MyoG in 50nM PFTα treated Pax7nGFP satellite cells. B) Locked Nucleic Acid primer validation of *miR-133*a and *miR-133*b isoforms following the transfection of siRNA targeting p53 (si-p53) or scramble control (SCR) 48 hours following transfection. (A-B) Error bars represent mean ±SEM; p-values: *=<0.05. (A) n=3 DMSO biological replicates, n=6 PFTa biological replicates, (B) n=3 biological replicates.

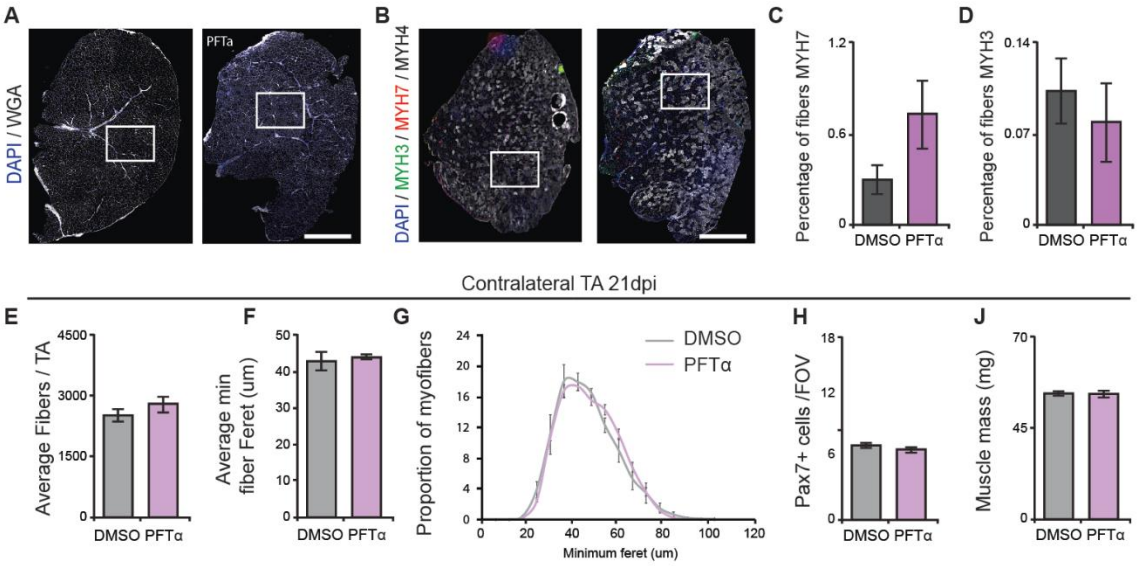


Figure S4: **PFTα limits myogenic differentiation in vivo, Relating to Figure 9.** Representative images of PFTα or DMSO treated TA muscle stained with A) DAPI (Blue) and Wheat Germ Agglutinin (White) or B) DAPI (Blue), MYH3 (Green), MYH7 (Red) and MYH4 (White). Quantification of the proportion of myofibres expressing C) MYH7 or D) MYH3 21 days post-injury in PFTα or DMSO treated TA muscle. Quantification of E) the average number of fibres per TA muscle, F) average minimum fibre Feret, G) minimum myofibre Feret proportion of total TA myofibres, H) Pax7-expressing cells per field of view (20x) and I) muscle mass from uninjured contralateral TA muscles 21 days post-PFTα or DMSO treatment in the right TA. (C-I) Error bars represent mean ±SEM; p-values: *=<0.05, (A-I) n= 3 DMSO replicates, n=4 PFTα replicates.

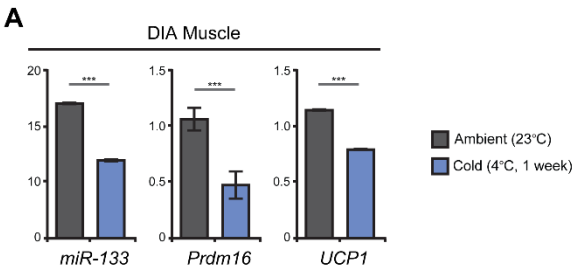


Figure S5: **MicroRNA-133 differentially regulated in response to cold, Relating to**

**Figure** 10**.** A) Quantitative Real-time PCR for *miR-133*, Prdm16 and UCP1 in Diaphragm muscle from cold (4°C, 1 week) exposed C57BL/6 mice. Error bars represent means ±SEM; p-values: ***=<0.005. n=3 biological replicates.

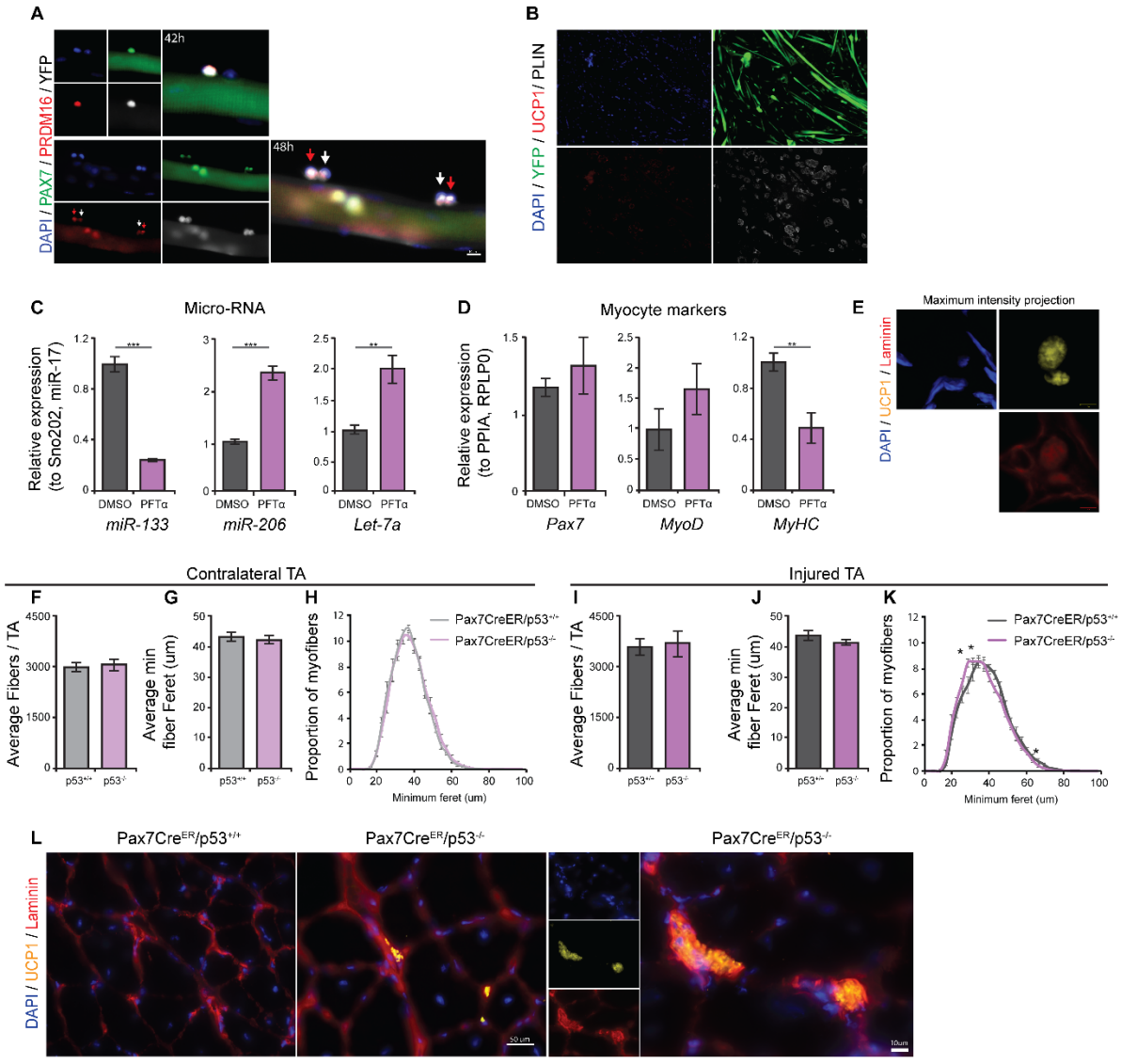


Figure S6: **Inhibition of p53 promotes satellite cell fate switching, Relating to Figure 11.** A) Representative images of DAPI (Blue) Pax7 (Green), PRDM16 (Red) and eYFP (White) expressing satellite cells cultured on EDL myofibres in adipogenic media for 42h (top panel) or 48h (bottom panel). Red arrows denote Pax7-, Prdm16-, eYFP-expressing satellite cell progeny while white arrows denote Pax7-, eYFP-expressing satellite cell progeny following a division asymmetric for PRDM16 expression. (B) Single-channel images of DAPI (Blue) eYFP (Green), UCP1 (Red) and PLIN (White) expressing adipose from Pax7Cre-eYFP myofibre cultures in adipogenic media. Quantitative Real-time PCR for (C) *miR-133*, *miR-206*, Let-7a and (D) Pax7, MyoD, MYHC in C2C12 myoblasts treated with 50nM PFTα and cultured under adipogenic conditions. E) Representative single-channel images of injured TA from C57BL/6 mice treated with 50nM PFTα stained with DAPI (Blue), UCP1 (Yellow) and Laminin (Red) showing interstitial brown adipocytes. Quantification of F) the average number of fibres per TA muscle, G) average minimum fibre Feret and H) minimum myofibre Feret proportion of total TA myofibres in uninjured contralateral TA muscle from Pax7Cre$^{ER}$/p53 mice. Quantification of I) the average number of fibres per TA muscle, J) average minimum fibre Feret and K) minimum myofibre

Feret proportion of total TA myofibres in injured TA muscle from Pax7Cre$^{ER}$/p53 mice. L) Representative images and single-channel images of injured TA muscle from Pax7Cre$^{ER}$/p53$^{+/+}$ and Pax7Cre$^{ER}$/p53$^{-/-}$ homozygous mice stained for DAPI (Blue), UCP1 (Yellow) and Laminin (Red) showing interstitial brown adipocytes. (C-D) Error bars represent mean ±SD, (E-K) Error bars represent mean ±SEM; p-values: *=<0.05, **=<0.01; ***=<0.005. (C-D) n=6 technical replicates, (A-B, E-K) n=3 biological replicates.

## Appendix B supplemental data for manuscript II

### EGFR-Aurora Kinase A signalling promotes satellite cell myogenic commitment

AUTHORS: Yu Xin Wang[1,2,4], Peter Feige[1,2,4], Caroline E. Brun[1,2], Bahareh Hekmatnejad[1,2], Nicolas A. Dumont[1,2], Jean-Marc Renaud[2,] Sharlene Faulkes[1,2], Daniel E. Guindon[1,2], and Michael A. Rudnicki [1,2,3,5].

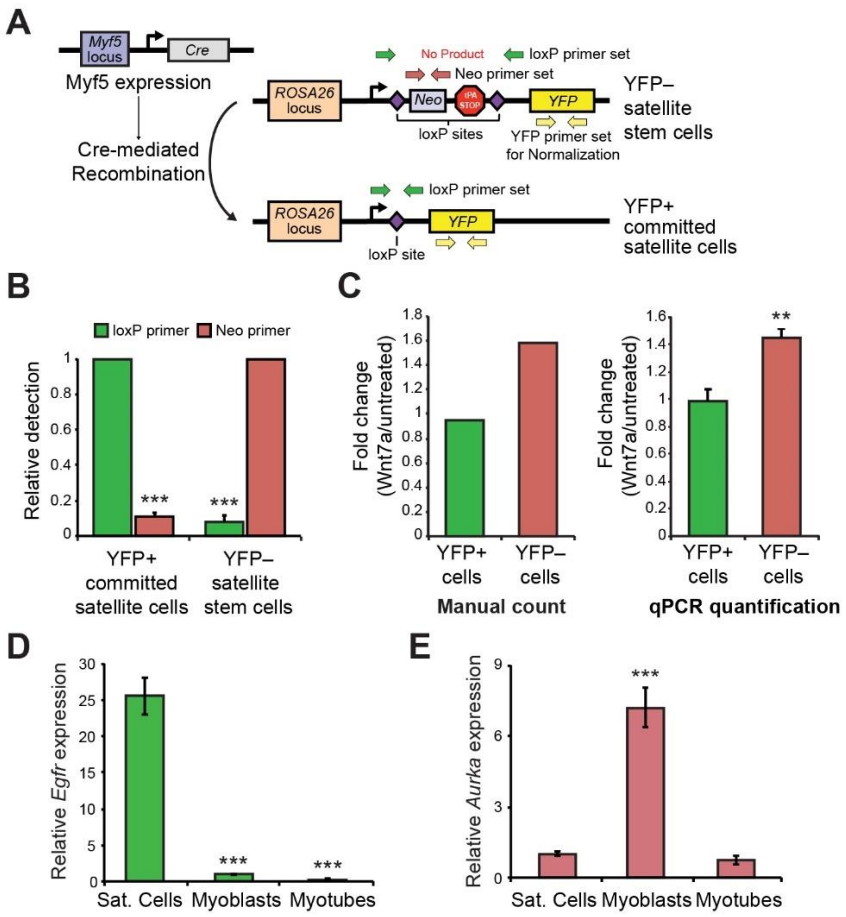


Figure S7: **RT-qPCR Enumeration of YFP+ and YFP– Cells.** (A) Schematic overview of Myf5-Cre mediated recombination at the R26R-eYFP allele and primer pair design to detect YFP status of cells by genotyping. When the Myf5 locus is expressed, Cre recombinase is expressed and excises the genetic region between the loxP sites at the ROSA26 locus. This removes a PKG-Neo cassette and triple polyadenylation terminator sequences, and allows the transcription of the eYFP cDNA. Primers were designed for the Neo cassette (red arrows), spanning the loxP sites (green arrows), and within the YFP cDNA (yellow arrows). (B) Quantitative Real-time PCR for Neo and loxP primer sets in myoblasts derived from $YFP^{+}$ committed satellite cells and $YFP^{-}$ satellite stem cells. Error bars represent means ± SEM; p-values: ***=< 0.005. (C) Direct comparison between manual counting and qPCR enumeration for $YFP^{+}$ committed satellite cells and $YFP^{-}$ satellite stem cells on cultured FDB myofibres at 42h of culture in the presence of PBS control or recombinant Wnt7a. Cultured fibres were split into 4 equal portions and quantified by manual counting and qPCR in triplicate, concurrently. Error bars represent means ± SEM; p-values: **=< 0.01. (D) Quantitative Real-time PCR for EGFR in satellite cells, myoblasts and myotubes. Error bars represent means ± SEM; p-values: ***=< 0.005. (E) Quantitative Real-time PCR for Aurka in satellite cells, myoblasts and myotubes. Error bars represent means ± SEM; p-values: ***=< 0.005.

| Synonyms | Annotated Primary Targets | Fold Change |
|---|---|---|
| ZM 449829 | Potent, selective JAK3 inhibitor | 6.768 |
| ZM 447439 | Inhibits Aurora kinase B | 4.214 |
| EKI-785, CL-387785 | EGFR (Irreversible) | 2.830 |
| PF-573228 | FAK | 2.651 |
| SD 169 | p38 MAPK | 2.543 |
| CHIR-98014 isomer, CT-98014 | GSK-3 | 2.412 |
| BX-795 | PDK1, TBK1 | 2.256 |
| PQ401 | IGF1R | 2.214 |
| SB 216763 | GSK-3 | 2.160 |
| PP-2, PP2, AG-1879 | p56 LCK, p59 FYN, HCK, Src | 2.135 |
| SB 239063 | p38 MAPK | 2.024 |
| CT-99021, CHIR-99021 | GSK-3 | 2.019 |
| LY-364947, HTS 466284 | ALK5 | 1.967 |
| JNJ-7706621 | Aurora Kinase, CDK | 1.932 |
| GSK-461364, GSK461364 | PLK1, PLK3 | 1.863 |
| SB 203580, SB-203580 | p38 MAPK | 1.855 |
| ZM 39923 hydrochloride | Potent, selective JAK3 inhibitor | 1.831 |
| Dorsomorphin dihydrochloride | Potent and selective AMPK inhibitor | 1.826 |
| TC-A 2317 hydrochloride | Aurora A | 1.800 |
| KU0063794, KU-0063794, KU-63794 | mTOR, TORC1, TORC2 | 1.795 |
| BIBU 1361 dihydrochloride | EGFR | 1.750 |
| GDC-0941 bismesylate, RG-7321 | PI3K | 1.690 |
| BIO | Potent, selective GSK-3 inhibitor | 1.646 |
| Chk2 Inhibitor II, 339253 | Chk2 | 1.634 |
| NU-6102 | CDK1, CDK2 | 1.628 |
| GW-5074 | c-RAF | 1.617 |
| Ro 08-2750 | Inhibits NGF binding to p75NTR and TrkA | 1.604 |
| PF-04217903 | MET | 1.584 |
| Lapatinib ditosylate, Tykerb, GW572016 | EGFR, erbB2 (HER2) | 1.581 |
| CI-1033, Canertinib, PD-183805, SN-26606 | EGFR, erbB2 (HER2) (covalent) | 1.579 |
| GTP 14564 | ITD-FLT3 | 1.570 |
| PD-184352, CI-1040 | MEK | 1.564 |
| PD 407824 | Selective inhibitor of Chk1 and Wee1 | 1.559 |
| AEG 3482 | JNK | 1.556 |
| XL-880, GSK-1363089, EXEL-2880, GSK-089, foretinib | MET, VEGFR2, FLT3, TEK | 1.552 |
| GW-843682X | PLK1, PLK3 | 1.544 |
| Vatalanib dihydrochloride, PTK-787, ZK-222584, CGP79787D | VEGFR, PDGFR | 1.537 |
| PIK-90 | PI3K p110a | 1.536 |
| NIK Kinase Inhibitor | NIK | 1.528 |
| ZM 39923 hydrochloride | JAK3 | 1.523 |
| AMG-Tie2-1 | TIE-2, TEK | 1.519 |
| TPL2 | TPL2 Kinase (MAPKKK8) | 1.512 |

Table S2: **FDB screening hits with annotated primary targets related to Figure 13**.

CSC Wang et al Nov 2018 Movie S1 pEGFR 3D for submission.mp4

Movie S1: **3D reconstruction of a satellite cell expressing polarized p-EGFR 2 days post injury related to Figure 15**. Myofibres were stained for DAPI (blue), Pax7 (red) and p-EGFR (green). Series of pictures was taken by confocal microscopy and reconstructed into a 3D image using ImageJ. Also available in the online version of the article: https://doi.org/10.1016/j.stem.2019.01.002

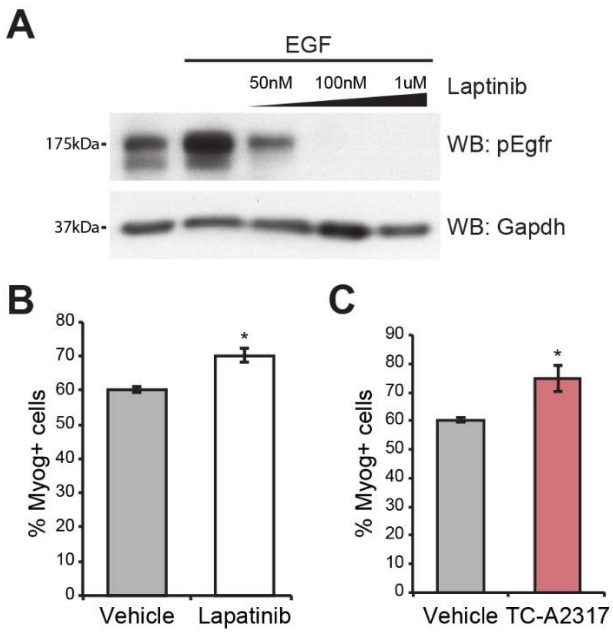


Figure S8: **Validation of lead compounds Lapatinib and TC-A2317.** (A) Immunoblotting analysis of p-EGFR in myoblasts cultured in the presence of vehicle control or recombinant EGF with 50nM, 100nM, or 1uM of Lapatinib. Gapdh was used as loading control. (B) Percentage of Myog+ cells relative to the total number of cells in myotubes differentiated for 2-day in the presence of DMSO control (vehicle) or Lapatinib. (C) Percentage of Myog+ cells relative to the total number of cells in myotubes differentiated for 2-day in the presence of DMSO control (vehicle) or TC-A2317. (B–C) Error bars represent means ± SEM; p-values: *=< 0.05. (B–C) n=4 biological replicates.

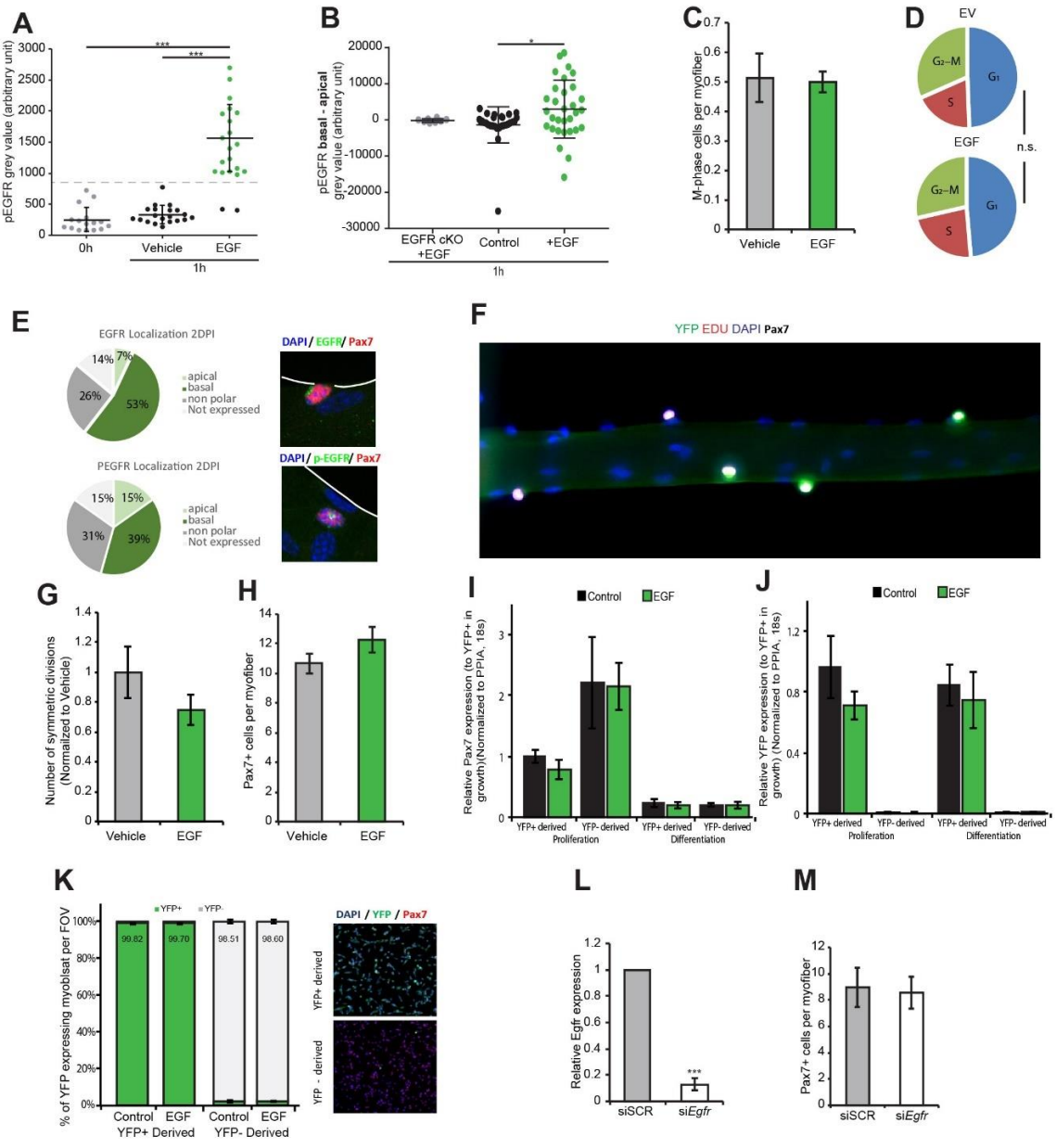


Figure S9: **EGFR Signalling in Satellite Cells and Myoblasts.** (A) Dot plot of p-EGFR staining intensity in satellite cells on EDL myofibres fixed immediately after dissection (0h), and after 1h culture in Ham's F10 media with vehicle control or 100ng/mL of recombinant EGF (EGF). (B) Dot plot of basal vs apical p-EGFR staining intensity in satellite cells on EDL myofibres from mdx mice fixed after 1h culture in Ham's F10 media with vehicle control or 100ng/mL of recombinant EGF (EGF). Fibres from tamoxifen treated EGFR cKO mice cultured in 100ng/ml recombinant EGF served as a biological reference control. (C) Quantification of mitotic satellite cells per myofibre at 36h of culture in the presence of 1% BSA in PBS control (vehicle) or recombinant EGF. (D) Cell cycle kinetics of primary myoblasts cultured in the presence of 1% BSA in PBS control (vehicle) or recombinant EGF for 24h. (E) Analysis of EGFR (n= 43 pictures) and p-EGFR (n=46 pictures) localization from injured EDL muscle fixed 2 days post injury and manually dissociated

then stained with DAPI (blue), EGFR or p-EGFR (green) and Pax7 (red). (F) Representative image of myofibres isolated from Myf5cre/R26R-eYFP mice cultured in control or 100ng/ml recombinant EGF containing media supplemented with EDU for 20h and allowed 20h chase prior to fixing and staining with DAPI (blue), EDU (red), YFP (green) and Pax7(gray). (G) Relative number of symmetric satellite stem cell divisions per myofibre at 42h of culture in the presence of 1% BSA in PBS control (vehicle) or recombinant EGF. (H) Quantification of Pax7+ satellite cells per myofibre at 42h of culture in the presence of 1% BSA in PBS control (vehicle) or recombinant EGF. (I-J) Quantitative Real-time PCR for Pax7 and YFP in myoblasts derived from YFP+ committed satellite cells and YFP- satellite stem cells. Error bars represent means ± SEM. (K) Proportion of YFP+ myoblast derived from YFP+ committed satellite cells and YFP- satellite stem cells treated with control or 100ng/ml EGF and stained for DAPI (blue), YFP (green) and Pax7 (red). Error bars represent means ± SEM. (L) Quantitative Real-time PCR for EGFR in cultured myoblasts 48h after transfection with scrambled control siRNA (siSCR) or siRNA against EGFR (siEGFR). (M) Quantification of Pax7+ satellite cells per myofibre at 42h of culture after transfection with scrambled control siRNA (siSCR) or siRNA against EGFR (siEGFR). (A-B) Error bars represent means ± SD; (C-M) Error bars represent means ± SEM; p-values: *=< 0.05; ***=< 0.005. (A) n > 15 cells for each condition; (B) n>25 for each experimental condition (C) n=6 mice; (D) n=3 biological replicates; (E) n=43 and n=46 cells respectively (G-H) n=4 mice. (I and J) n=3 biological replicates; (K) n=3 biological replicates; (L and M) n=6 mice.

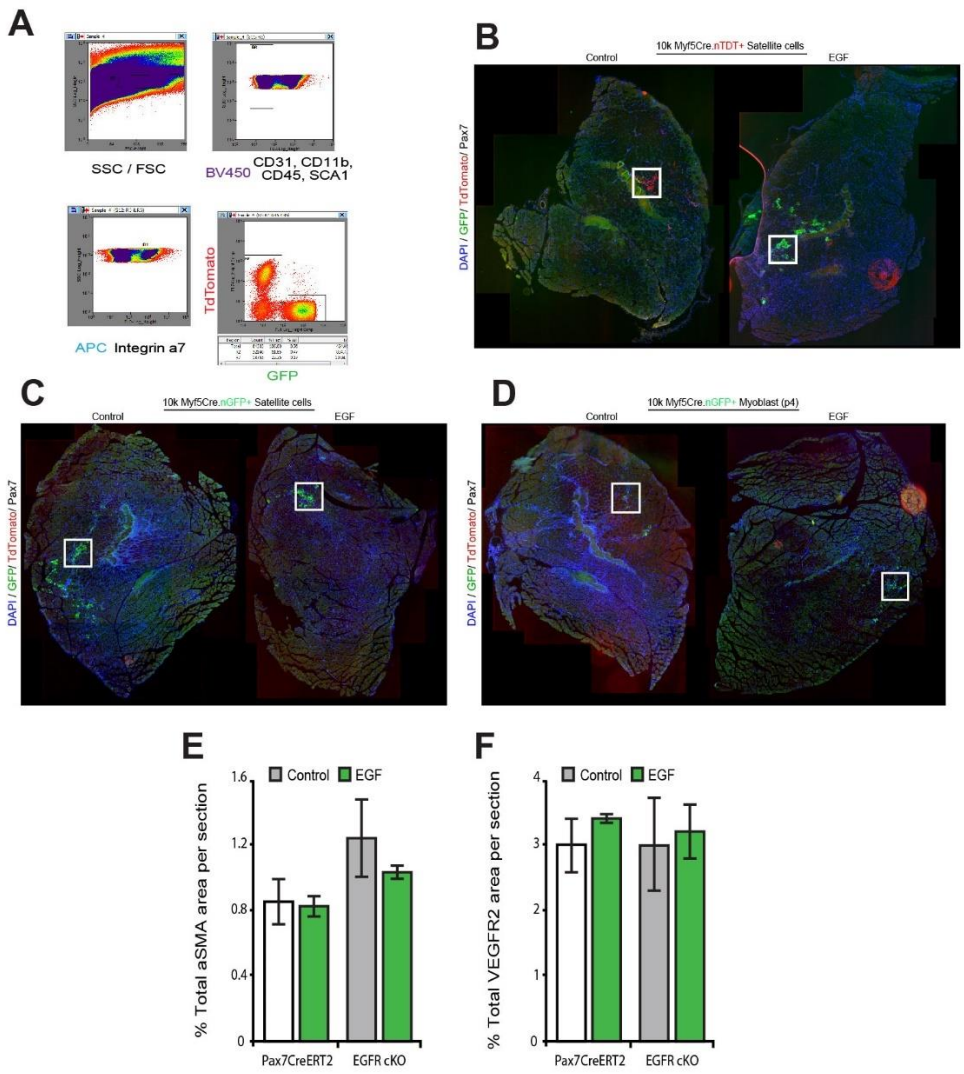


Figure S10: **EGFR signalling in satellite stem cells promotes asymmetric division.** (A) FACS gating strategy for the isolation of quiescent satellite cells from Myf5Cre.nTnG mice. Cells are selected based on forward and side scatter profile, purified by selecting lineage-low (CD31, CD11b, CD45, Sca1 – V450), integrin a7 (APC) and then separated based on TdTomato and GFP signal. (B-D) Representative stitched imaged of whole transplanted *Tibialis Anterior* muscle immunostained for DAPI (blue), GFP (green), TdTomato (red) and Pax7 (gray). Contrast was enhanced for viewing. (E) Quantification of aSMA+ areas in TA muscle of Pax7CreERT2 or EGFR cKO mice 10 days after injury and intramuscular saline or recombinant EGF. (F) Quantification of VEGFR2+ areas in TA muscle of Pax7CreERT2 or EGFR cKO mice 10 days after injury and intramuscular saline or recombinant EGF. (E-F) Error bars represent means means ± SEM; (B) n=3 mice per condition; (C) n=4 mice per condition; (D) n=3 mice per condition; (E–F) n=3 mice per condition.

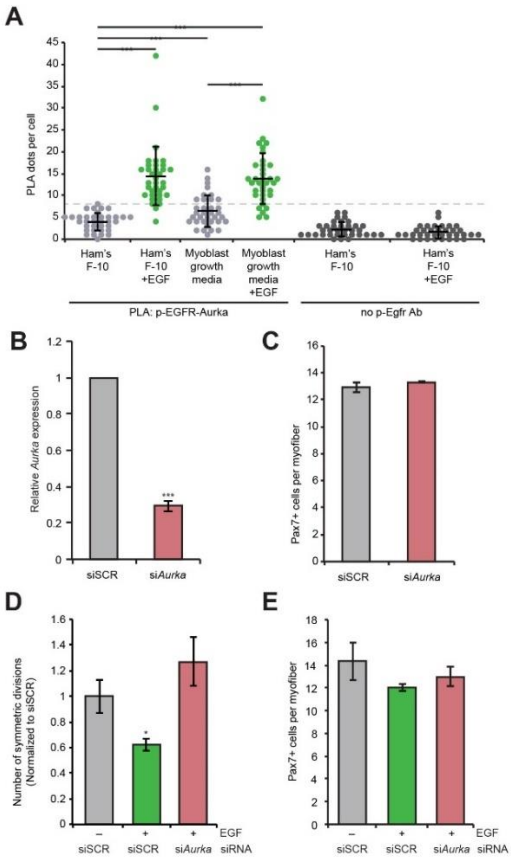


Figure S11: **EGFR-Aurka Interactions in Satellite Cells and Myoblasts.** (A) Quantification of PLA interactions between Aurka and p-EGFR (dots) in serum-starved Pax7-nGFP myoblasts that were refed with Ham's F-10 media, Ham's F-10 media supplemented with recombinant EGF, growth media, or growth media supplemented with recombinant EGF for 1h. Error bars represent means ± SD; p-values: ***=< 0.005; n=35 cells for each condition. Control PLA experiements performed without p-EGFR antibody (Ab) was used as control. The dashed line represents three standard deviations from the average number of dots in serum-starved Pax7-nGFP myoblasts that were refed with Ham's F-10 media stained without p-EGFR antibody. (B) Quantitative Real-time PCR for Aurka in cultured myoblasts 48h after transfection with scrambled control siRNA (siSCR) or siRNA against Aurka (siAurka). Error bars represent means ± SEM; p-values: ***=< 0.005. (C) Quantification of Pax7+ satellite cells per myofibre at 42h of culture after transfection with scrambled control siRNA (siSCR) or siRNA against Aurka (siAurka). (D) Relative number of symmetric satellite stem cell divisions per myofibre at 42h of culture in the presence of 1% BSA in PBS control (vehicle) after transfection with scrambled control siRNA (siSCR), or recombinant EGF after transfection with scrambled control siRNA (siSCR) or siRNA against Aurka (siAurka). (E) Quantification of Pax7+ satellite cells per myofibre at 42h of culture in the presence of 1% BSA in PBS control (vehicle) after transfection with scrambled control siRNA (siSCR), or recombinant EGF after transfection with scrambled control siRNA (siSCR) or siRNA against Aurka (siAurka). (B–E) Error bars represent means ± SEM; p-values: *=< 0.05. (C) n=3 mice; (D–E) n=3 mice.

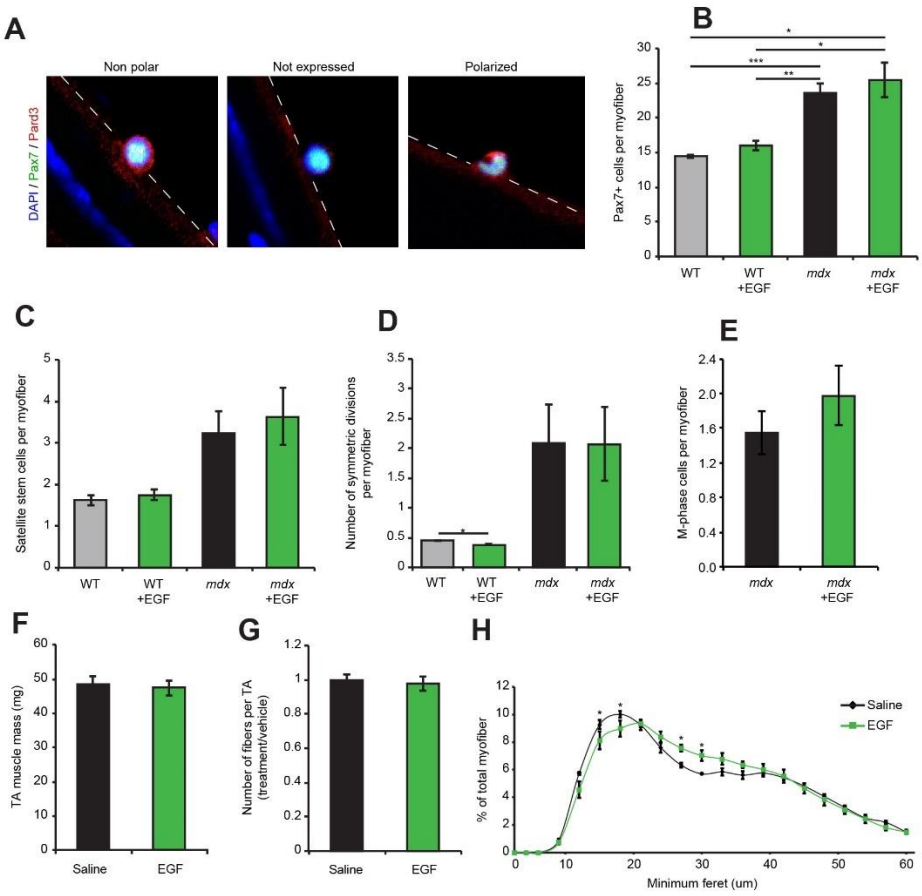


Figure S12: **EGFR-Aurka Signalling During Muscle Regeneration.** (A) Representative pictures of 36h cultured myofibres immunostained for DAPI (blue), Pax7 (green) and Pard3 (red). (B) Quantification of Pax7+ satellite cells per myofibre in WT and mdx myofibres at 42h of culture in the presence of 1% BSA in PBS control (vehicle) or recombinant EGF. (C) Quantification of YFP- satellite stem cells per myofibre in WT and mdx myofibres at 42h of culture in the presence of 1% BSA in PBS control (vehicle) or recombinant EGF. (D) Quantification of symmetric satellite stem cell divisions per myofibre in WT and mdx myofibres at 42h of culture in the presence of 1% BSA in PBS control (vehicle) or recombinant EGF. (E) Quantification of mitotic satellite cells per myofibre in mdx myofibres at 36h of culture in the presence of 1% BSA in PBS control (vehicle) or recombinant EGF. (F) Muscle mass of regenerating mdx TA muscles 10 days post cardiotoxin-induced injury, treated with saline (vehicle), or recombinant EGF protein normalized to their contralateral legs. (G) Number of myofibres in regenerating mdx TA muscles 10 days post cardiotoxin-induced injury, treated with saline (vehicle), or recombinant EGF protein. (H) Distribution of minimum Feret of myofibres from regenerating mdx TA muscles 10 days post cardiotoxin-induced injury and treated with saline (vehicle), or recombinant EGF protein. (B–H) Error bars represent means ± SEM; p-values: *=< 0.05; **=< 0.01; ***=< 0.005. (B–D) n=3 WT mice and 7 mdx mice; (E) n=4 mice; (F–G) n=4 mice for each group; (H) n=4 mice for each group.

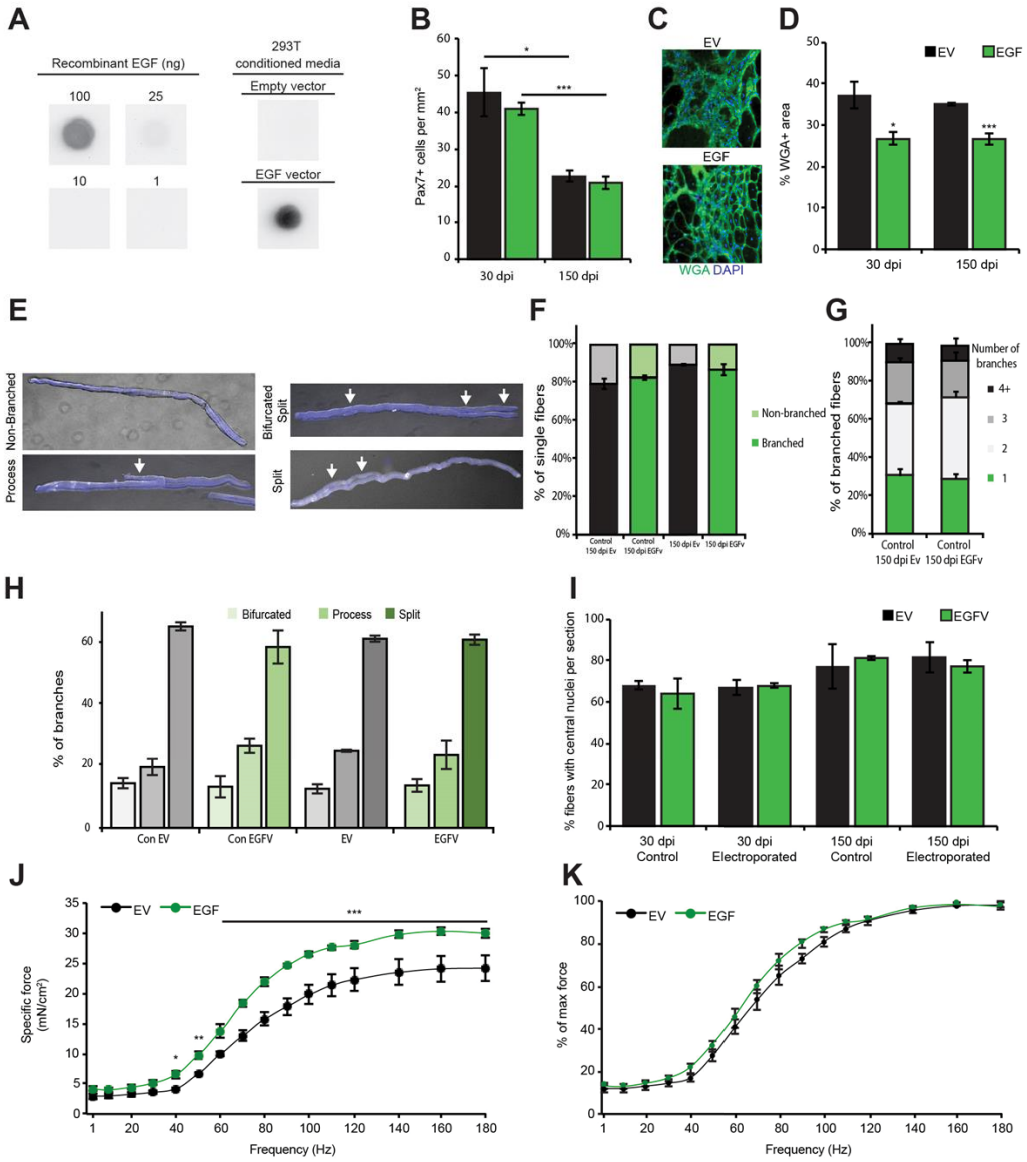


Figure S13: **Short and Long-term EGF Supplementation in mdx Muscles.** (A) Dot blot of EGF protein expression levels in conditioned media of 293T cells transiently transfected with empty vector (EV) or EGF expression vector (EGF). 1, 10, 25, and 100ng of recombinant EGF protein were loaded as a standard curve. (B) Quantification of Pax7+ cells on cross-sections TA muscles of mdx mice 30 or 150 days after electroporation with empty vector (EV) or EGF expression vector (EGF). (C) Representative image of wheat-germ agglutinin (WGA) stained fibrotic deposits on frozen sections from TA muscles of mdx mice 30 or 150 days after electroporation with empty vector (EV) or EGF expression vector (EGF). DNA is stained with DAPI (blue). (D) Quantification of WGA+ fibrotic areas in TA muscle of mdx mice 30 or 150 days after electroporation with empty vector (EV) or EGF expression vector (EGF). (E) Representative images of myofibres isolated from electroporated and control (non-electroporated) EDLs of mdx mice 150 days after electroporation with empty vector (EV) or EGF expression vector (EGF) stained with DAPI (blue) and imaged in brightfield showing myofibres branching in process, split and bifurcated profiles. (F) Quantification of branched and unbranched fibres isolated from

electroporated and control (non-electroporated) EDLs of mdx mice 150 days after electroporation with empty vector (EV) or EGF expression vector (EGF). (G) Quantification of the number of branches in fibres isolated from control (non-electroporated) EDLs of mdx mice 150 days after contralateral electroporation with empty vector (EV) or EGF expression vector (EGF). (H) Proportion of branch types in fibres isolated from electroporated and control (non-electroporated) EDLs of mdx mice 150 days after electroporation with empty vector (EV) or EGF expression vector (EGF). (I) Proportion of myofibres with centrally located nuclei in TA muscles of mdx mice 30 and 150 days after electroporation with empty vector (EV) or EGF expression vector (EGF) or non-electroporated muscle. (J) Force frequency response of TA muscles mdx mice 30 days after electroporation with empty vector (EV) or EGF expression vector (EGF). (K) Normalized force frequency response of TA muscles mdx mice 30 days after electroporation with empty vector (EV) or EGF expression vector (EGF). (B–D and F-K) Error bars represent means ± SEM. (B–K) n=4 mice for each group at 30 dpi and 3 mice for each group at 150 dpi.

## Appendix C supplemental data for manuscript III

### Isolation of satellite cells and transplantation into mice for lineage tracing in muscle

AUTHORS: Peter Feige[1,2,3] and Michael A. Rudnicki[1,2,3,4]

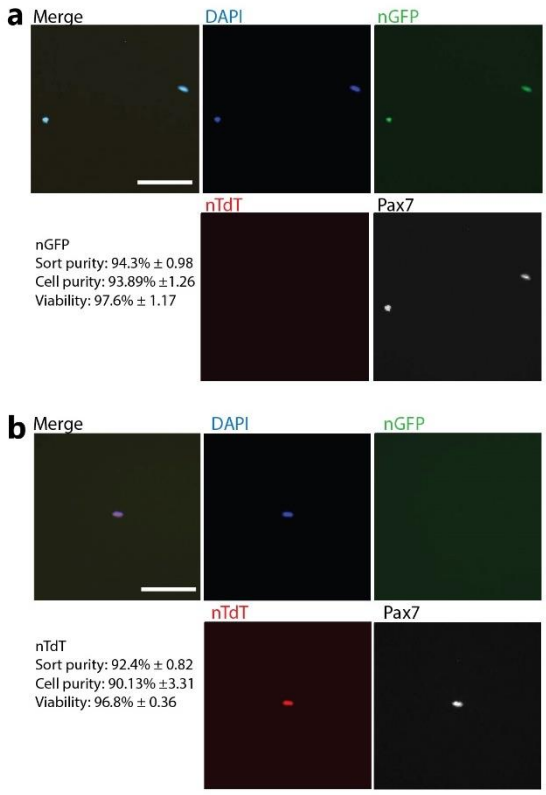


Figure S14: **Cell purity quality control prior to engraftment.** Representative immunofluorescence images with single channels for (a) committed satellite cell transplants and (b) satellite stem cell transplants. Blue: DAPI, Green: nGFP, Red: nTdTomato, White: Pax7. Scale bar, 50um. N=3, average ± s.d. Experimental protocols for mice used in this study were performed in accordance with the guidelines established by the University of Ottawa Animal Care Committee, which is based on the guidelines of the Canadian Council on Animal Care.

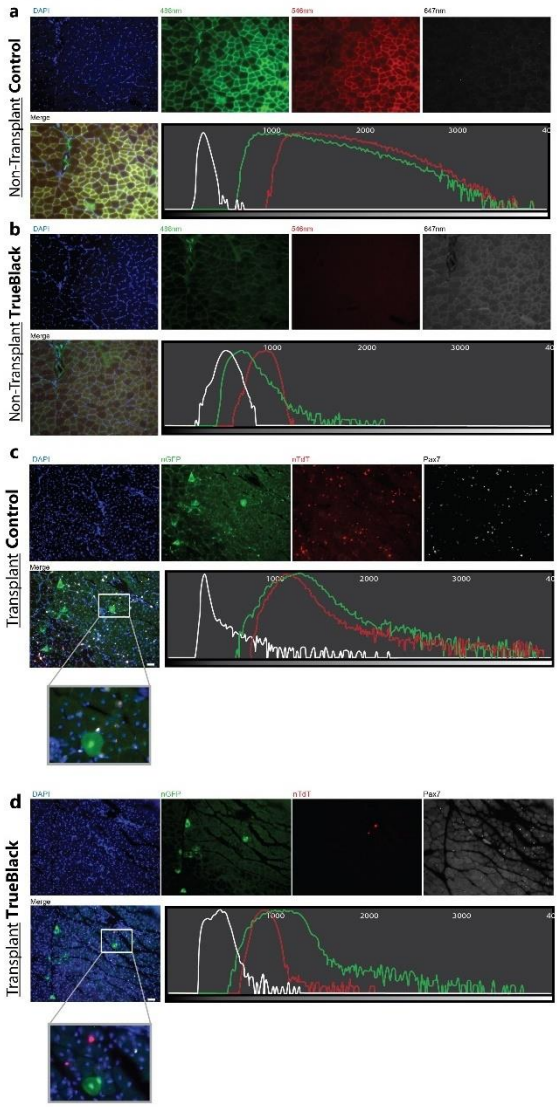


Figure S15**: Lipofuscin quenching validation for transplanted tissue.** (a) Representative immunofluorescence images of non-injured, non-transplanted muscle show the high levels of autofluorescence present within skeletal muscle. A trace of the 12 Bit histogram from Zen 2.5 for 488nm, 546nm and 647nm is shown. (b) Lipofuscin quenched sections from serial sections have significantly decreased background in 488nm and 546nm with a slight increase in 647nm autofluorescence. (c-d) Representative immunofluorescence images from satellite stem cell (nTdTomato) transplants treated without TrueBlack (c) show the significant presence of non-cellular (DAPI-negative) autofluorescence artifact within injured skeletal muscle which impede the ability to detect real signal from transplanted cells as shown following blocking with TrueBlack (d). Blue: DAPI, Green: nGFP, Red: nTdTomato, White: Pax7. Scale bar, 100um. Experimental protocols for mice used in this study were performed in accordance with the guidelines established by the University of Ottawa Animal Care Committee, which is based on the guidelines of the Canadian Council on Animal Care.

| **Cell population** | **Estimated total cell number from hindlimb muscle (n=3) (average ± s.d.)** | **Sort purity (n=3) (average ± s.d.)** | **Cell purity (Pax7+) (n=3) (average ± s.d.)** |
|---|---|---|---|
| All cells | 2,810,538 ± 1,133,009 | | |
| Single cells by FSC | 2,015,627 ± 931,449 | | |
| Single cells by SSC | 1,568,226 ± 832,752 | | |
| $CD11b^-$, $CD31^-$, $CD45^-$, $SCA1^-$ | 898,128 ± 489,943 | | |
| ITGA7 | 102,579 ± 4798 | | |
| nGFP | 70721 ± 6292 | 94.3% ± 0.98 | 93.89% ±1.26 |
| nTdTomato | 25464 ± 1873 | 92.4% ±0.82 | 90.13% ±3.31 |

Table S3**: Yield and purity for the transplantation protocol.**

## Appendix D supplemental data for manuscript IV

### Muscle regeneration is impaired in the *mdx* mouse model

Caroline E. Brun[1,2,4], Peter Feige[1,2,4], Marie-Claude Sincennes[1,2], Michael A. Rudnicki[1,2,3,*]

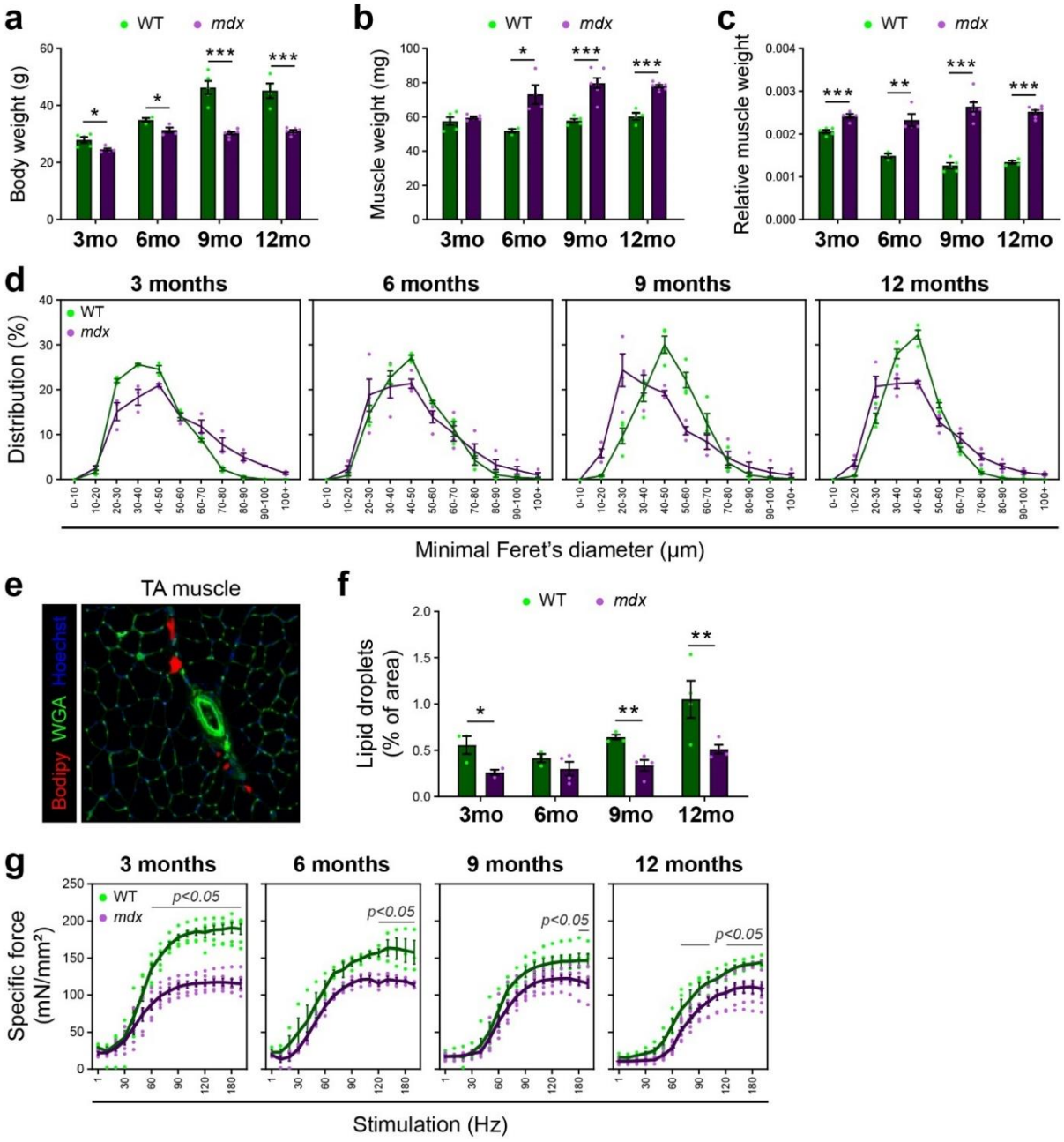


Figure S16: **Progressive degeneration in mdx muscle impairs physiological force, Related to Figure 25.** A) Quantification of mouse body weight increase from WT and *mdx* mice 3-12 months in age. B) Quantification of TA muscle weight increase from WT and *mdx* mice 3-12 months in age. C) Quantification of relative TA muscle weight to body weight from WT and *mdx* mice 3-12 months in age. D) Quantification of minimum fibre Feret distribution from WT and *mdx* mice 3-12 months in age. E) Representative image of TA muscle stained with Hoechst (Blue), Wheat germ agglutinin (Green) and Bodipy (Red). F) Quantification of lipid content from Bodipy stained TA cross-sections from WT and *mdx* mice 3-12 months in age. G) Quantification of specific force responses from WT and *mdx* mice 3-12 months in age. (A-D, F-G) Error bars represent mean ±SEM; p-values: *=<0.05, **=<0.01; ***=<0.005. (A-G) n= 3-7 mice, where individual data points represent independent animals

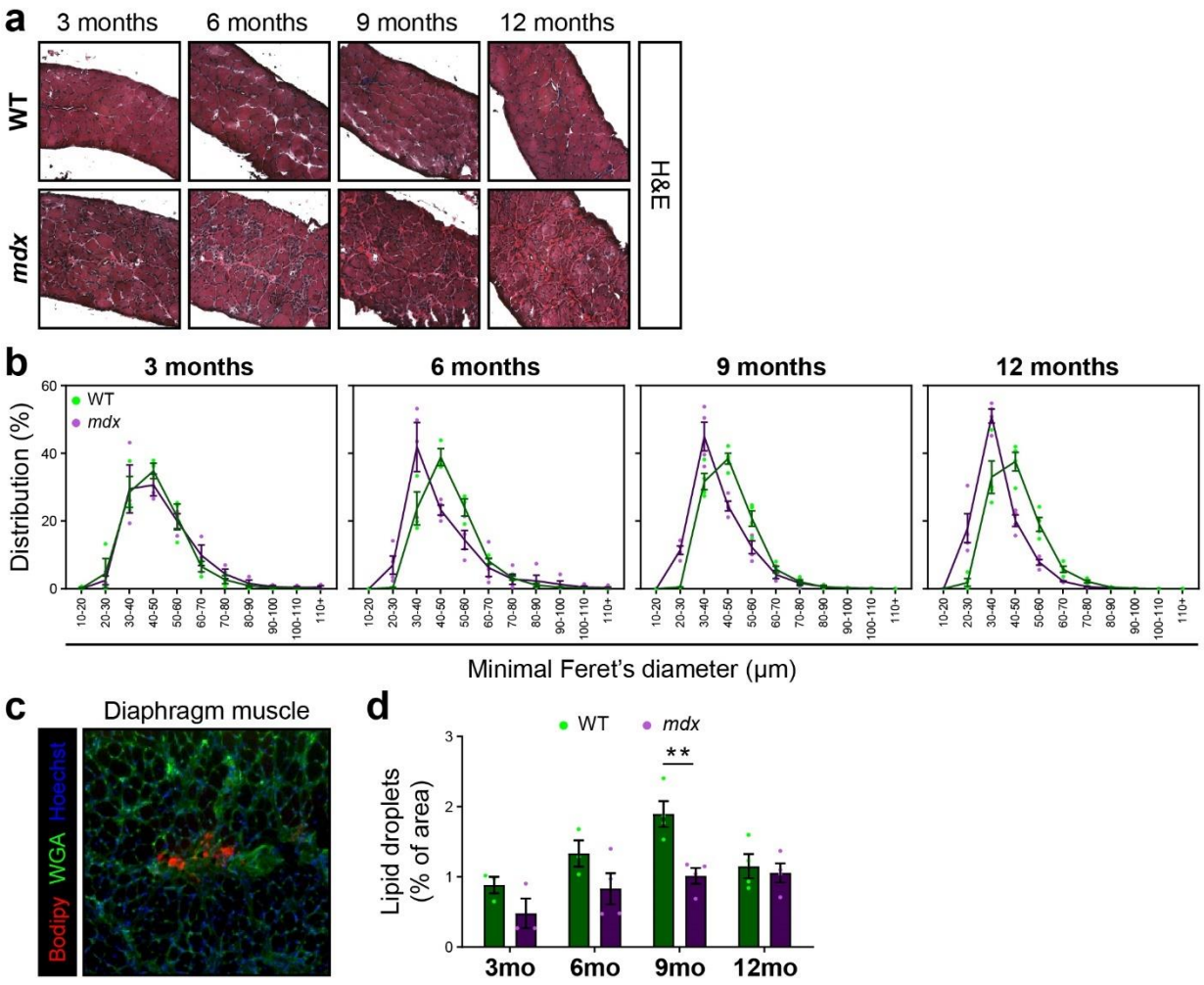


Figure S17: **Diaphragm muscle is acutely impacted in mdx mice, Related to Figure 26.** A) Representative images of wild-type and *mdx* Diaphragm cross sections labelled by Hematoxylin and Eosin from 3-12 month aged mice. B) Quantification of minimum fibre Feret distribution from WT and *mdx* mice 3-12 months in age. C) Representative image of Diaphragm muscle stained with Hoechst (Blue), Wheat germ agglutinin (Green) and Bodipy (Red). D) Quantification of lipid content from Bodipy stained TA cross-sections from WT and *mdx* mice 3-12 months in age. (B, D) Error bars represent mean ±SEM; p-values: **=<0.01 (B,D) n= 3-4 mice, where individual data points represent independent animals.

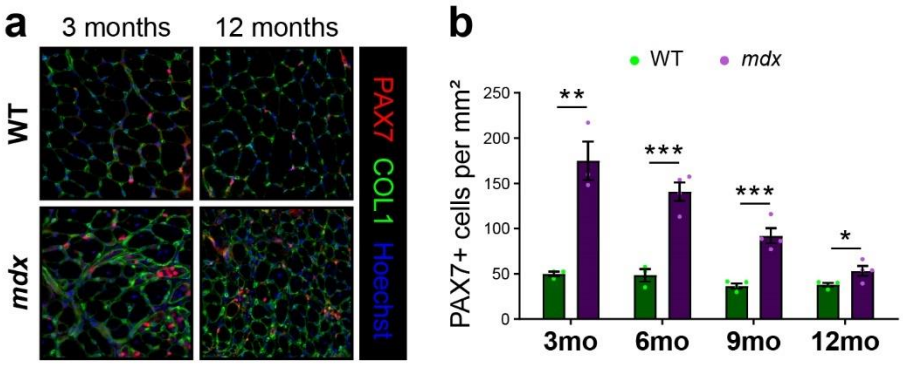


Figure S18: **Dystrophin-deficiency impacts satellite cell signalling, Related to Figure 27.** A) Representative images of WT and *mdx* Diaphragm cross-sections stained by immunofluorescence for Hoechst (Blue), Collagen (Green), and Pax7 (Red). B) Quantification of Pax7-expressing cell quantity per $mm^2$ in WT and *mdx* mice Diaphragm cross sections from 3-12 months in age. (B) Error bars represent mean ±SEM; p-values: *=<0.05, **=<0.01; ***=<0.005 (B,D) n= 3-4 mice, where individual data points represent independent animals.

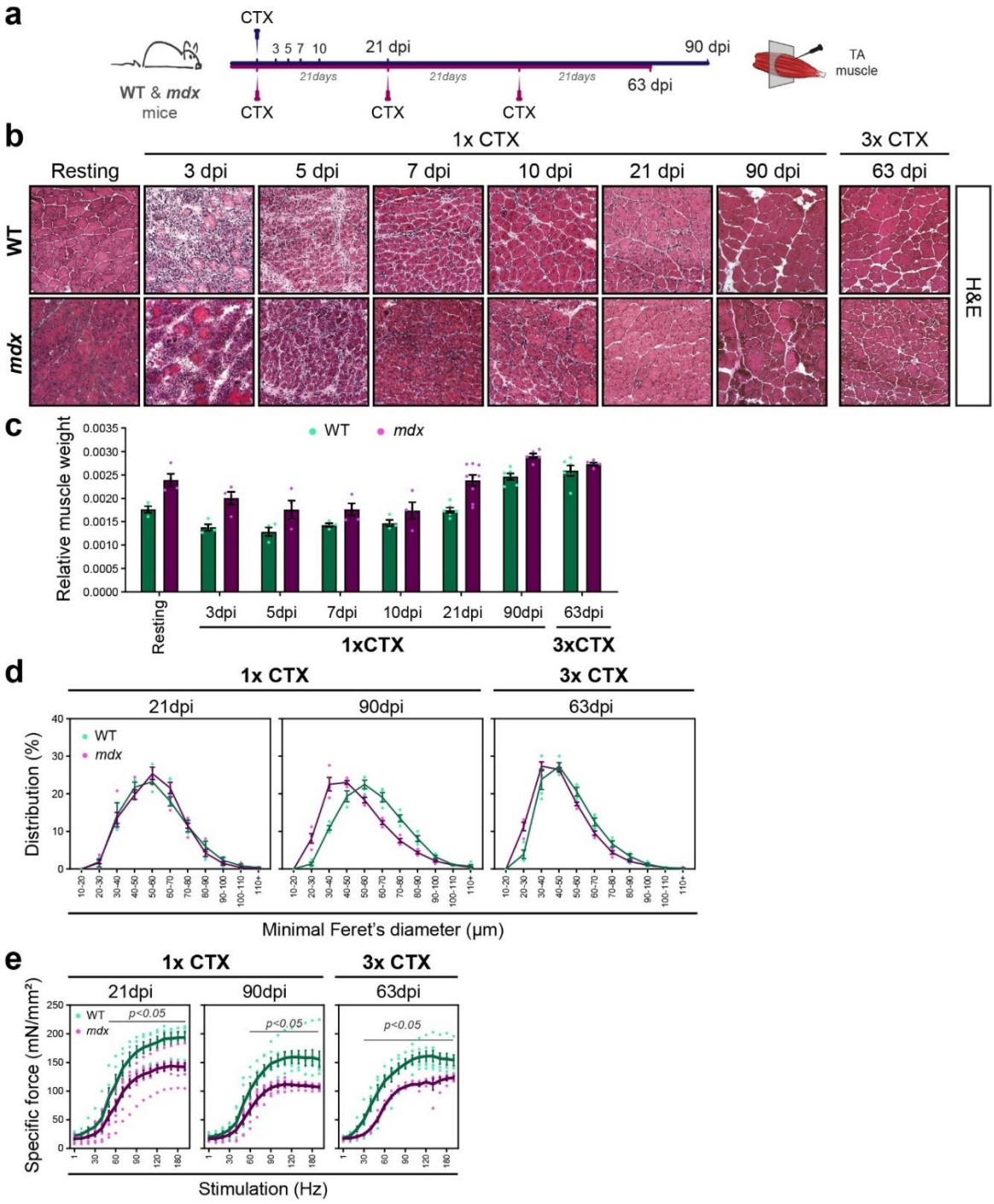


Figure S19: **Regeneration is impaired following injury in *mdx* muscle, Related to Figure 28.** A) Schematic overview of the injury time course. B) Representative images of injured WT and *mdx* TA muscle cross-sections stained with Hematoxylin and Eosin. C) Quantification of relative injured TA muscle weight to body weight from WT and *mdx* mice. D) Quantification of minimum fibre Feret distribution from injured WT and *mdx* TA muscle. E) Quantification of specific force responses from injured TA muscle from WT and *mdx* mice. (A-E) Error bars represent mean ±SEM; p-values: are provided in the panels. (A-G) n= 3-8 mice, where individual data points represent independent animals.

## Appendix E supplemental data for manuscript V

### Ex vivo culture of in-niche human satellite cells

AUTHORS: Peter Feige[1,2,3], Eve Tsai[4] Michael A. Rudnicki[1,2,3,5]

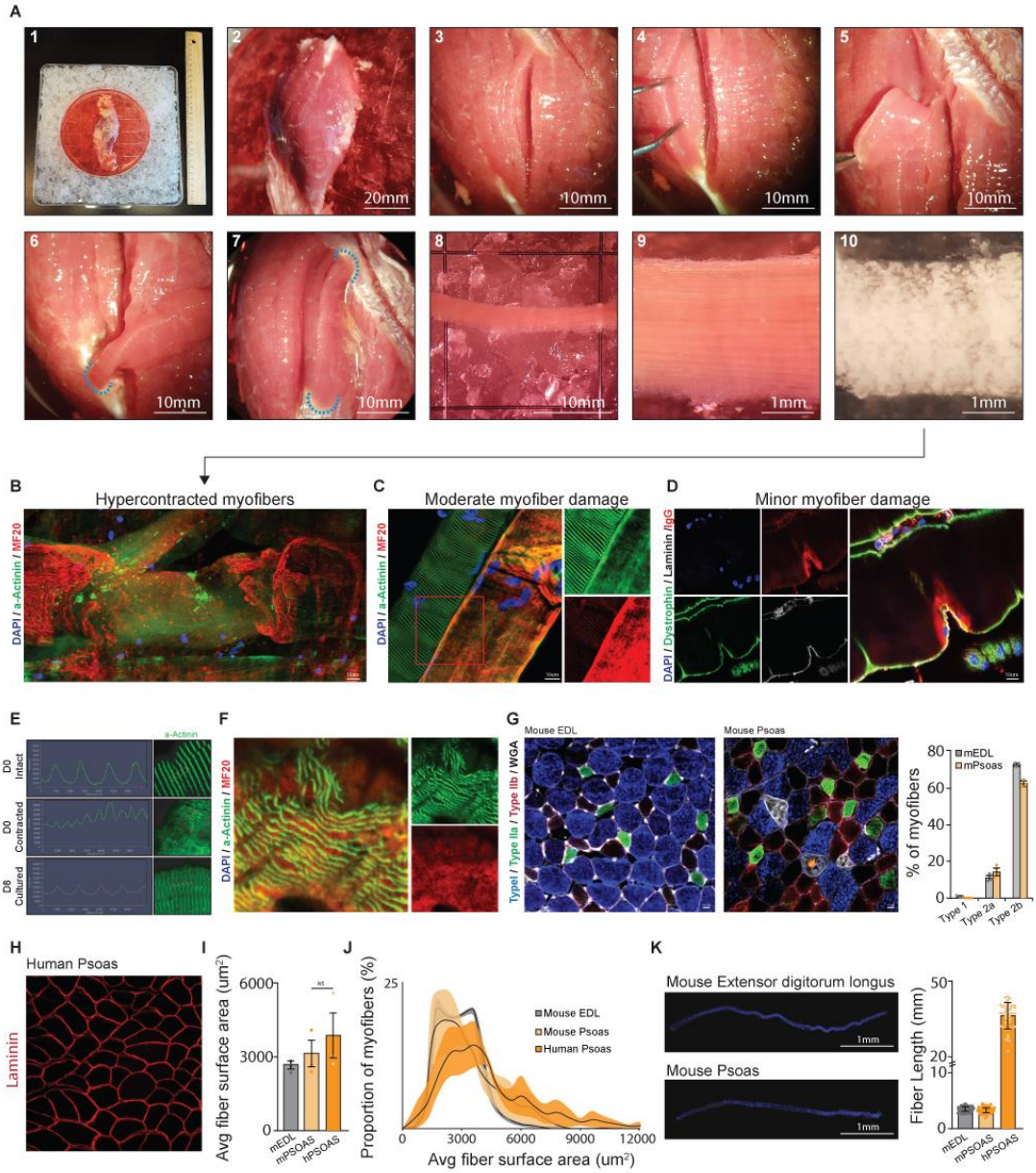


Figure S20: **Myofibres from human *Psoas* muscle can be maintained *in situ*, Related to Figure 31.** A) Photographic overview of human *Psoas* minor myofibre bundle isolation showing expanded images of intact myofibre bundles (panel 9) and hypercontracted myofibre bundles (panel 10). Representative images of B) hypercontracted myofibres and C) myofibres with moderate damage stained for DAPI (Blue), α-Actinin (Green) and Myosin heavy chain (MF20, Red). D) Representative image of myofibres with minor damage stained for DAPI (Blue), Dystrophin (Green), Laminin (White) and IgG (Red). E) Representative images of single myofibre sarcomeres from intact, contracted and cultured myofibres stained with α-actinin (Green) showing representative histograms of staining intensity and sarcomere spacing. F) Representative image of disorganized sarcomeres from injured myofibres stained with α-Actinin (Green) and MF20 (Red). G) Representative images and quantification of myofibre type from mouse *Extensor Digitorum Longus* and mouse *Psoas* muscle stained with Type 1 myofibres (Blue), Type 2a myofibres (Green),

Type 2b myofibres (Red) and Wheat germ agglutinin (White). H) Representative image of human *Psoas* muscle cross-sections stained with Laminin (Red) with I) quantification of average myofibre surface area and (J) myofibre surface area proportion from human *Psoas* myofibres compared to mouse *Extensor Digitorum Longus* and mouse *Psoas* muscles using SMASH software. K) Representative image and quantification of mouse *Extensor Digitorum Longus* and mouse *Psoas* myofibre lengths from isolated single myofibres. (K) Error bars represent mean ± SD, (G-J) Error bars represent mean ±SEM; (G, I-J) n = 3 biological replicates, (K) n = 40 myofibres per condition.

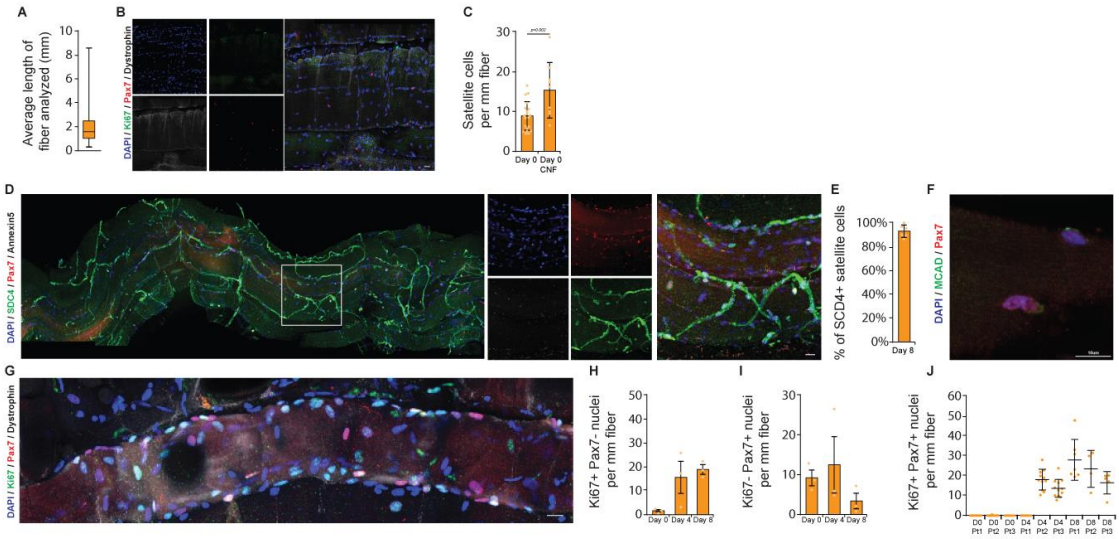


Figure S21*:* **Human satellite cells expand in situ, Related to Figure 32.** A) Quantification of the average length of myofibre analyzed per experiment, whiskers represent min and max. B) Representative image of human myofibres showing centrally located nuclei stained with DAPI (Blue), Ki67 (Green), Pax7 (Red) and Dystrophin (White) and C) quantification of satellite cells per mm myofibre present at isolation on centrally nucleated fibres (CNF). D) Representative image of myofibres stained with DAPI (Blue), SDC4 (Green), Pax7 (Red) and Annexin-5 (White) with E) quantification of satellite cells expressing SDC4 at day 8 in culture. F) Representative image of satellite cells expressing M-Cadherin after isolation stained for DAPI (Blue), MCAD (Green) and Pax7 (Red). G) Representative image of satellite cell expansion on myofibres following 8 days in culture stained with DAPI (Blue), Ki67 (Green), Pax7 (Red) and Dystrophin (White) and quantification of H) Ki67 expression non-satellite cells per mm of myofibre, I) the number of KI67 negative satellite cells per mm of myofibre and J) Ki67 expressing satellite cells per mm of myofibre across samples. (A, C, E, J) Error bars represent mean ± SD, (H-I) Error bars represent mean ± SEM; (A) n = 351 myofibres. (C) n = averages from 20 (non-CNF) and 9 (CNF) myofibres, (E) n = 6 myofibres. (H-I) n = 3 biological replicates. (J) n = averages from 4-22 myofibres, where individual data points represent individual myofibres.

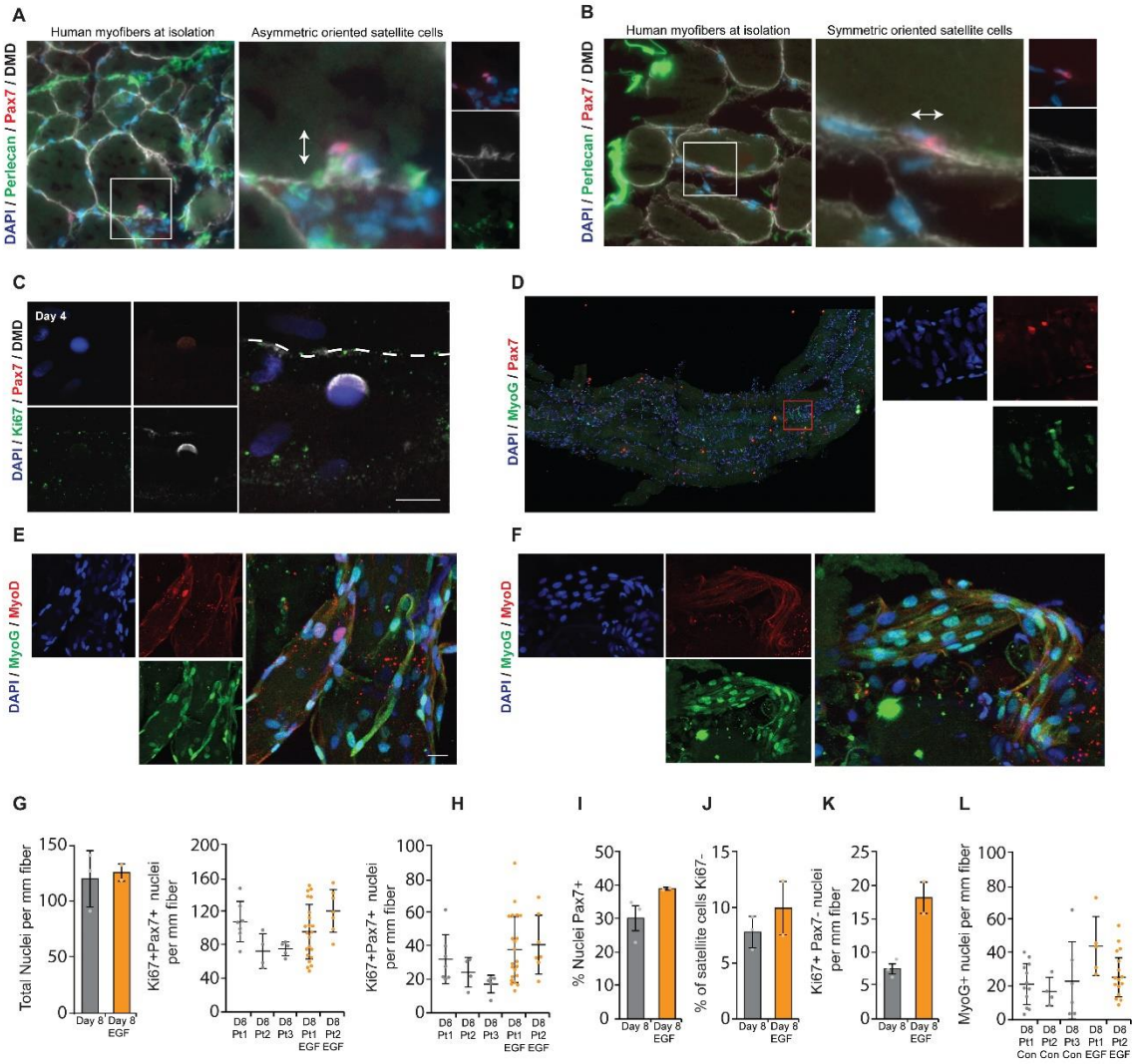


Figure S22*:* **Myofibre culture unveils unique regenerative phenomena, Related to Figure** 33. Representative images of A) apical-basal oriented and B) planar oriented satellite cells in the niche at isolation stained with DAPI (Blue), Perlecan (Green), Pax7 (Red) and Dystrophin (White). C) Representative image of human satellite cells cultured for four days and stained with DAPI (Blue), Ki67 (Green), Pax7 (Red) and Dystrophin (White). D) Representative image of cultured myofibre bundle stained for DAPI (Blue), MyoG (Green) and Pax7 (Red). E) Representative image of myogenic progenitors and F) *in situ de novo* myofibre repair from fibres stained with DAPI (Blue), MyoG (Green) and MyoD (Red). Quantification of G) total nuclei per mm of myofibre and across samples. H) Quantification of human satellite cells expressing Ki67 per mm of fibre across samples following culture in control or EGF containing media. I) Quantification proportion of nuclei expressing pax7 per myofibre. Quantification of J) proportion of satellite cells stained negative for Ki67 and K) proportion of non-satellite cells expressing Ki67 following culture in control or EGF containing media. L) quantification of MyoG-expressing nuclei per mm of myofibre across samples. (G, H, L) Error bars represent mean ±SD, (G, I-K) Error bars represent means ± SD (EGF) and mean ± SEM (Control); (G-K) n= 2 biological replicates

EGF, 3 biological replicates control, (G, H, L) n = 4-32 myofibres, where individual data points represent individual myofibres.

| Patient # | Date of isolation | Sex | Age | Clinical complication | *Psoas* mass | *Psoas* length | Notes (perfusion solution) |
|---|---|---|---|---|---|---|---|
| 1 | 15 April 2019 | F | 68 | Subarachnoid hemorrhage anoxic brain injury | 22.10 g | 10.95cm | Perfadex organ presentation solution |
| 2 | 23-May-19 | F | 64 | Subarachnoid hemorrhage | 12.06 g | 9.55cm | Belzer UW cold storage solution |
| 3 | 7-Jul-19 | M | 50 | Unknown | 38.9g | 13.78cm | Custadiol HTK |

Table S4***:*** **Patient information used in this study**. Patient information including date of isolation, sex, age, clinical complication, *Psoas* muscle mass, length and perfusion solution used during isolation.